

Iridium oxohydroxide electrocatalysts for the oxygen evolution reaction

vorgelegt von
Master of Science
Cyriac Massué
geb. in Strasbourg (Frankreich)

von der Fakultät II - Mathematik und Naturwissenschaften
der Technischen Universität Berlin
zur Erlangung des akademischen Grades

Doktor der Naturwissenschaften
- Dr.rer.nat. -

genehmigte Dissertation

Promotionsausschuss:

Vorsitzender: Prof. Dr. rer. nat. Martin Lerch
Berichter/Gutachter: Prof. Dr. rer. nat. Martin Muhler
Berichter/Gutachter: Prof. Dr. rer. nat. Robert Schlögl
Berichter/Gutachter: Prof. Dr. rer. nat. Peter Strasser

Tag der wissenschaftlichen Aussprache: 9. Mai 2016

Berlin 2016

“Scio me nihil scire“

-Socrates-

Acknowledgements

I hereby would like to express my sincere gratitude to my advisor Prof. Dr. Robert Schlögl, Director of the Department of Inorganic Chemistry at the Fritz-Haber-Institute of the Max-Planck-Society for his constant support and scientific guidance. He has been the source of numerous inspiring suggestions and remarks that opened up new perspectives onto the present subject. My position in his department provided me with the opportunity to use a wide array of powerful characterization techniques, while relying on the advice of experienced scientists.

I would also like to express many thanks to my supervisor Dr. Sébastien Cap, leader of the “Electrochemistry and charge transport” group, for his continuous help and pertinent suggestions, which proved especially helpful during the writing process.

I would like to particularly acknowledge Prof. Dr. Peter Strasser and Prof. Dr. Martin Muhler, who accepted to invest their time in reviewing this work. Additional gratitude goes to Prof. Dr. Martin Lerch for taking the chair of the examination board.

I thank my co-authors for their contributions to the manuscripts included in this dissertation, in alphabetical order: Gerardo Algara-Siller, Sébastien Cap, Xing Huang, Johannes Noack, Verena Pfeifer, Chinmoy Ranjan, Robert Schlögl, Maurice Van Gastel. I would especially like to thank Verena Pfeifer for her tremendous support during several beam times at Bessy and all the technical staff of the department for their invaluable help with sample characterization.

Scientific discussions with Verena Pfeifer and Michael Scherzer in the framework of the monthly “Ir-coffee” played a crucial role in directing my scientific progression. Further discussions with Andrey Tarasov, Pierre Schwach and Detre Teschner were essential in uncovering fundamental aspects of the present work. Last but not least, special thanks go to my colleagues for the many pleasant moments spent together during and outside work that made me enjoy my time at the institute.

I also thank the Bundesministerium für Wirtschaft und Industrie for providing funding to the “Ekolyzer” project in the framework of which this work was conducted.

Last but not least I would like to thank my friends and family for their unwavering support.

Abstract

The synthesis of a highly active and yet stable electrocatalyst for the anodic oxygen evolution reaction (OER) remains a major challenge in making proton exchange membrane (PEM)-based water splitting an industrially relevant solution for chemical energy storage. Under the highly acidic and corrosive conditions of PEM-based water splitting, Ir-electrocatalysts have so far yielded the most promising results but lead to high material costs. In order to improve Ir-utilization, we loaded iridium on conductive antimony-doped tin oxide (ATO)-nanoparticles via a microwave-supported hydrothermal route. The resulting Ir-nanoparticles on ATO were identified as highly hydrated Ir^{III/IV}-oxohydroxides, which showed superior OER-performance in comparison with benchmarks reported in the literature. Gradual alterations to the Ir-phase via thermal treatment showed that the unprecedented OER-performance was prominently linked to the superior intrinsic activity of the produced Ir^{III/IV}-oxohydroxide.

In order to gain a deeper understanding of the OER-relevant features of such amorphous Ir-oxohydroxides without the influence of a support, we prepared a series of pure Ir-oxohydroxides via a microwave-supported hydrothermal route. Systematic synthesis parameter variations led to the preparation of a series of Ir-oxohydroxides within a wide range of oxidation states, chemisorbed water fractions and related OER-performance. For electrode loadings as low as 20 $\mu\text{g}_{\text{Ir}}\cdot\text{cm}^{-2}$, excellent OER-performance was achieved for the best compounds. Therefore such amorphous Ir^{III/IV}-oxohydroxides bridge the gap between electrodeposited amorphous IrO_x-films prone to corrosion and less active crystalline IrO₂-electrocatalysts prepared via calcination routes.

Structural differences within a vast portfolio of Ir-oxohydroxides were compared to trends in OER-performance in order to identify performance-relevant species. An ab-initio calculated model allowed us to identify reactive, formally O⁻-species stabilized in an Ir^{III}-rich environment. These O 2p hole states were studied using synchrotron-based XPS and XAS and were quantified via reactive CO-titration. Concomitant trends in O⁻-amounts and OER-performance allowed us to relate the outstanding electrocatalytic OER-performance of Ir^{III/IV}-oxohydroxides to their ability to accommodate stable O⁻-rich precursor sites. The CO-titration also highlighted the ability of sub-surface O⁻ to migrate to the surface, suggesting the involvement of the 3D-structure of Ir-oxohydroxides during OER-catalysis. The identification of these key features controlled by synthetic parameters of our microwave-supported hydrothermal synthesis allows for a new targeted approach to Ir-based OER-catalyst design.

Zusammenfassung

Die Herstellung eines hoch aktiven und stabilen Elektrokatalysators für die anodische Wasseroxidation stellt eine mächtige Hürde für die kommerzielle Anwendung von Proton-Austausch-Membranen (PEM)-basierender Wasserspaltung für chemische Energiespeicherung dar. Unter den stark korrodierenden sauren Bedingungen in einer PEM-Zelle zeigen Ir-basierende anodische Elektrokatalysatoren bisher die beste Kombination von hoher Aktivität und Stabilität. Ihre Anwendung führt aber zu hohen Materialkosten. Um die Verwendung des teuren Ir-Materials zu optimieren wurde leitfähiges Antimon-gedoptes Zinnoxid (ATO) über eine Mikrowellen-gestützte hydrothermale Syntheseroute mit Ir- beladen. Die resultierenden Ir-Nanopartikel auf ATO wurden als stark hydratisierte Ir^{III/IV}-Oxohydroxide identifiziert, die im Vergleich mit Literaturwerten überlegene Leistung in der sauren anodische Sauerstoffentwicklungsreaktion vorweisen. Stufenweise thermische Behandlung des Ir/ATO-Elektrokatalysator zeigte dass die überragende elektrokatalytische Leistungsfähigkeit größtenteils aus der hohen intrinsischen Aktivität der Ir^{III/IV}-Oxohydroxide resultiert.

Um ein tieferes Verständnis der elektrokatalytisch relevanten Merkmale der amorphen Ir^{III/IV}-Oxohydroxide ohne den Einfluss des Trägermaterials zu gewinnen, wurde eine Reihe von reinen Ir^{III/IV}-Oxohydroxiden über eine Mikrowellen-gestützte Hydrothermalsynthese hergestellt. Die systematische Variation relevanter Syntheseparameter führte zur Herstellung einer Reihe von Ir^{III/IV}-Oxohydroxiden in einem breiten Bereich von Oxidationszuständen, chemisorbierter Wasseranteile und damit verbundener OER-Leistungen. Für Elektrodenbeladungen von 20 $\mu\text{g}_{\text{Ir}}\cdot\text{cm}^{-2}$, konnte ausgezeichnete OER-Leistung für die besten Materialien erreicht werden. Somit bilden amorphe Ir^{III/IV}-Oxohydroxide ein Bindeglied zwischen galvanisch abgeschiedenen leicht korrodierenden amorphen IrO_x-Filmen und kristallinen wenig aktiven IrO₂-Elektrokatalysatoren, die meistens über Kalzinierungsschritte hergestellt werden.

Strukturelle Unterschiede innerhalb eines umfangreichen Portfolios von Ir^{III/IV}-Oxohydroxiden wurden mit Trends in der OER-Leistungsfähigkeit verglichen um Aktivitäts-relevante Spezies und strukturelle Eigenschaften zu identifizieren. Ein ab-initio gerechnetes Modell erlaubte uns reaktive, formale O⁻-Sauerstoffspezies zu identifizieren, die von einem Ir^{III}-reichen Umfeld stabilisiert werden. Diese O 2p Loch-Zustände wurden unter Verwendung von Synchrotron-XPS und XAS untersucht und wurden über reaktive CO-Titration quantifiziert. Übereinstimmende Trends in O⁻-Gehalt und elektrokatalytischer Leistung erlaubten es uns, die hervorragende Leistungsfähigkeit von Ir^{III/IV}-Oxohydroxiden mit ihrer Fähigkeit stabile O⁻-Sauerstoffspezies aufzunehmen, in Verbindung zu bringen. Die CO-Titration zeigt auch die Fähigkeit der tiefer gelegenen O⁻-Sauerstoffspezies an die Oberfläche zu wandern, was auf die Beteiligung der 3D-Struktur von Ir^{III/IV}-Oxohydroxiden während der Wasseroxidation hinweist. Die Identifizierung dieser wichtigen Merkmale amorpher Ir-Oxohydroxide ermöglicht eine neue zielgerichtete Herangehensweise an die Synthese Ir-basierender Elektrokatalysatoren für die saure Wasseroxidation, mittels Mikowellen-gestützter Hydrothermalsynthese.

Table of Contents

Acknowledgements.....	v
Abstract.....	vii
Zusammenfassung	ix
Table of Contents.....	xi
List of Tables	xiv
List of Figures	xiv
Abbreviations.....	xvii
1. Introduction	1
1.1. The energy transition: A systemic challenge	1
1.2. Hydrogen-based chemical energy storage	2
1.3. H ₂ -production from water splitting	3
1.3.1. Thermodynamic aspects	4
1.3.2. Mechanistic aspects of the OER.....	6
1.3.3. Predicted activity trends of OER-electrocatalysts.....	7
1.4. Practical OER-electrocatalysis.....	9
1.4.1. Electrolysis in basic vs. acidic media	9
1.4.2. Iridium for OER: the challenge of rare metals	13
1.4.3. Synthesis strategies of Ir-based OER-catalysts	13
1.4.4. OER-catalyst supports.....	16
1.4.5. Stability-influencing factors	17
1.5. Aims and outline of the present work	20
1.6. References	22
2. Identification of key features in a high-performance Ir/ATO-electrocatalyst for the Oxygen Evolution Reaction	25
2.1. Abstract.....	25
2.2. Introduction	25
2.3. Experimental.....	27
2.3.1. ATO synthesis.....	27
2.3.2. Ir-loading of ATO	28
2.3.3. Sample characterization	28
2.3.4. Electrochemical characterization.....	30
2.4. Results and discussion	31

2.4.1.	Catalyst support (ATO) synthesis and characterization	31
2.4.2.	MW-assisted hydrothermal synthesis of MW-Ir/ATO	32
2.4.3.	Physico-chemical characterization of MW-Ir/ATO	33
2.4.4.	XPS-analysis of Ir-species	36
2.4.5.	OER-performance of MW-Ir/ATO	37
2.4.6.	Effect of thermal treatment on MW-Ir/ATO.....	38
2.4.7.	Thermally-induced structural changes.....	38
2.4.8.	Effect of thermal treatment on OER-performance.....	47
2.5.	Conclusion.....	49
2.6.	Acknowledgements.....	49
2.7.	Supporting information	50
2.8.	References	59
3.	Synthesis of stable and highly active Ir-oxohydroxides for electrochemical oxidation of water .	61
3.1.	Abstract.....	61
3.2.	Introduction	61
3.3.	Experimental.....	62
3.3.1.	MW-assisted hydrothermal synthesis of Ir-oxohydroxides	62
3.3.2.	Sample characterization	62
3.3.3.	Electrochemical characterization.....	63
3.4.	Results and discussion	64
3.4.1.	Importance of the initial KOH:Ir-ratio.....	64
3.4.2.	Sample composition.....	66
3.4.3.	OER-performance.....	67
3.5.	Conclusion.....	70
3.6.	Acknowledgements.....	70
3.7.	Supporting information	70
3.8.	References	83
4.	OER-relevant fingerprints of Ir-oxohydroxide electrocatalysts	85
4.1.	Abstract.....	85
4.2.	Introduction	85
4.3.	Experimental.....	87
4.3.1.	TEM of beam sensitive samples.....	87
4.3.2.	Synchrotron-base X-ray Photoemission and absorption spectroscopy.....	87
4.3.3.	Raman spectroscopy and DFT-calculations of Ir-structures	87

4.3.4.	Electrochemical characterization.....	87
4.3.5.	CO-titration of reactive oxygen species.....	88
4.3.6.	DRIFTS of low-temperature CO-adsorption.....	88
4.4.	Results and discussion	88
4.4.1.	OER-performance.....	88
4.4.2.	TEM-investigation of Ir-oxohydroxides.....	89
4.4.3.	Raman-spectroscopy of Ir-oxohydroxides	90
4.4.4.	X-ray photoemission spectroscopy.....	93
4.4.5.	X-ray absorption spectroscopy	94
4.4.6.	CO-titration of reactive oxygen species.....	95
4.4.7.	Low-temperature CO-adsorption.....	98
4.4.8.	CO-titrated O-species and link with OER-performance	100
4.5.	Conclusion.....	102
4.6.	Acknowledgements.....	102
4.7.	Supporting information	103
4.8.	References	115
5.	Summary and final conclusions	117
	References	120
6.	Appendix I : List of samples.....	121
7.	Appendix II: UV-Vis study of redox-processes and hydrolysis in K_2IrCl_6/KOH -solutions.....	123
7.1.	UV-Vis studies of solvated Ir-species in the literature.....	123
7.2.	UV-Vis study of precursor solution for the MW-synthesis	125
7.3.	References	128
8.	Appendix III: ICP-OES-study of Ir-dissolution during OER-catalysis	129
8.1.	Experimental setup	129
8.2.	Results.....	130
9.	Information about the author.....	133
	Personal information	133
	Education	133
	List of publications	133
	Talks at conferences	134
	Poster contributions at conferences as presenting author	134

List of Tables

Table 2.1 Summary of sample designations used throughout the text.....	27
Table 2.2 Benchmarking parameters for the most performant samples compared to previously reported reference compounds during a galvanostatic measurement at $10 \text{ mA}\cdot\text{cm}^{-2}$	38
Table 2.3 Specific surface areas of MW-Ir/ATO and thermally treated products	39
Table 2.4 Characteristic values extracted from TPR-profiles including the H_2 -uptake at RT ($n_{\text{H}_2,\text{RT}}$), the H_2 -consumption during TPR ($n_{\text{H}_2,\text{TPR}}$) and the resulting calculated average oxidation state of Ir.....	46
Table 3.1 Benchmarking parameters for the best MW-compound (KOH:Ir=5:1) compared to previously reported compounds and reference samples	68
Table 6.1 List of relevant samples described in this work with corresponding nomenclature and their associated FHI-database ID.....	121
Table 7.1 Absorption bands of iridium-complexes reported in the literature	125

List of Figures

Figure 1.1 OER-activity trends for oxides. The negative theoretical overpotential is plotted against the standard free energy of $\Delta G_{\text{HO}} * -\Delta G_{\text{O}}$ -step. Taken from ref. ²⁶	8
Figure 1.2 Standard electrochemical cell consisting of three compartments separated by fine-porosity glass frits.	9
Figure 1.3 Schematic representation of an alkaline water electrolysis cell	11
Figure 1.4 Schematic representation of a PEM water electrolysis cell.....	12
Figure 2.1 Diffuse reflectance UV-Vis spectra of commercial reference samples (dotted lines) as well as ATO obtained from the MW-treatment of a colloidal Sb/Sn-suspension at various temperatures (full lines).....	31
Figure 2.2 ADF-STEM imaging of MW-Ir/ATO with corresponding EDX-based elemental mapping	33
Figure 2.3 TG-MS curves for the decomposition of MW-ATO and MW-Ir/ATO in oxidative ($21\% \text{O}_2/\text{Ar}$) and inert (Ar) gas streams.....	34
Figure 2.4 TPR-profiles of MW-ATO, MW-Ir/ATO and SA-IrO ₂	35
Figure 2.5 XPS of MW-Ir/ATO in the Ir4f-region fitted using the models developed by Pfeifer et al. ^{42,43}	37
Figure 2.6 ADF-STEM imaging of Ir ₂₅₀ O ₂ (a) and Ir ₃₅₀ O ₂ (b).....	39
Figure 2.7 <i>In-situ</i> STEM observation of Ir ₃₅₀ O ₂ over 210 s showing the evolution of sample morphology under the electron beam. The ADF-STEM imaging allows to relate contrast changes to heavier (brighter) or lighter (darker) atoms.	40
Figure 2.8 DRIFTS measurements ($5500\text{-}2000 \text{ cm}^{-1}$) of MW-Ir/ATO during stepwise treatment at various temperatures in $21\% \text{O}_2/\text{Ar}$, $100 \text{ mL}\cdot\text{min}^{-1}$. Kubelka-Munck transformation of the reflectance spectra (a) and corresponding difference spectra between said temperature and 100°C (b).....	41
Figure 2.9 DRIFTS measurement of MW-Ir/ATO (Kubelka-Munck transformation, $1000\text{-}500 \text{ cm}^{-1}$) during stepwise treatment at various temperatures in $21\% \text{O}_2/\text{Ar}$, $100 \text{ mL}\cdot\text{min}^{-1}$	42
Figure 2.10 Raman spectra of the support (MW-ATO), of the as prepared MW-Ir/ATO as well as after thermal treatment at 250 or 350°C in $21\% \text{O}_2/\text{Ar}$ (a) or $100\% \text{ Ar}$ (b).....	44
Figure 2.11 TPR-profiles of MW-Ir/ATO (green line), and the samples obtained after treating MW-Ir/ATO in $21\% \text{O}_2/\text{Ar}$ (full lines) and Ar (dotted lines) at 250°C (a, orange) and 350°C (b, red).	45

Figure 2.12 Loading-dependent mass activity at $\eta=0,35V$ before (plain bars) and after CP at 10 mA.cm ⁻² (patterned bars) for (a) MW-Ir/ATO (a) and its thermally treated products (b) Ir_250_O ₂ , (c) Ir_350_O ₂ , (d) Ir_250_Ar and (e) Ir_350_Ar.	48
Figure 3.1 SEM of the catalyst synthesized with KOH:Ir = 5:1 (a) shows a highly nanostructured material, whereas for KOH:Ir = 50:1 (b) big clusters are formed. Secondary electron contrasted-imaging of such a split cluster (c) reveals a core-shell structure, where the metallic iridium (bright twin-cores, A) is coated with a thick layer of oxidic iridium (B). (d) Linescan (green arrow) confirms lower O/Ir-ratio in the cores.	65
Figure 3.2 Temperature programmed reduction in 4.92% H ₂ /Ar exhibits sharp reduction features below 100°C that are significantly distinct from the characteristic reduction feature of IrO ₂ to Ir ⁰ above 200°C as observed with the benchmark catalyst SA-IrO ₂	66
Figure 3.3 OER-activity and -stability of samples prepared at 250°C, 1h correlate and show that the most active and stable sample has been produced with a ratio KOH:Ir of 5:1 at 250°C during 60 minutes.	67
Figure 3.4 MS-coupled (m/z=18) thermogravimetric analysis shows that the most active samples exhibit a strong fraction of hydroxyl groups ($\chi_{H_2O.chem.}$) removed in TGMS at temperatures above approx. 140°C (blue bars). The quantification of hydrogen uptake by the sample at room temperature and during TPR allows for the determination of an average oxidation state for the oxidic phase. The best sample (KOH:Ir=5:1) is highlighted in the red dashed box.....	69
Figure 4.1 OER-activity reflected by the overpotential η needed to reach $j=10$ mA.cm ⁻² (red bars) and OER-stability indicated by stable operation at 15 mA.cm ⁻² (green bars) tend to worsen for the MW-samples with increasing average oxidation state of the oxidic Ir-phase (blue crosses). Black numbers indicate X in MW_X, the initial KOH:Ir ratio.	89
Figure 4.2 The SAED patterns and radial profiles for MW_5 (a) under low electron dose and (b) with high electron dose shows the complete transformation of the initial amorphous Ir-oxohydroxide to metallic iridium after beam irradiation.....	90
Figure 4.3 Raman-spectra of the MW-prepared Ir-oxohydroxides show distinctive features in the 300-750 cm ⁻¹ area. Average oxidation states indicated on the right have been calculated from H ₂ -TPR.	91
Figure 4.4 DFT-calculated structure of a bis- μ -oxo Ir ^{IV} -trimer. Blue atoms are H, red atoms are O, purple atoms are Ir.	92
Figure 4.5 DFT-calculated structure of a reduced Ir ^{III/IV} -trimer. Blue atoms are H, red atoms are O, and purple atoms are Ir.	92
Figure 4.6 XPS-spectra of (a) MW_5 and (b) MW_100 in the Ir4f-region for 450 eV excitation energy show the contributions from Ir ^{III} - and Ir ^{IV} -species. The average oxidation state calculated from the fit is indicated in the top right corner.	93
Figure 4.7 NEXAFS-spectra observed for MW-prepared Ir ^{III/IV} -oxohydroxides as well as reference samples SA-IrO ₂ and AA-IrO _x	94
Figure 4.8 A CO-feed in inert gas was used to titrate O*. Numbers correspond to the KOH:Ir-ratio X identifying the samples MW_X.(a) Gas detected for MW_5 during two subsequent switches from pure He to 1%CO/He. (b) Total amount of evolved CO ₂ (blue bars) and CO ₂ :Ir-ratio (black dots). (c) The Ir-specific OER mass activity at $\eta=0,35V$ is shown as a function of the total amount of evolved CO ₂ . (d) Initial CO ₂ -evolution rates plotted against the specific surface area.	96
Figure 4.9 DRIFTS spectra of MW_5 under 10 mbar CO during the warm-up procedure from liquid-nitrogen- to room-temperature (a) in the OH-region and (b) in the CO ₂ -region. The inset in (b) shows	

the approx. area under the CO ₂ -related peak as a function of temperature during the first experiment and during its repetition with the same sample.	99
Figure 4.10 CO-treated MW_5 was tested (a) for OER-activity using LSV and (b) for OER-stability using CP and compared to pristine MW_5 for electrode loadings of 20 μg _{Ir} .cm ⁻²	101
Figure 7.1 UV-Vis absorbtion spectra of different KOH/K ₂ IrCl ₆ solutions at RT one hour after mixing (K ₂ IrCl ₆ 0,01 mol.L ⁻¹ , varying KOH:Ir ratio).	126
Figure 7.2 UV-Vis absorbtion spectra of a KOH/K ₂ IrCl ₆ (KOH:Ir=1:1) solution at RT after mixing over 15 days	126
Figure 7.3 UV-Vis absorbtion spectra of a KOH/K ₂ IrCl ₆ (KOH:Ir=4:1) solution at RT after mixing over 15 days	126
Figure 7.4 UV-Vis absorbtion spectra of a KOH/K ₂ IrCl ₆ (KOH:Ir=50:1) solution at RT after mixing over 15 days	126
Figure 7.5 Enlargement of the UV-Vis spectra obtained for KOH:Ir=50:1	127
Figure 8.1 Ir-species detected via ICP-OES (blue lines) in the electrolyte flowing through an electrochemical water splitting cell during a CP-measurement conducted at 10 mA.cm ⁻² (anode potentials in black vs. SHE) for anodes coated with (a) AA-IrO _x , (b) MW_5, (c) MW_7, (d) MW_50.	130
Figure 8.2 LSV-measurements (5 mV.s ⁻¹) before (black line) and after the 2h-CP-stability test (red line) for (a) AA-IrO _x , (b) MW_5, (c) MW_7, (d) MW_50.	131

Abbreviations

ADF-STEM	annular dark field contrasted scanning transmission electron microscopy
BE	binding energy
BET	Brunauer Emmett Teller
CE	counter-electrode
DFT	density functional theory
DSA	dimensionally stable anode
ECSA	electrochemically active surface area
HAADF-STEM	high angle annular dark field- scanning transmission electron microscopy
HER	hydrogen evolution reaction
LMCT	ligand-to-metal charge transfer
MS	mass spectrometry
OER	oxygen evolution reaction
PCmET	proton coupled multi electron transfer
RDE	rotating disk electrode
RHE	reversible hydrogen electrode
RRDE	rotating ring disk electrode
RT	room temperature
SAED	Selected area electron diffraction
SCE	saturated calomel electrode
SEM	scanning electron microscopy
SHE	standard hydrogen electrode
TEM	transmission electron microscopy
TGMS	thermogravimetry coupled with MS-analysis of evolved gas
TPR	temperature-programmed reduction
WE	working electrode

1. Introduction

1.1. The energy transition: A systemic challenge

At the beginning of the 20th century, the development of the Haber-Bosch process enabled the industrial production of inexpensive nitrogen-based fertilizers, thus securing the food supply of the world's growing population. This invention allowed us to overpass the symbolic four billion people barrier.¹ One century later humanity is facing yet another major challenge: demographic pools are booming in rapidly developing countries and this time the supply of energy is becoming a risk factor: The growing demand for Western living standards will ultimately lead to a need for energy unseen on this scale. Authors estimate that if the world population of 9.4 billion projected for 2050 was to adopt the current standard of living of a U.S. resident, this would lead to an astronomical energy consumption rate of 106 TW in 2050, compared to 16.2 TW in 2007.^{2,3} Even the most conservative predictions foresee twice our current energy demand for 2050 and three times as much for 2100. Established industrial nations have a role model to play but it's the path that developing countries will take, that will tip the balance.

The temptation is great to meet this demand with traditional energy sources. Since the Second Industrial Revolution, great industrial nations have built up an extensive centralized power distribution system where energy is produced in sizable power plants from elite natural resources by few big energy companies. As an example, China's energy needs rely by 70% on coal and considering the current evolution and future trend, the easiest way to meet the demand would be the expansion of the extensive network of coal mines, distribution facilities and coal-powered power plants.³ This is a general scheme in fast developing countries. However if the energy demand of such nations is met with fossil energy carriers like coal, oil and gas, the atmospheric CO₂-concentration is likely to have tripled by the end of the century.⁴ Regardless of the potentially disastrous consequences of such greenhouse gas emissions, our current energy sources cannot support such an evolution in a sustainable way. In the case of oil, the IAE sent a deep shock wave through the international community when they pointed out in their 2010 World Energy Outlook report that the world's oil production had reached its global peak in 2006 at around seventy million barrels per day.⁵ From now on, oil production will start to decrease as production costs rise. Coal and natural gas should follow much similar patterns once they reach their respective production peaks in the early 21st century. Hence, the shift away from fossil energy carriers is not only an imperative in order to limit our soaring greenhouse gas emissions. Above all, it's a simple economic imperative.

Nuclear power is often advocated as the ripest alternative to fossil energy sources. Nuclear fission-based energy production is a CO₂-emission free process. However accidents like Three Mile Island (1979), Chernobyl (1986) and the latest Fukushima incident (2011) have considerably altered public acceptance due to the potential risk it poses to human health. Also waste management and disassembly of retired power plants is a considerable and costly challenge that requires technical know-how and extensive management facilities. Those issues combined with the sizeable investment a single nuclear power plant represents, make it difficult to implement such energy sources in fast developing countries that lack available financial resources and qualified personnel, not to mention the geopolitical threat the proliferation of radioactive material can represent in politically unstable countries. Another long established alternative, hydro-electrically generated

power is also limited in its scope as its implementation at a given geographic location strongly depends on topography and hydrography of the region.

As a result, great hopes rely on renewable energy sources (RES) like wind turbines and solar photovoltaics. Sunlight is by far the biggest energy reserve available to mankind. The sun dispenses more free energy onto the earth in one hour than humanity consumes over a whole year.³ However, the intermittent nature of renewable energy sources (RES) considerably inhibits their widespread use for the time being. As an example, in Spain, on November 9th 2009 wind generated power reached a record high of 54% of instant demand, whereas on June 26th 2010, power harvested from wind represented only 1% of the demand.⁶ This illustrates why the implementation of RES into the power grid doesn't come down to the simple one-to-one replacement of one energy source by another. The energy grid from the production source to the final consumer is a complex interconnected network. A central issue for the reliable implementation of RES into the power grid is the integration of efficient energy storage technologies into the energy supply chain in order to maintain constant electricity flow over different periods of low and high demand and/or production. Such systems will regulate the amount of electricity fed to the grid, enabling a stable and reliable contribution from RES. Thus an efficient storage system is a bottleneck condition for the gradual replacement of traditional energy sources by RES.

1.2. Hydrogen-based chemical energy storage

Some technologies, like pumped hydro-electric storage have already been in use on a daily basis for decades. The pumped energy storage plant of "Lac Blanc-Lac Noir" in the French Vosges for instance was built in 1933.⁷ However such storage facilities can only be implemented in a limited number of locations. Rechargeable batteries have come under intense focus as they allow for the storage of electrical energy in mobile devices ranging from mobile phones to cars.⁸ Due to low storage capacities, their scope of implementation remains however adapted mostly to small-scale applications. In this regard, chemical energy storage has been identified as the most promising technology for large-scale energy storage:⁹ In such a scenario, when the supply of energy harvested from RES exceeds the demand, the excess is used to produce stable molecules, which store chemical energy reversibly in their bonds. Such energy carriers should then be able to release the stored energy upon demand.

Hydrogen has been identified as a key carrier molecule.^{3,9-13} Indeed hydrogen can be produced from water electrolysis driven by an external voltage. In the case of such an electrochemical process, the respective anodic and cathodic half reactions are catalyzed at the surface of the electrodes following the overall reaction (1.1).



If the required voltage is obtained from RES, this reaction is a carbon-free process as the other by-product is oxygen.¹⁴ Hydrogen is the carrier with the highest energy content per mass unit, up to three times more than methane or gasoline. The stored energy can be recovered by reaction of H₂ with O₂, which produces clean water. This is either done by combustion in turbines or by using fuel cell technologies.¹⁵ H₂ is also a key reactant used by the chemical industry, for instance in the

production of ammonia via the Haber-Bosch process mentioned in the introduction. 96% of the world's hydrogen is currently being produced from steam reforming of fossil fuels, which consists of stripping hydrocarbons of their hydrogen atoms and releases green-house active gases like CO and CO₂. Only the remaining 4% are produced from water electrolysis.¹¹ As a result, the development of efficient hydrogen production through water electrolysis would not only be a key advance for the energy transition but would at the same time provide the chemical industry with one of its most important chemicals in a sustainable way.

For on-site storage, mobile applications and transport, there is however a need to improve the volumetric energy density of H₂. For this purpose chemical and physical storage solutions are under investigation. Especially physical storage solutions in the form of cryogenic and high pressure H₂-tanks developed by major car constructors have attained a high state of technological maturity and cost efficiency.¹⁶ It remains that in a scenario where H₂ is produced in large quantities on local production sites and needs to be redistributed in large volumes, transport of molecular H₂ in large volumes represents a security issue.

As a result, it is desirable to be able to convert hydrogen into safe carrier molecules. It has been proposed to take advantage of carbon capture technologies implemented at large CO₂-emitting facilities like steel mills. These systems could provide CO₂ as a raw material for the H₂-driven production of methanol and other useful hydrocarbons. Such molecules have the advantage that their transport is already being dealt with on a daily basis. Although the theoretical basis of the mechanisms involved in the synthesis of such synthetic fuels is well understood, catalytic systems allowing for large-scale commercial applications remain to be optimized.⁹ An alternative industrial process that is already being used on a very large scale is the previously mentioned synthesis of ammonia from nitrogen and hydrogen.¹⁷ This efficient process has been in place for decades, which implies that large-scale production, storage and transport facilities already exist. Moreover the reverse reaction, the ammonia decomposition reaction, which liberates the stored H₂ is also well-understood, rendering this process one of the most potent candidates for safe H₂-storage and -transport.

Overall it appears that hydrogen will be a fundamental pillar of the energy transition, irrespective of the fact which scenario will predominate. Hydrogen produced from water electrolysis is the only truly renewable scheme for storing energy from RES. It is already an all-important feedstock for the chemical industry and thus some of the infrastructure needed for the new "hydrogen-economy" envisioned by the likes of J. Rifkin¹⁸ is already in place. One can think of large-scale ammonia production and distribution that could be used for chemical H₂-storage. We will now focus on the actual water electrolysis and the technical challenges that constitute a major bottleneck in rendering this technology economically viable.

1.3. H₂-production from water splitting

There are two low-temperature approaches to performing water splitting: In the direct approach, electrocatalysts are coupled to a light-absorbing semi-conductor. The electron-hole pairs induced by solar irradiation of the semi-conductor are captured by the electrocatalysts who perform the half-reactions. Integrated photocatalytic systems inspired by nature's light-harvesting PSII complex have lately received a lot of attention, partly due to D. Nocera's highly advertised Co-based systems.¹⁹⁻²¹

However, photocatalytic water splitting relies on a single type of renewable energy source : solar energy.

In this study we will focus on the indirect approach, which is more suitable for energy storage from multiple sources differing in nature. In this approach, current produced through light-induced charge separation in photovoltaics, induction in wind turbines or any other (renewable) energy source is redirected through wires to two electrodes covered in electrocatalytic material in an electrolyzing setup. There, the resulting difference of potential between the electrodes is used as a driving force for the splitting of water. At the anode, in order to produce one molecule of O₂, two water molecules are oxidized at highly oxidizing potentials and 4 protons as well as 4 electrons are released. At the cathode, the desired hydrogen is produced as a result of the reduction of protons. Hence, water splitting is a proton-coupled four-electron transfer process.

1.3.1. Thermodynamic aspects

The fundamental thermodynamic quantities governing the reaction yield the lower limits to how much electric and thermal energy is needed to drive the water electrolysis.^{11,22} Considering an electrolytic cell operating at constant temperature and pressure, the energy that has to be put into the system in order to drive the water splitting reaction corresponds to the change in enthalpy of the system described by Scheme 1.2. In order to calculate the standard change of enthalpy (standard enthalpy of reaction, ΔH°), one can use the Hess relation :

$$\Delta H^\circ = \sum \nu H_{f,\nu}^\circ \quad (1.2)$$

Knowing that the enthalpy of formation H_f° of an element in its standard state at standard conditions of temperature and pressure is 0:

$$\Delta H^\circ = -H_f^\circ(H_2O) + \frac{1}{2}H_f^\circ(O_2) + H_f^\circ(H_2) = 285.84 \text{ kJ} \cdot \text{mol}^{-1} == 2.96 \text{ eV} \quad (1.3)$$

Knowing that the standard entropies are tabulated as well as the standard enthalpies of formation, one can calculate the standard free Gibbs energy of reaction:²³

$$\Delta G^\circ = \Delta H^\circ - T\Delta S^\circ = 285,84 - 298 \times 0.1631 = 237.21 \text{ kJ} \cdot \text{mol}^{-1} == 2.46 \text{ eV} \quad (1.4)$$

As a result, the water splitting is an endothermic ($\Delta H^\circ > 0$) and nonspontaneous ($\Delta G^\circ > 0$) process. Furthermore two electric quantities can be defined: The reversible electrolysis cell voltage V_{rev} , that is the lowest voltage that has to be applied to the cell in order to drive the reaction :

$$V_{rev} = \frac{\Delta G}{nF} \quad (1.5)$$

Where F is the Faraday constant ($F = 96485.3365(21) \text{ C} \cdot \text{mol}^{-1}$), n is the number of transferred electrons per mol of split water. However this doesn't take into account the change in standard enthalpy ΔS° , which corresponds to additional energy in the form of heat or electricity that has to be

added to the system. Thus, a second minimum standard electrolysis cell potential V_{HHV} known as the higher-heating value potential V_{HHV} can be defined. This potential corresponds to the cell voltage required to drive the electrolysis without additional heating. In an ideal setup, the total energy required corresponds to the enthalpy change ΔH and if the energy corresponding to the term $T\Delta S$ is provided in the form of electricity instead of heating, then one can express V_{HHV} as follows :

$$V_{HHV} = \frac{\Delta H}{nF} \quad (1.6)$$

According to the calculated values, for an ideal electrolysis cell performing water splitting at standard conditions: $V_{rev}^{\circ} = 1,23$ V and $V_{tn}^{\circ} = 1,48$ V. However in a real setup, thermodynamic irreversibilities arise, calling for additional energy input. These are mostly due to water steam in the gas flows, heating the water up to the setup conditions and thermal losses. As a result, the electrolysis cell voltage V_{cell} where water splitting actually occurs is usually superior to V_{HHV} : $V_{cell} > \Delta H / (nF)$.¹¹

$$V_{cell} = V_{rev} + V_{ohm} + V_{act} + V_{con} \quad (1.7)$$

- V_{ohm} corresponds to diverse ohmic losses inside the real electrolysis setup. V_{ohm} is usually proportional to the electric current flowing through the cell.
- V_{con} is due to mass transport limitations in the reactant flow towards- and the product flow from the electrode. It is known as the “concentration overvoltage”. It is usually small compared to other overpotentials.
- V_{act} is known as the “activation overvoltage”. This overvoltage corresponds to the energy activation barrier that electrons have to overcome to go from the reactants to the electrode (oxidation at the anode) or from the electrode to the reactant (reduction at the cathode). In the case of water splitting, the overpotentials mostly arise at the anode : Only two electrons are required to produce one hydrogen molecule, however the concerted release of four electrons is necessary at the anode in order to produce one molecule of oxygen. This process is called a proton coupled multi electron transfer (PCMET).



The water splitting reaction (see Scheme 1.10) produces hydrogen from water, while releasing only oxygen as a side product. The anodic reaction is the oxygen evolution reaction (OER), while the cathodic reaction produces hydrogen through the hydrogen evolution reaction (HER)

In order to minimize energy losses, the overpotentials in the real setup have to be reduced. Minimization of V_{ohm} is mostly achieved through optimization of the conductivity of the cell elements. The activation overvoltage V_{act} at the anode can be reduced by carefully choosing the electrocatalytic material covering the anode.

In order to determine overpotentials at the anode, it is important to know the theoretical equilibrium potential at the electrode under the temperature, pressure and pH-conditions of the setup. This potential is given by the Nernst equation for equation 1.11:

$$E_{O_2/H_2O} = E_{O_2/H_2O}^0 - \frac{RT}{4F} \ln \left(\frac{a_{H_2O}^2}{a_{O_2} a_{H^+}^4} \right) \quad (1.11)$$

Under standard conditions of temperature and pressure, and knowing $E_{O_2/H_2O}^0 = 1.23$ vs. SHE, the equilibrium potential vs. SHE can be expressed as:

$$E_{O_2/H_2O} = 1.23 - 0.059 \times pH \quad (1.12)$$

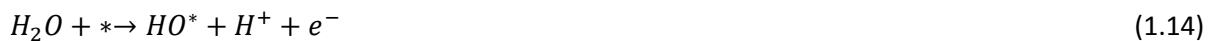
As a result, the overpotential η at the anodic working electrode (WE) driven to a potential E_{WE} (vs. SHE) can be expressed as:

$$\eta = E_{WE} - (1.23 - 0.059 \times pH) \quad (1.13)$$

1.3.2. Mechanistic aspects of the OER

As previously mentioned, most of the overpotentials arise at the anodic OER due to the complexity of the PCmET, which involves several types of adsorbed reaction intermediates. In order to allow for a rational and targeted search for a catalytic material most adapted to minimizing these overpotentials, a lot of effort has gone into understanding the mechanistic aspects of the OER. Indeed, resolving which sequence of elementary steps occurs on what type of material will allow to identify the rate-limiting step, which is responsible for the minimal overpotential required to drive the OER. Depending on the type of catalytic material, three types of reaction on the catalyst surface have been proposed:^{22,24}

Associative OER-mechanism



Dissociative OER-mechanism



Peroxo mechanism



The experimental attribution of one mechanism to a certain catalyst proves to be difficult. Indeed the interpretation of kinetic data and the observation of adsorbed reaction intermediates faces many challenges due in part to the complex three-phase reaction medium at the anode interface.

1.3.3. Predicted activity trends of OER-electrocatalysts

In order to allow for a targeted approach to finding the right catalytic material for OER, theoretical studies have focused on trying to find universal descriptors able to predict the OER-activity on any type of electrocatalytic compound. Studies based on density functional theory (DFT) have been used to show how the binding strength of reaction intermediates to the anode surface during the OER determines the overpotential required to drive the overall reaction.^{25,26} For instance, calculations of the free energies of intermediates on noble metal surfaces (Pt and Au) showed that the difficult step in the reaction consists of the addition of an *OH-group to an adsorbed oxygen atom in order to form adsorbed *OOH.²⁶

Latest attempts by the groups around J. Rossmeisl and J. Nørskov even go a step further and aim at a systematic understanding of electrocatalytic activity of different materials.^{22,25,26} Their calculations show that there is a correlation between the binding energies of the OER-reaction intermediates bound to the same surface. These binding energies, independent of the exact reaction mechanism, scale proportionally to each other. As a result, the study claims that the reaction free energy diagrams decomposing the OER into its elementary steps according to each catalyst can be analyzed using one universal descriptor for a large class of materials ranging from noble metals to transition metal oxides.²⁵ The authors propose the difference between the adsorption energy of bound O* and HO*, $\Delta G_{O^*}^0 - \Delta G_{HO^*}^0$, as such a descriptor. Thus, volcano-shaped curves can be constructed, where

the OER overpotential, directly related to the activity of a catalyst, is plotted against the standard free energy of the $\Delta G_{O^*}^0 - \Delta G_{HO^*}^0$ (see Figure 1.1).

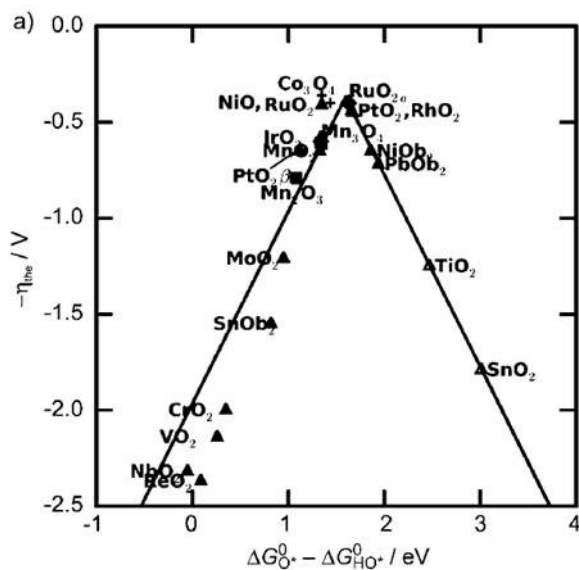


Figure 1.1 OER-activity trends for oxides. The negative theoretical overpotential is plotted against the standard free energy of $\Delta G_{HO^*}^0 - \Delta G_{O^*}^0$ -step. Taken from ref.²⁵

The predictions are in good agreement with experimental studies throughout the literature as far as activity trends on well-defined surfaces go.²⁵ However, one should keep in mind that the model 2D-surfaces used for DFT-calculations may fail to capture the complexity of a polycrystalline surface. For instance, contrary to what is observed experimentally, Co_3O_4 should require a slightly lower overpotential than RuO_2 .²⁴ Strongly localized defects can lead to a breach of the scaling relationships usually observed between the binding strengths of the different reaction intermediates. Halck et al. recently proposed the targeted modification of surface sites in RuO_2 via the incorporation of Co or Ni as a possibility to go beyond the limitations of the scaling relationships on a homogenous 2D-surface.²⁷

Another important result of the DFT-calculations is that the OER always proceeds on oxidized surfaces. Diaz-Morales et al. recently proposed a theoretical study of the potential-dependent OER on Au. The results were backed by isotopic labelling of oxygen detected via MS. The study showed the involvement of Au-lattice oxygen in the OER-mechanism via several potential-dependent mechanisms. This links up to another important characteristic of a suitable OER-catalyst: It must be stable under the operation conditions chosen, mostly pH and temperature. The fact that lattice-O might be involved such as in the case of Au means that during the complex PCmET of OER, reactive oxygen species have a chance to react with the catalyst itself through side-reactions, which might well lead to irreversible damage to the catalytic material through corrosion or important changes to the phase or morphology.

1.4. Practical OER-electrocatalysis

1.4.1. Electrolysis in basic vs. acidic media

The general setup used for water splitting consists of two electrodes in contact with water and separated by an electrolyte showing ionic conductivity necessary for the exchange of anions and cations in order to retain charge neutrality in the compartments. A direct current is used as the driving force for the water splitting reaction. An ion-conducting diaphragm separates the oxygen produced at the anode from the hydrogen produced at the cathode in order to avoid their recombination. In the case where the focus is on the anodic OER, the anode will be designated as the working electrode (WE) and the cathode as the counter-electrode (CE). The overpotentials needed to drive the OER and ORR are minimized by covering the electrodes in catalytically active material. Potentials are measured against a reference electrode. A commonly used system is the saturated calomel electrode (SCE). Under standard conditions, the redox potential of the SCE is independent of pH and equal to 0,244 V vs. SHE.

Figure 1.2 depicts a standard electrochemical cell used for laboratory electrolysis experiments. The electrode are placed in three electrolyte-filled compartments separated by fine-porosity glass frits that act as gas separators but allow for ionic exchange. The cathodic counter-electrode (CE) often consists of a Pt-wire, while the working electrode (WE) depicted here is a rotating disk electrode (RDE). The RDE rotates along its own axis at adjustable speeds, which allows for removal of oxygen gas bubbles formed during the OER. Also experiments conducted at different rotation speeds can yield kinetic data such as the reaction order and apparent activation energies. Such studies have been commonly reported for the oxygen reduction reaction (ORR).²⁸⁻³⁰

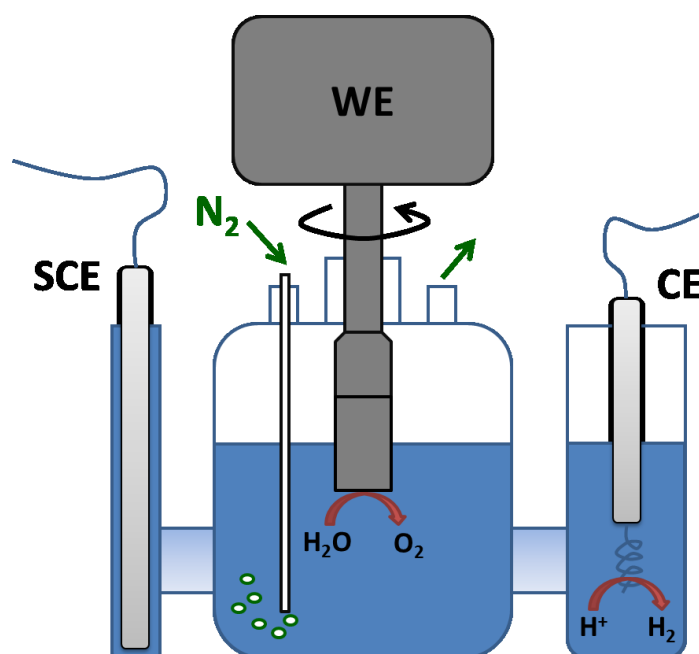


Figure 1.2 Standard electrochemical cell consisting of three compartments separated by fine-porosity glass frits.

Electrolysis modules for commercial applications have to answer a series of technical and financial requirements such as safety, economic feasibility in terms of manufacturing, distribution and

installation costs, compact designs (especially for mobile applications) and stability under operational conditions over periods of years, while maintaining efficiencies close to the experimental systems. These aspects are crucial if the water electrolysis technology is to contribute to a RES-based commercial electric grid operation.

These constraints especially impact the catalytic material covering the electrodes: Electrocatalysts should be highly conductive and operate at high current densities, low overpotential, wide range of pHs and electrolyte compositions. Ideally, such a catalyst should be composed of earth-abundant materials and involve a low-cost method of manufacturing and preparation. Another important factor is corrosion resistance, allowing electrode operation periods on a time-scale of several years without maintenance or replacement. All other parts of the setup should of course exhibit similar physical and chemical stability.

Additionally, an ideal catalyst would work for OER as well as for oxygen reduction reaction (ORR), which is the ubiquitous cathode reaction in fuel cells. That way the same device could store and release energy through subsequent water splitting and reforming. Alloys of Pt, Ir, and Ru have been developed as the most efficient bifunctional oxygen electrode catalysts.³¹ However for reasons of cost, those precious metal alloys cannot be implemented in commercial systems on a large scale.

Alkaline water electrolysis

Alkaline electrolyzers are currently the most advanced designs for commercial large-scale production of hydrogen. A schematic representation of their operating principle is shown by Figure 1.3 and equations 1.26 to 1.28. These systems rely on a highly purified liquid KOH electrolyte (25-30 wt.%). The caustic electrolyte may cause corrosion of metallic parts and represents a safety issue in case of leakage. Moreover, diaphragms used to separate the anodic (reaction 1.26) and cathodic (reaction 1.27) compartments have so far failed at completely preventing gas diffusion from one compartment to another, which lowers efficiency through reduction of oxygen at the cathode (ORR) and presents a risk if hydrogen concentration at the anode reaches the lower explosion limit.³² The electrolyte and diaphragm are also responsible for high ohmic losses between the electrodes. Last but not least, due to the liquid state of the electrolyte, operation conditions are limited to low operating pressure, inhibiting more compact designs. However the investigation of more compact electrode assemblies (zero-gap configuration), advanced diaphragm design and the development of high temperature alkaline water electrolyzers operating at higher pressures have greatly enhanced the potential applications of these systems.¹¹ An additional advantage of the alkaline conditions is that they allow for the use of earth-abundant catalysts for the OER, such as Ni-, Co- or Mn-base systems.^{33,34} Indeed such catalysts are stable at basic pH and reach activities comparable to those of precious metal systems. Some systems have even been reported to act as catalysts for both the OER and ORR, which would be of great advantage in a combined electrolyzer/fuel cell system.³⁵

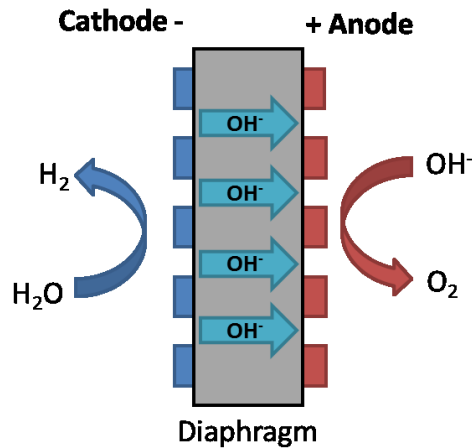


Figure 1.3 Schematic representation of an alkaline water electrolysis cell



Solide Oxide Electrolyzers (SOE)

Solide Oxide Electrolyzers (SOE) setups perform water splitting at high temperatures (600-900°C) directly from water steam. Water is reduced at the cathode to hydrogen and the resulting O^{2-} anions travel through a solid oxide membrane towards the anode where they are oxidized to gaseous oxygen. This option becomes interesting when a high temperature heat source is available, such as in a nuclear power plant or even using geothermal sources. However the commercial applications of these setups are still inhibited by the low stability of the material constituting the electrolysis cells at these temperatures.³²

PEM-based water electrolysis

The development of proton exchange membranes (PEM) constitutes a promising advance to overcome the drawbacks of alkaline electrolyzers. PEM are thin cross-linked polymeric membranes conducting protons thanks to acidic functional groups such as sulfonic acid groups ($-\text{SO}_3\text{H}$) (see Figure 1.4). The most commonly used membrane polymer is Nafion[®], a sulfonated fluoropolymer commercialized by DuPont[®]. In electrolyzer setups operated at neutral or acidic pH, a PEM can be used as the diaphragm separating the two electrode chambers. At the anode, water is oxidized to oxygen and protons (reaction 1.29). These protons, circulating across the exchange membrane are then reduced at the cathode to hydrogen (reaction 1.30). The low thickness of the PEM allows for compact systems, while providing fast proton exchange and little gas crossovers. No liquid electrolyte is present and as PEM are sufficiently stable, high operation pressures of up to 30 bar are

possible.³² Thanks to the proton-based ionic conductivity, PEM-electrolyzers allow for a better response to power fluctuations (OH-ions in alkaline electrolyzers have greater inertia). These setups can reach current densities of up to $2 \text{ A}\cdot\text{cm}^{-2}$.^{11,32} Also the purity of the produced gases is usually higher than in alkaline electrolyzers thanks to the extremely low gas-crossover.

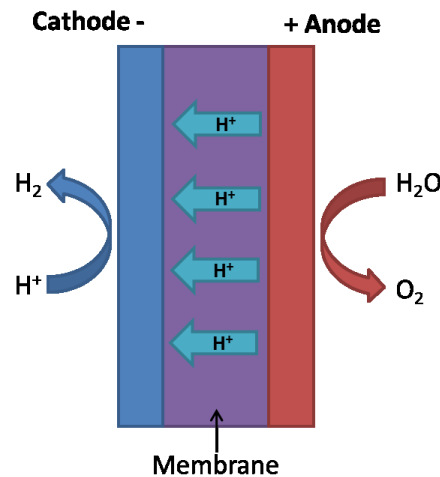


Figure 1.4 Schematic representation of a PEM water electrolysis cell



So far PEM-electrolyzers however suffer from several drawbacks that have limited their use to small-scale applications. Thin membranes don't tolerate pressures above 100 bar and increasing thickness leads to lower conductivity. Optimization of production costs of the membranes is a central R&D target. The highest potential for cost optimization is however linked to the resilience of the materials used in the setup. The high currents and harsh corrosive conditions (pH<3) lead to corrosive degradation of the current collectors and separator plates used in the setups. The highly oxidizing potentials used may even lead to corrosion of Ti-parts and significant research efforts are devoted to finding passivating coatings.³⁶ Even more critical is the corrosion of the catalytic material used for the OER. Recent benchmarking efforts by McCrory et al. have shown that catalyst systems based on abundant earth metals degraded much too fast under acidic OER-conditions to be of any relevance for PEM-electrolyzers, even though some mixed metal oxides including Mn-Mo-Sn-systems have

been shown to exhibit improved corrosion stability.^{37,38} Even Pt-based anodes exhibit mediocre OER-activities and high corrosion rates in acidic media.³⁹ The only realistic candidates showing appreciable OER-performance in terms of stability and activity were Ru- and Ir-based systems. However, even though Ru-based anodes are more active than Ir-systems, they corrode very fast under acidic OER-conditions.^{32,40} Recent research efforts have therefore been directed towards understanding the good OER-performance of Ir in order to allow for a targeted design of affordable Ir-based OER-catalysts. The reduction of precious metal loadings on the anode is the ultimate goal in order to make PEM-electrolyzers an economically viable option. In the following paragraphs we will focus on the economic feasibility of Ir-based OER-catalysts for PEM-electrolysis and advances reported so far in the literature.

1.4.2. Iridium for OER: the challenge of rare metals

Iridium is part of the group of the nine least abundant elements present in the earth's crust with an estimated average of 0.001 ppm.^{32,41} Early on in our planet's history, while the crust was still molten, iridium is suspected to have migrated towards the earth's core due to its high density and affinity to Fe.⁴² Much higher Ir-concentrations are found in extraterrestrial objects such as meteorites, which explains high Ir-concentration anomalies in soil layers linked to meteorite crash events.⁴³ The recent "Report of the Ad-hoc Working Group on defining critical raw materials" of the European Commission has listed iridium as one of the twelve most critical raw materials, within the Pt-metal group.⁴⁴ Indeed, mining sites are scarce and geographically very localized, which poses a high risk in terms of securing a constant supply. Iridium mostly occurs naturally in the form of sulfide inclusions or alloys with osmium, nickel or copper at sites where magmatic intrusions from below the earth's crust have occurred.⁴⁵ Few Ir-rich mining sites be found in South Africa, Russia and Canada.⁴⁶ Recently, with the development of Ir-based high-temperature crucibles for the growth of oxide single crystals for electronic applications, the demand for Ir has started to grow.

The Ir-price remains below the Au-price so far, nonetheless the development of Ir-based electrodes for OER or fuel cells could rapidly test the existing production capacities and lead to soaring prices.³² As a result, the minimization of Ir-loadings required to drive OER under commercially relevant conditions is of prime importance if Ir-based OER-catalysts are to be employed on a large scale. So far, inefficient utilization of Ir-coatings leads to anodic loadings around $2 \text{ mg}_{\text{Ir}} \cdot \text{cm}^{-2}$ in most projects oriented on PEM-electrolysis under industrially relevant conditions.³² The projected shortage and cost of iridium lead to the conclusion that a reduction in anodic Ir-loadings of at least one order of magnitude is necessary for industrial applications.

1.4.3. Synthesis strategies of Ir-based OER-catalysts

Various synthesis strategies have been used in order to prepare Ir-based anodic coatings for OER. Due to the previously mentioned material cost issue, the target of most recent studies has shifted towards strategies allowing for the reduction of Ir-loadings, while maintaining a stable catalyst. As mentioned in paragraph 1.3.3, OER takes place on oxidized surfaces. As a result, preparation strategies of an OER-active Ir-catalyst usually include an oxidizing step in order to maximize the amount of OER-active material.

Unfortunately, comparing reports on catalysts for acidic OER results in an apples-and-oranges kind of situation which cannot be avoided, unless a standardization of measurements and pre-treatment procedures has been adopted. Parameters having a critical influence on reported results include: the nature of the electrolyte, the deposition procedure, catalyst loading, pre-treatment of the catalyst (typically CV), potential range and faradaic efficiency. We will compare our samples to the most extensive benchmarking effort recently published by McCroy et al.⁴⁷ Nonetheless, a review of published studies on Ir-based OER-catalysts yields important clues towards the design of a synthesis scheme towards highly active and stable Ir-based OER-electrocatalysts

Dimensionally stable anodes (DSA)

An important step towards the precise assessment of Ir-specific activity, was the controlled loading of electrodes with the active material. A straight-forward approach is the preparation of dimensionally stable anodes (DSA) consisting of thick porous oxide layers commonly deposited on Ti-substrates by impregnation with a solution containing soluble Ir-salts. Various dissolved Ir-precursors can be used such as H_2IrCl_6 ^{48,49}, Ir(III)-acetate^{50,51} or IrCl_3 ⁵². Small volumes of the solutions are deposited on the substrate and fired at temperatures over 250°C in air. High loadings between 100 $\mu\text{g}_{\text{Ir}}\cdot\text{cm}^{-2}$ and 1 $\text{mg}_{\text{Ir}}\cdot\text{cm}^{-2}$ are usually employed and yield meager results in terms of OER-activity.

In order to improve the Ir-utilization in DSA, mixed metal oxides such as Ir/Sn-oxides have been reported early on.⁵²⁻⁵⁴ Cheaper elements such as Sn were used as diluents. However such coatings often suffered from poor conductivity. Promising results have recently been reported for Ir/Ni-mixed oxide-DSA produced at 450°C, which showed a 20-fold improvement in Ir-specific OER activity compared to pure Ir oxides.⁵⁵ However, stability tests are needed in order to assess the long-term stability of such systems. An interesting alternative that showed high OER-activity combined with significant lifetimes is the famous crystalline $\text{IrO}_2/\text{Ta}_2\text{O}_5$ -system, which received a lot of attention in the 90s.⁵⁶⁻⁵⁹ The corresponding DSA is usually prepared via decomposition of dissolved Ir- and Ta-chlorides at 450°C. Xu et al. have shown in several papers that for a molar ratio of Ir:Ta = 7:3, lifetimes of 500 to 700 hours can be achieved at 2 $\text{A}\cdot\text{cm}^{-2}$.⁵⁷⁻⁵⁹ Drastic conditions are applied in these accelerated lifetime tests, such as 9 V vs. SCE in the steady state region, raising the question what amount of current corresponds to faradaic processes and how much comes from corrosion. Ir-loadings exceeded 500 $\mu\text{g}\cdot\text{cm}^{-2}$, not to mention the expensive Ta-additive. Mraz and Krysa predicted a service life of more than five years under industrial conditions for these anodes, using similar accelerated lifetime tests and similarly high loadings.⁵⁶ It is however doubtful whether these systems will ever find commercial application in water splitting, due to high loadings (over 500 $\mu\text{g}\cdot\text{cm}^{-2}$) of iridium and tantalum, both listed as critically rare raw materials by the European Commission.⁴⁴

Other strategies for the preparation of dry Ir-oxides

Other strategies allowing for a better control of synthesis parameters during the formation of mixed oxides have been proposed. Rasten et al. used the Adams fusion method⁶⁰, where metal chloride precursors are mixed with molten NaNO_3 , which acts as the oxidizing agent during calcination over 340°C. However anodic loadings over 2 $\text{mg}_{\text{IrO}_2}\cdot\text{cm}^{-2}$ were required. Hutchings et al. reported on a (Sn,Ru,Ir) O_2 -based OER-catalyst prepared under similar conditions. Their catalyst achieved superior stability in an accelerated lifetime test but required loadings of 5 $\text{mg}\cdot\text{cm}^{-2}$. In general, high stability and low Ir-mass specific activity have been reported for crystalline Ir-based OER-catalysts produced

via a high-temperature calcination route. Resulting high electrode loadings have inhibited their widespread use so far.

Preparation of hydrated, amorphous Ir-oxide films

Early electrochemical studies have focused on amorphous Ir-based films like anodically grown iridium oxide films (AIROFs)^{61,62} and sputtered iridium oxide films (SIROFs)⁶³. Commercially, especially AIROFs are of little interest since they rely on the electrochemical oxidation of metallic iridium foils or wires, leading to high material costs. Nonetheless, the study of the produced amorphous, hydrated and oxidized iridium species was a first important step in developing synthesis strategies targeting the production of intrinsically more active Ir-phases.

Frazer and Woods studied AIROFs anodically grown by potentiodynamic cycling of metallic iridium anodes in concentrated sulfuric acid. The result was a linear increase of OER-activity and -stability with increasing cycling time and thickness of the grown amorphous oxide film.⁶¹ However, at constant potentials, the high currents obtained from AIROFs decrease rapidly in a matter of minutes, indicating the destruction of the grown active film. Better results were achieved by Beni et al. who studied SIROFs sputtered in a humidified oxygen discharge procedure.⁶³ They compared the stability of bare metallic iridium, AIROFs and SIROFs when holding at 1.85V vs. RHE. As in Frazer and Wood's case, after 20min at 1,85V vs. RHE, the activity of AIROFs went down to that of bare metallic iridium (30 mA.cm⁻²). However, in the case of SIROFs, currents seemed to stabilize at 45 mA.cm⁻² after for over 17 hours. Some years later, Vukovic et al. reported a drastic improvement in the stability of AIROFs: When calcined at 200°C, the films exhibited lower but stable currents over a period of 5 hours.⁶² Higher calcination temperatures led to the formation of crystalline IrO₂, resulting in an almost complete loss in activity. These three papers were already all pointing towards the idea of an Ir-oxide/hydroxide phase, intrinsically more active than crystalline Ir-oxides.

These findings were recently confirmed by the group of P. Strasser, who studied the influence of calcination temperature on the stability and activity of Ir-oxide-anodes prepared by thermal decomposition of Ir-acetate precursors on Ti-substrates.^{50,51} They suggested that at the lowest possible decomposition temperature of 250°C, an active and comparatively stable Ir-oxide/hydroxide species was formed. Increase of the calcination temperature led to the formation of crystalline rutile-IrO₂ and a high decline in OER-activity. These findings already strongly suggested that a careful tuning of preparation conditions could lead to the formation of an amorphous Ir-oxide/hydroxide-species combining high activity and stability under acidic OER-conditions.

Wet chemical synthesis

Wet chemical synthesis approaches have been used to produce a variety of powdered homogenous mixed oxides including Ir. For electrochemical testing, the resulting products are usually dispersed in a mixture of water, isopropanol or ethanol and Nafion® acting as a binder ("catalyst inks") for deposition. A popular wet chemical method for the synthesis of nanostructured Ir-particles is the polyol method, where polyol solvents also act as a reduction agent upon hydrothermal treatment.⁶⁴ ⁶⁶ This methods however requires subsequent calcination over 450°C as OER-inactive metallic iridium is obtained. The OER-properties of resulting crystalline IrO₂-particles are disappointing.^{65,66}

In order to obtain a solid Ir-product, soluble iridium salts can also be hydrolyzed in aqueous solution using a strong base: Hydrolysis of iridium chlorides like K_2IrCl_6 or $IrCl_3$ with NaOH has been reported in several papers.⁶⁷⁻⁷² At high $pH > 12$, stable colloids of Ir-oxyhydroxo-nanoparticles are obtained. These can be directly electroflocculated onto an electrode for further testing.^{69,70} Despite the nanostructuring of the catalyst, low activities were reported. Thermal treatment of the hydrolysis products above $400^\circ C$ was reported in several studies.^{68,73} The result was again crystalline Ir-oxides with low OER-activities requiring high loadings. Despite the nanostructuring of Ir-based OER-catalysts prepared via hydrolysis, no satisfying balance could be found in the literature between low-temperature oxohydroxy-species and dehydrated crystalline oxide-species obtained via calcination. Both exhibit mediocre OER-performance.

An alternative approach to calcination of dried hydrolysis products is hydrothermal treatment of the basic suspension of hydrolyzed metal precursors. Sardar et al. report the preparation of a basic suspension of hydrolyzed Ir- and Bi-precursor salts. They added N_2O_2 as an oxidant before treating the suspension for 120h at $240^\circ C$ in an autoclave. This synthesis yields polycrystalline $Bi_2Ir_2O_7$ with an average particle size of 10 nm. This pyrochlore-material has a long history with fuel cells. Typically the Bi leaches out very easily leaving disordered IrO_x . For electrochemical testing, the equivalent of $150 \mu g \cdot cm^{-2}$ of iridium were deposited on a gold-disk-RDE and tested via LSV to 1.6V vs. RHE. At 1.6V vs. RHE, current densities of $40 mA \cdot cm^{-2}$ were achieved, which is in line with the activity of the most active iridium-compounds reported. This activity didn't change after voltammetric cycling hinting at good stability of the catalyst. However cycling without actually holding at high potentials, doesn't yield much information about the stability to be expected under real industrial conditions.

We concluded from the above-mentioned reports on active and stable Ir-oxohydroxide species^{50,51,61-63} that a promising synthesis strategy for the preparation of amorphous OER-relevant Ir-compounds would be the exploration of the direct hydrothermal treatment of hydrolyzed Ir-precursors in aqueous solution. Such a strategy aims at producing intrinsically more active Ir-compounds instead of setting the primary target on the morphological optimization of the catalyst. Microwave-supported hydrothermal synthesis has only recently become a powerful tool as new setups developed by companies such as Anton Paar allow for fast heating ramps, short synthesis times, precise parameter control and homogenous temperature fields inside the vessels.

1.4.4. OER-catalyst supports

Several authors have stressed the positive effect of dispersing small nanoparticles of precious OER-catalysts on a conductive support acting as a current collector.^{24,67} The observed improvement of mass activity over bulk catalysts is often attributed to increase in the available electrochemically active surface area (ECSA).⁶⁷ Jirkovsky et al. reported on small supported RuO_2 -nanoparticles and stressed the positive effect of a high fraction of Ru-particle-edges on OER-activity.⁷⁴ This finding indicates that nanostructuring through dispersion of the OER-active material on a conductive support can also increase the surface concentration of intrinsically more active sites for the OER.

Once a right approach has been found for the synthesis of an active and stable Ir-based material, one should find a conductive support that could accommodate the active Ir-species in a highly dispersed manner in order to increase catalytic efficiency. Besides the work of Marshall et al. on Ir/Ru-catalysts on ATO reported earlier⁷⁵, only few papers have dealt so far with Ir-based OER-

electrocatalysts dispersed on conductive inexpensive supports. T. Reier et al. have studied Ru-, Ir- and Pt- nanoparticles supported on carbon black.⁶⁷ They obtained small metallic iridium nanoparticles of 2 ± 1.1 nm by impregnation of carbon black with iridium acetate and calcination at 250°C in reductive atmosphere. In their work, they emphasized the great potential of nanostructured noble metal catalysts: The number of active sites for OER, determined by CO stripping experiments, increased seven times between bulk iridium and nanostructured carbon-black-supported iridium. CV-measurements show a characteristic oxidation peak at 0,2V vs. RHE, indicating that the NP-surface consists mostly of metallic iridium. For a 20wt.-%-Ir/C catalyst with a loading of metal Ir of only $2 \mu\text{g}\cdot\text{cm}^{-2}$ they report during LSV ($6 \text{ mV}\cdot\text{s}^{-1}$) a current of $49 \text{ mA}\cdot\text{cm}^{-2}$ at 1.63 V vs. RHE. This compares to $46 \text{ mA}\cdot\text{cm}^{-2}$ during LSV ($5 \text{ mV}\cdot\text{s}^{-1}$) at the same potential for an iridium loading of $20 \mu\text{g}\cdot\text{cm}^{-2}$ in our study. However they also report that after LSV to 1.65V vs. RHE, at least half the electrode's Ir-content was found in the electrolyte. This indicates very low corrosion stability of the produced nanostructured catalysts and correlates with the previous literature indicating low stability of metallic iridium species.⁶³ Another issue is the stability of carbon-based supports. The oxidative degradation of carbon materials under anodic potentials was extensively examined by Yi et al.⁷⁶ Fast oxidative degradation of all carbon materials is observed at anodic potentials, although passivation of CNTs remains a possibility.

Alternatively, antimony-doped tin oxide (ATO) is known to be a stable material at highly anodic potentials in chlorine-free acidic electrolytes.⁷⁷ ATO has the advantage of being much cheaper than indium-doped tin oxide (ITO) and can be synthesized via wet chemical routes involving no dangerous precursors, unlike F-doped tin oxide (FTO). It has already been used in the past as a corrosion-stable conductive support for noble metal OER-catalysts as reported earlier from the work of Marshall et al. who reported effective reduction of the iridium loading but no stability data.⁷⁵ Tseung and Dhara studied pristine Pt and Pt supported on ATO and carbon balck under harsh conditions in H_3PO_4 at 150°C under reflux.⁷⁸ They showed that the highest stability under potentiostatic conditions was achieved for ATO-supported Pt electrocatalysts. This indicates that there might also be a synergetic stabilizing effect between the ATO support and certain noble metal electrocatalysts.

Tin oxide by itself is an insulator with a wide band gap of about 3.8 eV.⁷⁹ However, high n-type conductivity is achieved in Sb-doped SnO_2 . Sb^{III} - and Sb^{V} - precursors can be used, it is however the substitution of Sn^{IV} by Sb^{V} that leads to the increase in conductivity.^{80,81} There has been mainly two synthesis pathways used in the literature in order to obtain powdered ATO : Dissolved Sb- and Sn-precursors can either be fired at temperature over 900°C⁸²⁻⁸⁴ or treated hydrothermally in acidic solutions in an autoclave at temperatures between 200 and 300°C.^{79,81,85-87} Hydrothermal synthesis can lead to particle sizes as low as 7 nm, as reported by Nütz et al.⁷⁹

1.4.5. Stability-influencing factors

A wide array of phenomena can lead to the deactivation of the OER-electrocatalyst. Such mechanisms are hard to deconvolute in the complex three-phase heterogenous catalytic OER-system. Moreover, mechanisms are strongly dependent on the constituents of the catalyst. We will nonetheless give a brief overview of phenomena that might play a role in deactivating OER-electrocatalysts with emphasis on acidic media.

In certain cases, spectator species like electrolyte anions may play an important role. The poisoning effect of sulfates strongly adsorbing on Pt-electrodes has been repeatedly described as a nuisance in the oxygen reduction reaction (ORR).^{88,89} In the case of Pb-oxide-based electrodes for the OER, Amadelli et al. reported on the negative effect of certain anions.⁹⁰ SO_4^{2-} and CF_3SO_3^- tend to strongly adsorb. As a result the water discharge and desorption of reaction intermediates become hindered. Especially fluorides in the electrolyte modify the hydrous Pb-surface layer and thus hinder the efficient water discharge and intermediate desorption. On the other hand, Lodi et al. reported no effect of perchlorate and sulfate anions on the performance of RuO_2 -based electrodes in OER.⁹¹ It seems that anion effects are strongly dependent on the type of material and the electrochemical reaction in play. In line with this, we didn't observe any effect of switching between a perchlorate- and a sulfate-based electrolyte during the electrochemical testing of Ir-based electrocatalysts for the OER.

As mentioned in § 1.3.3, the OER is predicted to proceed on oxidized surfaces. Buckley et al. observed the concomitant oxidation of a metallic Pt-surface and rapid decrease in activity during OER in both acidic and basic medium.³⁹ They attributed the decreasing currents to the progressive build-up of an oxidized passivating Pt-layer, which inhibits electron transfer, despite being intrinsically more OER-active than metallic Pt. Thus, the formation of the active layer can in this particular case lead to the deactivation of the overall system via inhibition of efficient current collection. In the case of Ru and Ir however, their respective oxides RuO_2 and IrO_2 exhibit metallic conductivities of approx. $10^4 \text{ S}\cdot\text{cm}^{-1}$ for single crystals.⁹² As a result, the formation of oxidized Ru- or Ir-films on the anode, has no detrimental effect on the OER-activity. On the contrary, the oxidation of metallic Ru- or Ir-anodes is commonly used as an activation procedure before OER, as in the AIROF-technique mentioned in § 1.4.3.

One of the most prominent phenomena responsible for catalyst deactivation is corrosion. In the case of Ru, even though Ru-based anodes exhibit the highest OER-activities in acidic media,⁴⁷ their utilization has been limited by their fast degradation during OER. Kötzt et al. described the corrosive processes involved in the loss of OER-active material during OER.⁴⁰ They propose the formation of a RuO_4 -species acting as reactive intermediate both in the catalytic OER-cycle as well as in the irreversible corrosion process. Ir is not impervious to corrosion either, however the onset of Ir-corrosion seems to be located at higher potentials, allowing for a tight window where stable catalytic OER is possible without loss of the catalytically active material. Early on Buckley et al. described the potential-dependant competition of OER and Ir-corrosion.^{39,93} They reported that loss of Ir-material to the electrolyte starts above 1.6 V vs. SHE. More recently Fierro et al. suggested the involvement of lattice-O in the catalytic OER on IrO_2 . This suggests that various oxidized Ir-species might be involved in the catalytic OER-cycle.³⁹ These species might in turn be involved in a potential-dependent irreversible corrosion in competition with the OER as in the case of Ru.

Early electrochemical studies had raised the suspicion that the OER-performance of amorphous Ir-oxide/hydroxides might differ from IrO_2 . For instance Vuković et al. showed that an AIROF annealed at mild temperatures showed higher activity and stability than the crystalline IrO_2 -counterpart produced at higher temperatures.⁶² The groups around P. Strasser and K. Mayrhofer recently studied the influence of the chemical nature of the Ir-phase on OER-performance in highly acidic electrolyte. They showed that an Ir-oxide/hydroxide phase characterized by sharp H_2 -TPR-reduction features

below 100°C combined both high OER-activity and stability.⁵¹ In contrast crystalline IrO₂ produced at higher temperatures showed a sharp decrease in OER-activity. Cherveko et al. confirmed the superior OER-performance of the amorphous Ir-oxide/hydroxide produced by Reier et al. using MS-based analysis of Ir-dissolution during a potential-dependent OER-assessment of the Ir-catalysts.⁵⁰ They could show that high activity could be combined with relative stability for the Ir-oxide/hydroxide. This is an important indication on the importance of the chemical and structural nature of the catalyst precursors used for the OER. These reports suggest that some forms of amorphous Ir-oxide/hydroxides shows higher specific OER-activity and at the same time inhibit corrosion in the moderate potential-region. This could indicate alternative OER-mechanisms for such species, where no common intermediate for OER and corrosion exists, or kinetic inhibition of the corrosion reaction.

Formation of oxygen gas bubbles on the anode surface has also been described as a relevant parameter for the stability of the anodic coating.²⁴ Gas bubbles formed rapidly in micropores can cause local overpressures and lead to mechanical disruption of the coating. Additionally, if bubbles are allowed to grow on the anode and only slowly removed, part of the electrocatalyst film is not in contact with water anymore, leading to increased localized performance-demand on the accessible catalyst regions. High local current densities can lead to corrosion phenomena. This stresses the importance of efficient bubble removal in the electrolyzer setup, once a high-performance OER-electrocatalyst has been found. Morphological features of catalyst films such as cracks, channels and pores have been shown to play an important role for efficient bubble removal.⁹⁴

The rather empirical combination of elements has often been used as strategy to combine OER-activity and -stability of certain compounds. Such combinatorial approaches have been used to produce Ir/Ru/Sn-systems showing enhanced stability if compared to pure Ru-oxides.⁹⁵ We also cited the case of the much advertised Ir/Ta-system in §1.4.3.⁵⁶⁻⁵⁹ However, the involved synergetic phenomena remain little understood, inhibiting a targeted synthesis strategy. Also high precious metal loadings are still required.³² A strategy directed at isolating the chemical and structural features leading to superior OER-performance seems to be a more promising solution. Such an approach has long been inhibited by the notion that the most OER-active catalysts will simultaneously suffer from the highest corrosion rates.⁹⁶ However recent reports on amorphous oxide/hydroxide Ir-phases^{50,51} seem to indicate a possible combination of high OER-activity and -stability for specific electrocatalyst materials. Uncovering the structural and chemical features leading to such enhanced OER-performance would pave the way towards a more rational design of high-performance electrocatalysts for the acidic OER.

1.5. Aims and outline of the present work

In the context of the foreseen energy transition towards RES, finding an active, stable and cost-effective OER-electrocatalyst constitutes a central bottleneck in making H₂-based energy storage a commercially viable solution. This issue is especially challenging in the case of the promising technology of PEM-based electrolyzer setups. In acidic media most OER-catalysts rapidly deteriorate under operational conditions.

Based on the numerous reports stressing the superior intrinsic properties of Ir-based electrocatalysts in terms of activity and stability in acidic OER, we decided to examine the potential for optimization of an Ir-based system. Our initial approach was to maximize the available Ir-surface area in order to enhance Ir-utilization and thus permit cost reduction. A stable Ir-based OER-catalyst operating under industrially relevant conditions at Ir-loadings below 100 μg_{Ir}.cm⁻² would constitute a major step in making the PEM-technology an affordable solution for energy storage.³²

We used the strategy of dispersing Ir-nanoparticles on a conductive and corrosion stable ATO-support. Chapter 2 of the present work describes the novel microwave (MW)-supported hydrothermal synthesis procedure used for the synthesis of the ATO-support and the dispersion of Ir on ATO. We report on the successful production of this highly nanostructured Ir/ATO-compound. The produced Ir/ATO showed extremely promising OER-performance compared to available reference materials and literature reports. Thorough characterization allowed us to identify the Ir-particles as an amorphous highly hydrated Ir^{III/IV}-oxohydroxide. Recent literature reports on the possible OER-relevance of such compounds⁵¹ raised the question whether the exceptional catalytic efficiency was due to the structural design or rather to a higher intrinsic activity of the Ir^{III/IV}-oxohydroxide. In order to identify OER-relevant features of the Ir-phase, we carefully altered the Ir/ATO-compound via calcination at moderate temperatures and studied the effect on OER-performance. The dramatic depletion of OER-performance that was observed with increasing treatment temperatures could not be attributed solely to morphological changes such as sintering of Ir-particles leading to a decrease in available OER-active surface area. The calcined compounds were thoroughly characterized via vibrational spectroscopy and TPR in order to uncover key structural features of the Ir-phase that were affected by the thermal treatment. Our ultimate goal was to link the identified features to the OER-performance of the MW-produced Ir^{III/IV}-oxohydroxide.

In order to gain a deeper understanding of the role played by the Ir^{III/IV}-oxohydroxide phase in OER, we prepared a series of pure Ir-oxohydroxides via a systematic variation of relevant synthesis parameters in the MW-supported preparation procedure. Such an approach allows to exclude the influence of the catalyst support. The MW-supported hydrothermal synthesis of pure Ir-oxohydroxides is described in Chapter 3. We identified the initial ratio of base to Ir-chloride precursor KOH:Ir as a key synthesis parameter in controlling the Ir-particle morphology and composition. Physico-chemical characterization methods relying on the temperature-dependent behavior of the compounds in different gas phases (TGMS, TPR) were used in order to gain a better understanding of the sample composition. This first assessment allowed for a comparison between trends in sample composition and OER-performance determined via electrochemical tests.

Based on the prepared portfolio of Ir-oxohydroxides, Chapter 4 describes the analytical approach used to obtain deeper insight into OER-relevant features. Careful TEM-investigation and Raman-

spectroscopy supported by DFT-calculated model structures allowed for a better structural understanding of the XRD-amorphous Ir-oxohydroxide phase. Particular attention was given to the electronic structure of the compounds as well as to the identification of species involved in the structure of active site precursors. In order to obtain more surface-sensitive information on the samples, synchrotron-based X-ray photoemission and absorption spectra of the samples were analyzed using the ab-initio calculated model developed by Pfeifer et al.^{97,98} The aim of this characterization was to confirm the mixed Ir^{III/IV}-oxidation state of the samples via XPS. NEXAFS was used to identify reactive oxygen species predicted by Pfeifer et al. in the Ir^{III}-rich environment of OER-active amorphous Ir-oxohydroxides.^{97,98} In order to obtain a quantitative estimate of available reactive oxygen species, a CO-titration procedure was employed. Possible correlations between the amount of reactive oxygen species and the OER-performance were studied. We emitted the hypothesis that such O-species stabilized in the particular Ir^{III}-rich environment of Ir-oxohydroxides play a central role for the compound's OER-performance as precursor sites for the OER. The reactivity during CO-titration was also analyzed in order to gain insight into the OER-relevant mobility of reactive oxygen species within the Ir-oxohydroxide matrix.

Chapter 5 constitutes a summary of the results obtained throughout the present work.

Appendix I provides a listing of the relevant samples described in the present work with their associated FHI-database ID for future reference. Appendix II describes the results of a UV-Vis-study aiming at a better understanding of the processes involved in the basic hydrolysis of Ir-chlorides in the precursor solution. Appendix III is dedicated to the study of potential-dependent corrosion processes of the Ir-oxohydroxide electrocatalysts under acidic OER-conditions. The potential dependent catalyst corrosion was probed in a flow-through electrolyzer setup coupled to ICP-OES for analysis of species dissolved in the electrolyte.

1.6. References

- (1) Erisman, J. W.; Sutton, M. A.; Galloway, J.; Klimont, Z.; Winiwarter, W. *Nature Geoscience* **2008**, *1*, 636.
- (2) Kanan, M. W.; Nocera, D. G. *Science* **2008**, *321*, 1072.
- (3) Lewis, N. S.; Nocera, D. G. *PNAS* **2006**, *103*, 15729.
- (4) *Climate Change 2007: Mitigation of Climate Change*, IPCC, 2007.
- (5) *World Energy Outlook 2010: Executive Summary*, International Energy Agency, 2010.
- (6) Rifkin, J. *The Third Industrial Revolution: How Lateral Power Is Transforming Energy, the Economy, and the World*; First Printing (Numerals Begin with 1) ed.; Palgrave Macmillan, 2011.
- (7) Courier, M. *La Houille Blanche* **1982**, 403.
- (8) Bruce, P. G.; Scrosati, B.; Tarascon, J.-M. *Angewandte Chemie International Edition* **2008**, *47*, 2930.
- (9) Schlögl, R. *ChemSusChem* **2010**, *3*, 209.
- (10) Hajimiragha, A.; Fowler, M. W.; Cañizares, C. A. *International Journal of Hydrogen Energy* **2009**, *34*, 5275.
- (11) Ursua, A.; Gandia, L. M.; Sanchis, P. *Proceedings of the IEEE* **2012**, *100*, 410.
- (12) Wendt, H.; Imarisio, G. *J Appl Electrochem* **1988**, *18*, 1.
- (13) Züttel, A.; Borgschulte, A.; Schlapbach, L. *Hydrogen as a Future Energy Carrier*; John Wiley & Sons, **2008**.
- (14) Cook, T. R.; Dogutan, D. K.; Reece, S. Y.; Surendranath, Y.; Teets, T. S.; Nocera, D. G. *Chemical Reviews* **2010**, *110*, 6474.
- (15) Steele, B. C. H.; Heinzl, A. *Nature* **2001**, *414*, 345.
- (16) Ulrich Eberle, B. M. *Energy & Environmental Science* **2012**, *5*, 8790.
- (17) Schlögl, R. *Angewandte Chemie International Edition* **2003**, *42*, 2004.
- (18) Rifkin, J. *Engineering Technology* **2008**, *3*, 26.
- (19) Nocera, D. G. *Accounts of Chemical Research* **2012**, *45*, 767.
- (20) Pijpers, J. J. H.; Winkler, M. T.; Surendranath, Y.; Buonassisi, T.; Nocera, D. G. *PNAS* **2011**, *108*, 10056.
- (21) Reece, S. Y.; Hamel, J. A.; Sung, K.; Jarvi, T. D.; Esswein, A. J.; Pijpers, J. J. H.; Nocera, D. G. *Science* **2011**, *334*, 645.
- (22) Dau, H.; Limberg, C.; Reier, T.; Risch, M.; Roggan, S.; Strasser, P. *ChemCatChem* **2010**, *2*, 724.
- (23) Keenan, J. H.; Keyes, F. G.; Hill, P. G.; Moore, J. G. *Steam Tables: Thermodynamic Properties of Water Including Vapor, Liquid, and Solid Phases*; 1 ed.; John Wiley & Sons, **1969**.
- (24) Katsounaros, I.; Cherevko, S.; Zeradjanin, A. R.; Mayrhofer, K. J. J. *Angewandte Chemie International Edition* **2014**, *53*, 102.
- (25) Man, I. C.; Su, H.-Y.; Calle-Vallejo, F.; Hansen, H. A.; Martínez, J. I.; Inoglu, N. G.; Kitchin, J.; Jaramillo, T. F.; Nørskov, J. K.; Rossmeisl, J. *ChemCatChem* **2011**, *3*, 1159.
- (26) Rossmeisl, J.; Logadottir, A.; Nørskov, J. K. *Chemical Physics* **2005**, *319*, 178.
- (27) Halck, N. B.; Petrykin, V.; Krtil, P.; Rossmeisl, J. *Physical Chemistry Chemical Physics* **2014**, *16*, 13682.
- (28) A. L. Ocampo, R. H. C.
- (29) Itoe, R. N.; Wesson, G. D.; Kalu, E. E. *Journal of the Electrochemical Society* **2000**, *147*, 2445.
- (30) Paulus, U. A.; Schmidt, T. J.; Gasteiger, H. A.; Behm, R. J. *Journal of Electroanalytical Chemistry* **2001**, *495*, 134.
- (31) Zhang, Y.; Wang, C.; Wan, N.; Mao, Z. *International Journal of Hydrogen Energy* **2007**, *32*, 400.
- (32) Carmo, M.; Fritz, D. L.; Mergel, J.; Stolten, D. *International Journal of Hydrogen Energy* **2013**, *38*, 4901.
- (33) Gorlin, Y.; Jaramillo, T. F. *Journal of the American Chemical Society* **2010**, *132*, 13612.
- (34) McCrory, C. C. L.; Jung, S.; Peters, J. C.; Jaramillo, T. F. *Journal of the American Chemical Society* **2013**, *135*, 16977.

- (35) Liang, Y.; Li, Y.; Wang, H.; Zhou, J.; Wang, J.; Regier, T.; Dai, H. *Nature Materials* **2011**, *10*, 780.
- (36) Selamet, Ö. F.; Becerikli, F.; Mat, M. D.; Kaplan, Y. *International Journal of Hydrogen Energy* **2011**, *36*, 11480.
- (37) El-Moneim, A. A., *Material Transactions* **2005**, *46*, 309.
- (38) El-Moneim, A. A.; Bhattarai, J.; Kato, Z.; Izumiya, K.; Kumagai, N.; Hashimoto, K. *ECS Trans.* **2010**, *25*, 127.
- (39) Buckley, D. N.; Burke, L. D. *Journal of the Chemical Society, Faraday Transactions 1: Physical Chemistry in Condensed Phases* **1976**, *72*, 2431.
- (40) Kötz, R.; Stucki, S.; Scherson, D.; Kolb, D. M. *Journal of Electroanalytical Chemistry and Interfacial Electrochemistry* **1984**, *172*, 211.
- (41) Mitchell, R. H.; Keays, R. R. *Geochimica et Cosmochimica Acta* **1981**, *45*, 2425.
- (42) Renner, H.; Schlamp, G.; Kleinwächter, I.; Drost, E.; Lüscho, H. M.; Tews, P.; Panster, P.; Diehl, M.; Lang, J.; Kreuzer, T.; Knödler, A.; Starz, K. A.; Dermann, K.; Rothaut, J.; Drieselmann, R.; Peter, C.; Schiele, R. In *Ullmann's Encyclopedia of Industrial Chemistry*; Wiley-VCH Verlag GmbH & Co. KGaA: **2000**.
- (43) Orth, C. J.; Gilmore, J. S.; Knight, J. D.; Pillmore, C. L.; Tschudy, R. H.; Fassett, J. E. *Science* **1981**, *214*, 1341.
- (44) *Critical raw materials for the EU*, European Commission, **2010**.
- (45) Xiao, Z.; Laplante, A. R. *Minerals Engineering* **2004**, *17*, 961.
- (46) Seymour, R. J.; O'Farrelly, J. I. In *Kirk-Othmer Encyclopedia of Chemical Technology*; John Wiley & Sons, Inc.: **2000**.
- (47) McCrory, C. C. L.; Jung, S.; Ferrer, I. M.; Chatman, S. M.; Peters, J. C.; Jaramillo, T. F. *Journal of the American Chemical Society* **2015**, *137*, 4347.
- (48) Krysa, J.; Maixner, J.; Mraz, R.; Rousar, I. *Journal of Applied Electrochemistry* **1998**, *28*, 369.
- (49) Hu, J. M.; Meng, H. M.; Zhang, J. Q.; Cao, C. N. *Corrosion Science* **2002**, *44*, 1655.
- (50) Cherevko, S.; Reier, T.; Zeradjanin, A. R.; Pawolek, Z.; Strasser, P.; Mayrhofer, K. J. J. *Electrochemistry Communications* **2014**, *48*, 81.
- (51) Reier, T.; Teschner, D.; Lunkenbein, T.; Bergmann, A.; Selve, S.; Kraehnert, R.; Schlögl, R.; Strasser, P. *Journal of the Electrochemical Society* **2014**, *161*, F876.
- (52) De Pauli, C. P.; Trasatti, S. *Journal of Electroanalytical Chemistry* **2002**, *538–539*, 145.
- (53) Ardizzone, S.; Fregonara, G.; Trasatti, S. *Electrochimica Acta* **1990**, *35*, 263.
- (54) De Pauli, C. P.; Trasatti, S. *Journal of Electroanalytical Chemistry* **1995**, *396*, 161.
- (55) Reier, T.; Pawolek, Z.; Cherevko, S.; Bruns, M.; Jones, T.; Teschner, D.; Selve, S.; Bergmann, A.; Nong, H. N.; Schlögl, R.; Mayrhofer, K. J. J.; Strasser, P. *Journal of the American Chemical Society* **2015**, *137*, 13031.
- (56) Mráz, R.; Krýsa, J. *Journal of Applied Electrochemistry* **1994**, *24*, 1262.
- (57) Xu, L. K.; Scantlebury, J. D. *Corrosion Science* **2003**, *45*, 2729.
- (58) Xu, L. K.; Scantlebury, J. D. *Journal of the Electrochemical Society* **2003**, *150*, B254.
- (59) Xu, L.; Xin, Y.; Wang, J. *Electrochimica Acta* **2009**, *54*, 1820.
- (60) Adams, R.; Shriener, R. L. *Journal of the American Chemical Society* **1923**, *45*, 2171.
- (61) Frazer, E. J.; Woods, R. *Journal of Electroanalytical Chemistry and Interfacial Electrochemistry* **1979**, *102*, 127.
- (62) Vuković, M. *Journal of Applied Electrochemistry* **1987**, *17*, 737.
- (63) Beni, G.; Schiavone, L. M.; Shay, J. L.; Dautremont-Smith, W. C.; Schneider, B. S. *Nature* **1979**, *282*, 281.
- (64) Fievet, F.; Lagier, J. P.; Blin, B.; Beaudoin, B.; Figlarz, M. *Solid State Ionics* **1989**, *32–33, Part 1*, 198.
- (65) Marshall, A.; Børresen, B.; Hagen, G.; Tsyppkin, M.; Tunold, R. *Materials Chemistry and Physics* **2005**, *94*, 226.
- (66) Marshall, A.; Børresen, B.; Hagen, G.; Tsyppkin, M.; Tunold, R. *Electrochimica Acta* **2006**, *51*, 3161.

- (67) Reier, T.; Oezaslan, M.; Strasser, P. *ACS Catalysis* **2012**, *2*, 1765.
- (68) Lervik, I. A.; Tsytkin, M.; Owe, L.-E.; Sunde, S. *Journal of Electroanalytical Chemistry* **2010**, *645*, 135.
- (69) Nakagawa, T.; Beasley, C. A.; Murray, R. W. *Journal of Physical Chemistry C* **2009**, *113*, 12958.
- (70) Nakagawa, T.; Bjorge, N. S.; Murray, R. W. *Journal of the American Chemical Society* **2009**, *131*, 15578.
- (71) Bestaoui, N.; Prouzet, E. *ChemInform* **2010**, *28*
- (72) Zhao, Y.; Hernandez-Pagan, E. A.; Vargas-Barbosa, N. M.; Dysart, J. L.; Mallouk, T. E. *J. Phys. Chemical Letters* **2011**, *2*, 402.
- (73) Marshall, A. T.; Sunde, S.; Tsytkin, M.; Tunold, R. *International Journal of Hydrogen Energy* **2007**, *32*, 2320.
- (74) Jirkovský, J.; Hoffmannová, H.; Klementová, M.; Krtíl, P. *Journal of the Electrochemical Society* **2006**, *153*, E111.
- (75) Marshall, A. T.; Haverkamp, R. G. *Electrochimica Acta* **2010**, *55*, 1978.
- (76) Yi, Y.; Tornow, J.; Willinger, E.; Willinger, M. G.; Ranjan, C.; Schlögl, R. *ChemElectroChem* **2015**, *2*, 1929.
- (77) Cachet, H.; Froment, M.; Zenia, F. *Journal of the Electrochemical Society* **1996**, *143*, 442.
- (78) Tseung, A. C. C.; Dhara, S. C. *Electrochimica Acta* **1975**, *20*, 681.
- (79) Nütz, T.; Felde, U. z.; Haase, M. *The Journal of Chemical Physics* **1999**, *110*, 12142.
- (80) Mishra, K. C.; Johnson, K. H.; Schmidt, P. C. *Physical Review B* **1995**, *51*, 13972.
- (81) Nütz, T.; Haase, M. *Journal of Physical Chemistry B* **2000**, *104*, 8430.
- (82) Orel, Z. C.; Orel, B.; Hodošček, M.; Kaučič, V. *J Mater Sci* **1992**, *27*, 313.
- (83) Szczuko, D.; Werner, J.; Oswald, S.; Behr, G.; Wetzig, K. *Applied Surface Science* **2001**, *179*, 301.
- (84) Zhang, J.; Gao, L. *Materials Research Bulletin* **2004**, *39*, 2249.
- (85) Bai, F.; He, Y.; He, P.; Tang, Y.; Jia, Z. *Materials Letters* **2006**, *60*, 3126.
- (86) Jeon, H.-J.; Jeon, M.-K.; Kang, M.; Lee, S.-G.; Lee, Y.-L.; Hong, Y.-K.; Choi, B.-H. *Materials Letters* **2005**, *59*, 1801.
- (87) Lili, L.; Liming, M.; Xuechen, D. *Materials Research Bulletin* **2006**, *41*, 541.
- (88) Kozawa, A. *Journal of Electroanalytical Chemistry (1959)* **1964**, *8*, 20.
- (89) Marković, N. M.; Ross Jr, P. N. *Surface Science Reports* **2002**, *45*, 117.
- (90) Amadelli, R.; Maldotti, A.; Molinari, A.; Danilov, F. I.; Velichenko, A. B. *Journal of Electroanalytical Chemistry* **2002**, *534*, 1.
- (91) Lodi, G.; Sivieri, E.; Battisti, A.; Trasatti, S. *Journal of Applied Electrochemistry* **1978**, *8*, 135.
- (92) Galizzioli, D.; Tantardini, F.; Trasatti, S. *Journal of Applied Electrochemistry*, *4*, 57.
- (93) Buckley, D. N.; Burke, L. D. *Journal of the Chemical Society, Faraday Transactions 1: Physical Chemistry in Condensed Phases* **1975**, *71*, 1447.
- (94) Zeradjanin, A. R.; Ventosa, E.; Bondarenko, A. S.; Schuhmann, W. *ChemSusChem* **2012**, *5*, 1905.
- (95) Hutchings, R.; Müller, K.; Kötz, R.; Stucki, S. *Journal of Materials Science*, *19*, 3987.
- (96) Bockris, J. O. M.; Otagawa, T. *Journal of Applied Electrochemistry* **1984**, *131*, 290.
- (97) Pfeifer, V.; Jones, T. E.; Velasco Velez, J. J.; Massue, C.; Greiner, M. T.; Arrigo, R.; Teschner, D.; Girgsdies, F.; Scherzer, M.; Allan, J.; Hashagen, M.; Weinberg, G.; Piccinin, S.; Havecker, M.; Knop-Gericke, A.; Schlögl, R. *Physical Chemistry Chemical Physics* **2016**, *18*, 2292.
- (98) Pfeifer, V.; Jones, T. E.; Velasco Vélez, J. J.; Massué, C.; Arrigo, R.; Teschner, D.; Girgsdies, F.; Scherzer, M.; Greiner, M. T.; Allan, J.; Hashagen, M.; Weinberg, G.; Piccinin, S.; Hävecker, M.; Knop-Gericke, A.; Schlögl, R. *Surface and Interface Analysis* **2015**, n/a.

2. Identification of key features in a high-performance Ir/ATO-electrocatalyst for the Oxygen Evolution Reaction

2.1. Abstract

The synthesis of a highly active and yet stable electrocatalyst for the anodic oxygen evolution reaction (OER) remains a major challenge for electrocatalytic water splitting on an industrial scale. We report the synthesis of a high-performance OER-catalyst obtained by loading iridium on conductive antimony-doped tin oxide (ATO)-nanoparticles via a microwave-supported hydrothermal route. The effect of thermal treatment in various dry atmospheres indicates that the observed unprecedented OER-performance is prominently linked to the nature of the produced Ir-phase, which consists of an amorphous, highly hydrated Ir^{III/IV}-oxohydroxide. This finding is in contrast with the stable but poor OER-activity of crystalline IrO₂-based compounds produced via more classical calcination routes. Our investigations demonstrate the immense potential of amorphous Ir-oxohydroxides, which constitute promising candidates for stable high-current water electrolysis.

2.2. Introduction

Chemical energy storage through hydrogen production from water splitting has come under focus as one of the most promising answers to the transient nature of renewable energy sources.^{1,2} The electrocatalytic splitting of water can be driven by any type of power supply and its combination with intermittent renewable sources could ensure the storage of excess energy in the chemical bond of hydrogen. Electrolyzer setups are being seen as a particularly versatile solution as they could be implemented into smart grids running on a variety of power sources on a de-centralized level.³ In particular, proton exchange membrane (PEM)-based electrolyzers allow for the production of high-purity H₂ at elevated pressure in compact designs.⁴ The separation of O₂ and H₂ produced respectively in the anodic and cathodic compartments is ensured via polymeric membranes by proton exchange capabilities, *e.g.*, Nafion[®]. However, these sulfonic-acid-functionalized membranes require a highly acidic environment, which poses a major challenge to the employed electrocatalysts, especially in the anodic oxygen evolution reaction (OER).

The optimization of an active, stable, and yet cost-effective OER-electrocatalyst material has emerged as one of the toughest hurdles in the design of a commercially relevant PEM-electrolyzer system. In general, earth-abundant transition metal oxides such as Co₃O₄, Fe₂O₃ and MnO_x show minimal stability under acidic OER-conditions⁴ and even Ru-based anodes have been shown to corrode at fast rates.^{5,6} The only promising candidates so far, are Ir-based compounds, which seem to be able to combine high activity with relative stability in the acidic OER.⁶ Due to the scarcity of iridium and resulting high material costs, the minimization of the anodic Ir-loading is of prime importance in making it a financially viable solution. Strategies include the synthesis of highly active precursor phases of iridium, as well as the maximization of electrocatalytically active surface area, by means of dispersing iridium on a conductive support.

In regards to the catalyst support, Reier et al. have recently highlighted the potential of supported noble metal OER-catalysts, by showing that homogeneously dispersed nanoparticles presented a higher density of active sites compared to bulk materials.⁷ They obtained nanosized metallic Ru-, Ir-

and Pt- nanoparticles supported on carbon black via impregnation with iridium acetate and calcination at 250°C in reductive atmosphere. In the case of supported iridium, a sevenfold increase in the number of OER-active sites over bulk iridium was observed. However, low stability under OER-conditions was reported and indicates that an important part of the observed current might originate from the corrosion of the carbon-support. The oxidative degradation of carbon materials under anodic potentials was extensively examined by Yi.⁸ Fast oxidative degradation of all carbon materials was observed at anodic potentials in acidic electrolytes.

As an alternative to carbonaceous support suspected to corrode while OER is proceeding, antimony-doped tin oxide (ATO) is a suitable alternative as conductive support for electrocatalytic applications, such as OER. Tin oxide by itself is an insulator with a wide band gap of about 3.8 eV.⁹ However, significant n-type conductivity is achieved by doping SnO₂ by Sb.^{10,11} At elevated Sb doping (approx. 5%) of SnO₂, ATO exhibits quasi-metallic conductivity and is known for its stability under anodic potentials in chlorine-free acidic electrolytes.¹² ATO has also the advantage of being cheaper than indium-doped tin oxide (ITO) and can be synthesized via wet chemical routes involving safe precursors, unlike fluorine-doped tin oxide (FTO).¹³ A method of choice for ATO-synthesis is hydrothermal synthesis as smaller particles are usually obtained than via calcination routes.^{9,11} ATO has been successfully employed as a support for precious metal OER-catalyst under acidic conditions. Tseung and Dhara studied Pt supported on ATO versus carbon black under harsh conditions in H₃PO₄ at 150°C.¹⁴ They showed that the highest stability under potentiostatic conditions was achieved for ATO-supported Pt electrocatalysts and suggested a synergetic effect between the ATO support and the noble metal electrocatalysts. Similarly, Liu et al. reported significant OER-activity enhancement of ATO-supported IrO₂-nanoparticles over bulk IrO₂ due to higher Ir-dispersion and a resulting higher electrochemically active surface area.¹⁵

Besides the catalysts support, producing the “right” chemical state of iridium is critical in achieving stable OER. Early electrochemical studies have shown that metallic iridium films are inefficient in OER and needed to be activated under oxidative conditions.¹⁶ Active Ir-oxide-films were formed as anodically grown iridium oxide films (AIROF)^{17,18} or sputtered iridium oxide films (SIROF)¹⁶. The authors repeatedly emphasized the important role played by amorphous Ir-oxohydroxides in high-current, stable OER-electrocatalysis. Such compounds compare favorably to crystalline IrO₂ often resulting from the production of powdered catalysts via calcination steps above 400°C.¹⁹⁻²⁶ Such crystalline IrO₂-compounds exhibit high stability but limited Ir-mass specific OER-activity, which results in high electrode loadings in the order of 2 mg_{Ir}.cm⁻².²⁷

Some recent studies have focused on the OER-relevance of amorphous hydrous Ir-phases. For instance, Ir-acetate calcined at 250°C yielded amorphous and hydrated Ir-species combining both activity and relative stability in acidic OER.²⁸ Higher thermal treatment had a detrimental effect on OER-performance, as crystalline IrO₂ was forming. Bernicke et al. also confirmed the competition between the classically evoked electrochemically accessible surface area (ECSA) and the chemical nature of OER-active Ir-sites.²⁹ However, in order to remove carbohydrate ligands, such synthesis pathways are limited to temperatures above 250°C. The hydrothermal treatment of hydrolyzed Ir-precursors in aqueous media would constitute a unique tool for exploring intermediate temperature ranges of 150-300°C. We suspected that such an approach would give access to the promising amorphous Ir-oxide/hydroxides.

In the present study, we report the MW-assisted hydrothermal synthesis of Ir-oxohydroxide particles dispersed on a conductive ATO-support. Unprecedented OER-activities and stabilities were achieved under relevant experimental conditions for a 30 mol.%-Ir/ATO-catalyst. In order to establish links between structural properties and OER-performance, we studied the effects of thermal treatment on the MW-prepared compound under inert and oxidative atmospheres. We determined that the exceptional OER-performance of the synthesized electrocatalyst is strongly related to the chemical nature of the deposited Ir-oxohydroxide.

In the following text, MW-ATO refers to the selected ATO-support material, while MW-Ir/ATO is the loaded 30 mol.%-Ir/ATO prepared in the MW. Ir_T_Ar/O₂ refers to MW-Ir/ATO thermally treated at a temperature T (°C) respectively under 100% Ar or 21% O₂/Ar-streams.

Table 2.1 Summary of sample designations used throughout the text.

Label	Comment
MW-ATO	Selected ATO-support prepared via MW-supported hydrothermal synthesis at 270°C
MW-Ir/ATO	30mol.% Ir loaded on MW-ATO via MW-supported synthesis
Ir_250C_O ₂	MW-Ir/ATO, calcined 250°C, 21%O ₂ /Ar
Ir_250C_Ar	MW-Ir/ATO, calcined 250°C, Ar
Ir_350C_O ₂	MW-Ir/ATO, calcined 350°C, 21%O ₂ /Ar
Ir_350C_Ar	MW-Ir/ATO, calcined 350°C, Ar
SA-IrO ₂	Crystalline IrO ₂ -benchmark (Sigma-Aldrich)
AA-IrO _x	Amorphous IrO _x -benchmark (Alfa Aesar)

2.3. Experimental

2.3.1. ATO synthesis

Antimony-doped tin oxide (ATO) was obtained from SnCl₄·5H₂O (Sigma Aldrich) and SbCl₃ (Sigma Aldrich) dissolved in a 95:5 molar ratio in a 0.5%-HCl/H₂O solution. The metal chloride solution was added to 200mL H₂O under constant stirring at a speed of 5g.min⁻¹ using an automated laboratory reactor system (Mettler-Toledo, Labmax). During addition, reactor-pH was automatically maintained at pH=4 using 1%-NH₃/H₂O. During addition, the solution was maintained at 50°C and further aged for 1h at 50°C. The resulting colloidal suspension was subjected to hydrothermal treatment in a microwave synthesis reactor (Multiwave PRO, Anton Paar). 50mL of solution are poured into an 80mL-quartz vessel and four such vessels at a time are heated at 290°C for 1h in the microwave (ramp : 10 K.min⁻¹). The product changed color from cream white to blue, typical for ATO. The vessel content was centrifuged at 5000rpm for 10 min, redissolved in micropore-filtered water and re-centrifuged until the conductivity of the supernatant was below 0.05 mS.cm⁻¹. The solid product was then dried at 80°C for 12h and ground in a mortar.

For the purpose of measuring resistivities, ATO-powders were pressed as 13mm-pellets of thickness below 1µm using a pressing dye at 7 tons for 5 min. The four-point-probe-measurement head

consisted of four 2mm-spaced gold tips mounted in a row. The two outer tips were coupled to a DC precision current source Keithley 6220, whereas potential differences between the two inner tips were measured using a Keithley 6514 electrometer. The resulting apparent resistance was converted to sheet resistance taking into account the finite pellet dimensions using the geometry correction factors provided by Smits.³⁰

2.3.2. Ir-loading of ATO

The ATO-support was then loaded with OER-active Ir. For this purpose, 310 mg of MW-ATO was added to a 100 mL-PTFE-vessel. The vessel was then filled with 62mL H₂O containing 425.5 mg dissolved K₂IrCl₆ (Alfa Aesar, kept under Ar) under constant stirring. The pH of the resulting suspension was slowly adjusted to pH=13 using a 1M NaOH-solution. The pH was maintained for 30 min at pH=13 under constant stirring. The mixture was then allowed to age for an hour under gentle shaking. Four such vessels were then placed in the microwave synthesis reactor and heated up to 250°C using a 10 K.min⁻¹ ramp under constant agitation provided by magnetic PTFE-stirrers. The temperature was maintained at 250°C for 1h. The resulting black product was centrifuged at 8000rpm for 10 min, redissolved in micropore-filtered water and re-centrifuged until the conductivity of the supernatant was below 0.05 mS.cm⁻¹. The solid product was then dried at 80°C for 12h and ground in a mortar.

2.3.3. Sample characterization

X-ray powder diffraction (XRD) measurements were performed on a STOE STADI-P transmission diffractometer equipped with a primary focusing germanium monochromator (Cu K α 1 radiation) and a linear position sensitive detector. The samples were mounted in the form of small amounts of powder sandwiched between two layers of polyacetate film and fixed with a small amount of X-ray amorphous grease. The surface area determination was carried out in a volumetric N₂-physisorption setup (Autosorb-6-B, Quantachrome) at the temperature of liquid nitrogen. The sample was degassed in dynamic vacuum at a temperature of 80°C for 2 h prior to adsorption. Full adsorption and desorption isotherms were measured. The linear range of the adsorption isotherm ($P/P^0 = 0.05-0.3$) was considered to calculate the specific surface area according to the BET-method. Diffuse reflectance UV-Vis spectra of ATO-powders were measured using a Agilent Technologies Cary 5000 UV-Vis_NIR spectrometer equipped with a Harrick diffuse reflectance attachment. Spectra were recorded at room temperature. The Kubelka–Munk function $F(R)$ was used to convert diffuse reflectance data into absorption spectra using BaSO₄ as white standard. Sample powders were diluted 1:10 with BaSO₄ due to strong absorption features.

Thermogravimetric analysis (TGA), differential scanning calorimetry (DSC) and evolved gas analysis of the decomposition reaction of the samples under a 21% O₂/Ar- or 100% Ar-stream (100 mL.min⁻¹, 10 K.min⁻¹, 800°C) were performed on a Netzsch STA 449 thermobalance connected to a quadrupole mass spectrometer (QMS200 Omnistar, Balzers). The measurements were performed with approximately 25 mg sample in a temperature range of 30-800°C (10Kpm). For the specific question of determining the remaining water (chemisorbed and physisorbed) in the sample after thermal treatment in various gas atmospheres, the hydrothermally prepared 30%IrO_x/ATO was heated up in a 21% O₂/Ar- or 100% Ar-stream (100mL.min⁻¹, 10 K.min⁻¹) using subsequent 1h-steps of 250°C and 350°C.

Temperature-programmed reduction (TPR) of the samples was performed in a fixed bed reactor in a 5 vol.% H₂/Ar-stream (80 mL.min⁻¹) at a heating rate of 6 K.min⁻¹. Due to the high heat release during the low-temperature reduction feature of Ir, the measurements were performed in a temperature range of 30-800°C with approximately 25 mg sample in order to avoid temperature spikes due to massive heat releases. The H₂-consumption was monitored with a thermal conductivity detector (TCD). The TCD detector was calibrated by reducing a known amount of CuO. The samples were initially kept under Ar-flow for 1h (80mL.min⁻¹) in order to remove physisorbed water. The comparison of H₂-signals during the initial switch from 100% Ar to 4.92% H₂/Ar streams before and after TPR (see Figure S2.8) allows to quantify the amount of H₂ initially absorbed by the sample. The hydrogen consumption rate profiles were normalized by the mass of dry sample, using the mass fraction of chemisorbed and physisorbed water determined via TGMS.

For the morphological study of ATO, a Philips CM200FEG microscope operated at 200 kV and equipped with a field emission gun, the Gatan imaging filter, and energy-dispersive X-ray (EDX) analyzer was used for TEM investigations. The coefficient of spherical aberration was Cs = 1.35 mm, and the information limit was better than 0.18 nm. High-resolution images with a pixel size of 0.016 nm were taken at the magnification of 1083000X with a CCD camera. The Ir/ATO-samples were prepared by drop-casting two small drops of sample solution (powder+water) on carbon coated Cu grids. (S)TEM images and EDX elemental mapping were taken on an aberration-corrected JEOL JEM-ARM200 operated at 200 kV. The microscope is equipped with a high angle Silicon Drift EDX detector with the solid angle of up to 0.98 steradians from a detection area of 100mm².

Diffuse reflectance infra-red Fourier Transform Spectroscopy (DRIFTS) was recorded with an MCT detector at a resolution of 4 cm⁻¹ by accumulating 1024 scans, using a Praying Mantis™ high temperature reaction chamber (ZnSe window) placed in a Bruker IFS 66 spectrometer controlled by OPUS software. Measurements were performed in an in-situ cell capable of heat treatment under gas flow conditions (Bronkhorst mass flow controllers). The samples were degassed under 10 mL.min⁻¹ flow over night. A background spectrum of pure KBr was performed at the room temperature. The used gases were supplied by Westfalen (99.99% purity at least). Ar was further purified by passing through Hydrosorb and Oxysorb cartridges. The Ir_XXX_Ar and Ir_XXX_O₂ samples (XXX=250 or 350°C) were heated under Ar and 21%O₂/Ar flows respectively.

Raman spectroscopic investigation was performed at 532 nm excitation wavelength using a confocal microscope setup (S&I GmbH, Warstein Germany) equipped with a PyLoN:2kBUV CCD camera and 750 mm focal length of the monochromator (Princeton Instruments,). The laser intensity density on the samples was chosen low enough to exclude decomposition of the amorphous IrO_x structure. At higher laser intensities, sharp peaks corresponding to the IrO₂-rutile modes appeared, indicating transformation of the amorphous Ir-oxohydroxide into IrO₂ due to local heating. Spectra resemble an average of multiple measurements at different spots of the sample.

XPS-analysis of the a.s. 30 mol.%-Ir/ATO was performed at room temperature using non-monochromatized Al-K α -radiation (1486.7 eV) and a hemispherical analyzer (Phoibos 150, SPECS). The binding energy was calibrated with respect to the Fermi edge.

2.3.4. Electrochemical characterization

For electrochemical measurements, the samples were deposited on the anode using catalyst inks. Catalyst inks were prepared by suspending 4mg of sample in 6 mL Millipore-filtered H₂O, 3.96 mL isopropanol (Sigma Aldrich) and 40 μ L of a Nafion[®] suspension (5%-Nafion[®] perfluorinated resin solution, Sigma Aldrich). The suspension was sonicated in an ultrasonic bath for 30min. A rotating ring disk electrode (RRDE, Pine Research Instrumentation, 0.2475 cm² glassy carbon disk, 0.1866 cm² Pt ring) was used as a working electrode support. Prior to use, the RRDE was repeatedly cleaned with Millipore-filtered water and isopropanol, mirror-polished with alumina bead slurries (Buehler, 1 μ m and 0.05 μ m) on a polishing cloth, rinsed, sonicated for 15min in isopropanol in an ultrasonic bath and finally rinsed with Millipore water and isopropanol. Defined volumes of catalyst ink were then cast onto the RRDE using a micropipette in order to insure constant iridium-loadings. The loaded anode was dried for 30min at 60°C. All activity and stability measurements were conducted in a standard electrochemical cell containing approx. 100mL of H₂SO₄ (0.5mol.L⁻¹) distributed between three compartments separated by fine-porosity glass frits. The central and biggest compartment contained the loaded working electrode (anode) mounted on a rotator (MSRX, Pine Research Instrumentation) ensuring a constant rotation of 1600 rpm. The reference electrode was a saturated calomel electrode (SCE) at +0.241V vs SHE, the counter-electrode was a platinized wire. The electrolyte was constantly purged with nitrogen at least 20 min before measurements started. Measurements were carried out with a VSP-multichannel potentiostat (Biologic Instruments). All measurements were corrected at 85% for ohmic drop using high-frequency impedance determination of the ohmic resistance (4 measurements, 100kHz, 20mV amplitude, open circuit potential (E_{oc})). Anode potentials E are reported in V vs. Reversible Hydrogen Electrode (RHE). Contributions from the glassy carbon (GC)-support as well as the dried ink can be neglected as shown by the corresponding LSV in Figure S2.10.

MW-Ir/ATO and Ir_{250/350}_Ar/O₂ were subjected to a thorough screening procedure designed to yield a series of key performance indicators representative of OER-performance. The uncompensated ohmic resistance is then determined via electronic impedance spectroscopy (EIS) using a high-frequency impedance measurement (4 measurements, 100kHz, 20mV amplitude) and used by the EC-Lab software to automatically compensate for the ohmic drop in all following measurements. The electrode potential is then ramped to 1V vs. RHE (5 mV.s⁻¹). Subsequent step 1 assesses the initial OER-activity and consists of a LSV from 1 to 1.8 V vs. RHE and back to 1 V vs. RHE (5 mV.s⁻¹). In order to account for possible changes in the electrolyte, the uncompensated ohmic resistance is then measured again via EIS at E_{oc} . Step 2 is designed to test catalyst stability under relevant OER-conditions using a chronopotentiometric measurement of the anode potential at constant current densities of 10 mA.cm⁻². The target current density is reached via a galvanodynamic ramp of 10 μ A.cm⁻². After the CP-measurement, a third step comprises another LSV-measurement performed as in step 2 in order to assess loss in activity over the 2h-CP-scan. This procedure is repeated three times for each compound with three different loadings (20, 50 and 100 μ g_{Ir}.cm⁻²) in order to ensure some statistical certainty on the results with the additional advantage of providing information if the catalyst operates in kinetic control or whether mass-transfer/utilization effects come into play.

2.4. Results and discussion

2.4.1. Catalyst support (ATO) synthesis and characterization

The first synthesis-step involves the peptization of an acidic $\text{Sb}^{\text{III}}/\text{Sn}^{\text{IV}}$ -chloride solution at $\text{pH}=4$. We have selected a 5%-Sb-doping level based on literature reports indicating that above 7-9%, Sb tends to segregate from the ATO-phase.^{9,31,32} In order to synthesize a high surface-area ATO-compound, we adapted the hydrothermal synthesis of Nütz et al.^{9,11} to our MW-supported hydrothermal reactor setup. The hydrolyzed Sn/Sb-suspension was treated at various temperatures (180-290°C) for 1h. Nütz et al. used a similar pathway with a classical autoclave, which required higher treatment times (up to 16h).^{9,11} The resulting dried products were analyzed via XRD determine the successful incorporation of Sb into the SnO_2 -lattice. XRD patterns show coherent crystalline domains associated with the rutile structure of SnO_2 cassiterite (Figure S2.1). No segregated Sb-oxide phase could be detected. It has been reported that ATO-compounds are characterized by increasingly intense absorption in the IR-region above 1500nm with rising Sb-doping levels.¹⁰ Mishra et al. attribute this broad absorption feature to the incorporation of Sb^{V} into the SnO_2 lattice upon hydrothermal treatment. At high Sb^{V} -doping levels, an impurity band that behaves in principle like a half-filled metallic band is created, which results in high n-type conductivity. The broad absorption in the IR-region, corresponds to the easy thermal excitation of electrons from the impurity band to the tin-like conduction band (approx. 1.5 eV). This results in a blue coloration.¹⁰ The intensity of this band is thus a relative measure of the successful Sb^{V} -doping.

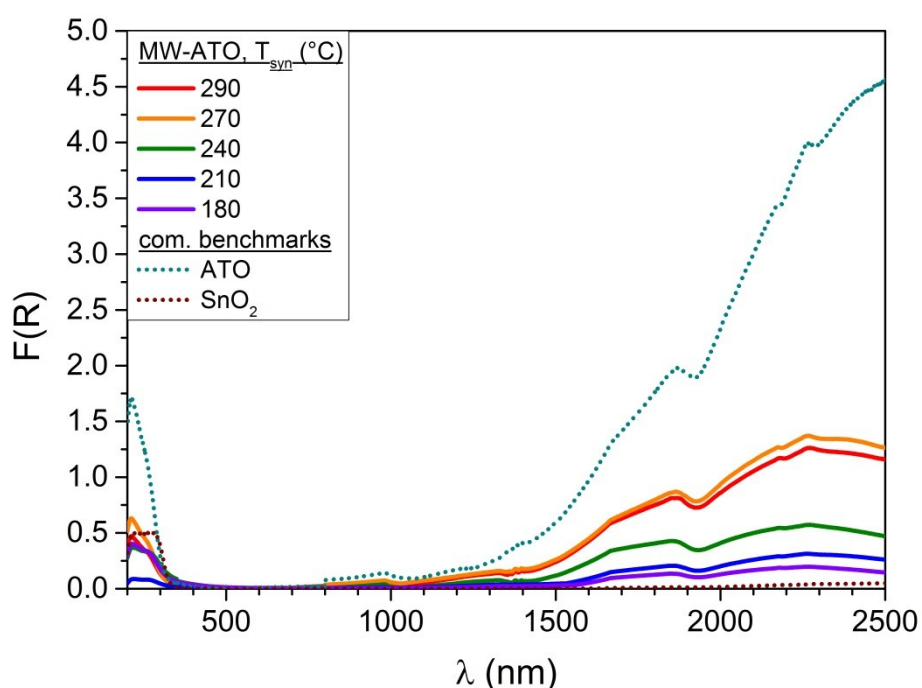


Figure 2.1 Diffuse reflectance UV-Vis spectra of commercial reference samples (dotted lines) as well as ATO obtained from the MW-treatment of a colloidal Sb/Sn-suspension at various temperatures (full lines).

Figure 2.1 shows the diffuse reflectance DR-UV-Vis spectra obtained for the ATO-samples prepared at various MW-treatment temperatures. We compare the spectra to two commercial reference samples, one crystalline SnO_2 (Aldrich, 99.9%) and one conductive ATO (Aldrich, 99.5%). All samples show adsorption in the UV-range below 320nm, which corresponds to the valence-to-conduction

band transition.¹¹ As expected, the undoped commercial SnO₂ shows no absorption in the IR region, whereas the commercial ATO is characterized by a broad absorption feature above 1500 nm corresponding to the successful Sb^V-incorporation. At high Sb^V-doping levels, an impurity band is created approx. 35 meV below the conduction band.³³ This impurity band has a nearly free-electron-like structure and behaves in principle like a half-filled metallic band. The resulting high n-type conductivity is also explained by the easy thermal excitation of electrons to the tin-like conduction band. As a result, ATO-compounds with high Sb-doping levels are characterized by a broad absorption peak in the IR-region, corresponding to excitations around 1.5 eV, resulting in a blue coloration.¹⁰ For the MW-produced ATO, the IR-absorption features grows in intensity with increasing treatment temperature and reaches a maximum for treatment temperatures of 270 and 290°C. The highest level of Sb^V-incorporation was thus expected for the ATO prepared above 270°C. Absolute comparison of spectral intensities with the commercial samples is difficult as the sample morphology plays an important role in the scattering process.

As expected from the DR-UV-Vis results, sample conductivities measured via the classical four-point-probe contact measurement technique on pressed powder pellets showed that the MW-samples with the highest absorption in the IR-range showed the best conductivities, *i.e.* the most efficient Sb^V-doping. For hydrothermal treatment temperatures of 270°C and 290°C, resistivities of respectively 17 and 11 Ω.cm were measured (see Table S2.1). Such results compare favourably to values reported in the literature^{9,34} as well as to the commercial ATO-benchmark (20 Ω.cm). In order to select the most suitable ATO-support, we compared the specific surface area (S_{BET}) of the most conductive samples. The ATO synthesized at 270°C exhibited by far the highest SBET with 207 m².g⁻¹, which compares to 184 m².g⁻¹ for the sample prepared at 290°C and 41 m².g⁻¹ for the commercial ATO. Hence the ATO-compound synthesized at 270°C was selected as the catalyst support and will be referred further on as MW-ATO. The energy-dispersive X-ray spectroscopy of MW-ATO, recorded on random agglomerates in Scanning Electron Microscopy (SEM-EDX) confirmed a homogenous Sb-distribution inside the SnO₂-matrix at 5.0% (see Figure S2.2). TEM-images show a homogenous material consisting of small, approx. 5 nm-particles (see Figure S2.3), which is well in-line with the broad XRD-peaks and the high specific surface area measured (see Table S2.1).

2.4.2. MW-assisted hydrothermal synthesis of MW-Ir/ATO

Several reports on mixed Ir/Sn-oxide OER-catalysts.^{19,20,35} highlighted that for Ir-loadings below 20 mol.%, mediocre OER-performance is achieved. This poor performance has been attributed to a sub-critical surface concentration of OER-active Ir-sites for low loadings.²³ Above 40%, De Pauli et al. also reported a sizeable decrease in mass normalized OER-performance of their Ir/Sn-materials, which they related to Ir-particle agglomeration.²⁰ As a result, we decided to aim for a nominal Ir-loading of 30 mol.% on ATO. This compound in its as synthesized state after MW-supported hydrothermal synthesis will be referred to as MW-Ir/ATO. The 30 mol.% Ir-loading of MW-ATO was achieved using K₂IrCl₆ dissolved in a highly basic suspension of MW-ATO. At basic pH, cations are readily adsorbed on ATO due the low isoelectric point of Sn-based compounds.³⁶ Another important goal in preparing these solutions is to hydrolyze Ir-chloride precursors. Indeed chloroiridate(IV)-complexes are stable in solution at high temperature and pressure and do not yield a solid product after hydrothermal treatment.³⁷ In presence of base, IrCl₆²⁻, which is a well-known outer-sphere oxidant, first reduces to IrCl₆³⁻ via water oxidation.³⁸ Evolution of oxygen bubbles can clearly be observed in the case of highly basic solutions. This phenomenon is also evidenced by the discoloration of the solution from red-

brown to pale yellowish, due to the loss of the $\text{Ir}^{\text{IV}}\text{Cl}_6^{2-}$ ligand-to-metal-charge-transfer-bands (LMCT).³⁹ The subsequent hydrolysis of IrCl_6^{3-} is a slow process occurring over days at room temperature and is still incompletely understood with respect to the suspected formation of mixed-valence iridium oligomers.^{37,39,40} In our case, the Ir-hydrolysis was performed under controlled synthesis conditions using the microwave-supported hydrothermal treatment of the solution (250°C, 1h). The product was centrifuged, repeatedly washed and dried.

2.4.3. Physico-chemical characterization of MW-Ir/ATO

The XRD-pattern of the prepared MW-Ir/ATO showed only the broad rutile-type pattern of MW-ATO (Figure S2.4). No crystalline Ir-oxide phase could be detected. X-ray fluorescence spectroscopy (XRF) confirmed the successful loading of Ir on MW-ATO with a determined loading of 33 mol.%, close to the nominal 30 mol.%.

STEM

The sample morphology of MW-Ir/ATO was studied using Scanning Transmission Electron Microscopy (STEM). Figure 2.2.a) shows an annular dark-field STEM (ADF-STEM) image of MW-Ir/ATO. In ADF-STEM mode, heavy elements such as Ir appear much brighter than the Sn/Sb-containing ATO support. Elemental mapping using EDX shows (Figure 2.2.b) that the Ir has been homogeneously loaded onto the ATO-support in the form of 2-4 nm particles (see also Figure S2.5). Some bigger spherical Ir/ATO-agglomerates could also be observed as shown in Figure S2.6.

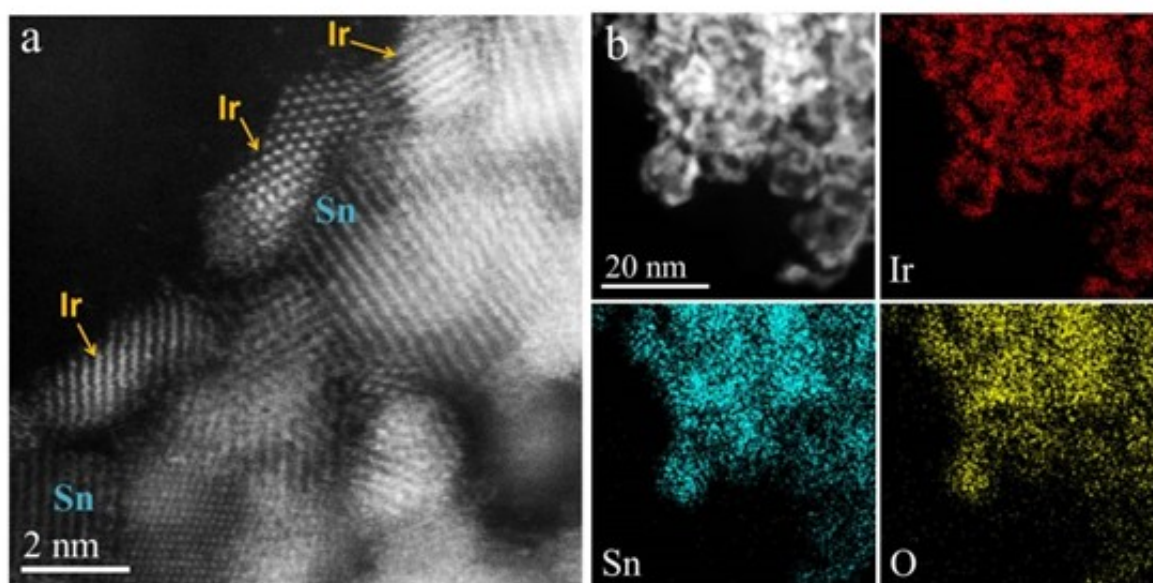


Figure 2.2 ADF-STEM imaging of MW-Ir/ATO with corresponding EDX-based elemental mapping

Since no crystalline Ir-phase could be detected in XRD, it was surprising to find that crystalline Ir-particles. Structural analysis (Figure S2.5) revealed that the observed crystal lattice corresponds to cubic metallic Ir. No oxidic iridium phase could be detected, even though the oxidic nature of the Ir-phase was confirmed via TPR and XPS (see corresponding paragraphs). We conclude that for MW-

Ir/ATO, the amorphous Ir-phase is immediately reduced under the electron beam to metallic Ir. (S)TEM-imaging can therefore only yield qualitative information on the sample morphology, *i.e.* the homogenous Ir-distribution. No reliable information on the chemical nature or crystal structure of Ir could be obtained.

TGMS

A powerful tool for the study of the sample composition is thermogravimetric-analysis coupled with mass-spectrometry (TG-MS). Mass changes and evolved gas products can be used to identify temperature-dependent decomposition mechanisms and phase transformations. MW-ATO and MW-Ir/ATO were calcined in 21% O₂/Ar (100 mL.min⁻¹) using a 10K.min⁻¹ heating ramp from room temperature to 800°C. Figure 2.3 shows the resulting mass loss profiles and the water evolution signals (m/z=18).

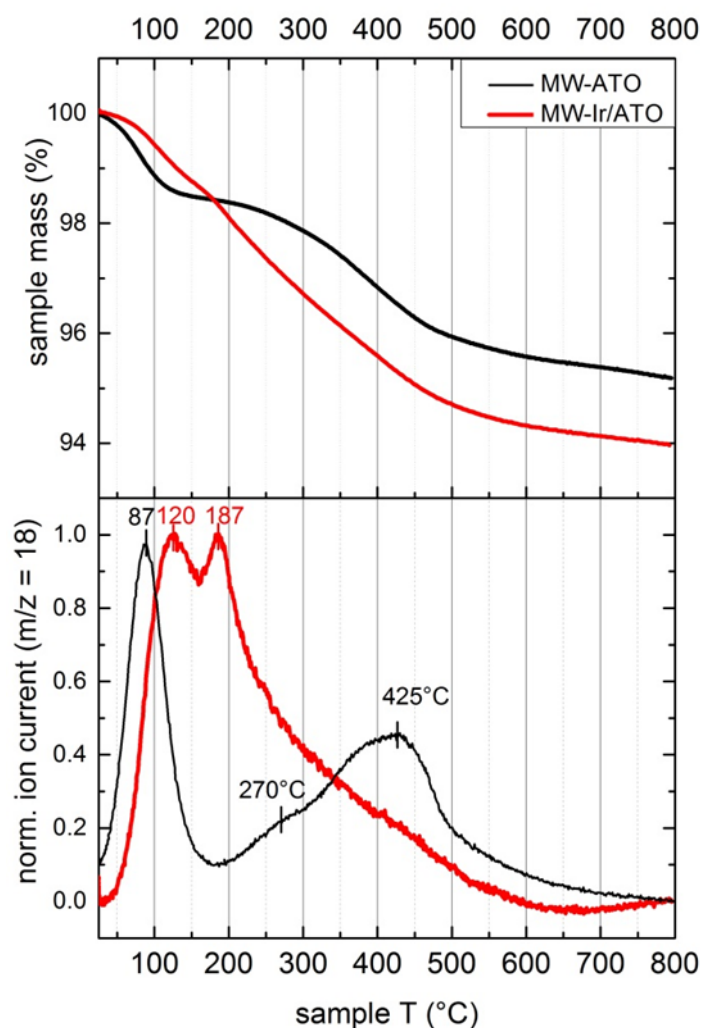


Figure 2.3 TG-MS curves for the decomposition of MW-ATO and MW-Ir/ATO in oxidative (21%O₂/Ar) and inert (Ar) gas streams.

A first mass loss event observed for both samples below 150°C can be attributed to the removal of weakly bonded physisorbed water, which occurs at 87°C for MW-ATO and 120°C for MW-Ir/ATO. This indicates that physisorbed water has a higher affinity for the Ir-loaded compound, which might

be expected for a good water oxidation catalyst. Subsequent mass loss between 150 and 500°C can be assigned to hydroxyl group decomposition as no other intense signals are detected in MS besides traces of carbon (CO₂ evolution, 180-220°C) and NH₃ (NO removal, 420-450°C). The bare MW-ATO-support features a late hydroxyl-decomposition-event in 21% O₂/Ar with a first shoulder at 270°C and a major peak centered around 425°C accounting for evolved water (m/z=18). The loss of chemisorbed water accounts for 3.3 wt.%, which results in a formal ATO formula of Sn_{0.95}Sb_{0.05}O_{1.71}(OH)_{0.58}·0.13H₂O. This speaks for a highly hydroxylated surface in line with the high S_{BET}. The chemisorbed water fraction in ATO compares to a chemisorbed water mass fraction of 5 wt.% in MW-Ir/ATO. This indicates that MW-Ir/ATO contains a significantly higher fraction of hydroxyl groups, which can be attributed to the iridium phase. The Ir-phase can therefore be seen as an Ir-oxide/hydroxide phase.

TPR

Figure 2.4 shows the temperature-programmed reduction (TPR) profiles obtained for MW-ATO, MW-Ir/ATO and the reference IrO₂-compound (SA-IrO₂). During TPR to 800°C, the samples were entirely reduced to metallic Ir, Sn and Ir/Sn-alloys. XRD showed no sign of remaining oxide phases. Before the start of the TPR, samples were purged for at least one hour in Ar. We also compared the transient H₂-signals obtained at room temperature during the switch from Ar to a 5%H₂/Ar-stream before and after TPR. Discrepancies between the two signals would indicate adsorption and/or consumption of H₂ by the sample at RT before the start of the TPR-program.

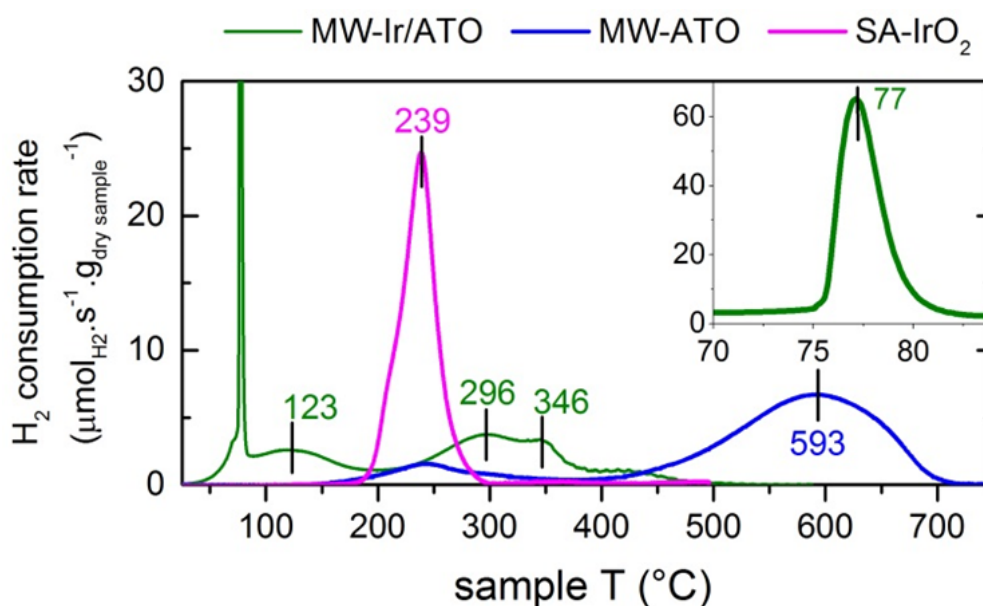


Figure 2.4 TPR-profiles of MW-ATO, MW-Ir/ATO and SA-IrO₂

The H₂-TPR profile of SnO₂ has been previously studied in the literature.⁴¹ Sasikala et al. observed a first small reduction peak at 295°C and a major event at 620°C using a 15K.min⁻¹ ramp. They assigned the first event to the reduction of distorted SnO₂-crystal domains on the surface of small nanoparticles. Our nanostructured MW-ATO reduces in a similar fashion (blue line, Figure 2.4: A first small reduction feature is observed at around 240°C, which probably corresponds to surface

reduction of distorted or defective Sb-doped SnO₂. The major reduction event presents as a broad H₂-consumption feature centered around 593°C. In order to identify the TPR-profile of crystalline IrO₂, we reduced a commercial IrO₂-reference (SA-IrO₂), which showed a main reduction peak at 239°C (purple line). Neither SA-IrO₂ nor MW-ATO showed H₂-consumption at room temperature when comparing the transient H₂-signals before and after TPR.

In contrast, significant amounts of hydrogen were adsorbed on MW-Ir/ATO (Figure S2.8). Such an observation is in line with the observation of Reier et al. that their amorphous Ir-oxide/hydroxide already started reducing at room temperature, in contrast to the more crystalline IrO₂-structures. Thus, H₂-adsorption at RT seems to be a specific feature of the amorphous Ir-oxohydroxide phase formed under hydrothermal treatment conditions. Since no hydrogen release is detected during the measurement, the amount of RT-adsorbed H₂ has to be taken into account when determining the amount of hydrogen consumed during sample reduction.

During TPR, a sharp reduction feature at 77°C was observed for MW-Ir/ATO (inset in Figure 2.4). This compares well with the signal attributed by Reier et al. to their amorphous Ir-oxide/hydroxide phase and allows us to identify this sharp peak with the reduction of the Ir-oxohydroxide phase. An additional feature at 123°C should also be attributed to the reduction of Ir and might account for a second reduction step or morphological effects, such as the reduction of the more compact spherical structures observed in TEM (Figure S2.6). The broad feature above 250°C with peaks at 296 and 346°C is assigned to the ATO-support. It seems that the Ir-loading has a dramatic effect on the reduction sensitivity of the ATO-matrix and poses the question whether the already reduced Ir-particles at the surface act as H₂-activation catalysts and/or preferential adsorption sites during TPR, thus modifying the ATO-reduction mechanism.

We determined the average oxidation state of Ir in MW-Ir/ATO via the quantification of the consumed hydrogen and by taking into account the content of physisorbed and chemisorbed water. As a result, Ir was determined to be in a +3.28 oxidation state. Even by taking into account experimental error due to the small masses used, it is clear that the Ir-oxohydroxide is a mixed oxide phase, involving Ir-oxidation states of less than IV.

2.4.4. XPS-analysis of Ir-species

In order to determine the oxidation state of Ir-species present in MW-Ir/ATO, the sample was studied using X-ray photoelectron spectroscopy (XPS). Due to the small 2-4 nm size of the Ir-particles observed in STEM (Figure 2.2), bulk as well as Ir-surface species contribute to the XPS-signals, which are thus an average over all Ir-species present in the sample. When studying OER-relevant Ir-based catalysts by XPS a major challenge is that even well-defined rutile IrO₂ presents an atypical Ir 4f-lineshape. The Ir 4f lines cannot be fitted with the Doniach-Šunjić function often applicable for asymmetric core level spectra of conductors. For this purpose, we recently developed an accurate Ir 4f fit model for rutile IrO₂ by combining theoretical calculations with experiments.^{42,43} Within a one-electron picture we found that Gaussian “shake-up” satellites add intensity to the Ir 4f spectrum 1 and 3 eV above the main lines. This model gives more solid ground for the identification of the contributions of Ir^{IV}-species to Ir 4f spectra and allows for a precise Ir 4f deconvolution in order to identify contributions from other Ir-oxidation states.

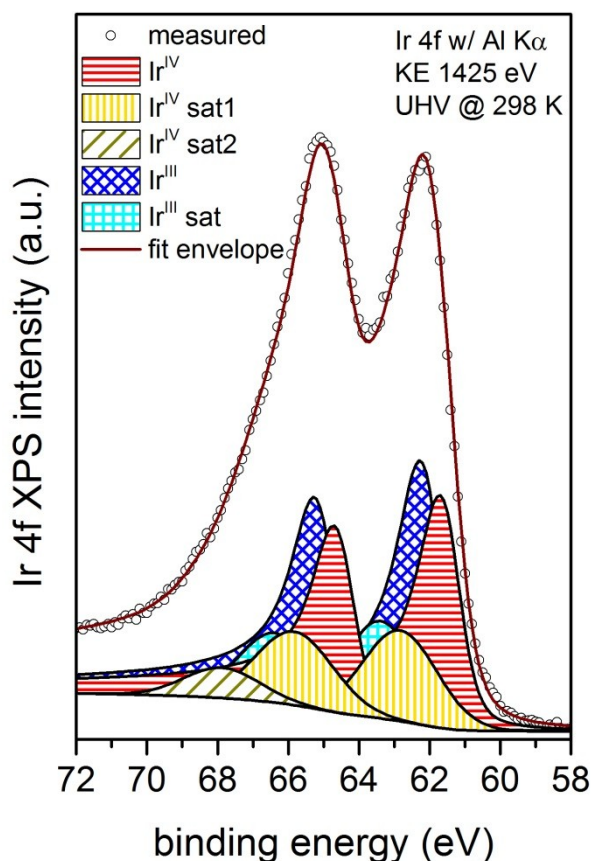


Figure 2.5 XPS of MW-Ir/ATO in the Ir4f-region fitted using the models developed by Pfeifer et al.^{42,43}

It was already noted in several studies on Ir-based OER-catalysts performed ex-situ⁴⁴ as well as in-situ⁴⁵ that OER-active compounds presented additional contributions in their Ir4f-spectra at higher binding energies than expected for Ir^{IV} (61.8 eV (Ir4f_{7/2}) and 64.8 eV (Ir4f_{5/2}). Based on the higher binding energies of the Ir4f-electrons of the additional species, Casalongue et al. attributed these contributions to Ir^V-species formed in-situ during the OER and involved in the catalysis of water oxidation.⁴⁵ However, caution should be used when assigning oxidation states based only on binding energy shifts. In our aforementioned investigation of the electronic structure of an amorphous Ir-oxohydroxide compound, we showed that Ir 4f intensity at higher binding energies can be attributed to Ir^{III}-species comprising satellite features. This model was used to fit the XPS data recorded for MW-Ir/ATO in the Ir4f-region (Figure 2.5). The obtained fit describes the experimental data accurately and confirms that the near-surface region of the Ir-particles probed at kinetic energies of 1425 eV consists of a mixed valence state Ir^{III/IV}-compound. Ir^{III}-species accounted for more than 50% of the observed intensity, which is well in line with the average Ir^{3.28}-oxidation state calculated from the TPR-results.

2.4.5. OER-performance of MW-Ir/ATO

In order to assess the OER-performance of MW-Ir/ATO, used a chronopotentiometric (CP)-test at 10 mA.cm⁻² (see Figure S2.9). This procedure has been used in recent benchmarking efforts in order to reference the most promising OER-catalysts^{6,46} and allows to compare our catalyst to the best reported benchmarks. We also tested AA-IrO_x, which is close in nature to MW-Ir/ATO and was used as a reference compound by Pfeifer et al.^{42,43}

The overpotentials η needed to maintain the current density of $10 \text{ mA}\cdot\text{cm}^{-2}$ after various amounts of time were used as indicators of activity and stability (see Table 2.2). At Ir-loadings of 50 and $100 \mu\text{g}_{\text{Ir}}\cdot\text{cm}^{-2}$, our MW-Ir/ATO proved to be the only OER-catalyst able to maintain rather constant overpotentials after 24h, which indicates excellent stability. It appears that in terms of stability-related OER-performance, MW-Ir/ATO used at loadings equal to or above $50 \mu\text{g}_{\text{Ir}}\cdot\text{cm}^{-2}$ surpasses all Ir-based benchmarks reported in peer reviewed literature under similar conditions.^{6,46}

Table 2.2 Benchmarking parameters for the most performant samples compared to previously reported reference compounds during a galvanostatic measurement at $10 \text{ mA}\cdot\text{cm}^{-2}$.

Catalyst	$\eta_{t=0}$ (V)	$\eta_{t=2h}$ (V)	$\eta_{t=24h}$ (V)	Ir-loading ($\mu\text{g}\cdot\text{cm}^{-2}$)
MW-Ir/ATO	0.35	0.37	-- ^b	20
MW-Ir/ATO	0.31	0.33	0.35	50
MW-Ir/ATO	0.31	0.32	0.34	100
AA-IrO _x	0.37	-- ^b	-- ^b	20
SIROF ⁴	0.34	0.36	0.44	n.r. ^a
Sputtered Ru ⁴	0.28	0.34	0.82	n.r. ^a
20wt.% Ir/C ²²	0.38	--	--	28
AIROF ²¹	0.28	0.30	--	--
[a] Reactive sputtering resulted in a >100nm thick Ir-film (see ref. ^{6,47})				
[b] Not reached as potentials overshoot the 1.8 V vs. RHE-mark earlier				

2.4.6. Effect of thermal treatment on MW-Ir/ATO

The characterization of MW-Ir/ATO revealed an ATO-supported Ir^{III/IV}-oxohydroxide with exceptional OER-performance. In order to determine to what extent the nature of the Ir-phase is responsible for the OER-performance, we decided to study the effect of thermal treatment at moderate temperatures. TGMS revealed that important removal of chemisorbed water from MW-Ir/ATO starts early on in the 150-200°C temperature range. We decided to submit the sample to thermal treatment at 250°C and 350°C under both inert (Ar) and oxidative (21% O₂/Ar)-streams.

Major changes to the Ir-phase are expected in this temperature region due to the dihydroxylation, changes in oxidation state and possible crystallization. Thus changes in the OER-performance of the resulting compounds could be related to structural changes and eventually lead to the identification of OER-relevant fingerprints.

2.4.7. Thermally-induced structural changes

The XRD-patterns of the calcined samples only revealed the rutile-type pattern of the ATO support (see Figure S2.11). No Ir-oxide phase could be identified, which indicates that no large aggregates of crystalline Ir-oxides were formed. The thermal treatment had little effect on S_{BET} at 250°C, whereas for 350°C, a clear diminution in S_{BET} is observed (see Table 2.3).

Table 2.3 Specific surface areas of MW-Ir/ATO and thermally treated products

Electrocatalyst	S_{BET} ($\text{m}^2 \cdot \text{g}^{-1}$)
MW-Ir/ATO	154
Ir_250_O ₂	140
Ir_350_O ₂	105
Ir_250_Ar	144
Ir_350_Ar	109

TG-analysis

The thermal treatment of MW-Ir/ATO was simulated in a stepwise TG-experiment where the sample was annealed stepwise at 250°C and 350°C for 1h in 21% O₂/Ar or Ar (100 mL.min⁻¹). The resulting mass loss profiles are shown in Figure S2.11. It can be observed that after 1h at 250°C in Ar-stream, MW-Ir/ATO loses 0.33% more mass than in oxidative stream. If one neglects other stream-dependent mass changes at 250°C, this indicates that a significantly higher amount of the hydroxyl-fraction attributed to the Ir-phase is lost after annealing MW-Ir/ATO at 250°C in Ar.

STEM

In order to gain insight into morphological changes upon thermal treatment, the samples upon calcination under oxidative atmosphere were analyzed using (S)TEM. The ADF-STEM image of Ir_250_O₂ is shown in Figure 2.6.a). Similar to the case of MW-Ir/ATO, only bright metallic Ir-particles of approx. 2-4nm could be detected, indicating that the Ir-phase was also immediately reduced by the electron beam. The observed structure confirms that no major changes in sample morphology occur upon thermal treatment at 250°C, as shown by the little change in S_{BET} . We extrapolate this observation to Ir_250_Ar due to the even more stable S_{BET} .

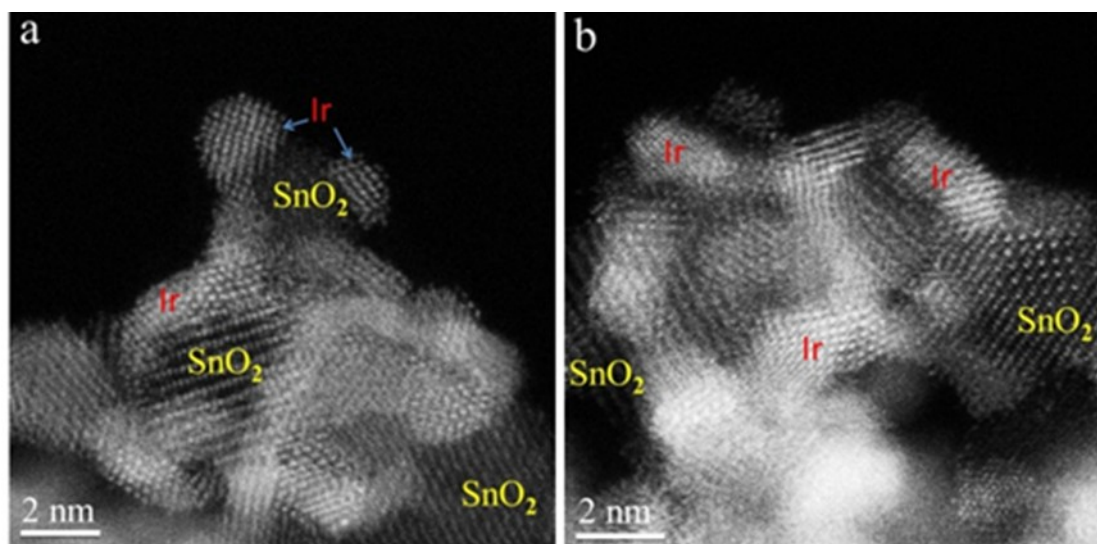


Figure 2.6 ADF-STEM imaging of Ir_250_O₂ (a) and Ir_350_O₂ (b).

For Ir_350_O₂, however, the morphology was found to differ from MW-Ir/ATO and Ir_250_O₂. Ir-particles seemed larger and showed a higher wetting on the ATO-support (Figure 2.6.b)). This is in line with the sharp 25%-decrease observed in S_{BET} between Ir_250_O₂ and Ir_350_O₂.

In some regions, we detected large portions of bare rutile-type ATO-support, which initially showed no presence of metallic Ir-particles (Figure 2.7.a). However brighter contrast on the outer shell of the central particle shown in Figure 2.7.a for instance, suggests that the ATO support is covered with a thin Ir-film in the same rutile-type structure. This would correspond to IrO₂-rutile. The time-dependent *in-situ* STEM observation of the same spot clearly showed that under beam irradiation, metallic Ir-particles blossomed in a matter of minutes where such brighter contrast could initially be observed (Figure 2.7.b and Figure 2.7.c). This indicates that the thin IrO₂-film is being reduced to Ir⁰. IrO₂ has usually been described as stable under the electron beam. At 350°C, we probably are in presence of a still highly defective, partially hydroxylated IrO₂-type phase. The transition towards IrO₂ at 350°C however explains our ability to observe the reduction to Ir⁰ under electron irradiation as the Ir-phase in Ir_350_O₂ is closer to IrO₂. Due to the difficulty of assigning phases formed or modified by the electron beam, the Ar-treated samples were not studied using STEM.

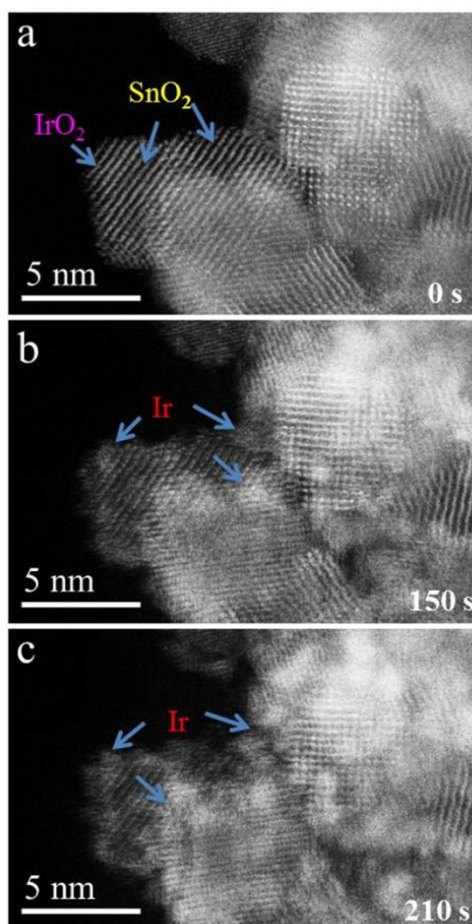


Figure 2.7 *In-situ* STEM observation of Ir_350_O₂ over 210 s showing the evolution of sample morphology under the electron beam. The ADF-STEM imaging allows to relate contrast changes to heavier (brighter) or lighter (darker) atoms.

Temperature-dependent DRIFTS

In order to obtain fingerprints of chemical bonds present in the samples, vibrational spectroscopy was required. The use of diffuse reflectance infrared Fourier transformed spectroscopy (DRIFTS) allows for the study of compounds in a loose, powdered state under gas streams and conditions close to the real thermal treatment. Structural changes during the calcination of MW-ATO and MW-Ir/ATO in 21%O₂/Ar were studied in-situ using DRIFTS during a stepwise heating experiment to 350°C.

The DRIFTS spectra recorded for the MW-ATO support during the stepwise heating experiment are discussed in further detail in the S.I. (Figure S2.12). The most prominent structural features are located below 1500 cm⁻¹. A strong signal is located at 760 cm⁻¹ and shifts to 778 cm⁻¹ above 250, while its intensity gradually increases. According to the TGMS-profile (see Figure 2.3), above 250°C, MW-ATO is being strongly dehydroxylated and thus forms more oxide-like structures. One would thus assign the strong contribution between 760 and 778 cm⁻¹ to O-(Sn/Sb)-O, (Sn/Sb)-O-(Sn/Sb) and other lattice vibrations. In the literature these features are usually being observed at lower wavenumbers in the 600-660 cm⁻¹-range.^{48,49} The important difference could be explained by varying tin doping levels as well as important differences in particle-sizes and -shapes, which have significant influence on peak positions.⁵⁰ Most FTIR-studies are being performed on ATO-films, in contrast to our 5 nm-particles. In general, the observed increasing intensity of lattice features in the DRIFTS-spectra of MW-ATO is in line with an increasing crystallinity of the ATO upon calcination.

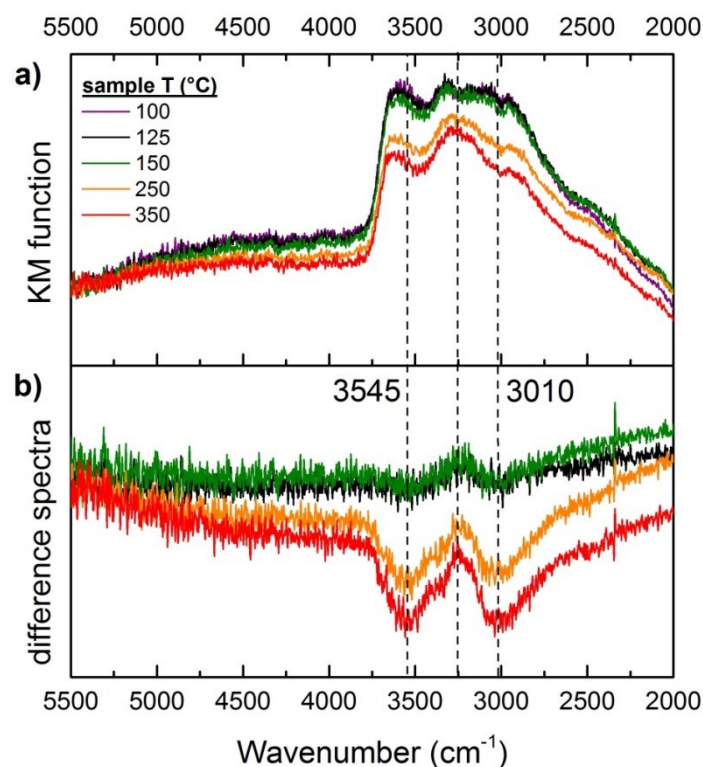


Figure 2.8 DRIFTS measurements (5500-2000 cm⁻¹) of MW-Ir/ATO during stepwise treatment at various temperatures in 21%O₂/Ar, 100 mL.min⁻¹. Kubelka-Munck transformation of the reflectance spectra (a) and corresponding difference spectra between said temperature and 100°C (b).

Important differences are observed for the Ir-loaded MW-Ir/ATO. Figure 2.8 shows the Kubelka-Munk-corrected DRIFTS-spectra obtained after treatment to or above 100°C in 21%O₂/Ar. According to TGMS-results, loosely physisorbed water has been removed after heating at 125°C and shouldn't contribute to the observed signal. Broad but pronounced features are observed in the 3000-3700 cm⁻¹-region, which indicates a high hydroxyl-fraction in the added Ir-phase (Figure 2.8.a). Such features indicating a highly hydroxylated nature were recently reported by Ito et al. for Ir-oxide films sputtered in a reactive wet atmosphere as opposed to dry oxygen.⁵¹ Hydroxyl groups showing up at 3700-3450 cm⁻¹ usually correspond to isolated OH-groups on the oxide surface, while the broad features in the 3400-3100 cm⁻¹-region should be assigned to more or less strongly H-bound hydroxyl groups and water molecules present in the bulk or strongly physisorbed on the surface. A broad feature around 2950 cm⁻¹ is assigned to C-H-stretching frequencies and might originate from C-contaminations from the atmosphere. Such features were also observed by Ito et al. but assigned to hydrogen-bonded OH-groups.

The effect of thermal treatment on the chemisorbed water fingerprint is evidenced when observing the difference spectra between the spectra recorded at a given temperature and the 100°C-spectra (Figure 2.8.b). Temperature-induced changes in the background scattering might account for overall baseline shifts, however two pronounced events can be isolated. At 250 and 350°C the spectra lose important contributions centered at 3545 cm⁻¹ and 3010 cm⁻¹. If we assign the contribution at 3545 cm⁻¹ to isolated surface hydroxyls, the Ir-surface seems to be strongly dehydroxylated above 250°C, while H-bonded hydroxyl groups probably located deeper in the bulk remain stable and will be removed at higher temperatures. The signal loss at 3010 cm⁻¹ would in turn be assigned to the removal of surface carbonaceous species. Unfortunately, signals were too broad to be used in a comparison of the dehydroxylation of MW-Ir/ATO in oxidative and inert atmosphere. Hence, we don't discuss DRIFTS-results for Ar-calcination here.

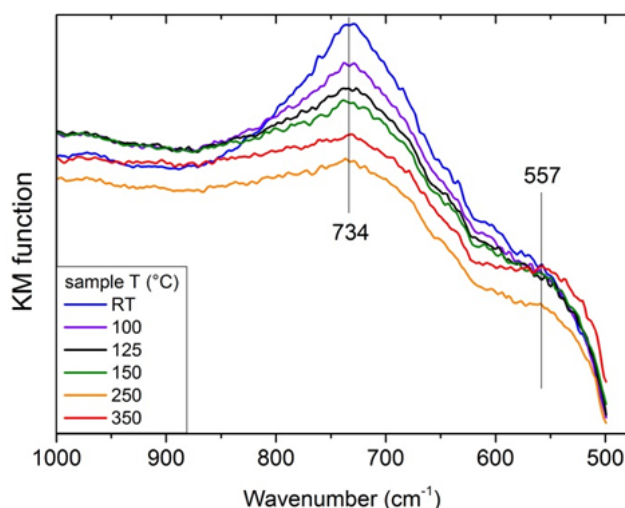


Figure 2.9 DRIFTS measurement of MW-Ir/ATO (Kubelka-Munck transformation, 1000-500 cm⁻¹) during stepwise treatment at various temperatures in 21%O₂/Ar, 100 mL.min⁻¹.

Additional information on the effect of thermal treatment can be found at lower wave numbers. Figure 2.9 shows the only feature that could be clearly assigned to the ATO-support in the spectra of MW-Ir/ATO. It corresponds to the strongest feature detected for MW-ATO at 760 cm^{-1} at room temperature. This feature is slightly shifted to 734 cm^{-1} in MW-Ir/ATO and instead of increasing in intensity with rising temperatures, it gradually shrinks. We suggest that the higher wetting of Ir-particles observed in STEM (Figure 2.6.b) and the suspected formation of an Ir-oxide film (Figure 2.7.a) are responsible for deduced for the diminution of the only clearly visible ATO-feature. IrO_2 is known for its reflective properties in the IR-region, which result from the characteristic plasma frequency and is dependent on the electronic density.⁵² If the Ir-oxohydroxide particles are being transformed into a film of more IR-reflective IrO_2 , this creates increased shielding of the ATO-support from the incident IR-radiation, thus a decreased contribution of the support to the overall spectrum. The formation of an IrO_2 -type phase is confirmed by an additional shoulder visible at approx. 557 cm^{-1} (Figure 2.9). Indeed absorption at around 550 cm^{-1} has been repeatedly attributed in the literature to lattice Ir-O-bonds in IrO_2 .^{51,53} This indicates that small crystalline IrO_2 -domains even start forming at 250°C .

Raman spectroscopy

Complementary vibrational fingerprints resulting from chemical bonds and lattice structures in the samples can be extracted from the Raman spectra of the samples. The Raman-active modes of crystalline rutile-type structures such as IrO_2 and SnO_2 have been calculated and experimentally assigned early on.^{54,55} In the case of crystalline SnO_2 , the three expected observable Raman modes E_g (476 cm^{-1}), A_{1g} (629 cm^{-1}), and B_{2g} (772 cm^{-1}) can be detected in the spectrum of MW-ATO (black line in Figure 2.10). Additional broad features, for instance at 570 cm^{-1} are usually assigned to surface Raman modes that cannot be neglected for small nanoparticles exhibiting distorted crystal structures towards the surface⁵⁶, as in the case of MW-ATO.

In MW-Ir/ATO (green line), the most prominent feature shows up at 493 cm^{-1} , which is clearly distinct from the Raman modes assigned to rutile- IrO_2 at 561 cm^{-1} (E_g), 752 cm^{-1} (A_{1g}) and 728 cm^{-1} (B_{2g}).⁵⁴ The Raman signature of the ATO-support is identified by two broad shoulders above 600 cm^{-1} . Deconvolution of the spectra is ambiguous because of the strongly overlapping broad features. XPS and TGMS have shown the $\text{Ir}^{\text{III/IV}}$ -oxohydroxide nature of MW-Ir/ATO. However, no theoretical data concerning the Raman modes of amorphous Ir-oxohydroxides is available.

Recently some studies described planar bis- μ -oxo di-Ir(IV) structures involved in the structure of active Ir-based catalysts formed from organometallic precursors under OER-relevant conditions.^{57,58} Hintermair et al. calculated the corresponding Raman-active vibrations and observed the Raman features of the bis- μ -oxo di-Ir(IV)-unit in-situ between 559 and 666 cm^{-1} .⁵⁷ Our main peak at 493 cm^{-1} is shifted compared to these values and smaller contributions cannot be distinguished from the complex ATO-signal. However, Huang et al. pointed out the relevance of such iridium-oxo-domains for the understanding of OER-relevant amorphous iridium-oxohydroxide-based catalysts. The characteristic peak observed at 493 cm^{-1} for MW-Ir/ATO might be assigned precisely to such an amorphous iridium oxo-domain.

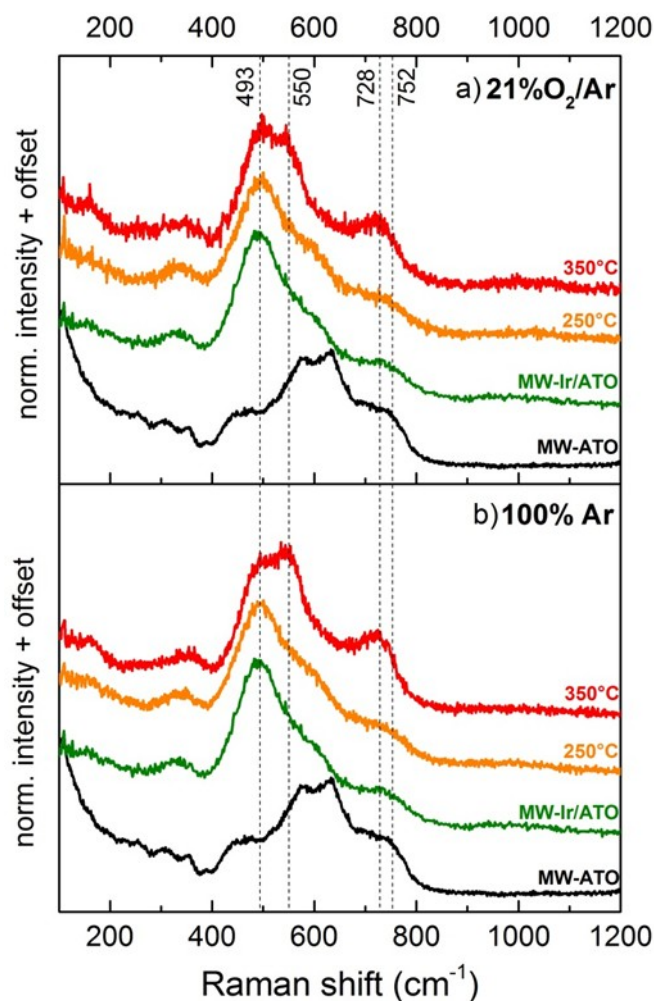


Figure 2.10 Raman spectra of the support (MW-ATO), of the as prepared MW-Ir/ATO as well as after thermal treatment at 250 or 350°C in 21%O₂/Ar (a) or 100% Ar (b).

The effect of thermal treatment on MW-Ir/ATO is clearly reflected in the Raman spectra recorded for the samples calcined at 350°C in 21% O₂/Ar and 100% Ar. Distinct strong peaks appear for Ir₃₅₀O₂ and Ir₃₅₀Ar at 550 cm⁻¹ as well as around 730 cm⁻¹. These features can be attributed to the E_g⁻, A_{1g}⁻ and B_{2g}⁻ modes of IrO₂-rutile and confirm the indications from STEM and DRIFTS that an IrO₂-phase is being formed. It seems that thermal treatment at 350°C in both atmospheres leads to the formation of IrO₂-rutile domains. However, it is also evident that the ratio between the IrO₂-E_g⁻ peak mode at 550 cm⁻¹ and the Ir-oxohydroxide-peak at 493 cm⁻¹ shift in opposite directions depending on the gas used for the thermal treatment. For Ir₃₅₀O₂, the 493 cm⁻¹-feature seems more intense than the IrO₂-E_g⁻ peak (Figure 2.10.a)), while the opposite trend is observed for Ir₃₅₀Ar (Figure 2.10.b)). This could indicate that the amorphous Ir-oxohydroxide featuring Ir-oxo domains linked to the 493 cm⁻¹-feature are decomposed faster in 100% Ar than in 21% O₂/Ar. For the samples prepared at 250°C, no IrO₂-features could be distinguished, indicating that IrO₂-domains detected in DRIFTS are still a minority phase comparing to the samples produced at 350°C.

TPR

TPR of the calcined samples yields indications on thermally-induced changes in Ir-phase and oxidation state. Figure 2.11 shows the TPR-profiles of the samples produced at 250°C (Figure 2.11.a) and 350°C (Figure 2.11.b) compared to MW-Ir/ATO (green profile). During TPR to 800°C, the samples were entirely reduced to metallic Ir, Sn and Ir/Sn-alloys. XRD showed no sign of remaining oxide phases.

In section 2.2., TPR of MW-Ir/ATO allowed us to identify the sharp reduction peak at 77°C as a characteristic reduction feature of the Ir-oxohydroxide phase deposited on ATO (Figure 2.4). Another distinctive feature of this phase was the important uptake of hydrogen at room temperature. The morphological observations and spectroscopic fingerprints reported above for the calcined samples, seem to indicate a gradual decomposition of the Ir-oxohydroxide, mostly to crystalline IrO₂. Diminution of the characteristic fingerprints linked to the Ir-oxohydroxide is thus expected for the calcined samples.

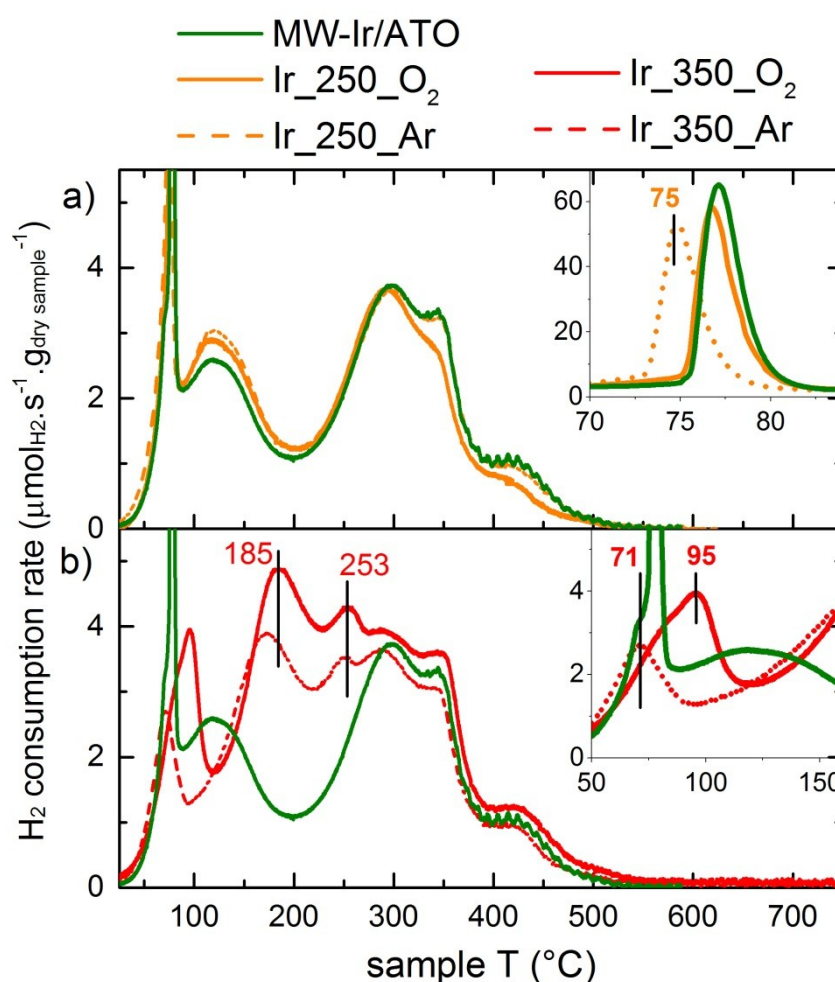


Figure 2.11 TPR-profiles of MW-Ir/ATO (green line), and the samples obtained after treating MW-Ir/ATO in 21%O₂/Ar (full lines) and Ar (dotted lines) at 250°C (a, orange) and 350°C (b, red).

We first assessed the H₂-uptake of the calcined samples at room temperature. Ir_250_Ar and Ir_250_O₂ both absorbed high amounts of H₂, comparable to the case of MW-Ir/ATO (see Table 2.4). For Ir_350_Ar and Ir_350_O₂, the amount of RT-adsorbed hydrogen clearly diminished. As Raman and IR-spectroscopy both confirm the partial transformation of the Ir-phase into crystalline IrO₂-domains at 350°C, the observed decrease of RT-adsorbed hydrogen is well in line with the behavior of the SA-IrO₂ reference (see Table 2.4 and Figure 2.4). On the opposite, the important H₂-uptake at RT indicates that the samples calcined at 250°C are still in a state close to the Ir-oxohydroxide present in MW-Ir/ATO.

The changes in TPR-profiles yield additional information on the thermally-induced changes in the Ir-phase. The features assigned to ATO-reduction above 250°C remain relatively stable independently of the thermal treatment, indicating that the bulk electronic structure of the ATO-support was little affected. On the other hand, important differences in the reduction profiles of the Ir-particles were observed. At 250°C (Figure 2.11.a)), changes are subtle: The sharp feature at 77°C only slightly diminishes for both Ir_250_O₂ and Ir_250_Ar, indicating a minor depletion in the Ir-oxohydroxide phase. For Ir_250_Ar, the characteristic peak also shifted from 77 to 75°C hinting at a higher reducibility of the Ir-oxohydroxide phase. In both atmospheres, a slightly higher amount of the species at 123°C seems to be formed, which might be attributed to morphological changes. The calculation of the average oxidation state showed no significant difference between Ir_250_O₂ and Ir_250_Ar (see Table 2.4). This confirms that the higher mass loss observed in stepwise TG-analysis of MW-Ir/ATO was indeed linked to faster dehydroxylation in Ar than in 21%O₂/Ar and not to oxygen uptake/release.

Table 2.4 Characteristic values extracted from TPR-profiles including the H₂-uptake at RT ($n_{H_2,RT}$), the H₂-consumption during TPR ($n_{H_2,TPR}$) and the resulting calculated average oxidation state of Ir.

Compound	$n_{H_2,RT}$ (mmol.g ⁻¹)	$n_{H_2,TPR}$ (mmol.g ⁻¹)	Avg. Ir-oxidation state
MW-Ir/ATO	1.07	9.80	3.28 ±0.07
Ir_250_O ₂	1.25	9.25	2.9 ±0.06
Ir_350_O ₂	0.38	11.21	4.06 ±0.08
Ir_250_Ar	1.17	9.49	3 ±0.06
Ir_350_Ar	0.64	9.61	2.52 ±0.05
SA-IrO ₂	0	9.07	4.09 ±0.08

The most notable changes in TPR-profiles are seen for the samples treated at 350°C (Figure 2.11.b)). Both compounds exhibit two additional reduction peaks centered at 185 and 253°C, which is in close range of the IrO₂-reduction feature obtained for SA-IrO₂ at 239°C (Figure 2.4). This is well in line with the identification of characteristic IrO₂-modes via DRIFTS and Raman spectroscopy. Features below 100°C, assigned to the Ir-oxohydroxide phase have been significantly reduced in both samples. The inset in Figure 2.11.b shows that a small residual reduction takes place for Ir_350_Ar at 71°C, while a broader and more important feature is detected for Ir_350_O₂ at 95°C. The observed differences in H₂-consumption are reflected in the calculated average oxidation state: Ir_350_Ar was found to be in an average Ir^{2.52+}-state. Since no additional features in the TPR-profile of Ir_350_Ar indicate an

additional Ir-oxide phase, we conclude that part of the Ir is reduced to metallic Ir⁰ upon thermal treatment at 350°C in Ar. The rest of the oxidic Ir transforms into an IrO₂-type phase detected via Raman and showing the same TPR-profile as Ir_350_Ar. Ir_350_O₂ was found to be in a Ir^{4.06}-oxidation state. This indicates that the oxidic Ir is completely transformed into an IrO₂-type phase in Ir_350_Ar.

We conclude that both in inert and oxidative atmosphere the Ir-oxohydroxide phase was transformed into small domains of an IrO₂-type phase at 350°C. Under Ar at 350°C however, part of the Ir is reduced, probably to metallic iridium. Vibrational spectroscopy confirms the presence of such IrO₂-domains. At 250°C, the oxidation state is less affected and the dominating event seems to be the faster dehydroxylation observed in Ar-atmosphere via TG-analysis.

2.4.8. Effect of thermal treatment on OER-performance

A systematic electrochemical testing protocol was designed for the testing of MW-Ir/ATO and Ir_(250/350)_(O₂/Ar). In order to compare the OER-performance of the catalysts under industrially relevant conditions, the OER-activity was assessed via LSV before and after a CP-based stability test at 10 mA.cm⁻². In order to improve the statistical relevance of the results, the test protocol was repeated three times for each compound with three different loadings (20, 50 and 100 μg_{Ir}.cm⁻²). For easy comparison, we report the loading-dependent mass activity of the iridium-catalysts at a typical overpotential of η=0.35 V.⁴⁶ Figure 2.6 shows a summary of the values obtained before and after the stability test.

If the catalyst operated under kinetic control, mass-normalized currents at a given overpotential would be independent of catalyst loading. It appears that for all compounds, the mass activity gradually decreases with increasing Ir-loading, which suggests that utilization effects come into play. A build-up of Ir-layers and decreasing Ir-utilization is to be expected from a drop-coating procedure. The comparison of initial activities (plain bars in Figure 2.12) shows that the untreated MW-Ir/ATO is the most active compound, with mass activities reaching 1.1 A.mg_{Ir}⁻¹ for the lowest loading. Thermal treatment led to a substantial decrease in initial mass activity independently of the atmosphere used. Interestingly, Ir_250_Ar was significantly more affected than Ir_250_O₂. The small differences in specific surface area between MW-Ir/ATO (154 m².g⁻¹), Ir_250_O₂ (140 m².g⁻¹) and Ir_250_Ar (144 m².g⁻¹) suggest that the notable decrease in OER-activity cannot be explained only by changes in sample morphology. As a result, we suspected that changes in the chemical nature of the Ir-phase might play a major role.

Ir_350_Ar and Ir_350_O₂ exhibited very similar initial mass activities about 65% lower than for MW-Ir/ATO. This is in line with the described transformation of the Ir-oxohydroxide into crystalline IrO₂. This is in line with the results presented by Reier in terms of OER-activity of Ir-catalysts calcined at higher temperatures where IrO₂ was formed.⁴⁴

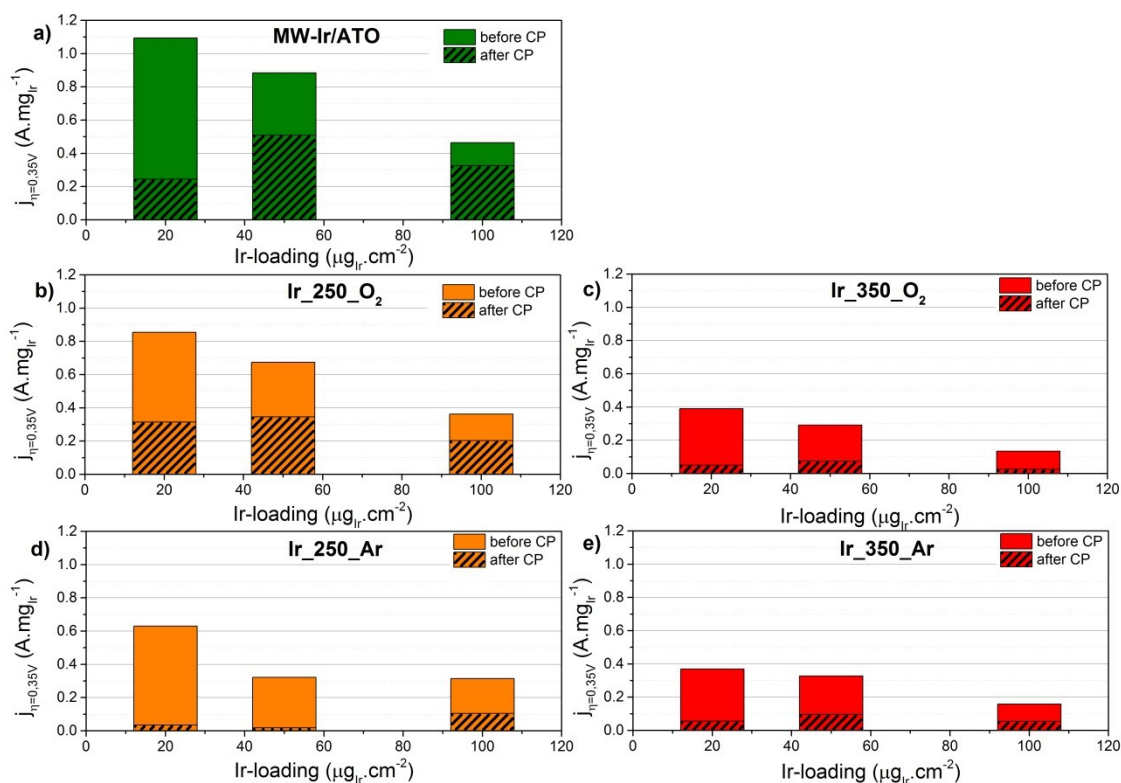


Figure 2.12 Loading-dependent mass activity at $\eta=0,35\text{V}$ before (plain bars) and after CP at $10\text{ mA}\cdot\text{cm}^{-2}$ (patterned bars) for (a) MW-Ir/ATO (a) and its thermally treated products (b) Ir_250_O₂, (c) Ir_350_O₂, (d) Ir_250_Ar and (e) Ir_350_Ar.

The study of the CP-curves (see Figure S2.14) showed that the samples seem to be deactivated following different regimes, depending on the overpotential region. Below 1.65V vs. RHE, potential curves are constant or slowly increasing. On the opposite, once potentials above 1.65V vs. RHE are reached, a much faster deactivation seems to occur as overpotentials needed to maintain the desired current density increase quickly. Cherevko et al. already reported on the potential-dependent dissolution rates of their calcined Ir-electrocatalysts, which is one possible deactivation mechanism.²⁸ Since loadings of $20\ \mu\text{g}_{\text{Ir}}\cdot\text{cm}^{-2}$ require initial anode potentials near 1.6 V vs. RHE to obtain $10\ \text{mA}\cdot\text{cm}^{-2}$, they reach the critical potential region faster and are subjected earlier to oxidative degradation. This explains the higher decrease of OER-activity observed at $20\ \mu\text{g}_{\text{Ir}}\cdot\text{cm}^{-2}$ after CP for all samples (patterned bars in Figure 2.12). MW-Ir/ATO was the only compound showing appreciable stability: During CP, overpotentials stabilized at approx. 1.56 V vs. RHE ($\eta=0.35\ \text{V}$) for loadings above $50\ \mu\text{g}_{\text{Ir}}\cdot\text{cm}^{-2}$ and loss of OER-activity is limited.

In the assessment of OER-mass activities after the stability test (Figure 2.3.b) the compounds seem to rank following the same order as initially: MW-Ir/ATO is still the most active compound, followed by Ir_250_O₂. Ir_250_Ar and the 350°C-calcined samples exhibit the lowest activities and have thus been deactivated the most. It becomes clear that thermal treatment at temperatures of 250/350°C in inert and oxidative atmospheres has an adverse effect on both catalyst activity and stability. The best OER-performance is obtained for the as synthesized MW-Ir/ATO.

The poor general OER-performance of the samples produced at 350°C is linked to the formation of small crystalline IrO₂-domains in both atmospheres, which is in line with the results of Reier et al.⁴⁴ The striking difference in OER-performance observed between Ir_250_O₂ and Ir_250_Ar might yield another important clue on OER-relevant features of the Ir^{III/IV}-oxohydroxide phase. Since oxidation states and morphologies were relatively similar, we isolated the observed faster dehydroxylation in Ar as a possible explanation for the great loss in OER-activity and -stability observed for Ir_250_Ar. This implies that the hydroxylated structure of the Ir^{III/IV}-oxohydroxide phase might play an important role in stabilizing precursor sites for the OER-catalysis. The thermally induced loss of the chemisorbed water fingerprint seems to be accelerated in Ar at 250°C and leads to the bad performance registered for Ir_250_Ar. This suggestion is in line with OER-relevant surface hydroxyl groups described recently by Reier et al. in a series of Ir/Ni-mixed oxides.⁵⁹

2.5. Conclusion

The reported study of hydrothermally prepared Ir-particles dispersed on ATO confirms the prominent role of the little investigated class of Ir-oxohydroxide compounds. The 30 mol.%-Ir/ATO obtained from MW-supported hydrothermal treatment of hydrolyzed Ir-precursors at 250°C showed exceptional OER-performance under commercially relevant conditions in comparison with reported benchmarks. Careful analysis revealed the Ir^{III/IV}-oxohydroxide nature of the Ir-phase. The detrimental effect of thermal treatment highlighted that the particular chemical nature of the Ir accounts for the high activity and stability. Activity-relevant hydroxyl groups were removed at 250°C, faster in inert than in oxidative atmosphere. This led to a sharp decrease in OER-performance. At 350°C, a further decrease in OER-performance was linked to the appearance of small crystalline IrO₂-domains observed via vibrational spectroscopy and TEM-imaging. As a result, we could confirm the major role played by amorphous Ir-structures for OER-electrocatalysis. Our proposed MW-supported pathway gives access to a synthesis parameter range that bridges the gap between low-temperature hydrolysis of iridium precursors and high-temperature calcination routes. The resulting Ir^{III/IV}-oxohydroxide compounds bypass the conundrum of having to sacrifice activity for stability by producing crystalline IrO₂-phases. We highlight the potential of such compounds for industrially relevant applications. In order to obtain a more thorough understanding of the Ir-oxohydroxide class without the influence of support-effects, follow-up work will focus on unsupported Ir-oxohydroxides in order to gain a better understanding of OER-relevant species hosted by the Ir^{III/IV}-oxohydroxide structure.

2.6. Acknowledgements

The authors gratefully acknowledge Jutta Kröhnert (DRIFTS), Jasmin Allan (XRD), Andrey Tarasov (TGMS), Wiebke Frandsen (SEM) and Matthias Friedrich (XPS) for fruitful discussions and support with the various characterization techniques. Financial support came from the German Federal Ministry for Economic Affairs and Energy in the framework of the “Ekolyzer”-project.

2.7. Supporting information

XRD-patterns of ATO-compounds

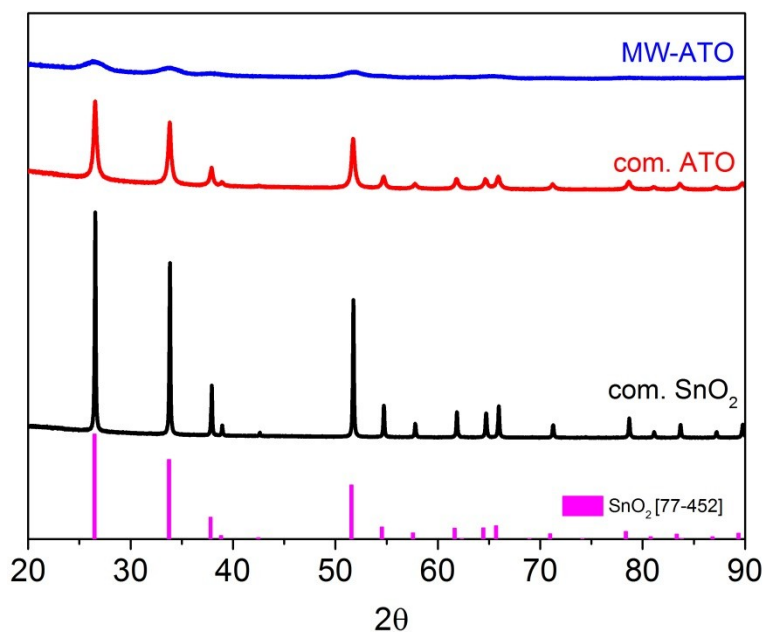


Figure S2.1 XRD of commercial SnO₂ and ATO samples as well as MW-Ir/ATO

Due to the very similar ionic radii of Sn^{IV}, Sb^{III} and Sb^V and the broad peaks resulting from small crystalline domains, the obtained XRD-patterns cannot be distinguished from the pure SnO₂-cassiterite.

ATO-conductivities

Table S2.1 Specific surface area and resistivities of commercial powders and samples prepared in the MW at various temperatures.

Compound	ρ [$\Omega\cdot\text{cm}$]	S_{BET} [$\text{m}^2\cdot\text{g}^{-1}$]
Com. SnO ₂	$1,28\cdot 10^4$	7
MW-ATO 180°C	$1,92\cdot 10^5$	--
MW-ATO 210°C	$1,55\cdot 10^4$	--
MW-ATO 240°C	$5,10\cdot 10^4$	--
MW-ATO 270°C	$1,71\cdot 10^1$	207
MW-ATO 290°C	$1,17\cdot 10^1$	184
Com. ATO	$2,02\cdot 10^1$	41

Electron microscopy of MW-ATO

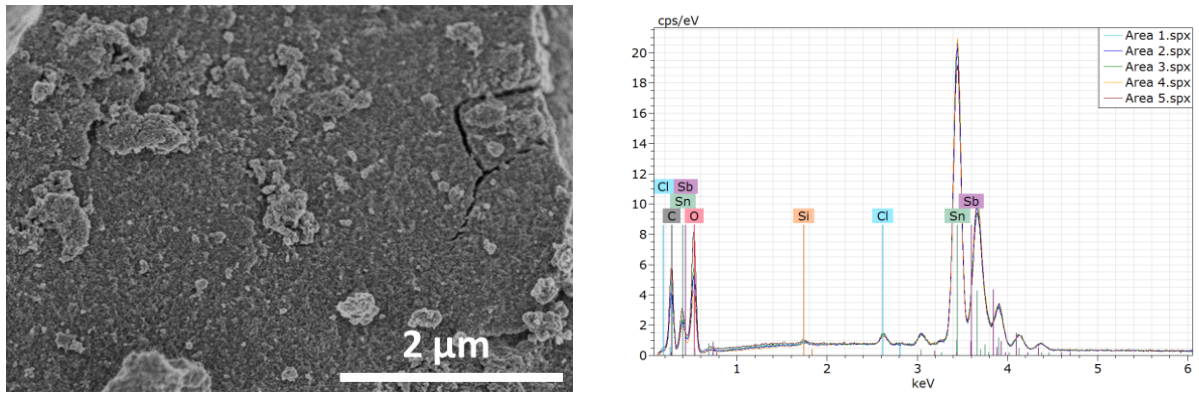


Figure S2.2 SEM-EDX of MW-ATO. The image represents a typical location for EDX. EDX-spectra were taken at a primary energy of 20kV in areas with a window size of 5μm×5μm on different agglomerates (interaction depth: 2μm).

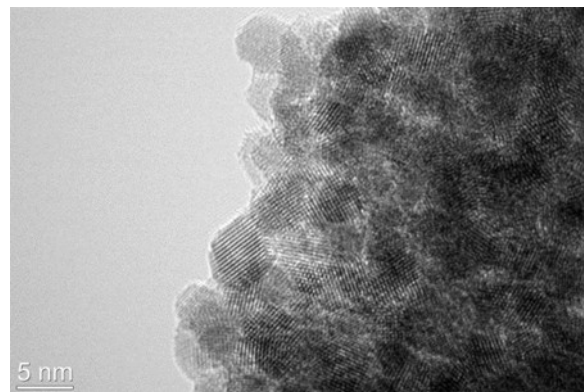


Figure S2.3 TEM-image of MW-ATO.

XRD of the Ir-loaded compounds

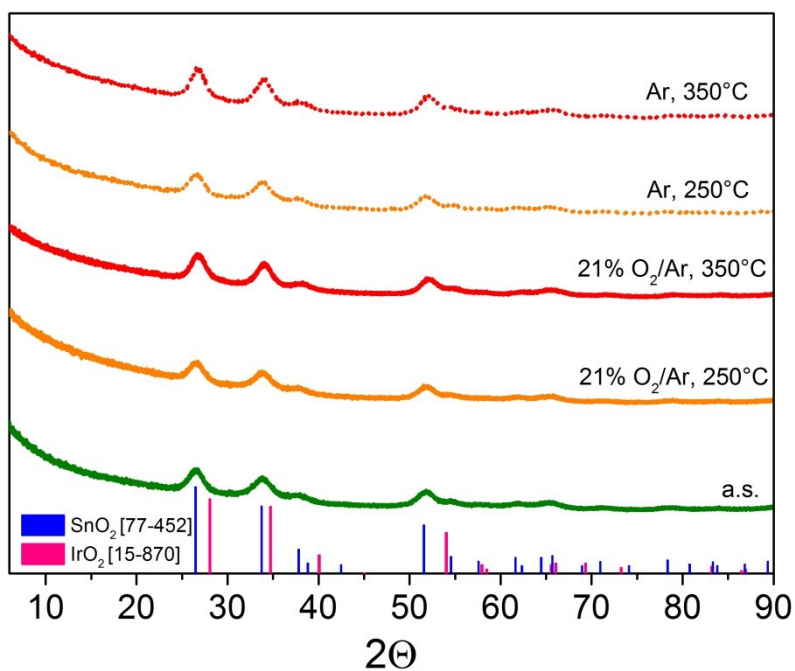


Figure S2.4 XRD of as synthesized MW-Ir/ATO (green line) and of thermal treatment products at 250°C (orange) and 350°C (red) under 100 mL.min⁻¹ of 21% O₂/Ar (full lines) or 100% Ar (dotted lines)

TEM of MW-Ir/ATO

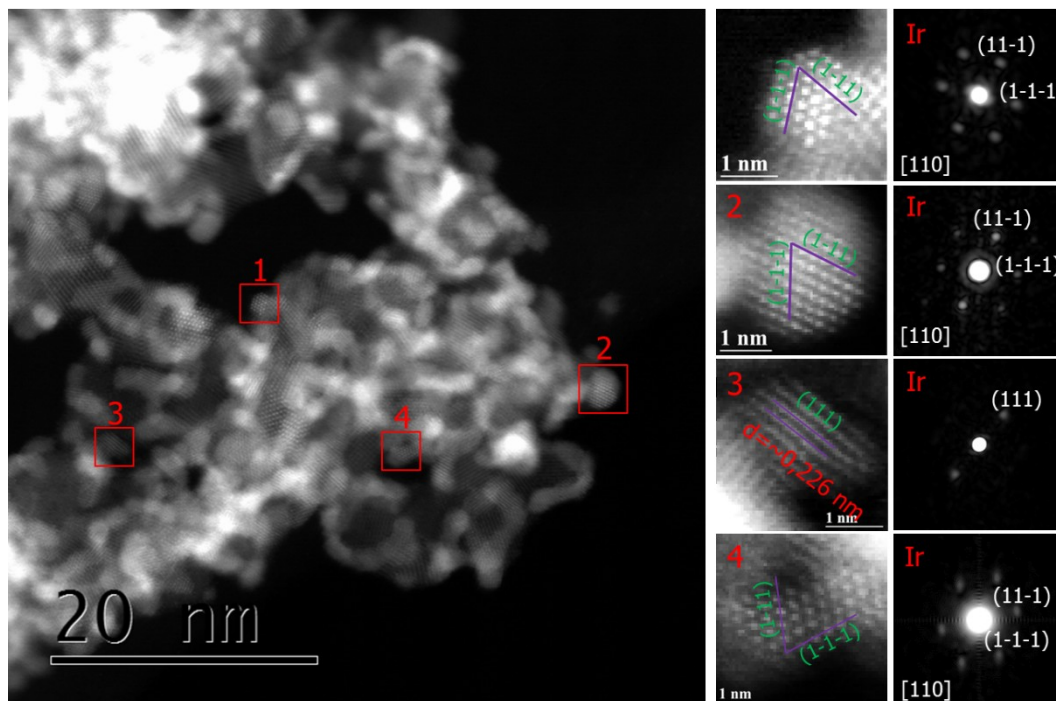


Figure S2.5 ADF-STEM imaging of MW-Ir/ATO including Fast-Fourier-transformation of selected areas corresponding to cubic metallic Ir-lattices

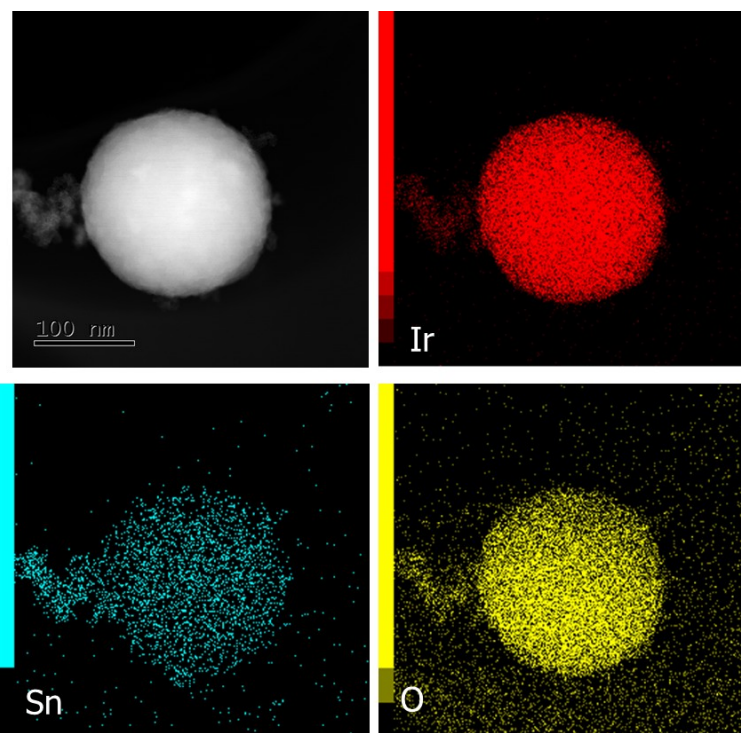


Figure S2.6 ADF-STEM imaging of MW-Ir/ATO including EDX-based elemental mapping of one of the Ir/ATO-clusters found in MW-Ir/ATO

TGMS of MW-Ir/ATO

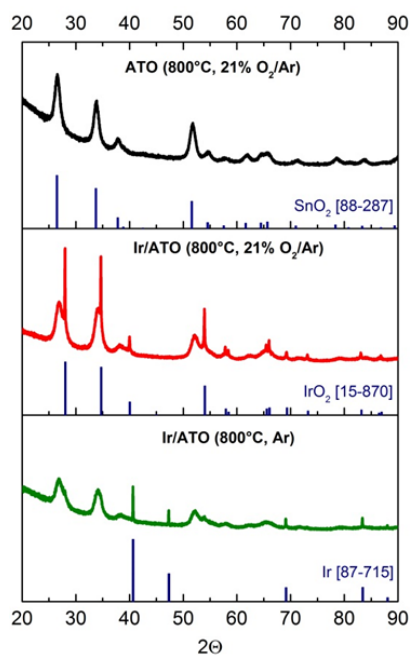


Figure S2.7 XRD the calcination products of the MW-ATO-support and the loaded MW-Ir/ATO after thermogravimetric analysis in oxidative (21% O₂/Ar) and inert (Ar) gas streams.

Temperature-programmed reduction (TPR)

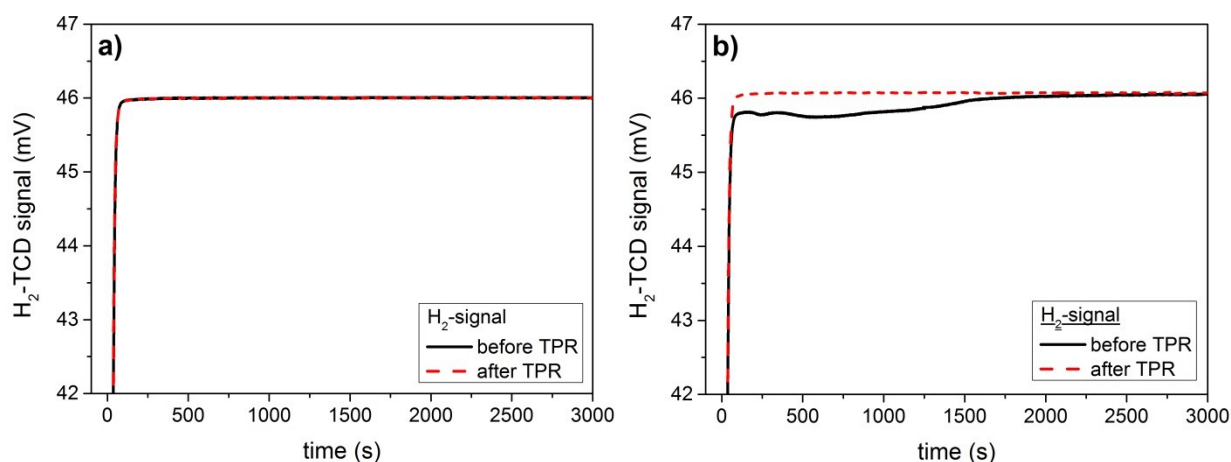


Figure S2.8 Time-dependent hydrogen signals detected via the Thermal Conductivity Detector (TCD) during the switch from a 100% Ar to a 5% H₂/Ar gas stream (80 mL.min⁻¹) before (dark line) and after the TPR (red dashed line) for (a) MW-ATO (a) and (b) MW-Ir/ATO.

OER-performance of MW-Ir/ATO

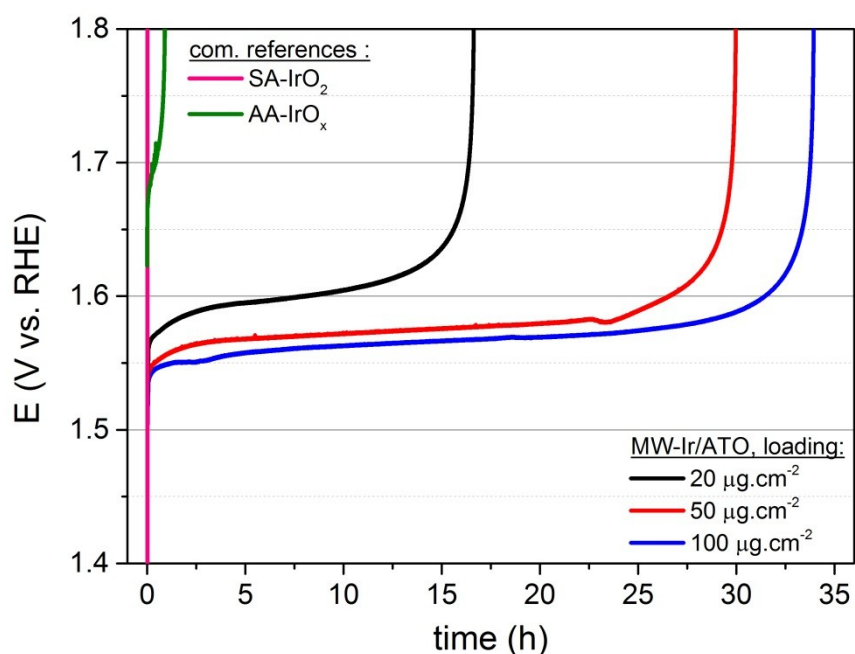


Figure S2.9 CP-based activity test at 10 mA.cm⁻² for MW-Ir/ATO for three loadings at 20, 50 and 100 µgIr.cm⁻² as well for the two commercial references AA-IrO_x and SA-IrO₂

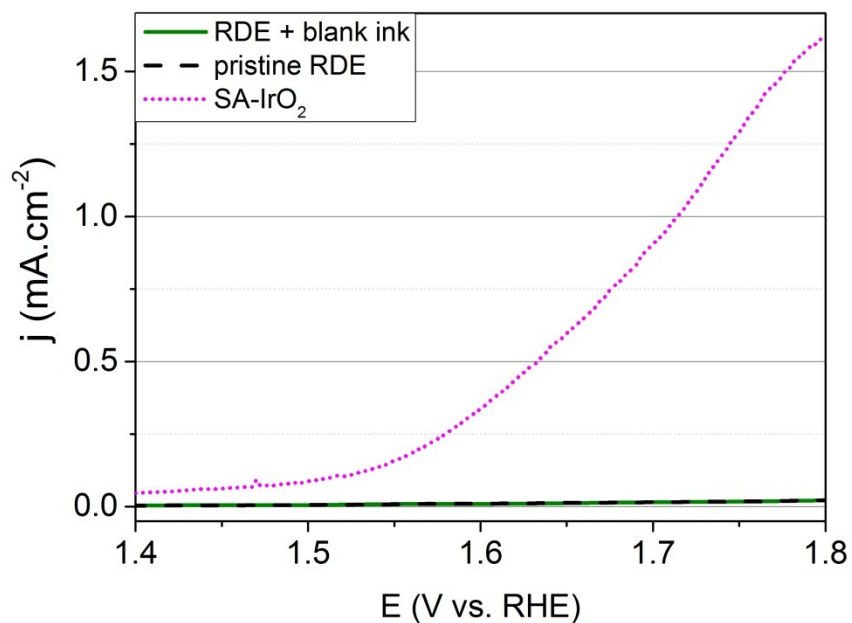


Figure S2.10 LSV of SA-IrO₂, the pristine GC-RDE and the GC-RDE loaded with blank ink (no catalyst, only H₂O, iPrOH and Nafion).

TG-analysis of the stepwise calcination of MW-Ir/ATO

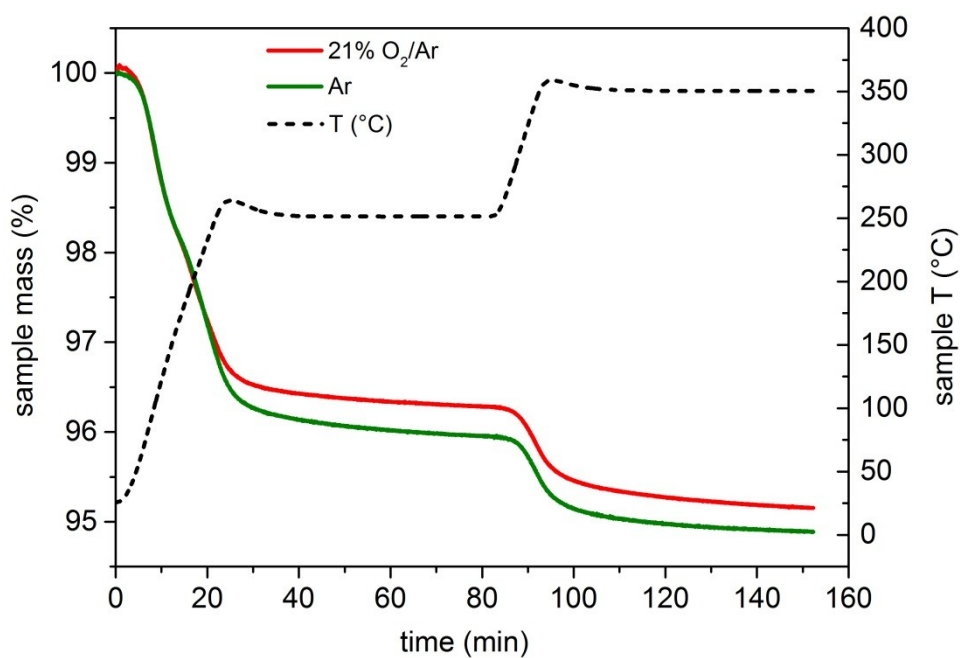


Figure S2.11 Thermogravimetric analysis of the stepwise annealing of MW-Ir/ATO in Ar and 21%O₂/Ar (100 mL.min⁻¹) at 250°C and 350°C for 1h.

DRIFTS

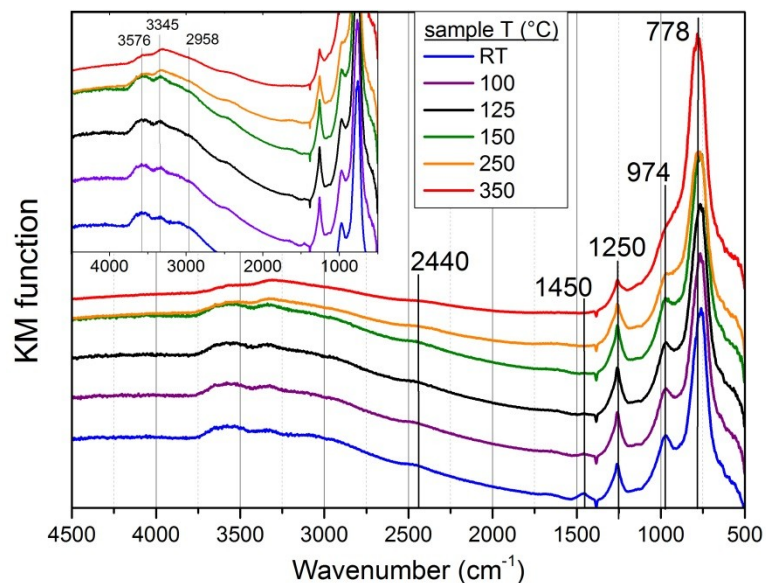


Figure S2.12 DRIFTS study of MW-ATO during stepwise treatment at various temperatures in 21% O_2/Ar , 100 $\text{mL}\cdot\text{min}^{-1}$. Kubelka-Munck transformation of the reflectance spectra (left) and corresponding difference spectra between said temperature and 100°C (right).

In Figure S2.11, the feature located at approx. 1450cm^{-1} and disappearing at 125°C might be attributed to a unidentate carbonate species adsorbed on MW-ATO during the synthesis and originating from atmospheric CO_2 dissolved during the synthesis. Features at 1250 and 974cm^{-1} can in turn be assigned to the vibration of hydroxyl-tin bonds according to the literature⁴⁹. The diminution of these features at 250 and 350°C is in agreement with the hydroxyl decomposition profile observed in TGMS. Weak peaks in the $3650\text{--}3250\text{cm}^{-1}$ -region can be assigned to more or less H-bonded hydroxyl groups. Additional broad feature around 2958cm^{-1} can be assigned to C-H stretching frequencies from carbon impurities adsorbed on the surface of the sample.

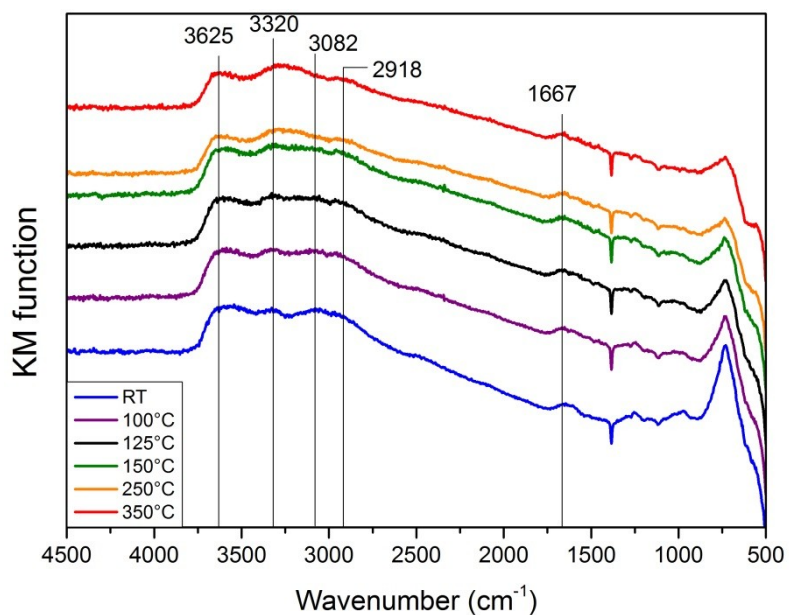


Figure S 2.13 DRIFTS study of MW-Ir/ATO (Kubelka-Munck transformation of the reflectance spectra) during stepwise treatment at various temperatures in 21%O₂/Ar, 100 mL.min⁻¹.

OER-performance after thermal treatment

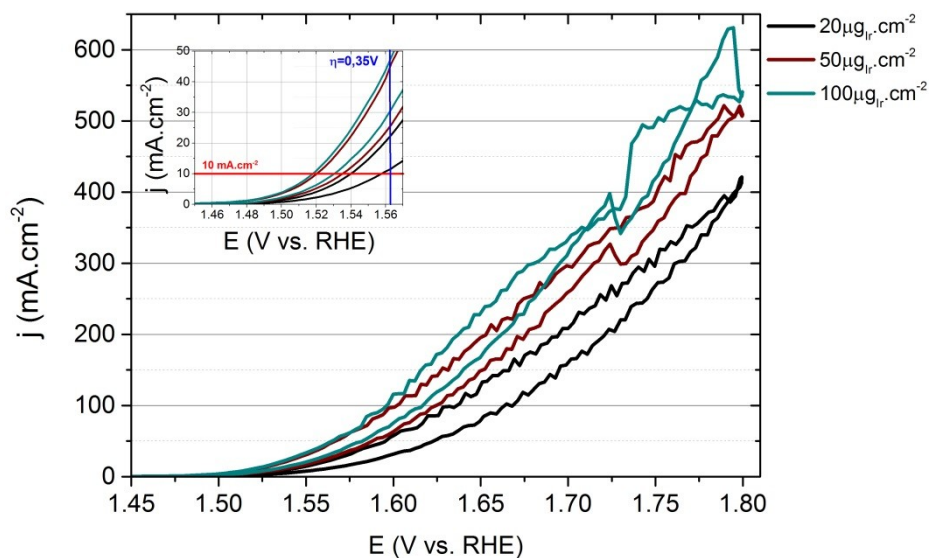


Figure S2.14 LSV-based activity test for MW-Ir/ATO for three loadings at 20, 50 and 100 μg_{Ir}.cm⁻².

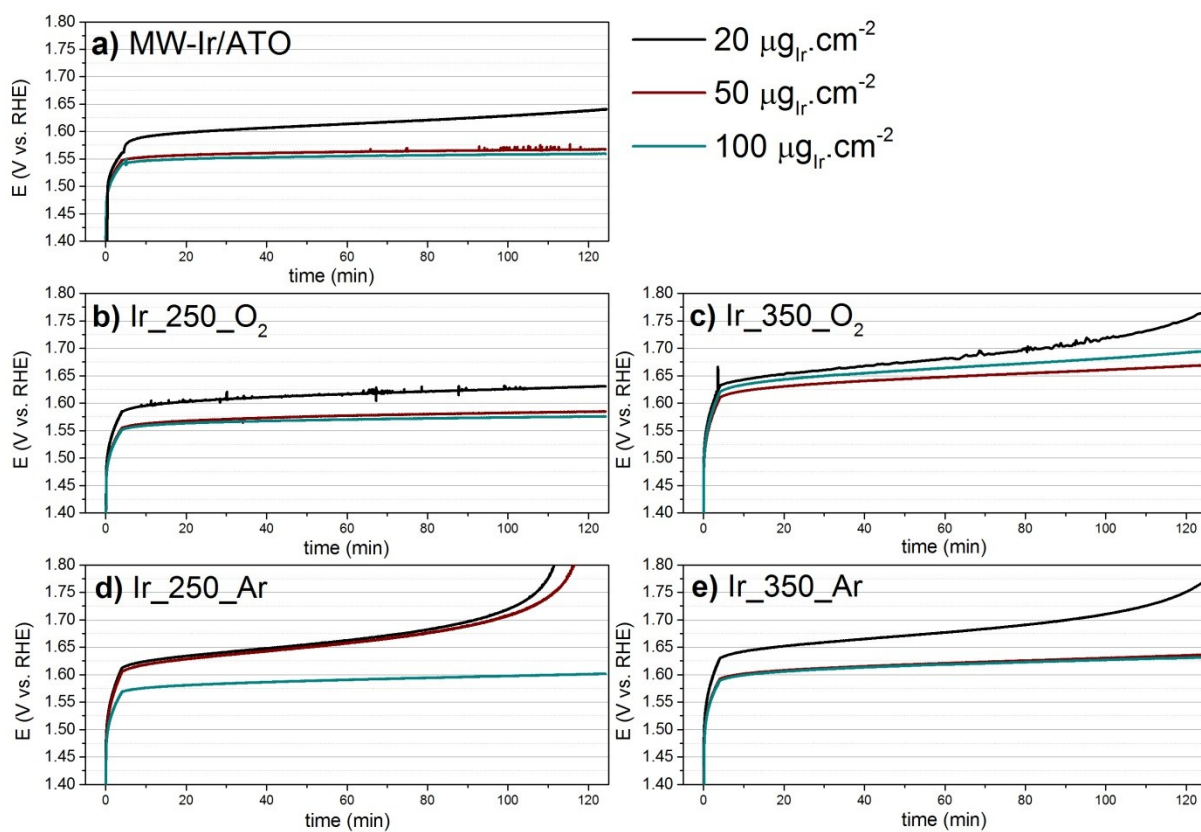


Figure S2.15 Stability-investigation of MW-Ir/ATO (a) and its thermally treated products (b) Ir_250_O₂, c) Ir_350_O₂, d) Ir_250_Ar and e) Ir_350_Ar) in a chronopotentiometric study for 2h at $10 \text{ mA} \cdot \text{cm}^{-2}$

2.8. References

- (1) Schlögl, R. *ChemSusChem* **2010**, *3*, 209.
- (2) Cook, T. R.; Dogutan, D. K.; Reece, S. Y.; Surendranath, Y.; Teets, T. S.; Nocera, D. G. *Chemical Reviews* **2010**, *110*, 6474.
- (3) Rifkin, J. *The Third Industrial Revolution: How Lateral Power Is Transforming Energy, the Economy, and the World*; First Printing (Numerals Begin with 1) ed.; Palgrave Macmillan, 2011.
- (4) Marcelo Carmo, D. L. F. *International Journal of Hydrogen Energy* **2013**, *38*, 4901.
- (5) Kötz, R.; Stucki, S.; Scherson, D.; Kolb, D. M. *Journal of Electroanalytical Chemistry and Interfacial Electrochemistry* **1984**, *172*, 211.
- (6) McCrory, C. C. L.; Jung, S.; Ferrer, I. M.; Chatman, S. M.; Peters, J. C.; Jaramillo, T. F. *Journal of the American Chemical Society* **2015**, *137*, 4347.
- (7) Reier, T.; Oezaslan, M.; Strasser, P. *ACS Catalysis* **2012**, *2*, 1765.
- (8) Yi, Y.; Tornow, J.; Willinger, E.; Willinger, M. G.; Ranjan, C.; Schlögl, R. *ChemElectroChem* **2015**, *2*, 1929.
- (9) Nütz, T.; Felde, U. z.; Haase, M. *The Journal of Chemical Physics* **1999**, *110*, 12142.
- (10) Mishra, K. C.; Johnson, K. H.; Schmidt, P. C. *Physical Review B* **1995**, *51*, 13972.
- (11) Nütz, T.; Haase, M. *Journal of Physical Chemistry B* **2000**, *104*, 8430.
- (12) Cachet, H.; Froment, M.; Zenia, F. *Journal of the Electrochemical Society* **1996**, *143*, 442.
- (13) Banerjee, A. N.; Kundoo, S.; Saha, P.; Chattopadhyay, K. K. *Journal of Sol-Gel Science and Technology* **2003**, *28*, 105.
- (14) Tseung, A. C. C.; Dhara, S. C. *Electrochimica Acta* **1975**, *20*, 681.
- (15) Liu, G.; Xu, J.; Wang, Y.; Wang, X. *Journal of Materials Chemistry A* **2015**, *3*, 20791.
- (16) Beni, G.; Schiavone, L. M.; Shay, J. L.; Dautremont-Smith, W. C.; Schneider, B. S. *Nature* **1979**, *282*, 281.
- (17) Frazer, E. J.; Woods, R. *Journal of Electroanalytical Chemistry and Interfacial Electrochemistry* **1979**, *102*, 127.
- (18) Vuković, M. *Journal of Applied Electrochemistry* **1987**, *17*, 737.
- (19) De Pauli, C. P.; Trasatti, S. *Journal of Electroanalytical Chemistry* **1995**, *396*, 161.
- (20) De Pauli, C. P.; Trasatti, S. *Journal of Electroanalytical Chemistry* **2002**, *538–539*, 145.
- (21) Marshall, A.; Børresen, B.; Hagen, G.; Tsyppkin, M.; Tunold, R. *Materials Chemistry and Physics* **2005**, *94*, 226.
- (22) Marshall, A.; Børresen, B.; Hagen, G.; Tsyppkin, M.; Tunold, R. *Electrochimica Acta* **2006**, *51*, 3161.
- (23) Marshall, A. T.; Haverkamp, R. G. *Electrochimica Acta* **2010**, *55*, 1978.
- (24) Marshall, A. T.; Sunde, S.; Tsyppkin, M.; Tunold, R. *International Journal of Hydrogen Energy* **2007**, *32*, 2320.
- (25) Ardizzone, S.; Bianchi, C. L.; Cappelletti, G.; Ionita, M.; Minguzzi, A.; Rondinini, S.; Vertova, A. *Journal of Electroanalytical Chemistry* **2006**, *589*, 160.
- (26) Mráz, R.; Krýsa, J. *Journal of Applied Electrochemistry* **1994**, *24*, 1262.
- (27) Carmo, M.; Fritz, D. L.; Mergel, J.; Stolten, D. *International Journal of Hydrogen Energy* **2013**, *38*, 4901.
- (28) Cherevko, S.; Reier, T.; Zeradjanin, A. R.; Pawolek, Z.; Strasser, P.; Mayrhofer, K. J. J. *Electrochemistry Communications* **2014**, *48*, 81.
- (29) Bernicke, M.; Ortel, E.; Reier, T.; Bergmann, A.; Ferreira de Araujo, J.; Strasser, P.; Kraehnert, R. *ChemSusChem* **2015**, *8*, 1908.
- (30) Smits, F. M. *Bell System Technical Journal* **1958**, *37*, 711.
- (31) Jeon, H.-J.; Jeon, M.-K.; Kang, M.; Lee, S.-G.; Lee, Y.-L.; Hong, Y.-K.; Choi, B.-H. *Materials Letters* **2005**, *59*, 1801.
- (32) Zhang, J.; Gao, L. *Materials Research Bulletin* **2004**, *39*, 2249.
- (33) Fonstad, C. G.; Rediker, R. H. *Journal of Applied Physics* **1971**, *42*, 2911.

- (34) Lee, K.-S.; Park, I.-S.; Cho, Y.-H.; Jung, D.-S.; Jung, N.; Park, H.-Y.; Sung, Y.-E. *Journal of Catalysis* **2008**, *258*, 143.
- (35) Balko, E. N.; Nguyen, P. H. *Journal of Applied Electrochemistry* **1991**, *21*, 678.
- (36) Kamada, K.; Tokutomi, M.; Enomoto, N.; Hojo, J. *Journal of Materials Chemistry* **2005**, *15*.
- (37) Bestaoui, N.; Prouzet, E. *Chem. Mater.* **1997**, *9*, 1036.
- (38) Ioroi, T.; Kitazawa, N.; Yasuda, K.; Yamamoto, Y.; Takenaka, H. *Journal of the Electrochemical Society* **2000**, *147*, 2018.
- (39) Pankratov, D. A.; Komozin, P. N.; Kiselev, Y. M. *Russian Journal of Inorganic Chemistry* **2011**, *56*, 1794.
- (40) Cruz, A. M.; Abad, L.; Carretero, N. M.; Moral-Vico, J.; Fraxedas, J.; Lozano, P.; Subías, G.; Padial, V.; Carballo, M.; Collazos-Castro, J. E.; Casañ-Pastor, N. *Journal of Physical Chemistry C* **2012**, *116*, 5155.
- (41) Sasikala, R.; Gupta, N. M.; Kulshreshtha, S. K. *Catalysis Letters* **2001**, *71*, 69.
- (42) Pfeifer, V.; Jones, T. E.; Velasco Vélez, J. J.; Massué, C.; Arrigo, R.; Teschner, D.; Girgsdies, F.; Scherzer, M.; Greiner, M. T.; Allan, J.; Hashagen, M.; Weinberg, G.; Piccinin, S.; Hävecker, M.; Knop-Gericke, A.; Schlögl, R. *Surface and Interface Analysis* **2015**, n/a.
- (43) Pfeifer, V.; Jones, T. E.; Velasco Vélez, J. J.; Massué, C.; Greiner, M. T.; Arrigo, R.; Teschner, D.; Girgsdies, F.; Scherzer, M.; Allan, J.; Hashagen, M.; Weinberg, G.; Piccinin, S.; Hävecker, M.; Knop-Gericke, A.; Schlögl, R. *Phys Chem Chem Phys* **2016**, *18*, 2292.
- (44) Reier, T.; Teschner, D.; Lunkenbein, T.; Bergmann, A.; Selve, S.; Kraehnert, R.; Schlögl, R.; Strasser, P. *Journal of the Electrochemical Society* **2014**, *161*, F876.
- (45) Sanchez Casalongue, H. G.; Ng, M. L.; Kaya, S.; Friebel, D.; Ogasawara, H.; Nilsson, A. *Angewandte Chemie International Edition* **2014**, *53*, 7169.
- (46) McCrory, C. C. L.; Jung, S.; Peters, J. C.; Jaramillo, T. F. *J. Am. Chem. Soc.* **2013**, *135*, 16977.
- (47) Spurgeon, J. M.; Velazquez, J. M.; McDowell, M. T. *Physical Chemistry Chemical Physics* **2014**, *16*, 3623.
- (48) Scipioni, R.; Gazzoli, D.; Teocoli, F.; Palumbo, O.; Paolone, A.; Ibris, N.; Brutti, S.; Navarra, M. A. *Membranes* **2014**, *4*, 123.
- (49) Zhang, J.; Gao, L. *Journal of Solid State Chemistry* **2004**, *177*, 1425.
- (50) Ocaña, M.; Serna, C. J. *Spectrochimica Acta Part A: Molecular Spectroscopy* **1991**, *47*, 765.
- (51) Ito, S.; Abe, Y.; Kawamura, M.; Kim, K. H. *Journal of Vacuum Science & Technology B* **2015**, *33*, 041204.
- (52) Brewer, S. H.; Wicaksana, D.; Maria, J.-P.; Kingon, A. I.; Franzen, S. *Chemical Physics* **2005**, *313*, 25.
- (53) Musić, S.; Popović, S.; Maljković, M.; Skoko, Z.; Furić, K.; Gajović, A. *Materials Letters* **2003**, *57*, 4509.
- (54) Huang, Y. S.; Lin, S. S.; Huang, C. R.; Lee, M. C.; Dann, T. E.; Chien, F. Z. *Solid State Communications* **1989**, *70*, 517.
- (55) Diéguez, A.; Romano-Rodríguez, A.; Vilà, A.; Morante, J. R. *Journal of Applied Physics* **2001**, *90*, 1550.
- (56) Rumyantseva, M. N.; Gaskov, A. M.; Rosman, N.; Pagnier, T.; Morante, J. R. *Chemistry of Materials* **2005**, *17*, 893.
- (57) Hintermair, U.; Sheehan, S. W.; Parent, A. R.; Ess, D. H.; Richens, D. T.; Vaccaro, P. H.; Brudvig, G. W.; Crabtree, R. H. *Journal of the American Chemical Society* **2013**, *135*, 10837.
- (58) Huang, J.; Blakemore, J. D.; Fazi, D.; Kokhan, O.; Schley, N. D.; Crabtree, R. H.; Brudvig, G. W.; Tiede, D. M. *Physical Chemistry Chemical Physics* **2014**, *16*, 1814.
- (59) Reier, T.; Pawolek, Z.; Cherevko, S.; Bruns, M.; Jones, T.; Teschner, D.; Selve, S.; Bergmann, A.; Nong, H. N.; Schlögl, R.; Mayrhofer, K. J. J.; Strasser, P. *Journal of the American Chemical Society* **2015**, *137*, 13031.

3. Synthesis of stable and highly active Ir-oxohydroxides for electrochemical oxidation of water

3.1. Abstract

The commercial relevance of water splitting for hydrogen production in acidic media has so far been limited by the poor stability of the anodic electrocatalyst devoted to the oxygen evolution reaction (OER). We report the synthesis of a new class of amorphous Ir-oxohydroxides produced via rapid microwave-supported hydrothermal synthesis. These compounds bridge the gap between electrodeposited amorphous IrO_x-films and crystalline IrO₂-electrocatalysts prepared via calcination routes. For electrode loadings as low as 20 μg_{Ir}.cm⁻², the synthesized compounds present a unique combination of high activity and stability under relevant OER-conditions in comparison to commercial samples and reported benchmarks, without any need of pre-treatment. Physical and chemical characterization reveal an amorphous, nanostructured Ir-oxohydroxide whose electrocatalytic properties are strongly linked to the chemisorbed water fingerprint revealed by thermogravimetry and the presence of Ir-species reducible below 100°C.

3.2. Introduction

Hydrogen formation via water splitting remains the only long term solution for a stable and versatile storage of renewable electricity in chemical form.¹ Proton exchange membrane (PEM) based electrolyzers offer the most efficient operating conditions with the option of producing high-purity H₂ at high pressure.² Such a design is based on polymeric membranes with proton exchange capabilities, *e.g.* Nafion®, which act as a gas separator between the anodic and the cathodic compartments. These sulfonic-acid-functionalized membranes require a highly acidic environment, which poses a major challenge to the electrocatalysts needed to minimize electrode overpotentials, especially for the anodic oxygen evolution reaction (OER).³ Most earth-abundant transition metal oxides such as Co₃O₄, Fe₂O₃ and MnO_x show minimal stability under these conditions.⁴ Expensive Ir- and Ru-based compounds on the other hand are the most active OER-catalysts in acidic media, but even Ru-based anodes corrode very fast under these conditions.^{5,6} So far, only Ir-based catalysts are reported to combine high activity with relative stability in acidic OER.⁶

Early on, it was shown that metallic iridium films are inefficient in OER and need to be activated by an oxidative electrochemical treatment. Accordingly, synthesis strategies were developed for the direct formation of OER-active Ir-films such as anodically grown iridium oxide films^{7,8} (AIROF) or sputtered iridium oxide films⁹ (SIROF). Most recent studies focus on the high-temperature synthesis of crystalline IrO₂ and mixed Ir-oxides, *e.g.* IrO₂/Ta₂O₅.¹⁰⁻¹³ This focus is due to the popular notion that crystalline IrO₂-rutile is the most promising candidate in terms of long-term OER-stability.^{3,14} However, early electrochemical studies⁷⁻⁹ emphasized the key role of amorphous Ir-oxohydroxides in high-current, stable OER-electrocatalysis in contrast to the less active crystalline IrO₂. Lately, the relevance of amorphous, hydrated Ir-species was further established by the electrochemical investigation of Ir-catalysts produced at low calcination temperatures by the teams around P. Strasser and K. Mayrhofer.^{15,16} Their work showed that Ir-acetates calcined at the lowest possible

decomposition temperature of 250°C formed amorphous Ir-oxide/hydroxide-species, combining both activity and relative stability in acidic OER.

Taking into account the many clues about the relevance of amorphous highly hydrated Ir-oxide/hydroxide species obtained under mild thermal treatment conditions, we decided to build our synthesis strategy on the use of a microwave-assisted hydrothermal setup, allowing for the thermal treatment of aqueous precursor solutions at temperatures $\leq 250^\circ\text{C}$. We report the successful synthesis of a novel class of Ir-oxohydroxides that were thoroughly characterized and evaluated in terms of OER-activity and -stability in order to gain insight into structural features critical to the OER-performance. Comparisons include literature references and two commercially available Ir-benchmarks: crystalline IrO_2 (Sigma-Aldrich), denoted SA- IrO_2 and an ultra-pure amorphous Ir-oxide/hydroxide (Alfa Aesar) denoted AA- IrO_x .

3.3. Experimental

3.3.1. MW-assisted hydrothermal synthesis of Ir-oxohydroxides

Eight aqueous KOH-solutions with $[\text{KOH}]$ spread between $10^{-3} \text{ mol.L}^{-1}$ and 1 mol.L^{-1} were prepared from milli-Q filtered water and KOH (AppliChem, p.a.). The solutions were kept under inert atmosphere via constant Ar bubbling. K_2IrCl_6 (Alfa Aesar, Ir 39% min.) was then added to each of the eight solutions in order to obtain a final Ir-concentration of $10^{-2} \text{ mol.L}^{-1}$ and left stirring at room temperature for 1h. Based on the above protocol, the precursor solutions have KOH:Ir ratios spread between 1:10 to 100:1. After one hour of ageing, 4x62mL of a precursor solution were added to four 100mL-PTFE-lined vessels. The four vessels were then placed inside the microwave reactor (Anton Paar, Multiwave PRO). The solutions were heated up using a 10K.min^{-1} ramp from room temperature (RT) to a selected temperature range between 150°C and 250°C , under constant stirring using a magnetic PTFE-stirrer and maintained at the selected temperature T_{syn} for 1h. Figure S3.1 shows the monitoring of the solution temperature in one vessel (black), pressure (green) and microwave power (orange) during a typical MW-assisted hydrothermal synthesis of Ir-oxohydroxides. The homogeneity of temperatures in the four vessels was verified via IR-measurements of the outer-wall temperature of the four vessels (dotted lines). After the treatment, the vessels were left to cool down to RT. The resulting black product was centrifuged at 8000 rpm for 10 min further dissolved in Millipore-filtered water, sonicated for 5 minutes and re-centrifuged until the conductivity of the supernatant was measured below 0.05 mS.cm^{-1} . The solid product was subsequently dried at 80°C for 12h and ground in a mortar.

3.3.2. Sample characterization

XRD patterns were collected on a STOE STADI P transmission diffractometer equipped with a primary focusing germanium monochromator with Cu $\text{K}\alpha_1$ radiation and a linear position sensitive detector. The samples were mounted in the form of small amounts of powder sandwiched between two layers of polyacetate film and fixed with a small amount of X-ray amorphous grease. The elemental ratios of K:Ir and Cl:Ir were obtained via X-ray fluorescence analysis (XRF) using a Sequential Pioneer S4 spectrometer (Bruker) under inert He-atmosphere for non-destructive analysis. Static nitrogen physisorption experiments were performed in an Autosorb-1C setup (Quantachrome). Prior to the measurements samples were degassed for 2 hours under dynamic vacuum conditions at 80°C . Using

the multipoint method, we derived from the obtained complete isotherm the value of the specific surface area (S_{BET}) of the analyzed samples given in Table S1. TGA/DSC and evolved gas analysis of the decomposition reaction of the samples under a 21% O_2/Ar -stream ($100 \text{ mL}\cdot\text{min}^{-1}$, $10 \text{ K}\cdot\text{min}^{-1}$, 800°C) were performed on a Netzsch STA 449 thermobalance connected to a quadrupole mass spectrometer (QMS200 Omnistar, Balzers). The total oxidation of the samples to rutile- IrO_2 and hollandite- $\text{K}_{0.25}\text{IrO}_2$ in case of K-containing samples was verified via XRD of the obtained material (not shown).

SEM-images were captured on a Hitachi S-4800 Field Emission Scanning Electron Microscope, working in the kV-range of 0.1 to 30 and equipped with a secondary electron detector (YAGBSE). The Energy Dispersive X-ray Analysis Data, including the linescan was detected with a Bruker EDX System applying a silicon drift detector (SDD). For high resolution transmission electron microscopy (HRTEM) and scanning transmission electron microscopy (STEM), samples were prepared by drop-casting two drops of aqueous sample solution on carbon coated Cu grids. (S)TEM images and EDX elemental mapping were taken on an aberration-corrected JEOL JEM-ARM200 operated at 200 kV. The microscope is equipped with a high angle Silicon Drift EDX detector with the solid angle of up to 0.98 steradians from a detection area of 100 mm^2 .

3.3.3. Electrochemical characterization

Commercial benchmarks

Two commercially available Ir-based catalysts were selected as benchmark samples. The first compound consists of amorphous ultrapure iridium oxohydroxide compound, labeled “AA- IrO_x ” (Ir(IV) oxide, Premion[®], 99.99% trace metals basis, Ir 84.5% min, Alfa Aesar). The second compound consists of crystalline IrO_2 and is labeled “SA- IrO_2 ” (99.9% trace metals basis, Sigma Aldrich). AA- IrO_x was selected among a vast portfolio of commercially available catalysts as it was found to have the highest purity in terms of chloride and alkali metals and simultaneously to have a superior OER activity in comparison with crystalline IrO_2 -materials.^{17,18} Note that numerous studies also use commercial carbon-supported precious metal catalysts as references (Etek, Premetek, etc.).^{19,20} However carbon material rapidly degrades under acidic OER-conditions, leading to high corrosion currents and low stability. Such reference materials were therefore avoided in the present study.²¹

Setup and measurements

Electrochemical measurements were carried out on a VSP-multichannel potentiostat (Biologic Instruments) with a glassy carbon rotating ring disk electrode (RRDE, Pine Research Instrumentation, glassy carbon disk (0.2475 cm^2), Pt ring (0.1866 cm^2) as a working electrode. The reference electrode was a saturated calomel electrode (SCE, $+0.241 \text{ V}$ vs. SHE) and the counter-electrode was a Platine wire. Prior to use the RRDE electrode surface was repeatedly cleaned with Millipore-filtered water and isopropanol, mirror-polished with alumina bead slurries (Buehler, $1 \mu\text{m}$ and $0.05 \mu\text{m}$) on a polishing cloth, rinsed, sonicated for 15 min in isopropanol in an ultrasonic bath and finally rinsed with Millipore water and isopropanol.

Electrochemical measurements were conducted in a standard electrochemical cell containing ca. 100 mL of H_2SO_4 ($0.5 \text{ mol}\cdot\text{L}^{-1}$) or HClO_4 ($0.5 \text{ mol}\cdot\text{L}^{-1}$) distributed in three compartments separated by fine-porosity glass frits. The electrolyte was constantly purged with nitrogen starting at least 20 min

before the measurements. The central compartment contained the loaded working electrode (anode) mounted on a rotator (MSRX, Pine Research Instrumentation) ensuring a constant rotation of 1600 rpm. Catalyst inks were prepared by suspending 4 mg of catalysts in 6 mL Millipore-filtered H₂O, 3,96 mL isopropanol (Sigma Aldrich) and 40 µL of a Nafion® suspension (5%-Nafion® perfluorinated resin solution, Sigma Aldrich). The Ir-concentration of the ink was quantified via the molar mass calculated for each compound. The ink was then drop-casted onto the RRDE using a micropipette in order to reach an iridium-loading of 20, 50 or 100 µg.cm⁻² and dried for 30 min at 60°C.

The catalyst activity was assessed using linear sweep voltammetry (LSV) performed at a sweep rate of 5 mV.s⁻¹ from E_{oc} to 2V vs. SHE. The overpotential needed to reach a current of j=10 mA.cm⁻² was used as a measure of the activity and corresponds to a commonly used value in literature.^{6,22} The overpotential has been determined by Equation (3.2) where η is the overpotential and E_{WE} the working electrode potential.

$$\eta = E_{WE} - (1,23 - 0,059 \times pH) \quad (3.2)$$

The electrochemical measurements were corrected at 85% for ohmic drop using high-frequency impedance spectroscopy (4 measurements, 100 kHz, 20 mV amplitude, open circuit potential, E_{oc}). In order to select the best catalyst, CP-stability testing was performed under severe experimental conditions at 15 mA.cm⁻² for Ir-loadings of 20 µg_{Ir}.cm⁻². The stability of the best catalyst was further assessed at currents of 10 mA.cm⁻² for three Ir-loadings (20, 50 and 100 µg_{Ir}.cm⁻²) in order to allow for comparison with benchmarks reported in the literature.^{6,22} A current density of 10 mA.cm⁻² is based on the typical currents expected for a 10%-efficiency solar-to-fuel device.^{6,19} The catalyst were considered deactivated when the working electrode potential (E_{WE}) reached 1.8 V vs. SHE in order to avoid oxidative damage to the GC-electrode support. The electrochemical measurements were corrected at 85% for ohmic drop using high-frequency impedance determination of the electrolyte resistance (4 measurements, 100 kHz, 20 mV amplitude, open circuit potential, E_{oc}).

3.4. Results and discussion

3.4.1. Importance of the initial KOH:Ir-ratio

The aqueous precursor solution contained dissolved potassium hexachloroiridate(IV) and KOH for hydrolysis of the Ir-chlorides. The solutions were treated in the microwave reactor at 250°C, 55 bars for 60 minutes. The resulting black powder was isolated via centrifugation, washed with milli-Q water and dried. At an early phase of the synthesis, it was recognized that the KOH:Ir-ratio was a key synthesis parameter as dissolved Ir-salts undergo a complex set of reactions under basic conditions.²³ Accordingly, we prepared a series of Ir-based catalysts at diverse initial KOH:Ir, from 1:1 to 100:1.

A key mechanism in obtaining a solid product during the hydrothermal treatment is the reduction of IrCl₆²⁻ to IrCl₆³⁻ in high pH media.²⁴ IrCl₆³⁻ is prone to hydrolysis, whereas IrCl₆²⁻ is stable in solution upon heating and results in lower yields of solid product. The pH has also been suspected to influence oligomerization and condensation processes of Ir-compounds.²⁵ Following the above observations, three synthesis scenarii were investigated: low, intermediate and high KOH:Ir ratios. In the case of low [KOH], *i.e.*, KOH:Ir≤4:1, the reduction to IrCl₆³⁻ and subsequent hydrolysis were

incomplete, resulting in significantly low synthesis yields (see Table S1). We confirmed that Ir-chlorides remained in solution after MW-treatment via UV-Vis spectroscopy (see Figure S3.2). On the opposite, with a large excess of KOH, *i.e.*, $\text{KOH}:\text{Ir} \geq 7:1$, stable hexahydroxoiridate(-III) remains in solution after hydrothermal treatment, due to fast hydroxyl-ligand exchange kinetics hindering condensation of Ir-hydroxides via oligomerization.^{23,25} The intermediate KOH:Ir ratios, *i.e.*, $4:1 \leq \text{KOH}:\text{Ir} \leq 7:1$ produced the highest synthesis yields ($\geq 97\%$) (see Table S1).

The x-ray diffraction pattern (Figure S3.3) of samples produced at high pH ($\text{KOH}:\text{Ir} \geq 7:1$) show the undesired formation of metallic Ir^0 with a characteristic peak at $2\theta = 40.5^\circ$, which gains in intensity with rising KOH:Ir. All samples are characterized by two broad XRD-peaks at $2\theta = 34^\circ$ and 56° similar to those reported for electrochemically grown Ir-oxohydroxides.^{26,27}

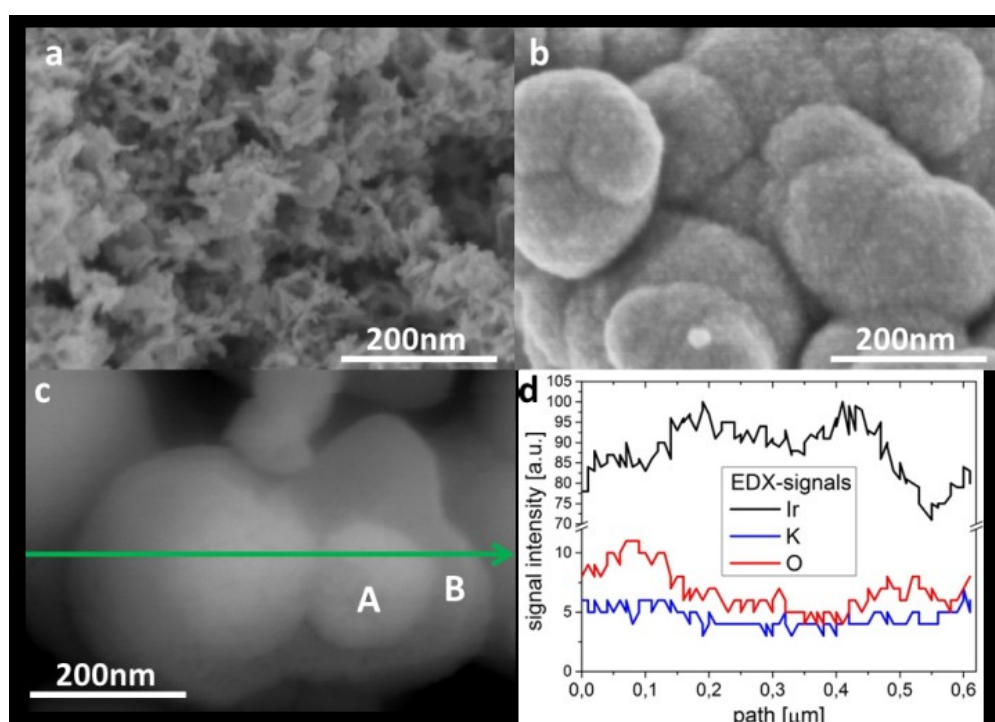


Figure 3.1 SEM of the catalyst synthesized with $\text{KOH}:\text{Ir} = 5:1$ (a) shows a highly nanostructured material, whereas for $\text{KOH}:\text{Ir} = 50:1$ (b) big clusters are formed. Secondary electron contrasted-imaging of such a split cluster (c) reveals a core-shell structure, where the metallic iridium (bright twin-cores, A) is coated with a thick layer of oxidic iridium (B). (d) Linescan (green arrow) confirms lower O/Ir-ratio in the cores.

SEM imaging and specific surface area (S_{BET}) analysis of the compounds produced at low $\text{KOH}:\text{Ir} \leq 4:1$ exhibit a highly nanostructured morphology in line with S_{BET} over $150 \text{ m}^2 \cdot \text{g}^{-1}$. XRF and EDX analysis also showed that these samples still contain chlorides, which is consistent with incomplete hydrolysis of Ir-chlorides (see Table S1). For intermediate $4:1 \leq \text{KOH}:\text{Ir} \leq 7:1$, a dominantly nanosized rod-structure is obtained (see Figure 3.1.a and Figure S3.5). Rod thickness increases with KOH:Ir, while S_{BET} decreases from 104 to $56 \text{ m}^2 \cdot \text{g}^{-1}$. At elevated $\text{KOH}:\text{Ir} \geq 10:1$, the nano-rod structure disappears, yielding an amorphous material. For KOH:Ir of 50 and 100 the material is composed of 200 nm-large spheres, leading to a dramatic decrease in surface area to 7 and $16 \text{ m}^2 \cdot \text{g}^{-1}$ respectively, (see Figure 3.1.b). Interestingly, some of the spheres were cracked open and EDX analysis revealed a core-shell structure comprising a metallic Ir-core coated with a thick oxidic Ir-layer (Figure 3.1.c and

Figure 3.1.d). We conclude that the Ir⁰ detected in XRD is located under such an oxidic Ir-layer. (see Figure S3.5 for further SEM images).

3.4.2. Sample composition

The decomposition of the samples to crystalline IrO₂ and the concomitant evolved water fingerprint were analyzed in a MS-coupled thermogravimetric experiment using a 10K.min⁻¹ heating ramp to 800°C in 21% O₂/Ar 100 mL.min⁻¹ (see Figure S3.8 and Figure S3.9). The results confirm the highly hydrated and hydroxylated nature of the oxidic Ir-phase. The samples first loose up to 2.5 wt.% of physisorbed water (first water evolution signal centered around 135°C in Figure S3.9). Then, water evolution through decomposition of hydroxyl groups proceeds till 500°C and accounts for up to 7 wt.%. Based on this high chemisorbed water fraction, we argue that the oxidic phase of our samples is an Ir-oxohydroxide of the form IrO_x(OH)_y. Interestingly, samples with KOH:Ir≤5:1 exhibit a strong component in their water evolution signal above 300°C corresponding to the decomposition of hydroxyl groups. The amount of metallic Ir⁰ was estimated from the sharp mass gain detected above 500°C for KOH:Ir≥7:1, which corresponds to the oxidation of Ir⁰ to Ir^{IV}. It appears that the fraction of undesired metallic iridium increases gradually with increasing KOH:Ir, reaching 24 wt.% for KOH:Ir=50:1, which is in agreement with the trend observed in XRD.

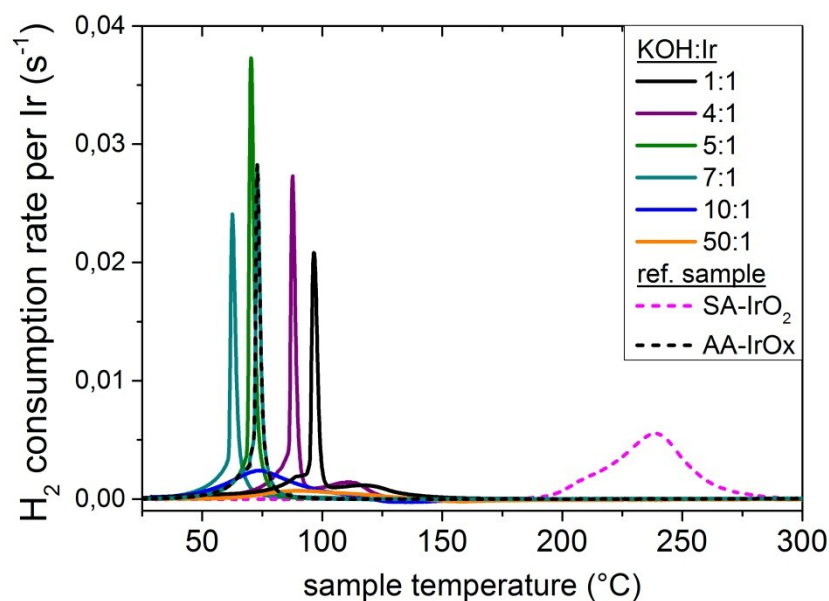


Figure 3.2 Temperature programmed reduction in 4.92% H₂/Ar exhibits sharp reduction features below 100°C that are significantly distinct from the characteristic reduction feature of IrO₂ to Ir⁰ above 200°C as observed with the benchmark catalyst SA-IrO₂.

The reduction behavior of the samples was studied in a temperature-programmed reduction experiment using a 4.92% H₂/Ar stream at a flow rate of 80 mL.min⁻¹ (see Figure 3.2). Upon heating the samples to 450°C with a heating ramp of 6 K.min⁻¹, sharp reduction peaks were observed between 65°C and 85°C for the catalysts synthesized with KOH:Ir≤7:1 as well as the AA-IrO_x benchmark. This reduction behavior is very distinct from the reduction feature above 200°C usually observed for crystalline Ir^{IV}O₂ (SA-IrO₂ in Figure 3.2).¹⁶ For KOH:Ir≥10:1, the TPR-profile broadened dramatically and shifted towards higher temperatures.

Interestingly, before the start of the temperature-program, significant amounts of H₂ are taken up by the sample at room temperature (see Figure S3.10). Since no concomitant water evolution is observed, this indicates that hydrogen enters the Ir-oxohydroxide structure without complete reaction. Such an early uptake of H₂ was also reported by Reier et al. for their best amorphous Ir-catalysts.¹⁶ Hydrogen uptake at room temperatures decreases with higher metallic iridium content (KOH:Ir \geq 7:1). No such adsorption is observed on SA-IrO₂. This finding supports the idea that significant hydrogen uptake is characteristic of amorphous Ir-oxohydroxide as opposed to crystalline IrO₂. Remarkably, HRTEM-study of the samples revealed a high sensitivity of the surface to the electron beam: the surface rapidly transforms into metallic iridium, which confirms the high reducibility of the Ir-oxohydroxide material in contrast with IrO₂ (Figure S3.7).

3.4.3. OER-performance

The electrochemical measurements were carried out by drop casting a suspension of the catalyst on a thoroughly cleaned glassy carbon rotating disk electrode and tested in a standard three-compartment cell containing H₂SO₄ (0.5 mol.L⁻¹) as electrolyte. A catalyst loading of 20 $\mu\text{g}_{\text{Ir}}\cdot\text{cm}^{-2}$ is used and the measurements were corrected for ohmic drop (see S.I. for further details). The OER-activities of the catalysts synthesized at diverse KOH:Ir ratios were determined using linear sweep voltammetry (LSV, 1600 rpm, 5 mV.s⁻¹) (see Figure S3.11). The OER-stability of the catalysts was characterized in an accelerated chronopotentiometric (CP) experiment with a current density of 15 mA.cm⁻² (see Figure S3.13).

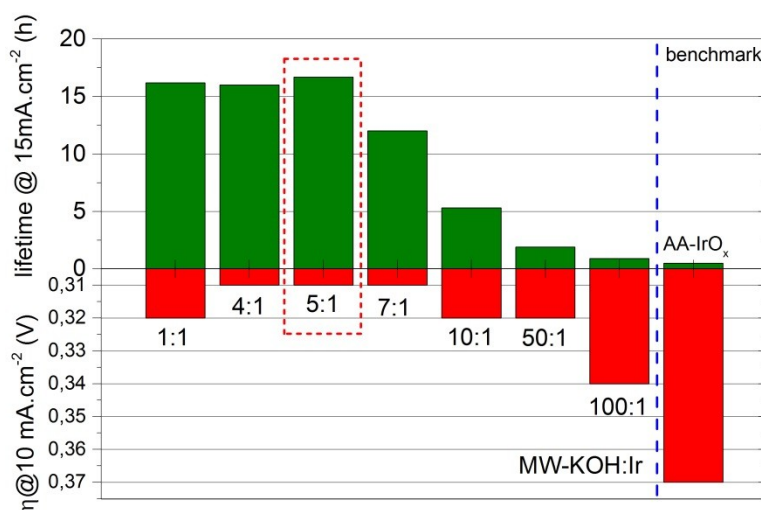


Figure 3.3 OER-activity and -stability of samples prepared at 250°C, 1h correlate and show that the most active and stable sample has been produced with a ratio KOH:Ir of 5:1 at 250°C during 60 minutes.

For comparison of the compounds' OER-performance, the data was conveniently summarized in Figure 3.3. For the OER-activity, the overpotential needed to reach a current density of 10 mA.cm⁻² was used as a widely accepted figure of merit and is reported as red bars.^{6,22} For OER-stability, we defined as catalyst lifetime the time-lapse required by the working electrode to reach a threshold potential of 1.8 V vs. SHE during the CP at 15 mA.cm⁻² (green bars on Figure 3.3). This threshold corresponds to the onset of carbon-oxidation.²⁸ It is readily observed that among the samples synthesized with various KOH:Ir ratios, the sample with KOH:Ir=5:1 shows a significant lifetime of

16,7h, thus ca. 33 times longer than the benchmark catalyst, AA-IrO_x and requires the lowest overpotential of 0.31 V.

In general, the samples for KOH:Ir≤5:1 show comparable OER-performance while the performance gradually worsens for KOH:Ir beyond 7:1. The catalyst synthesized at KOH:Ir=5:1 was selected as the target material due to the optimal synthesis yield and further tested in CP at 10 mA.cm⁻² for comparison with recent benchmarking efforts.^{6,22} As a result, even for Ir-loadings of 20 μg_{Ir}.cm⁻², our best catalyst surpassed the best literature benchmarks in terms of evolution of the overpotential needed to maintain current levels of 10 mA.cm⁻².

Table 3.1 Benchmarking parameters for the best MW-compound (KOH:Ir=5:1) compared to previously reported compounds and reference samples

Catalyst	$\eta_{t=0}$ (V)	$\eta_{t=2h}$ (V)	$\eta_{t=24h}$ (V)	Metal loading (μg.cm ⁻²)	electrolyte
KOH:Ir=5:1	0.31	0.33	0.35	20	H ₂ SO ₄ 0.5 mol.L ⁻¹
KOH:Ir=5:1	0.31	0.33	0.35	50	H ₂ SO ₄ 0.5 mol.L ⁻¹
KOH:Ir=5:1	0.30	0.32	0.33	100	H ₂ SO ₄ 0.5 mol.L ⁻¹
AA-IrO _x	0.37	- ^b	-	20	H ₂ SO ₄ 0.5 mol.L ⁻¹
SIROF ⁶	0.34	0.36	0.44	n.r. ^a	H ₂ SO ₄ 1 mol.L ⁻¹
Sputtered Ru ⁶	0.28	0.34	0.82	n.r. ^a	H ₂ SO ₄ 1 mol.L ⁻¹
20wt.% Ir/C ¹⁹	0.38	n.r.	n.r.	28	KOH 0.1 mol.L ⁻¹
AIROF ²²	0.28	0.30	n.r.	n.r.	NaOH 1 mol.L ⁻¹

a Reactive sputtering resulted in a >100nm thick film (see ref. ^{6,29}) ; b AA-IrO_x was active for only 1.02h

Our MW-assisted hydrothermal synthesis of Ir-compounds confirms the possible combination of activity and stability in OER-electrocatalysis in acidic media at commercially relevant current densities for the Ir-oxohydroxide class of materials.^{15,16}

In order to uncover OER-relevant structural features of the Ir-oxohydroxides we compared trends in structural features and OER-performance within the batches. Interestingly, the most active samples for KOH:Ir≤5:1 exhibit a strong tailing in their water evolution signal above 300°C corresponding to the decomposition of hydroxyl groups (see Figure S3.9). The corresponding mass loss indicates that these samples contain up to 7 wt.% chemisorbed water (see Figure 3.4). In contrast the chemisorbed water fraction rapidly diminishes with decreasing OER-performance (KOH:Ir≥7:1). The observed water evolution fingerprint thus indicates a link between a high fraction of hydroxyl groups stable at higher temperatures and the OER-performance of the samples. Hydroxyl groups are thus linked to a higher concentration of OER-active sites, *i.e.* lower overpotentials and might contribute to their stabilization under water splitting conditions, *i.e.* higher lifetimes.

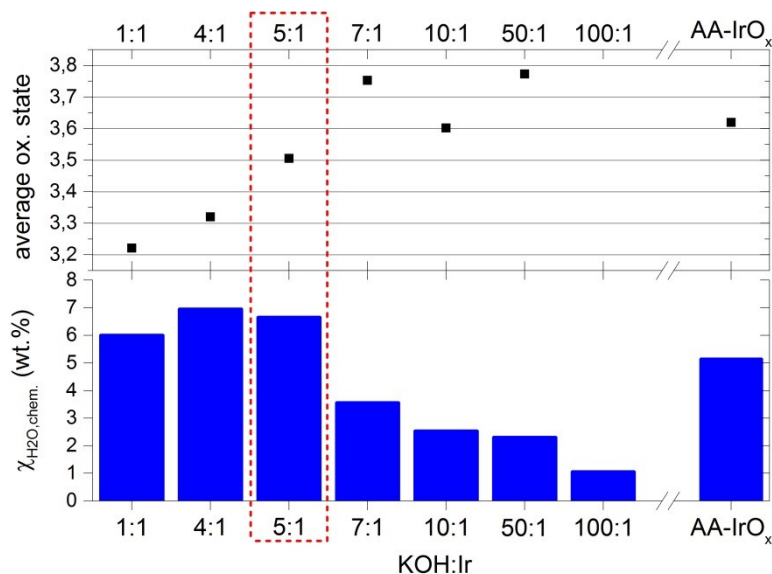


Figure 3.4 MS-coupled ($m/z=18$) thermogravimetric analysis shows that the most active samples exhibit a strong fraction of hydroxyl groups ($\chi_{H_2O.chem.}$) removed in TGMS at temperatures above approx. 140°C (blue bars). The quantification of hydrogen uptake by the sample at room temperature and during TPR allows for the determination of an average oxidation state for the oxidic phase. The best sample (KOH:Ir=5:1) is highlighted in the red dashed box.

The average Ir-oxidation state related to the oxidic phase was estimated from the total H₂-consumption and composition assessment of the samples (see calculations in S.I.). The black squares in Figure 3.4 show that the oxidation state of Ir increases almost linearly from +3.2 to 3.8 with increasing KOH:Ir from 1:1 to 50:1. This findings support the recent study by Pfeifer et al. that reported the coexistence of Ir^{III} and Ir^{IV} in AA-IrO_x.^{18,30} Due to the similarity of the characteristic TPR-profiles (sharp reduction peak below 100°C), we conjecture that the oxidic part of our samples also consists of such an Ir^{III/IV}-oxohydroxide. Remarkably, recent XAS-in-situ studies have stressed the relevance of the coexistence of Ir^{III} and Ir^{IV} during OER-catalysis.³¹ Thus, such a mixed III/IV-oxidation state might be key to understanding the remarkable OER-properties of Ir-oxohydroxides. The chemisorbed water fingerprint might in turn be linked to the stabilization of such a mixed oxidation phase, as the most hydroxylated samples also seem to possess the lowest oxidation state, *i.e.*, the highest amount of Ir^{III}-species.

Open questions include the possible presence of Ir-peroxo-species that have been evidenced by Pankratov et al. for hydrolyzed Ir-species in highly basic solutions close in nature to our precursors.³² Recent studies have taken advantage of synchrotron-based X-ray photoelectron emission spectroscopy to investigate surface species linked to the OER-performance of Ir-based compounds.³³ Ongoing XPS- and NEXAFS-studies will give closer insight into the electronic structure and species located in the surface region of our samples.

3.5. Conclusion

Ultimately, the observed contrast between crystalline IrO_2 and the MW-assisted hydrothermally synthesized amorphous $\text{IrO}_x(\text{OH})_y$ confirms that producing the right chemical state and structure of iridium-based catalyst precursors is critical in achieving stable OER-electrocatalysis at low Ir-loadings. Ir-oxohydroxides are suspected to accommodate $\text{Ir}^{\text{III/IV}}$ -precursor sites to OER-catalysis, stabilized in a highly hydroxylated environment and constitute a class of extremely promising candidates for affordable and stable OER-catalysis.

3.6. Acknowledgements

This work was supported by the German Bundesministerium für Wirtschaft und Energie as part of the Ekolyzer project. We thank Andrey Tarasov, Jasmin Allan and Wiebke Frandsen for their help with various characterization methods.

3.7. Supporting information

Parameter control in the MW-reactor

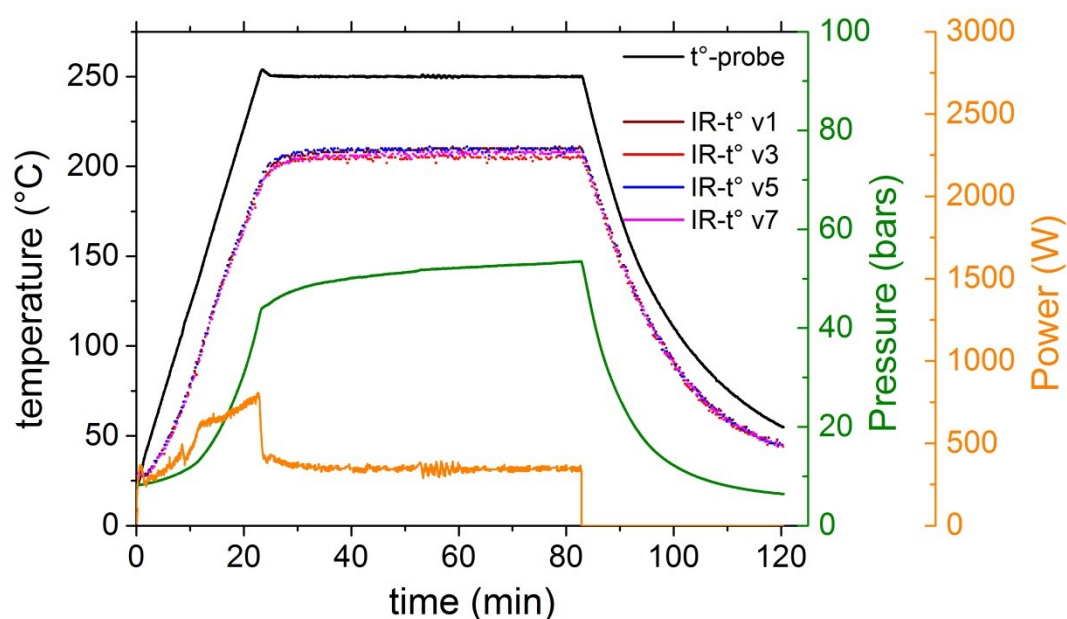


Figure S3.1 Representative process monitoring of the MW-assisted hydrothermal synthesis of Ir-oxohydroxides (KOH:Ir=5:1, 250°C, 1h).

UV-Vis of the supernatant after synthesis

The UV-Vis absorption of the supernatant after the first centrifugation allows for the detection of Ir-species still in solution after hydrothermal treatment (see Figure S3.2). For low KOH:Ir ratios, the UV-Vis spectra shows two weak absorption bands at 322 nm and 380 nm, attributed to partially hydrolyzed Ir-chloride complexes.^{34,35} These chloride-species exhibit strong stability against hydrolysis upon heating, which explains the low yield for KOH:Ir=1:1 ratio (see Table S1). On the other hand, for $4:1 \leq \text{KOH:Ir} \leq 10:1$ ratios, only a very weak absorption band in the far-UV-range attributed to KOH is observed.

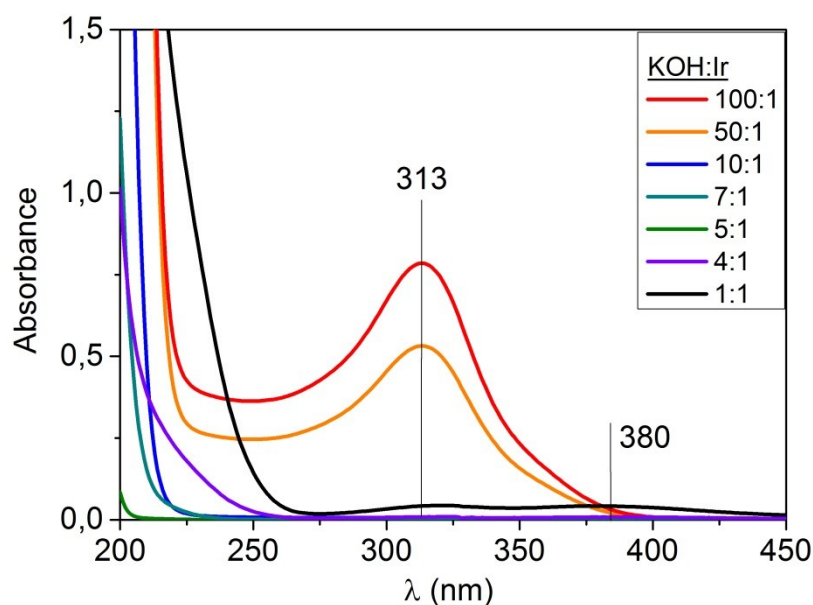


Figure S3.2 UV-Vis absorption spectra of the supernatant after the first centrifugation of the precursor solutions MW-treated at 250°C for 1h

For KOH:Ir=50:1 and 100:1 however, yields decrease sharply (see Table S1). A relatively strong absorption peak at 313 nm can be attributed to hexahydroxoiridate.^{36,37} Gamsjäger et al. studied the OH⁻ exchange kinetics of hexahydroxoiridate-(III) by ¹⁸O-labeling exchange experiments.²⁵ It was shown that at high [OH⁻], monomeric Ir(III)-species are strongly favored due to fast hydroxyl ligand exchange. This explain why at high [OH⁻], hexahydroxoiridate-(III) remains relatively stable towards condensation even under hydrothermal treatment conditions, resulting in low synthesis yields for KOH:Ir≥50:1 ratios. On the other hand, at lower [OH⁻], Gamsjäger et al. report the formation of polymeric Ir-species, which explains the efficient condensation and good synthesis yield in the optimal synthesis range of 4:1≤KOH:Ir≤10:1. Synthesis at 150°C and 200°C for KOH:Ir=5:1 shows that the yield does not vary much for decreasing synthesis temperature.

Characterization of the Ir-oxohydroxides

Table S3.1 Summary of the main synthesis parameters such as KOH:Ir and T_{syn} as well as synthesis yield, K- and Cl-contents and specific surface area (S_{BET}) of the produced compounds.

KOH:Ir	T _{syn} (°C)	Synthesis yield (%)	K:Ir (10 ⁻³)	Cl:Ir (10 ⁻³)	S _{BET} (m ² ·g ⁻¹)
1:1	250	51	2.5	433	217
4:1	250	97	3.9	299	165
5:1	250	99	18.4	0	104
5:1	200	-	-	-	99
5:1	150	92	93.1	0	103
7:1	250	100	91.0	0	56
10:1	250	99	112.6	0	175
50:1	250	72	92	0	7
100:1	250	35	36.4	0	16

The synthesis yield results from the ratio of the obtained sample mass and the theoretical mass based on the sample composition obtained for each KOH:Ir ratio according to XRF, TGMS and TPR.

X-Ray diffraction (XRD)

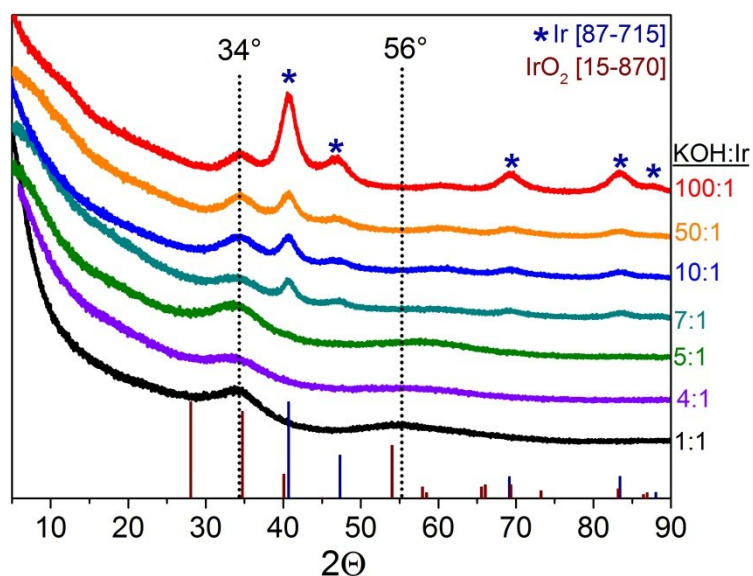


Figure S3.3 XRD patterns of samples synthesized with different KOH:IR ratios, at a synthesis temperature (T_s) of 250°C and a hold time of (t_{hold}) 60 min show two broad peaks at about 34° and 56° attributed to iridium oxohydroxide^{26,27} and the characteristic pattern of cubic metallic iridium for KOH:Ir \geq 7:1.

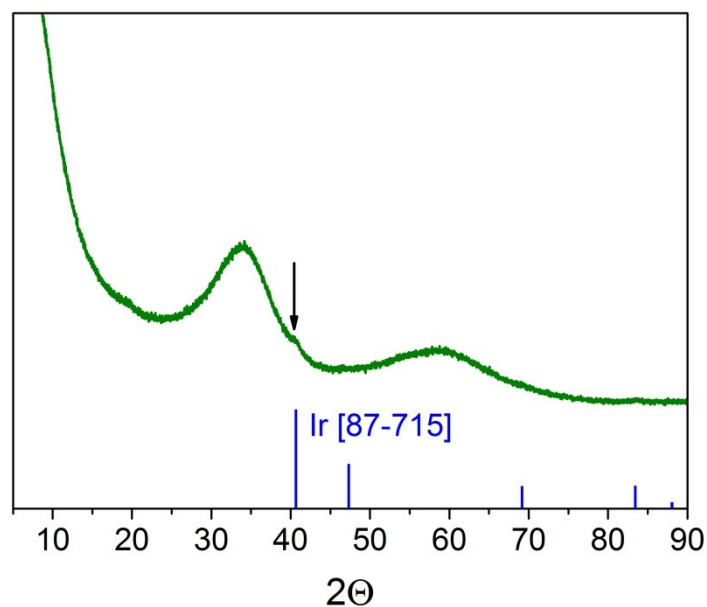


Figure S3.4 XRD pattern of the sample synthesized at (T_s) 250°C with a hold time of (t_{hold}) 60 min and a KOH:Ir ratio of 5:1 show possible weak Ir⁰ peak at 40.5° highlighted by an arrow.

Scanning Electron Microscopy (SEM)

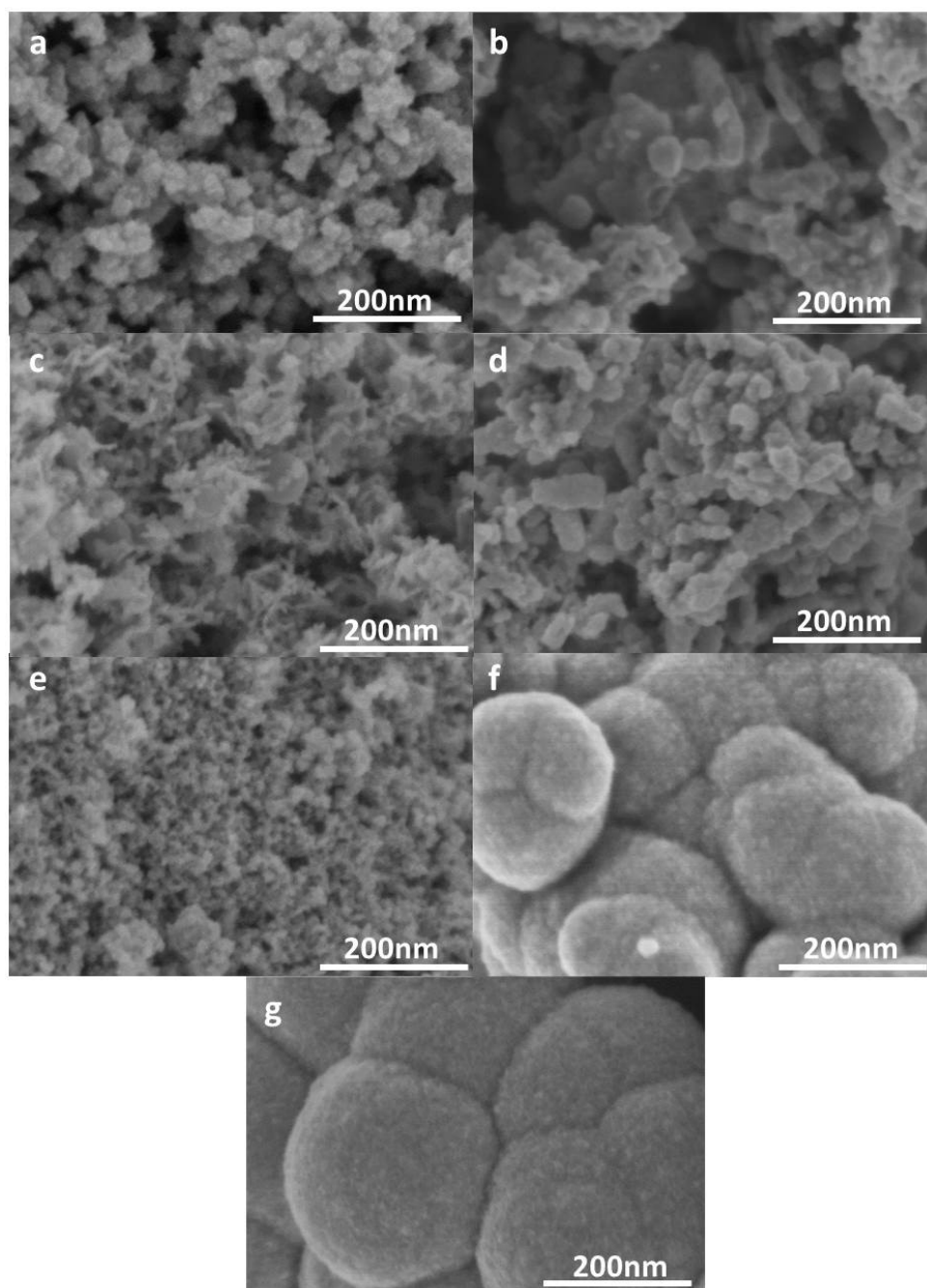


Figure S3.5 SEM-pictures (1.5KV) of the synthesized Ir-oxohydroxide at a temperature (T_s) of 250°C with a hold time (t_{hold}) of 60 min with a ratio KOH:Ir of 1:1 (a), 4:1 (b), 5:1 (c), 7:1 (d), 10:1 (e), 50:1 (f), 100:1 (g)

Transmission electron microscopy (TEM)

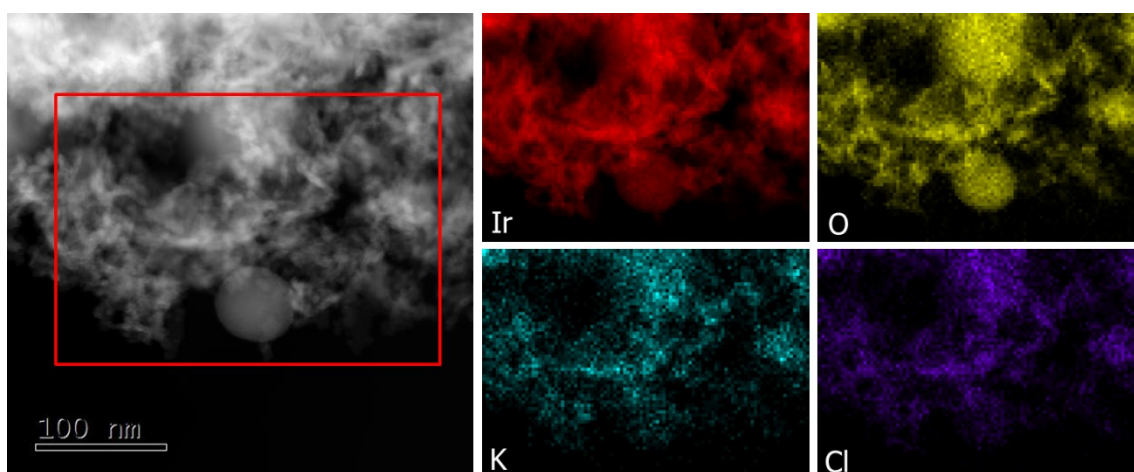


Figure S3.6 STEM pictures of the synthesized Ir-oxohydroxide at a temperature (T_s) of 250°C with a hold time (t_{hold}) of 60 min and a KOH:Ir ratio of 5:1 and the corresponding EDX-mapping of Ir, O, K and Cl.

The STEM-EDX study of the sample prepared from KOH:Ir=5:1 ratio at 250°C homogenous Ir- and O-contents as well as K- and Cl-traces. However, no reliable structural information about the crystallographic nature of the amorphous iridium-oxohydroxide phase could be extracted from HRTEM/STEM-investigations. Indeed, at higher magnification, under the electron beam the sample rapidly transformed into crystalline cubic iridium. Figure S3.7 shows the beam damage for a 15 μA -STEM electron beam over 213 s. Even the initial picture already shows bright spots corresponding to metallic iridium. These spots serve as nucleation sites for rapidly expanding Ir⁰-nanoparticles.

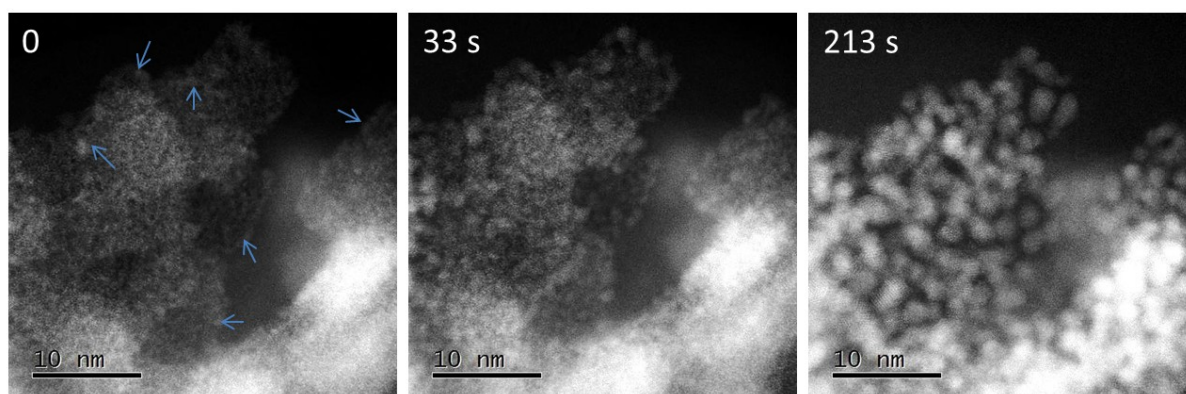


Figure S3.7 Beam effect of a 15 μA -electron beam of a sample having a KOH:Ir=5:1 ratio in STEM-mode initially, after 33 s and 213 s.

MS-coupled thermogravimetry (TGMS) and differential scanning calorimetry (DSC)

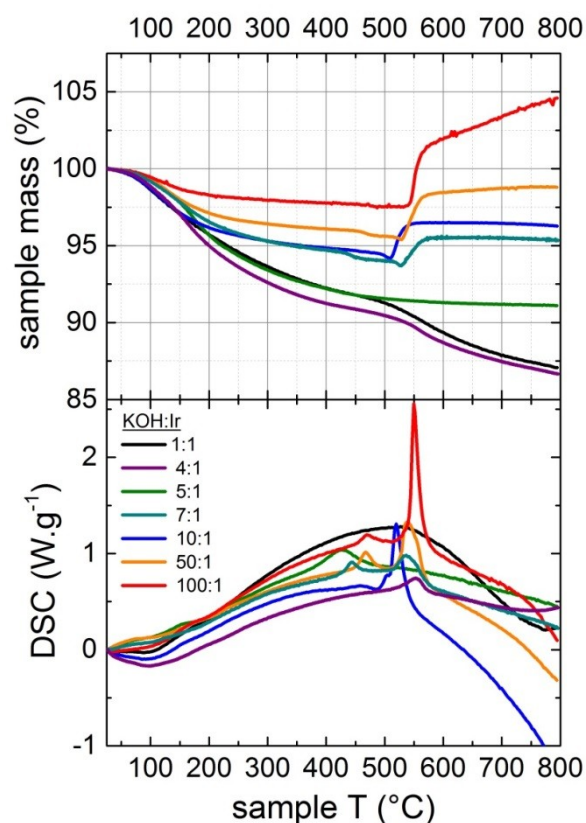


Figure S3.8 Thermogravimetric analysis (top) and corresponding DSC signals (bottom) of samples synthesized with various KOH:Ir ratios (see figure caption) at a temperature (T_s) of 250°C with a hold time (t_{hold}) of 60 min.

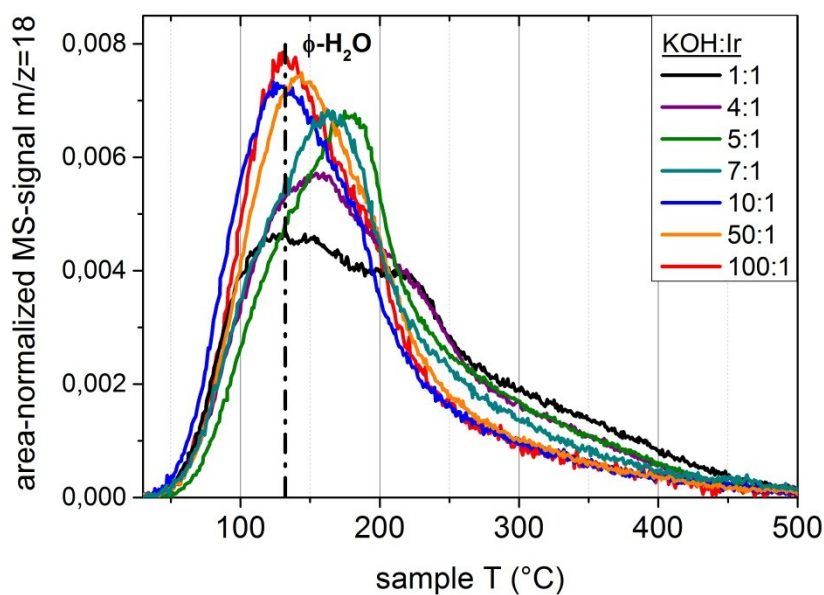


Figure S3.9 MS-coupled ($m/z=18$) thermogravimetric analysis shows that the most active samples, *i.e.*, with a KOH:Ir=5:1 ratio, exhibit a strong fraction of hydroxyl groups stable at high temperatures.

Temperature programmed reduction (TPR)

TPR of the calcined sample was performed in a fixed-bed reactor in 5 vol.% H₂/Ar (80 mL min⁻¹) at a heating rate of 6 K min⁻¹ (80 mL min⁻¹, 450°C). The H₂ consumption was monitored with a thermal conductivity detector (TCD). The TCD detector was calibrated by reducing a known amount of CuO. The samples were initially kept under Ar-flow for 1h (80 mL min⁻¹). The comparison of H₂-signals during the initial switch from Ar to 4.92% H₂/Ar before (dark line in Figure S3.10) and after TPR (red line in Figure S3.10) allows to quantify the amount of H₂ initially absorbed by the sample. No concomitant evolution of water is detected at room temperature, indicating that hydrogen is merely adsorbed on the sample. Once heating starts, H₂-consumption features correlate with evolved water detected in the gas outlet via mass spectrometry (MS), indicating reduction of oxidic Ir to Ir⁰ via Eq. (S3.1):

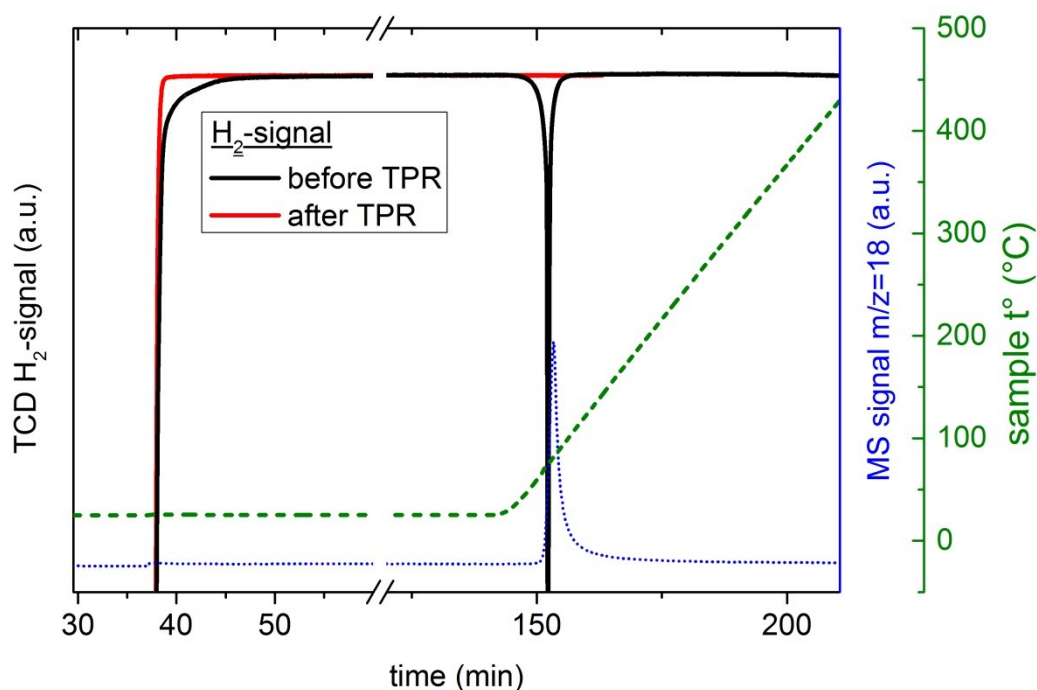
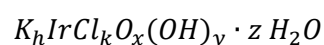


Figure S3.10 Temperature programmed reduction of the sample synthesized with a KOH:Ir ratio of 5:1 at a temperature (T_s) of 250°C with a hold time (t_{hold}) of 60 min.

Sample composition and average Ir-oxidation state

In order to determine the average oxidation state of iridium in the compounds from hydrogen consumption during TPR, the nominal composition and molar mass of the compounds are required. Taking into account all possible contaminants from initial reactants, the formula is:



The average oxidation state of iridium is $l + 2x + y$. The formula of each sample must thus be elucidated in order to assess its average oxidation state.

The molar mass of the compound is given by :

$$M = M_K \times h + M_{Cl} \times k + M_{Ir} + M_O \times x + M_{OH} \times y + M_{H_2O} \times z$$

K/Ir-, and Cl/Ir-ratios (h,k) were determined easily from XRF (see Table S1)

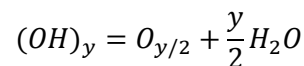
TGMS gives access to the amount of physisorbed ($n_{H_2O}^\varphi$) and chemisorbed ($n_{H_2O}^x$) water (two equations linking y and z) via the subsequent mass loss corresponding to the removal of first physisorbed water (mass fraction x_{m,H_2O}^φ) and later chemisorbed water through hydroxyl decomposition (mass fraction x_{m,H_2O}^x).

Physisorbed water:

$$z \times n_{tot} = n_{H_2O}^\varphi \Leftrightarrow z \times \frac{m_{tot}}{M} = \frac{m_{H_2O}^\varphi}{18}$$

$$M \times x_{m,H_2O}^\varphi = 18z$$

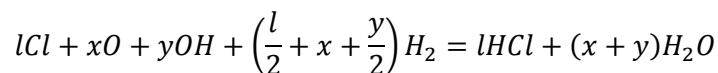
Chemisorbed water:



$$\frac{y}{2} \times n_{tot} = n_{H_2O}^x \Leftrightarrow \frac{y}{2} \times 18 = M \times x_{m,H_2O}^x$$

$$M \times x_{m,H_2O}^x = 9y$$

TPR yields a third equation linking x and y :



$$n_{H_2} = \left(\frac{l}{2} + x + \frac{y}{2}\right)n_{sample} = \left(\frac{l}{2} + x + \frac{y}{2}\right)\frac{m_{sample}}{M}$$

$$n_{H_2} \times M = \left(\frac{l}{2} + x + \frac{y}{2}\right)m_s$$

The result is a system of three linear equations in x,y and z, that was solved numerically using Wolfram Mathematica software, after inserting known coefficients $h,k,l, x_{m,H_2O}^\varphi, x_{m,H_2O}^x, n_{H_2}$ and m_s :

$$M \times x_{m,H_2O}^{\varphi} = 18z \quad (S3.2)$$

$$M \times x_{m,H_2O}^{\chi} = 9y \quad (S3.3)$$

$$n_{H_2} \times M = \left(\frac{l}{2} + x + \frac{y}{2}\right)m_s \quad (S3.4)$$

Remarks concerning coefficients x_{m,H_2O}^{φ} , x_{m,H_2O}^{χ} , n_{H_2} and m_s :

- The mass fraction of physisorbed water x_{m,H_2O}^{φ} corresponds to the mass loss detected via TGMS between room temperature and approx. 135°C (see Figure S3.8 and Figure S3.9).
- The mass fraction of hydroxyl groups x_{m,H_2O}^{χ} corresponds to the mass loss between approx. 135°C and 500°C. We neglect mass gain due to oxidation of Ir³⁺ to Ir⁴⁺ and mass loss due to the decomposition of surface carbonate and formate species.
- For the determination of n_{H_2} , the amount of hydrogen adsorbed at room temperature is taken into account. Indeed no release of the adsorbed hydrogen is detected before or during heating, meaning that during TPR the adsorbed hydrogen participates in the reduction. The complete reduction of the sample to Ir⁰ is verified via XRD.
- In order to relate the average oxidation state solely to the oxidic phase, the amount of metallic Ir⁰ is estimated from the sharp mass gain detected above 500°C in samples MW_7 to MW_50. This mass gain is associated to the oxidation of Ir⁰ to IrO₂ and the initial molar Ir⁰-content (x_{mol,Ir^0}) can be estimated following:

$$\%_{mass\ gain, Ir^0 \rightarrow IrO_2} = \frac{32 \times x_{mol,Ir^0}}{M_{ini}} \quad (S3.5)$$

Table S3.2 H₂-uptake at room temperature (RT) and consumption during TPR as well as the resulting average oxidation state of iridium in the samples related to the non-metallic phase.

KOH:Ir	T _{syn} (°C)	x_{m,H_2O}^{ϕ}	x_{m,H_2O}^{χ}	$n_{H_2} \cdot n_{Ir}^{-1}$ @ RT	$n_{H_2} \cdot n_{Ir}^{-1}$ TPR	Ir ⁰ -content (mol.%)	Ir-redox state
1:1	250	2.7	6.0	0.05	1.39	0	3.22
4:1	250	2.6	7.0	0.36	1.33	0	3.32
5:1	250	1.9	6.7	0.53	1.22	0	3.51
7:1	250	1.9	3.6	0.65	0.98	13.2	3.75
10:1	250	2.6	2.5	0.63	0.91	14.6	3.60
50:1	250	1.7	2.3	0.24	1.20	23.6	3.77
100:1	250	1.2	1.05	n.d.	n.d.	n.d.	n.d.
5:1	150	2.7	5.8	0.70	1.07	0	3.59
SA-IrO ₂	-	0.1	0	0	2.04	0	4.08
AA-IrO ₂	-	0.9	5.1	0.59	1.21	2.4	3.62

Electrochemical characterization

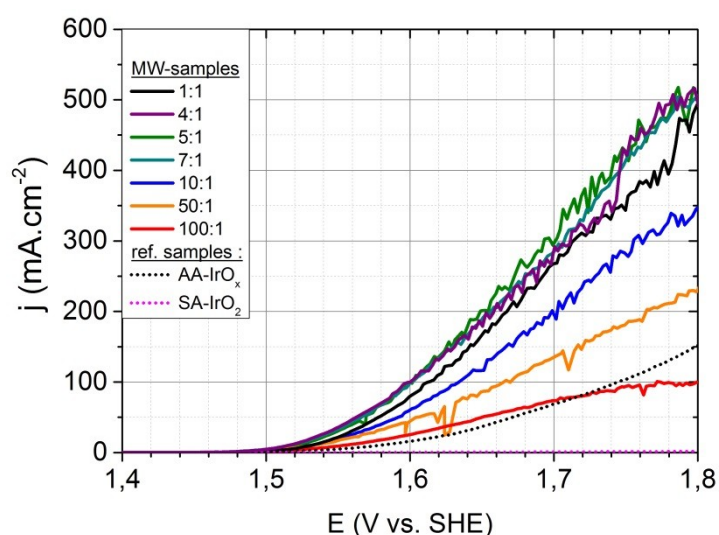


Figure S3.11 Linear sweep voltammograms of the samples produced with diverse KOH:Ir ratios at a temperature of 250°C allow for comparison of OER-activities and indicates superior activity compared to commercial benchmarks.

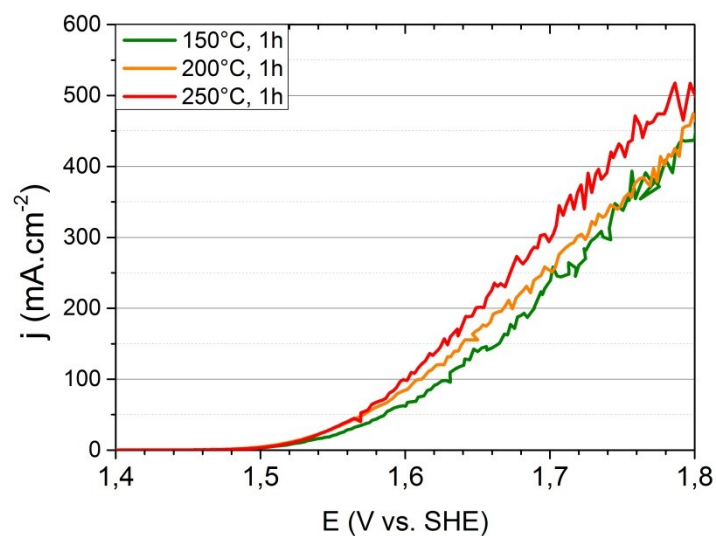


Figure S3.12 Linear sweep voltammograms of samples synthesized at KOH:Ir=5:1 and $T_s = 150^\circ\text{C}$, 200°C and 250°C show that the sample synthesized at the highest temperature, *i.e.* 250°C , is the most active catalyst.

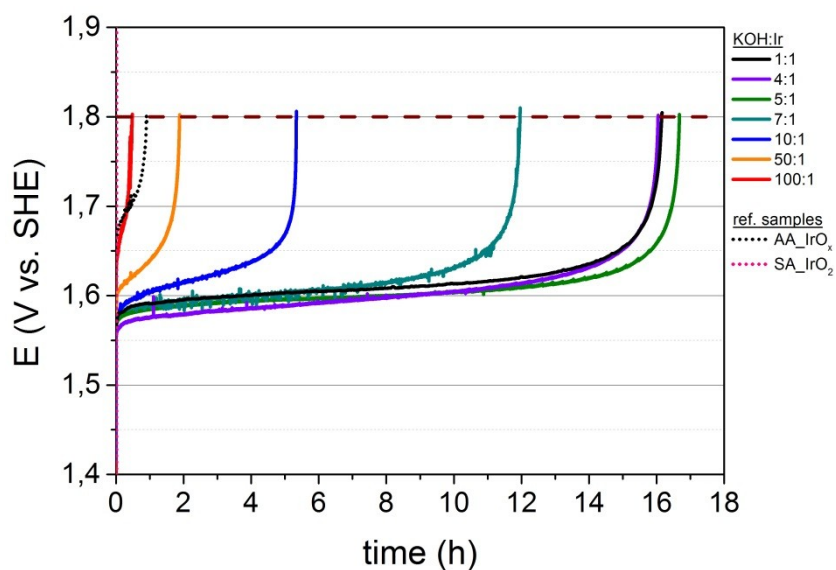


Figure S3.13 CP at $15 \text{ mA}\cdot\text{cm}^{-2}$ of samples synthesized with various KOH:Ir at $T_{\text{syn}}=250^\circ$ shows that our best sample (KOH:Ir=5:1) lasted ca. 33 times longer than the AA-IrO_x benchmark catalyst. The catalyst loading in terms of Ir mass for all samples was $20 \mu\text{g}_{\text{Ir}}\cdot\text{cm}^{-2}$.

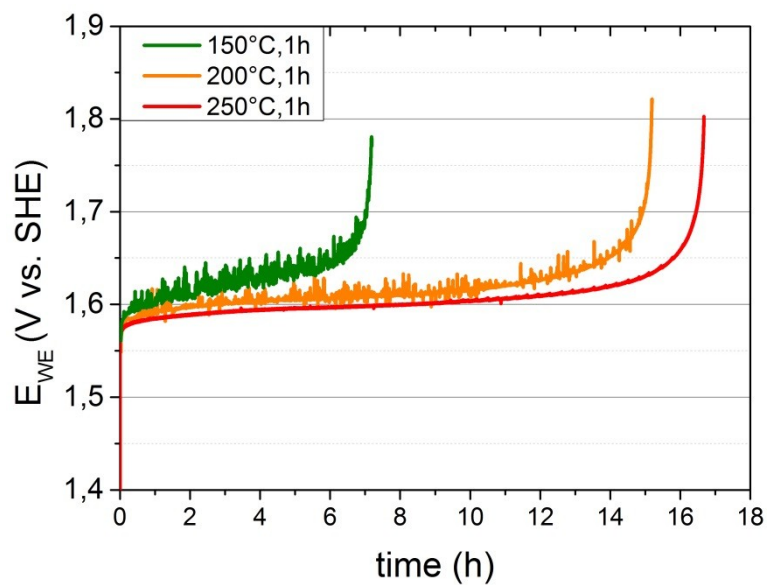


Figure S3.14 CP at $15 \text{ mA}\cdot\text{cm}^{-2}$ of the samples synthesized at $\text{KOH}:\text{Ir}=5:1$ for $T_{\text{syn}}=150^\circ\text{C}$, 200°C and 250°C shows that the sample synthesized at 250°C yields the most stable catalyst.

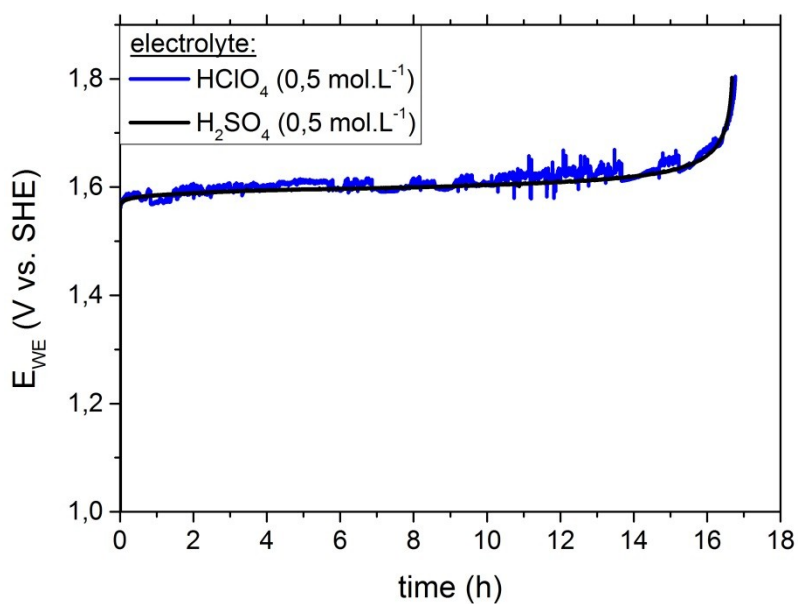


Figure S3.15 CP at $15 \text{ mA}\cdot\text{cm}^{-2}$ of the sample synthesized at $\text{KOH}:\text{Ir}=5:1$ for $T_{\text{syn}}=250^\circ\text{C}$ in H_2SO_4 ($0.5 \text{ mol}\cdot\text{L}^{-1}$) and HClO_4 ($0.5 \text{ mol}\cdot\text{L}^{-1}$) as electrolyte. No significant influence of the electrolyte could be observed.

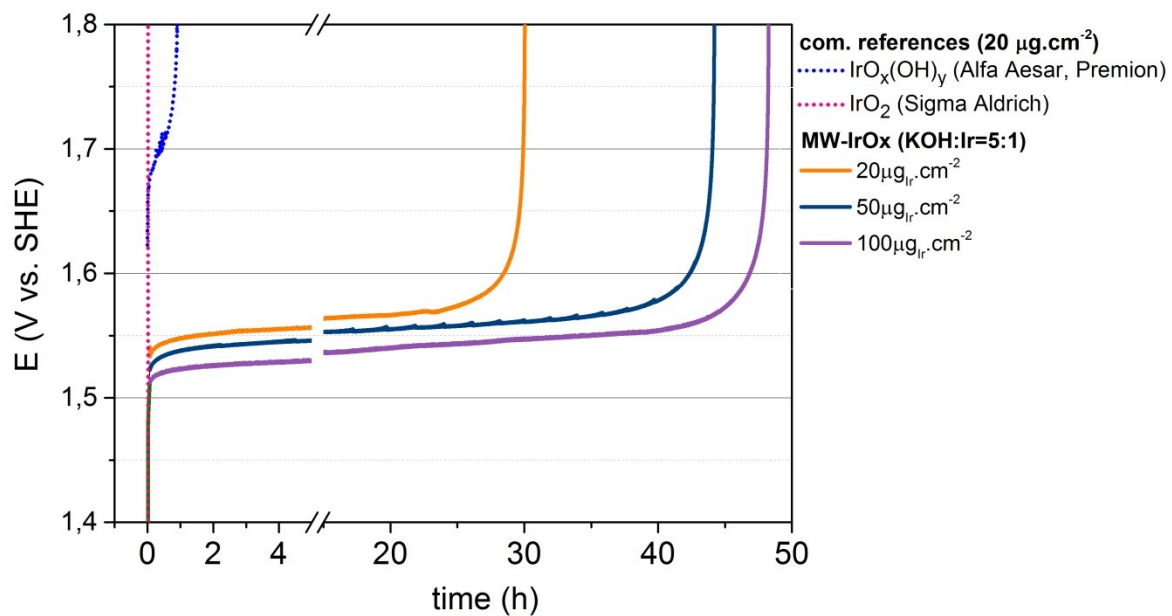


Figure S3.16 CP at 10 $\text{mA}\cdot\text{cm}^{-2}$ for three loadings of 20, 50 and 100 $\mu\text{g}_{\text{Ir}}\cdot\text{cm}^{-2}$ for the best OER-catalyst (KOH:Ir=5:1, $T_{\text{syn}}=250^\circ\text{C}$) allows for the comparison with reported literature benchmarks under commercially relevant OER-conditions.^{6,22}

3.8. References

- (1) Schlögl, R. *ChemSusChem* **2010**, *3*, 209.
- (2) Carmo, M.; Fritz, D. L.; Mergel, J.; Stolten, D. *International Journal of Hydrogen Energy* **2013**, *38*, 4901.
- (3) Katsounaros, I.; Cherevko, S.; Zeradjanin, A. R.; Mayrhofer, K. J. J. *Angewandte Chemie International Edition* **2014**, *53*, 102.
- (4) Marcelo Carmo, D. L. F. *International Journal of Hydrogen Energy* **2013**, *38*, 4901.
- (5) Kötz, R.; Stucki, S.; Scherson, D.; Kolb, D. M. *Journal of Electroanalytical Chemistry and Interfacial Electrochemistry* **1984**, *172*, 211.
- (6) McCrory, C. C. L.; Jung, S.; Ferrer, I. M.; Chatman, S. M.; Peters, J. C.; Jaramillo, T. F. *Journal of the American Chemical Society* **2015**, *137*, 4347.
- (7) Frazer, E. J.; Woods, R. *Journal of Electroanalytical Chemistry and Interfacial Electrochemistry* **1979**, *102*, 127.
- (8) Vuković, M. *Journal of Applied Electrochemistry* **1987**, *17*, 737.
- (9) Beni, G.; Schiavone, L. M.; Shay, J. L.; Dautremont-Smith, W. C.; Schneider, B. S. *Nature* **1979**, *282*, 281.
- (10) Mráz, R.; Krýsa, J. *Journal of Applied Electrochemistry* **1994**, *24*, 1262.
- (11) Xu, L. K.; Scantlebury, J. D. *Corrosion Science* **2003**, *45*, 2729.
- (12) Xu, L. K.; Scantlebury, J. D. *Journal of the Electrochemical Society* **2003**, *150*, B254.
- (13) Xu, L.; Xin, Y.; Wang, J. *Electrochimica Acta* **2009**, *54*, 1820.
- (14) Bockris, J. O. M.; Otagawa, T. *Journal of the Electrochemical Society* **1984**, *131*, 290.
- (15) Cherevko, S.; Reier, T.; Zeradjanin, A. R.; Pawolek, Z.; Strasser, P.; Mayrhofer, K. J. J. *Electrochemistry Communications* **2014**, *48*, 81.
- (16) Reier, T.; Teschner, D.; Lunkenbein, T.; Bergmann, A.; Selve, S.; Kraehnert, R.; Schlögl, R.; Strasser, P. *Journal of the Electrochemical Society* **2014**, *161*, F876.
- (17) Pfeifer, V.; Jones, T. E.; Velasco Vélez, J. J.; Massué, C.; Arrigo, R.; Teschner, D.; Girgsdies, F.; Scherzer, M.; Greiner, M. T.; Allan, J.; Hashagen, M.; Weinberg, G.; Piccinin, S.; Hävecker, M.; Knop-Gericke, A.; Schlögl, R. *Surface and Interface Analysis* **2015**, n/a.
- (18) Pfeifer, V.; Jones, T. E.; Velasco Vélez, J. J.; Massué, C.; Greiner, M. T.; Arrigo, R.; Teschner, D.; Girgsdies, F.; Scherzer, M.; Allan, J.; Hashagen, M.; Weinberg, G.; Piccinin, S.; Hävecker, M.; Knop-Gericke, A.; Schlögl, R. *Phys Chem Chem Phys* **2016**, *18*, 2292.
- (19) Gorlin, Y.; Jaramillo, T. F. *Journal of the American Chemical Society* **2010**, *132*, 13612.
- (20) Reier, T.; Oezaslan, M.; Strasser, P. *ACS Catalysis* **2012**, *2*, 1765.
- (21) Yi, Y.; Tornow, J.; Willinger, E.; Willinger, M. G.; Ranjan, C.; Schlögl, R. *ChemElectroChem* **2015**, *2*, 1929.
- (22) McCrory, C. C. L.; Jung, S.; Peters, J. C.; Jaramillo, T. F. *Journal of the American Chemical Society* **2013**, *135*, 16977.
- (23) Zhao, Y.; Vargas-Barbosa, N. M.; Strayer, M. E.; McCool, N. S.; Pandelia, M.-E.; Saunders, T. P.; Swierk, J. R.; Callejas, J. F.; Jensen, L.; Mallouk, T. E. *Journal of the American Chemical Society* **2015**, *137*, 8749.
- (24) Ioroi, T.; Kitazawa, N.; Yasuda, K.; Yamamoto, Y.; Takenaka, H. *Journal of the Electrochemical Society* **2000**, *147*, 2018.
- (25) Rodgers, K. R.; Gamsjaeger, H.; Murmann, R. K. *Inorganic Chemistry* **1989**, *28*, 379.
- (26) Cruz, A. M.; Abad, L.; Carretero, N. M.; Moral-Vico, J.; Fraxedas, J.; Lozano, P.; Subías, G.; Padial, V.; Carballo, M.; Collazos-Castro, J. E.; Casañ-Pastor, N. *Journal of Physical Chemistry C* **2012**, *116*, 5155.
- (27) Carretero, N. M.; Lichtenstein, M. P.; Pérez, E.; Cabana, L.; Suñol, C.; Casañ-Pastor, N. *Acta Biomaterials* **2014**, *10*, 4548.
- (28) Yi, Y.; Tornow, J.; Willinger, E.; Willinger, M. G.; Ranjan, C.; Schlögl, R. *ChemElectroChem* **2015**, *2*, 1929.

- (29) Spurgeon, J. M.; Velazquez, J. M.; McDowell, M. T. *Physical Chemistry Chemical Physics* **2014**, *16*, 3623.
- (30) Pfeifer, V.; Jones, T. E.; Velasco Velez, J. J.; Massue, C.; Greiner, M. T.; Arrigo, R.; Teschner, D.; Girgsdies, F.; Scherzer, M.; Allan, J.; Hashagen, M.; Weinberg, G.; Piccinin, S.; Havecker, M.; Knop-Gericke, A.; Schlögl, R. *Physical Chemistry Chemical Physics* **2016**, *18*, 2292.
- (31) Minguzzi, A.; Lugaresi, O.; Achilli, E.; Locatelli, C.; Vertova, A.; Ghigna, P.; Rondinini, S. *Chemical Science* **2014**, *5*, 3591.
- (32) Pankratov, D. A.; Komozin, P. N.; Kiselev, Y. M. *Russian Journal of Inorganic Chemistry* **2011**, *56*, 1794.
- (33) Reier, T.; Pawolek, Z.; Cherevko, S.; Bruns, M.; Jones, T.; Teschner, D.; Selve, S.; Bergmann, A.; Nong, H. N.; Schlögl, R.; Mayrhofer, K. J. J.; Strasser, P. *Journal of the American Chemical Society* **2015**, *137*, 13031.
- (34) Moggi, L.; Varani, G.; Manfrin, M. F.; Balzani, V. *Inorganica Chimica Acta* **1970**, *4*, 335.
- (35) Poulsen, I. A.; Garner, C. S. *Journal of the American Chemical Society* **1962**, *84*, 2032.
- (36) Beutler, P.; Gamsjäger, H. *J. Chem. Soc., Chemical Communications* **1976**, 554.
- (37) Heinz Gamsjäger, P. B. *Journal of the Chemical Society Dalton Transactions* **1979**, 1415.

4. OER-relevant fingerprints of Ir-oxohydroxide electrocatalysts

4.1. Abstract

Although oxidic Ir-structures have been identified as the most promising OER-electrocatalysts under acidic conditions, an exact description of the performance-relevant species has remained a challenge. We report on the characterization of hydrothermally prepared Ir-oxohydroxides exhibiting unprecedented OER-performance. These amorphous structures could be characterized via careful TEM-analysis and Raman-spectroscopy. A DFT-based model further allowed us to identify reactive, formally $O^{\cdot-}$ -species stabilized in an Ir^{III} -rich environment. These O 2p hole states were studied using synchrotron-based XPS and XAS and were quantified via reactive CO-titration. Concomitant trends in $O^{\cdot-}$ -concentration and OER-performance allowed us to relate the outstanding electrocatalytic OER-performance of Ir-oxohydroxides to their ability to accommodate stable $O^{\cdot-}$ -rich precursor sites. The CO-titration also highlighted the ability of sub-surface $O^{\cdot-}$ to migrate to the surface, suggesting the involvement of the 3D-structure of Ir-oxohydroxides during OER-catalysis. The identification of these key features controlled by synthetic parameters of our microwave-supported hydrothermal synthesis allows for a new targeted approach to OER-catalyst design in view of commercial applications.

4.2. Introduction

There is a growing consensus in the literature that under acidic conditions, Ir-based OER-catalysts are the most suitable candidates in terms of activity and stability.¹⁻³ The current debate is focused on the understanding of the structure and chemical nature of such Ir-structures. So far, rutile-type IrO_2 has often been suggested as the target material.^{2,4} However, there is growing evidence in the literature that amorphous Ir-phases more elusive to characterization play a key role in OER-catalysis: Early electrochemical studies have shown that metallic iridium anodes need to be oxidatively activated via electrochemical cycling⁵⁻⁷ or reactive sputtering⁸ in order to show appreciable OER-performance. It was suggested that an amorphous hydrous Ir-oxide/hydroxide layer was formed during the activation procedure. Vuković et al. further reported on the thermal treatment of such an anodically grown iridium oxide film (AIROF).⁶ They noted that mild calcination in air at 200°C prior to OER-catalysis improved the catalyst stability. For higher calcination temperatures, at which the formation of crystalline IrO_2 was suggested, OER-performance drastically worsened. A similar evolution of OER-performance was recently reported by Reier et al. who studied pure Ir-based anodes prepared from Ir-acetate calcined at various temperatures.^{9,10} These studies suggest that an OER-active amorphous hydrous Ir-oxide/hydroxide can be stabilized at low calcination temperatures of 200-250°C.

The highlighted results show how crucial the preparation of the right Ir-precursor phase is to OER-performance. The exact identification of Ir-species with superior intrinsic activity in amorphous hydrous Ir-structures and the comparison to fingerprints observed *in-situ* during OER would allow for the rational design of an optimized catalyst precursor.

Amorphous iridium oxides have recently been investigated in several papers in order to bridge the gap between molecular and crystalline structures.¹¹⁻¹³ The blue-colored amorphous Ir-phase often formed electrochemically was modelled based on μ -oxo-bridged Ir^{IV}-oligomers, which allowed for a good agreement with the experimentally observed UV-Vis and Raman spectra. However, based on EPR measurements on similar systems, Zhao et al. suggested that a significant part of the OER-active Ir-compound was in the Ir^{III}-state.¹⁴ The involvement of mixed-valence states in the superior activity of amorphous hydrated IrO_x-films was also reported by Minguzzi et al. who performed in-situ XAS on such films during OER.^{15,16}

In order to investigate the electronic structure of the surface region in OER-active Ir-compounds, some studies have used XPS and assigned Ir-oxidation states based on binding energy shifts.¹⁷ However, it is crucial to point out that the analysis of the electronic structure of oxidic Ir-compounds is by no means trivial, as the structure of the electron-hole pair excitation spectra has to be taken into account when considering XPS core levels. We recently developed a reliable fit model for the Ir 4f peak of rutile-type IrO₂, distinct from the standard Doniach-Šunjić line shape often applicable to metallic conductors.^{18,19} When employing this model to an amorphous Ir-oxohydroxide reference, the presence of an additional species, namely Ir^{III}, was observed. In agreement with our calculations, the Ir^{III}-component shows up at higher binding energies than Ir^{IV}, which shows that speciation of Ir-species cannot be undertaken solely based on binding energy shifts. In the NEXAFS of the O K-edge, the amorphous Ir-oxohydroxide reference furthermore showed an additional pre-edge feature. The nature of this feature was revealed by theoretical calculations to be due to stable O 2p hole states, formally O⁻, that emerge in conjunction with Ir^{III}.

We reported on the microwave-supported hydrothermal synthesis of pure Ir-oxohydroxides in § 3, where the initial base:Ir-ratio was identified as a key parameter in tuning structural properties and OER-performance. For a moderate excess of base, hydrolysis of Ir-chloride precursors under hydrothermal conditions leads to the formation of a highly nanostructured, amorphous Ir^{III}-rich oxohydroxide with outstanding OER-performance. Higher amounts of base lead to the formation of metallic Ir deeply embedded into an oxidic Ir-shell which approaches the IrO₂-stoichiometry and is much less effective in catalyzing the OER.

The present study aims at relating the electronic structure and O-species present in the compounds to the electrocatalytic performance in OER. Sample structure was studied using careful TEM-investigation and Raman spectroscopy interpreted via DFT-calculated model compounds. We used our theoretical model^{18,19} to analyze the synchrotron-based X-ray photoemission and absorption spectra of the Ir-oxohydroxides. XPS yielded information on the Ir-oxidation states. NEXAFS were used to identify reactive oxygen species (O*). Reactive CO-titration, as proposed by Wang et al.²⁰, was used to quantify the O*-amount in the samples. Quantitative trends were compared to OER-performance indicators in order to identify OER-relevant features such as stable precursor species for the active site in OER. The identification of these OER-relevant structural features controlled by the synthetic parameters of our microwave-supported hydrothermal synthesis paves the way towards the design of targeted synthesis pathways of efficient OER-catalyst precursors for industrially relevant applications.

4.3. Experimental

4.3.1. TEM of beam sensitive samples

We used an aberration corrected TITAN 80-300 operated at 80kV. The sample was prepared for investigation by dispersing the dry powder in water followed by ultrasonication for 5 min. The dispersion was drop-casted between two graphene/quantifoil grids, left to dry and inserted into the microscope.

4.3.2. Synchrotron-base X-ray Photoemission and absorption spectroscopy

XPS and NEXAFS measurements were performed at the ISSS beamline at BESSYII/HZB (Berlin, Germany).²¹ The powders were pressed into self-supporting wafers (40 mg, 3 t, $\varnothing = 8$ mm) and subsequently measured in UHV ($\sim 10^{-6}$ Pa). The binding energy calibration was carried out after an evaluation of each corresponding Fermi edge. In NEXAFS, the photon energy was continuously scaled between 525 eV and 560 eV by moving the monochromator. The total electron yield (TEY) of the O K-edge was collected via a Faraday cup that had an accelerating voltage applied. The XPS spectra were fitted after subtraction of a Shirley background with the commercially available CasaXPS software (www.casaxps.com). In all fits, the peak separation and the peak area ratios between the Ir $4f_{7/2}$ and the Ir $4f_{5/2}$ components were constrained to 3 eV and 4:3, respectively. Deviations in the peak area ratios of 5 % were allowed to account for the inaccuracies in background subtraction and peak area determination of asymmetric peaks. The employed fit parameters for rutile IrO₂ and the amorphous IrO_x are listed elsewhere.^{18,19}

4.3.3. Raman spectroscopy and DFT-calculations of Ir-structures

Raman spectroscopy was performed at 532 nm excitation wavelength using a confocal microscope setup (S&I GmbH, Warstein Germany) equipped with a PyLoN:2kBUV CCD camera and 750 mm focal length of the monochromator (Princeton Instruments). The laser intensity density on the samples was chosen low enough to exclude decomposition of the amorphous Ir-structure. At higher laser intensities, sharp peaks corresponding to rutile-modes appeared, indicating transformation of the amorphous Ir-oxohydroxide into IrO₂ due to local heating. Spectra were averaged over multiple measurements at different spots of the sample.

All calculations were performed with the ORCA package.²² Structural models of monomeric Ir(OH)₆²⁻, dimeric (OH)₂(H₂O)₂Ir(μ -O²⁻)₂Ir(OH)₂(H₂O)₂, up to pentameric units were constructed by hand and subsequently geometry optimized (B3LYP functional²³, Def2-TZVP basis set²⁴, relativistic corrections by ZORA²⁵, dispersion corrections according to Grimme et al²⁶). Calculation of Raman spectra were performed as implemented in ORCA. The cartesian coordinates of each model are provided as supporting information.

4.3.4. Electrochemical characterization

We compare our results to two Ir-benchmarks previously used in our study on the electronic structure of Ir-oxide^{18,19}: an amorphous Ir-oxohydroxide (Premion, Alfa Aesar), noted AA-IrO_x and a crystalline high-purity rutile-type IrO₂ (Sigma Aldrich) noted SA-IrO₂.

Electrode loadings were always $20 \mu\text{g}_{\text{Ir}}\cdot\text{cm}^{-2}$. The activity was assessed using linear sweep voltammetry (LSV) at a sweep rate of $5 \text{ mV}\cdot\text{s}^{-1}$ from open circuit potential (E_{oc}) to 1.8 V vs. reversible hydrogen electrode (RHE). Stability was assessed in chronopotentiometric (CP) experiments at $15 \text{ mA}\cdot\text{cm}^{-2}$ (accelerated testing conditions) or $10 \text{ mA}\cdot\text{cm}^{-2}$ as in recent benchmarking efforts^{1,27}. The samples were considered deactivated when the working electrode potential (E_{WE}) reached 1.8V vs. RHE in order to avoid oxidative damage to the glassy carbon (GC) electrode support. The corresponding graphs are reported in § 3.7.

4.3.5. CO-titration of reactive oxygen species

CO-oxidation at room temperature (RT) was used as a stoichiometric titration reaction of reactive oxygen species by exposing the Ir-samples to a 1%CO/He flow ($100 \text{ mL}\cdot\text{min}^{-1}$). 25 mg of the catalyst, diluted by 250 mg of inert SiC (particle diameter: 250–355 μm) were used. The samples were dried in He, at RT for 1h prior to experiment. The switch from inert He- to 1-%CO/He-stream (both $100 \text{ mL}\cdot\text{min}^{-1}$) was performed with the help of 6-port switching valve (Valco, Vici) that excludes dead volumes. For the reactivation test of fresh MW_5 after the first CO-treatment, He was saturated with water using a gas-tight H_2O -bubbler connected to the He-line via a bypass.

4.3.6. DRIFTS of low-temperature CO-adsorption

Diffuse reflectance infra-red Fourier Transform Spectroscopy (DRIFTS) was recorded with an MCT detector at a resolution of 4 cm^{-1} by accumulating 1024 scans, using a Praying MantisTM reaction chamber (ZnSe window) placed in a Bruker IFS 66 spectrometer controlled by OPUS software. The in-situ cell was equipped with a liquid nitrogen cooling system and connected to a vacuum pump. A background spectrum of pure KBr was performed at room temperature. MW_5 was degassed in vacuum at 40°C overnight prior to measurements. After cool-down to 77 K, CO (Westfalen, >99.99% purity) was added stepwise until a pressure of 10 mbar was reached. The sample was then left to warm-up gradually to room temperature and left in CO overnight. After evacuation in vacuum, this cycle was repeated a second time.

4.4. Results and discussion

4.4.1. OER-performance

Figure 1 summarizes indicators of OER-activity and stability used to compare the electrocatalytic performance of the MW-produced Ir-oxohydroxides. As reported in § 3, within the MW-batch, OER-performance was best for low initial KOH:Ir. The sample prepared for KOH:Ir=5:1 constitutes an optimum with best OER-performance and high synthesis yield. On the other hand, with increasing KOH:Ir \geq 7:1, performance rapidly decreases. Concomitantly, we showed using H_2 -TPR (temperature-programmed reduction), that the average oxidation state gradually increases from +3.2 for KOH:Ir=1:1 towards +3.8 for KOH:Ir=50:1. Despite similar structural features (average oxidation state, TPR-profile, chemisorbed water fingerprint), the Ir-oxohydroxide benchmark AA-IrO_x showed the worst performance, which was an incentive to search for distinctive features in our MW-produced Ir-oxohydroxides, responsible for their superior OER-performance.

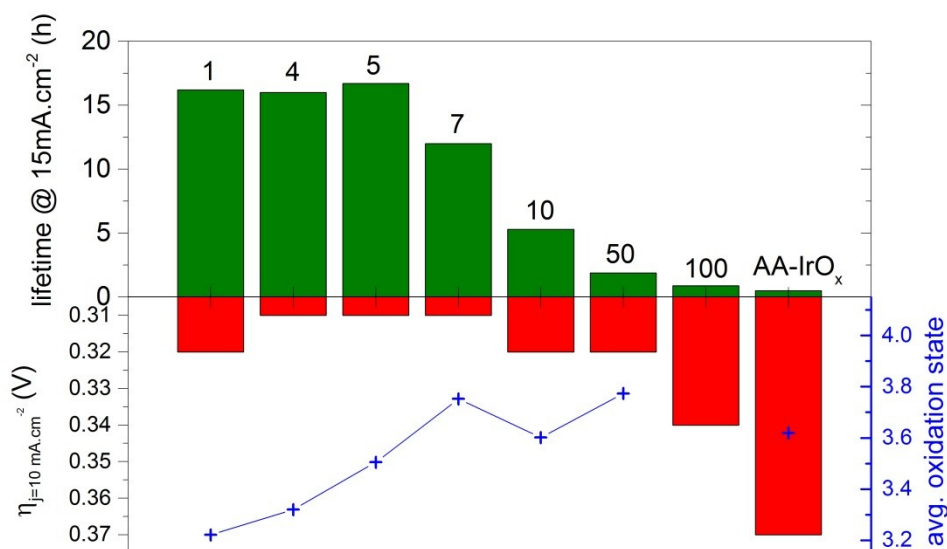


Figure 4.1 OER-activity reflected by the overpotential η needed to reach $j=10 \text{ mA}\cdot\text{cm}^{-2}$ (red bars) and OER-stability indicated by stable operation at $15 \text{ mA}\cdot\text{cm}^{-2}$ (green bars) tend to worsen for the MW-samples with increasing average oxidation state of the oxidic Ir-phase (blue crosses). Black numbers indicate X in MW_X, the initial KOH:Ir ratio.

In the following paragraphs, samples prepared via the MW-supported hydrothermal treatment are identified as “MW_X”, where X identifies the base to iridium ratio KOH:Ir=X:1 (see [ref.] and S.I. for synthesis details).

4.4.2. TEM-investigation of Ir-oxohydroxides

In § 3 devoted to the MW-supported hydrothermal synthesis of Ir-oxohydroxides, we mentioned the great difficulty of studying such compounds with electron microscopy due to the rapid transformation of the amorphous Ir-phase into metallic iridium. As a strategy to avoid radiation damage, we chose to encapsulate a MW-produced Ir-oxohydroxide between graphene sheets^{28,29}. We chose the best catalyst MW_5, which is also the purest compound produced in terms of Cl-contaminations and metallic Ir-traces (see § 3.4.2 and § 3.7). However, no significant improvement against radiation damage was observed during HRTEM imaging with electron dose rates $>10^5 \text{ e}\cdot\text{nm}^{-2}\cdot\text{s}^{-1}$. Nevertheless, structural results on the intrinsic structure of MW_5 were obtained using electron diffraction (ED) technique. By comparing an ED pattern with an electron dose rate of $80 \text{ e}\cdot\text{nm}^{-2}\cdot\text{s}^{-1}$ (Figure 4.2.a) and an ED pattern with high electron dose rate (Figure 4.2.b), *i.e.* $10^5 \text{ e}\cdot\text{nm}^{-2}\cdot\text{s}^{-1}$, it was possible to observe the structural transformation caused to the sample by electron irradiation. The diffraction patterns were analysed using a profile analysis tool PASAD.³⁰

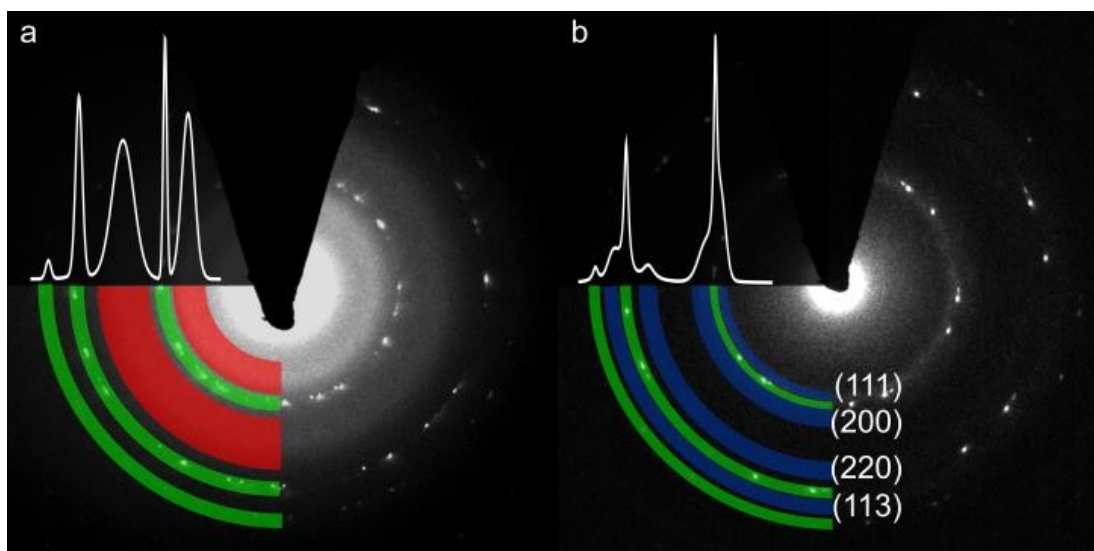


Figure 4.2 The SAED patterns and radial profiles for MW_5 (a) under low electron dose and (b) with high electron dose shows the complete transformation of the initial amorphous Ir-oxohydroxide to metallic iridium after beam irradiation.

The corresponding radial profiles and the diffraction patterns are shown in Figure 4.2. The contributions colored in green correspond to the $d=2.13$ Å and $d=1.23$ Å and $d=1.07$ Å graphene spacings. . The analysis of the recorded ED pattern exposed to an intense electron beam (Figure 4.2.b) shows intensity rings (blue arcs) that are attributed to the d -spacings of the (111)-, (200)- (220)- and (113)-planes in cubic metallic iridium (see ICSD [87-715]), confirming that most of the iridium had been reduced under the influence of the high dose beam. On the other hand, the radial profile obtained from the low dose ED pattern (Figure 4.2.a) exhibits a very distinct shape with two broad contributions at spacings corresponding to $d=2.69$ Å and $d=1.63$ Å (red arcs). We already pointed out the discrepancy of the Ir/O-stoichiometry from the 1:2-ratio expected for IrO_2 . The d -spacings observed initially for MW_5 confirm that the distribution of elements inside the amorphous Ir-oxohydroxide is very distinct from that in crystalline IrO_2 . Indeed reflections for IrO_2 would be expected at $d=3.18$ Å, 2.58 Å, 1.70 Å and 1.59 Å, which correspond respectively to the (110)-, (101)-, (211)- and (220)-planes of IrO_2 .

4.4.3. Raman-spectroscopy of Ir-oxohydroxides

We reported in § 2.4.7 that amorphous $\text{Ir}^{\text{III/IV}}$ -oxohydroxides deposited on ATO were characterized by a large Raman- signal centered around 493 cm^{-1} , that was distinct from the well-known contributions from IrO_2 -rutile, expected at 561 cm^{-1} (E_g), 752 cm^{-1} (A_{1g}) and 728 cm^{-1} (B_{2g}).³¹ The present batch of pure Ir-oxohydroxides yields the opportunity to relate changes in the recorded Raman spectra to structural variations between the samples.

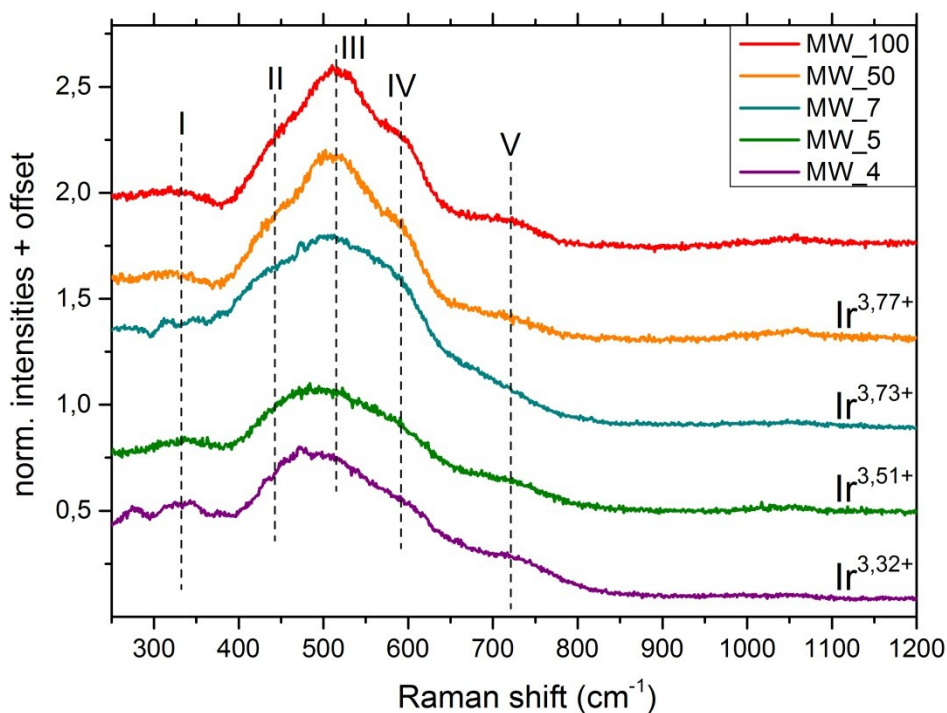


Figure 4.3 Raman-spectra of the MW-prepared Ir-oxohydroxides show distinctive features in the 300-750 cm^{-1} area. Average oxidation states indicated on the right have been calculated from H_2 -TPR.

Figure 4.3 shows the Raman spectra recorded for five MW-prepared samples. A qualitative five-component Gaussian fit was performed (see Figure S2.2) and resulted in two weak contributions at 320-340 cm^{-1} (I) and 675-720 cm^{-1} (V). Three major contributions were identified at 420-465 cm^{-1} (II), 510-520 cm^{-1} (III) and 565-600 cm^{-1} (IV). The fitting parameters show that the modes identified by component III clearly gain in importance for increasing KOH:Ir ratios, representing 22% of the integrated signal for MW_4 as compared to 64% for MW_100.

Considering that the average oxidation state determined via H_2 -TPR for the oxidic phase approaches Ir^{IV} with increasing KOH:Ir and bearing in mind the highly hydrated nature of the compounds, we chose amorphous hydrous Ir^{IV} -oligomers as a starting point to find a model structure for the synthesized compounds. Ir^{IV} -based structures have already been calculated by Hintermair et al. using Ir^{IV} -dimers with pyridyl ligands. They attributed signals observed at 560 and 730 cm^{-1} to vibrational Raman-active modes of the planar bis- μ -oxo Ir^{IV} -dimer.^{11,12} In order to model the suspected oligomeric nature of our compounds, we decided to use structures involving at least three Ir-atoms.

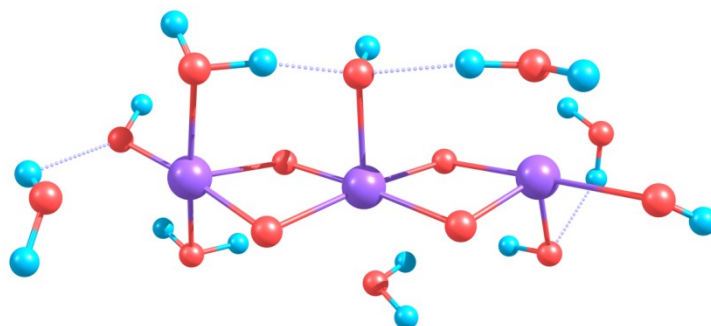


Figure 4.4 DFT-calculated structure of a bis- μ -oxo Ir^{IV} -trimer. Blue atoms are H, red atoms are O, purple atoms are Ir.

Figure 4.4 shows the optimized structure obtained via DFT for a formally Ir^{IV} -trimer involving μ -oxo-bridges, coordinated water molecules and hydroxyl terminations. The calculated Raman spectrum shows that contributions I and V correspond to vibrations mostly localized on the hydroxyl groups and surrounding water molecules, albeit with frequencies which are systematically calculated too high, as can be expected for a small trimeric unit. On the other hand, calculated Raman modes between 480 and 645 cm^{-1} , involve the bridging μ -oxo groups, giving rise to a series of concerted asymmetrical stretching, rocking and bending modes.

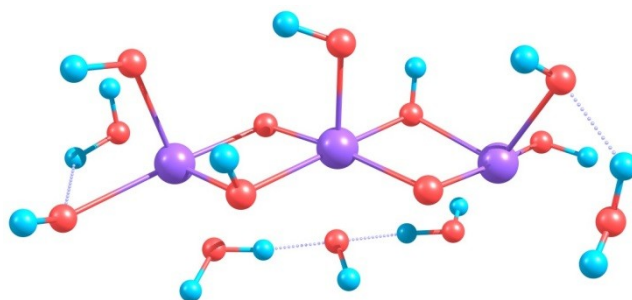


Figure 4.5 DFT-calculated structure of a reduced $\text{Ir}^{\text{III/IV}}$ -trimer. Blue atoms are H, red atoms are O, and purple atoms are Ir.

In order to model the presence of Ir^{III} -species in the Ir-oxohydroxides, the calculated trimeric Ir^{IV} -structure was reduced to a formally $\text{Ir}^{\text{IV}}\text{-Ir}^{\text{III}}\text{-Ir}^{\text{IV}}$ trimer. DFT-based optimization of the structure results in a rearrangement of protons such that two of the μ -oxo-bridging oxygens become bridging hydroxyls (see Figure 4.5).

The resulting calculated Raman-active modes do not include such concerted motions such as the rocking of all four bridging oxygens, as it is predicted at 553 cm^{-1} for the Ir^{IV} -trimer. In general, the incorporation of Ir^{III} -species diminishes the number of concerted Raman-active vibrations of the bridging oxygen species, which could explain the lower intensity of the modes contributing to component III. The spectrum is dominated by μ -oxo vibrations. These vibrations are more localized than the ones of the oxidized trimer and therefore shifted to higher frequencies as compared to those of the oxidized trimer. The dominating Raman-active modes are shown in S.I. (Figure S4.3 and Figure S4.4). The spontaneous protonation of two oxo bridges upon reduction of the trimeric cluster *in silico* indicates that Ir^{III} may disrupt the bis($\mu\text{-O}^{2-}$) bridging motif, which in turn may lead to an increased amorphicity and concomitant decrease of intensity of the oxo-related modes in the Raman spectrum (see Figure S4.5).

4.4.4. X-ray photoemission spectroscopy

Our report on the synthesis of the present batch of pure Ir-oxohydroxides in § 3 highlighted the low-temperature reduction features of the compounds and suggested a mixed Ir^{III/IV}-oxidation state. Observed trends in average oxidation state seemed to indicate that OER-performance improved for lower Ir^{IV}:Ir^{III}-ratios (see Figure 4.1).

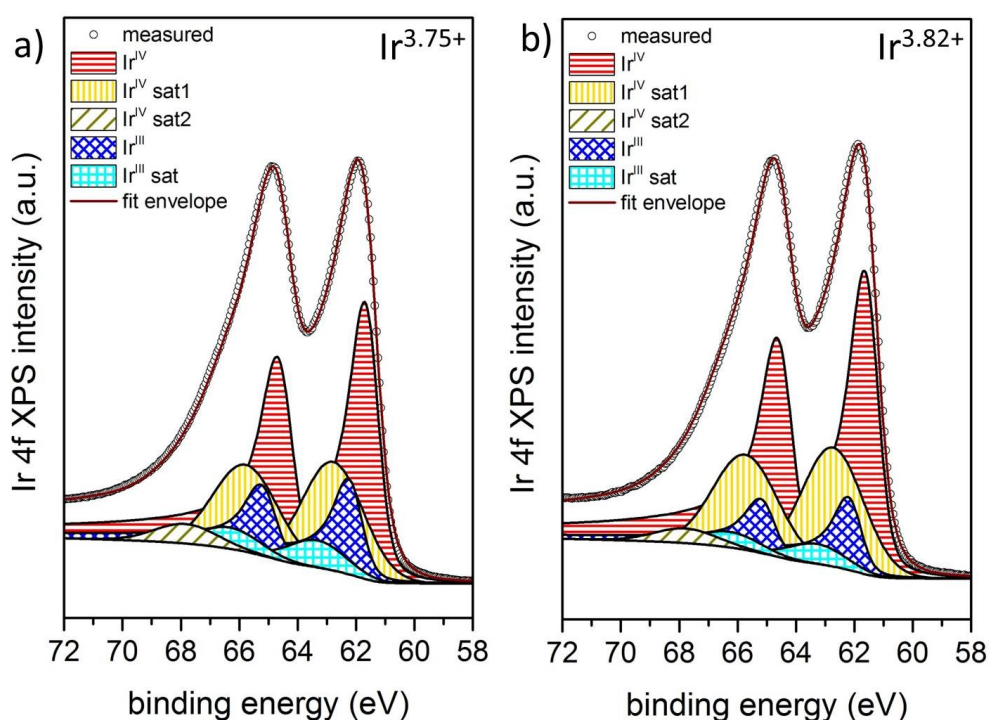


Figure 4.6 XPS-spectra of (a) MW_5 and (b) MW_100 in the Ir4f-region for 450 eV excitation energy show the contributions from Ir^{III}- and Ir^{IV}-species. The average oxidation state calculated from the fit is indicated in the top right corner.

In order to confirm the Ir^{III/IV}-nature of the compounds, XPS measurements were performed on MW_5, MW_10, MW_50 and MW_100. First of all, the high electronic density measured at the Fermi edge for all samples is in line with what has been observed by Reier et al.¹⁰ and confirms the metallic conductivity of the amorphous Ir-phase (see Figure S4.6). Furthermore, the analysis of the Ir 4f-lineshape confirms that the samples are in a mixed Ir^{III/IV}-state, with a general trend towards higher Ir^{IV}:Ir^{III}-ratios for higher KOH:Ir (see Figure 4.6). The presence of metallic Ir in the surface region can be excluded as no contribution at 60.9 eV is detected (Figure 4.6 and Figure S4.7).^{18,32} This is in line with the core-shell structure observed in SEM-EDX for higher KOH:Ir, which showed a metallic Ir⁰-core embedded in a thick oxidic overlayer (see § 3.3.2). According to our fit model described in the introduction, Ir^{III}-species contribute with an Ir 4f_{7/2}-binding energy of 62.4 eV, while Ir^{IV}-species are found at a lower binding energy of 61.8 eV. Ir 4f-peaks recorded at 130 and 450 eV kinetic energy of the photoelectrons and fitted using our model, show a similar picture (see Figure S4.7), indicating that Ir^{III}-species are not only present at the surface but also deeper inside the bulk. This finding in turn is in line with the large fraction of Ir^{III}-species suggested by the average oxidation

state determined from H₂-TPR (see Figure 4.1) and suggests a homogenous distribution of Ir^{III}- and Ir^{IV}-species throughout the oxidic Ir-phase. The concomitant decrease in OER-performance and Ir^{III}:Ir^{IV}-ratio observed with increasing KOH:Ir indicates the relevance of Ir^{III}-species for the OER-performance. This suggestion is in line with the noxious effect of thermally induced oxidation of ATO-supported Ir^{III/IV}-oxohydroxide towards Ir^{IV} as it was observed for MW-Ir/ATO treated at 350°C (see § 2.4.7 and § 2.4.8). It is important to highlight our finding of a possible link between Ir^{III}-species and OER-performance. The unambiguous description of the electronic structure of active Ir-based OER-catalysts has remained a challenge so far despite a few studies highlighting the possible role of mixed Ir-oxidation states.¹⁶

4.4.5. X-ray absorption spectroscopy

Recent studies, such as the one conducted by Fierro et al. have highlighted that part of the oxygen evolved during Ir-catalyzed OER originates from the Ir-oxide itself.³³ This means that oxygen species from the Ir-lattice are involved in the catalytic process. Hence, in addition to investigating active metal centers, the description of O-species present in the surface region is of prime importance in understanding OER-reactivity. For this purpose Reier et al. have analyzed the O 1s spectra of their mixed Ni/Ir-electrocatalysts before and after reaction and found a possible link between OER-reactivity and the coverage with reactive surface hydroxyl groups.³⁴ We generally observed a higher XPS intensity at approx. 531.1 eV binding energy for the more active samples (see Figure S4.7), which compares to the contribution at 531.4 eV attributed by Reier et al. to reactive surface hydroxyls. However an unambiguous deconvolution of the O 1s peak is rendered difficult by the manifold contributions to the O 1s spectra from water, hydroxyl groups as well as lattice-oxygen and other possible O-involving functional groups to the O 1s spectra. For this reason we decided to probe the density of unoccupied O 2p states by NEXAFS at the O K-edge. Using this technique, we observed characteristic features in the O K-edge of Ir-oxohydroxides. Based on theoretical calculations, we could assign these features to electronic defects in the anionic framework.^{18,19}

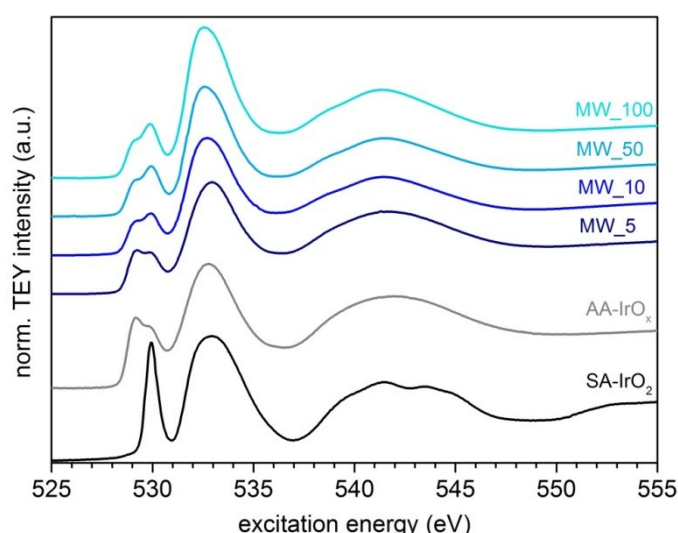


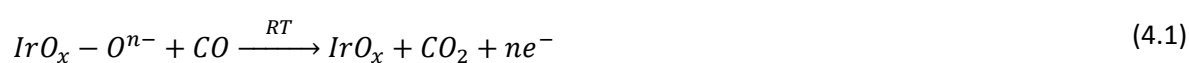
Figure 4.7 NEXAFS-spectra observed for MW-prepared Ir^{III/IV}-oxohydroxides as well as reference samples SA-IrO₂ and AA-IrO_x.

Figure 4.7 shows the NEXAFS-spectra of the MW-produced Ir-oxohydroxides, as well as the reference samples AA-IrO_x and SA-IrO₂. The main resonances of the rutile-type reference sample SA-

IrO₂ are found at excitation energies of 530 and 533 eV. The pre-edge feature observed in AA-IrO_x at 529 eV was attributed in our earlier study to O 2p hole states additionally present in the Ir-oxohydroxide reference sample AA-IrO_x.^{18,19} The smoothening of the NEXAFS spectrum of the AA-IrO_x when compared to SA-IrO₂ between 537 eV and 545 eV is attributed to the chemisorbed and physisorbed water present in the oxohydroxide. The O⁻ species present in the AA-IrO_x, as electrophilic oxygen are likely to play a key role for the OER-reactivity, explaining the vast predominance of AA-IrO_x when compared to SA-IrO₂ in terms of OER-performance. Furthermore the model established a direct link between the presence of such O⁻-species and Ir^{III}.¹⁹ A comparison of the O K-edge spectra of the MW-produced Ir-oxohydroxides from the present study shows that the ratio of the 529 eV and 530 eV features continuously changes with increasing KOH:Ir ratio, with MW_5 exhibiting the strongest 529 eV resonance and thus the highest amount of suspected formally O⁻ species. As a result, we suggest a direct link between a higher amount of Ir^{III}-stabilized O⁻ species and improved OER-performance for our batch of MW-produced Ir-oxohydroxides. The suspected OER-reactivity of these peculiar O-species and the fact that their chemical environment seems to stabilize them in the ex-situ catalyst takes us a step closer in the understanding of why the produced Ir^{III/IV}-oxohydroxides are such excellent precursors for OER-electrocatalysis. Nonetheless AA-IrO_x also exhibits a strong feature at 529 eV excitation energy, despite having the worst OER-performance. This proves that the trend observed within the MW-sample batch can't be taken as an absolute indicator of OER-performance and that other factors must play a key role.

4.4.6. CO-titration of reactive oxygen species.

Low-temperature oxidation of CO is commonly used as a prototypical reaction for the study of heterogeneous catalyst systems.³⁵ Typical systems consist of noble metal nanoparticles such as Pd³⁵, Pt³⁶ or Ir³⁷ supported on partially reducible oxides. The noble metal is usually described as a preferential adsorption site for CO, while the oxide support is thought to gather activated O₂ from the feed for the oxidation of CO to CO₂. In absence of O₂ in the feed, reactive oxygen pools in the catalyst can come into play. Recently, Lin et al. described the preferential oxidation of CO (PROX) on a Ir/Fe(OH)_x-system.³⁷ They showed that CO reacted with OH-species adsorbed on the Fe-support with much lower activation energies than with adsorbed O₂, such that complete CO oxidation was observed at room temperature. In a similar approach, Wang et al. used such CO-titration at room temperature to quantify reactive oxygen species (designated by O*) in Co₃O₄ catalysts, identified as O₂⁻ and O⁻ using O₂-TPD.²⁰ Inspired by these results, we calculated the reactivity of our suspected O⁻-species with CO and could show that such species could react with CO at RT.³⁸ Hence, in order to obtain a quantitative insight into the O*-amount in our samples, including the suspected O⁻-species, we decided to investigate the reactivity of our batch of pure Ir-oxohydroxides under a 1%-CO/He-flow at room temperature. Detected CO₂ is assigned to the CO-titration of reactive Oⁿ⁻-species designated by O* present in the Ir-matrix designated by IrO_x via the redox reaction (4.1).



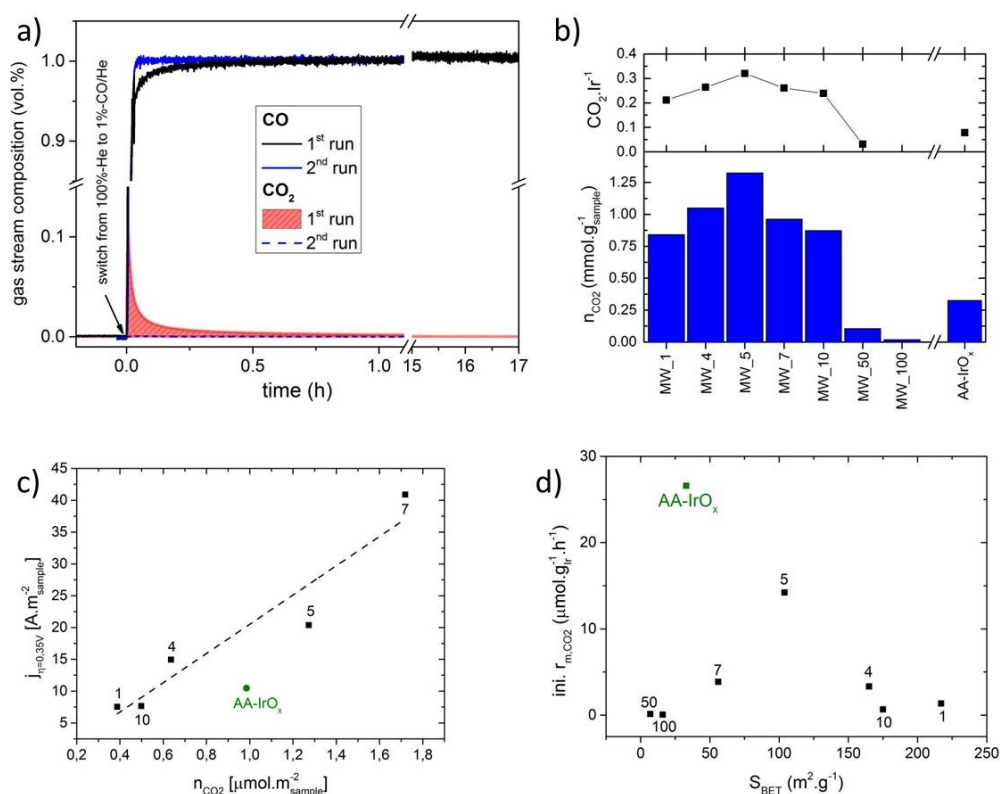


Figure 4.8 A CO-feed in inert gas was used to titrate O*. Numbers correspond to the KOH:Ir-ratio X identifying the samples MW_X. (a) Gas detected for MW_5 during two subsequent switches from pure He to 1%CO/He. (b) Total amount of evolved CO₂ (blue bars) and CO₂:Ir-ratio (black dots). (c) The Ir-specific OER mass activity at $\eta=0,35V$ is shown as a function of the total amount of evolved CO₂. (d) Initial CO₂-evolution rates plotted against the specific surface area.

Figure 4.8.a) shows the gas stream composition when testing our best OER-catalyst MW_5. During the initial switch from 100%-He to 1%-CO/He (100 mL.min⁻¹), a clear transient CO₂-signal was observed, indicating that CO was oxidized from a finite oxygen-source originating from the Ir-oxohydroxide. Once no more CO₂-evolution was detected, the reactor was purged with He and the sample was again subjected to a 1%-CO/He-stream. During this second titration, no CO₂-evolution was detected (dotted lines in Figure 4.8.a). The procedure was repeated for every compound (see Figure S4.9). For each sample we confirmed the irreversible nature of the reaction observed as a transient CO₂-evolution during the initial switch to 1%-CO/He. The AA-IrO_x reference compound, which consists of a similar Ir^{III/IV}-oxohydroxide material^{18,19} also produced CO₂ under the same conditions. Only the crystalline SA-IrO₂ showed no CO₂-evolution during CO-titration (Figure S4.9). We conclude that CO-oxidation at room temperature in inert carrier gas is specific to Ir^{III/IV}-oxohydroxide compounds and allows for the titration of O* present in these compounds.

In order to verify whether the O*-pool could be replenished, MW_5 was subjected in a separate experiment to a water-saturated He stream for 1h at room temperature after the first CO-titration. During a subsequent switch to 1%-CO/He no sign of a second CO₂-evolution could be detected. This shows that the O*-source couldn't be regenerated via H₂O at RT, unlike the reactive hydroxyl groups evidenced by Li et al. for PROX on the Ir/Fe(OH)_x-system.³⁷ In a similar experiment we showed that O* could neither be replenished in a 1%-O₂/He stream at room temperature.

The quantification of the total amount of CO₂ evolved for each sample (Figure 4.8.b) shows that up to 0.32 CO₂ are evolved per Ir in the case of MW_5 (see Figure 4.8.b). This shows that the titration of O* is not limited to the surface and involves O* located deeper in the bulk. Over 0.2 CO₂ are produced per Ir for the samples synthesized for 1:1 ≤ KOH:Ir ≤ 10:1. This high ratio indicates that for these samples O*-species probably migrate to the surface during the CO-titration. A sharp decrease in total evolved CO₂ is observed for samples MW_50 and MW_100, as well as AA-IrO_x, indicating that in these three samples less O* were accessible to CO. A decreasing O*-amount with increasing KOH:Ir would be in line with the same trend in the O⁻-amount evidenced via NEXAFS. However NEXAFS also showed that AA-IrO_x contained amounts of O⁻ comparable to MW_5. Since the CO-titration can involve bulk-O*, we conclude that the observed trends in evolved CO₂ also reflect to an important extent the ability of sub-surface O* to migrate to the sample surface to react with CO.

In order to study the OER-relevance of the evidenced O*-species, the Ir-specific OER mass activity of the samples was compared to the amount of titrated O*-species. Figure 4.8.c exhibits a loose linear trend for the MW-compounds, where the best OER-catalysts also contained the highest amount of O*-species, whereas the samples produced at higher KOH:Ir evolved only little CO₂. This suggests that the titrated O*-species are involved in the good OER-performance of the MW-produced Ir-oxohydroxides. As a result, the CO-titrated amount of O* could act as an indicator of the OER-performance of our samples. The comparison of our samples to the AA-IrO_x benchmark however suggests that the OER-performance involves a more complex set of parameters. The AA-IrO_x has been described previously as an Ir^{III/IV}-oxohydroxide close in nature to our compounds.^{18,19} Also the benchmark evolved a significantly higher amount of CO₂ than MW_50 and MW_100, which suggests that it contains more accessible O*. Nonetheless it is by far the sample with the worst OER-performance (see Figure 4.1 and Figure 4.8.c). This shows that isolated descriptors such as the amount of accessible O* present in the sample should only be used in relation to a batch of samples prepared under the same conditions, such as the MW-prepared Ir-oxohydroxides.

A closer look at the CO₂-evolution curves shown in Figure S4.9 shows that CO₂-evolution for AA-IrO_x was initially very fast but levelled off rapidly after one hour, whereas the MW-produced Ir-oxohydroxides kept evolving CO₂ for hours. This indicates different reactivities of the O*-species in the Ir-oxohydroxides and the AA-IrO_x-benchmark. In this regard, the initial CO₂-evolution rate can be a useful descriptor as it yields information on the reactivity of O*-species located on the surface. Figure 4.8.d) depicts the initial Ir-mass-specific CO₂-evolution rate for the MW-compounds as a function of specific surface area (S_{BET}). Assuming that the initial rate reflects only the titration of surface species, one would expect a linear increase with S_{BET}. Instead, the result is a volcano type plot showing the prominent nature of MW_5 as it exhibits the highest CO₂-evolution rate of the MW-compounds. On the other hand MW_4 exhibits a significantly lower initial rate, despite similar OER-performance. This speaks against a dependency of OER-performance solely on the reactivity of surface O*-species.

The observed differences in initial evolution rates and total amount of evolved lead us to suggest the following scenario: Surface-O*-species present in AA-IrO_x exhibit a higher reactivity towards CO than in the MW-compounds. However, the rapid arrival in the plateau region suggests that once surface O*-species have been consumed, O*-species located deeper in the bulk do not participate in the reaction to the same extent as in the MW-compounds. The compact morphology of AA-IrO_x, highlighted elsewhere via SEM,^{18,19} might play a major role in hindering the facile migration of O*-

species to the surface during CO-titration. Similarly, MW_50 and MW_100 also exhibit such a compact spheric structure, which would explain the difficult O*-exchange.

These observations clearly indicate that a complex set of parameters governs the O*-titration mechanism. The ability of O* located in the bulk to migrate to the surface seems to play a key role. The O*-environment is thus probably highly involved in this process, namely hydroxyl groups such as those highlighted by Reier et al. as possible descriptors of OER-reactivity.³⁴ The link observed between the O*-amount and OER-performance for the MW-compounds, indicates that this method allows for a quantitative estimation of OER-relevant O*-species. The comparison with AA-IrOx however highlights the need to use additional descriptors for predictions on OER-performance, such as the capacity of the samples for exchange between surface and sub-surface O*-species. In a scenario where lattice-O is involved in the Ir-catalyzed OER, as suggested by Fierro et al.³³, such exchange mechanisms might play an essential role in OER-reactivity and explain the superior performance of the MW-produced compounds in comparison with AA-IrO_x. This also suggests a three-dimensional aspect of OER-catalysis in Ir-oxohydroxides, where sub-surface O*-species take part in the catalytic OER.

4.4.7. Low-temperature CO-adsorption

In order to identify species and adsorbate structures involved in the oxidation of CO on Ir-oxohydroxide, the low-temperature adsorption of CO and subsequent oxidation to CO₂ at higher temperatures were studied in-situ via diffuse reflectance infrared spectroscopy (DRIFTS). A major challenge when using infrared spectroscopy on iridium oxide samples are the optical properties of such compounds. IrO₂ exhibits quasi-metallic properties and acts as a reflector for frequencies below its plasma frequency located in the near-IR region.³⁹ As a result the reflectance of Ir-oxide samples strongly increases for smaller wavenumbers, inhibiting the detection of diffusely scattered light. On the opposite, at higher frequencies the samples strongly absorb, which results in a non-linear background and noisy spectra. Only a small number of studies describing the IR-spectrum of IrO₂ or amorphous Ir-oxide films can be found in the literature.^{40,41}

The study was performed on the best OER-catalyst MW_5. After degassing of physisorbed water, the sample is mostly characterized by broad IR-bands in the 3700-2800 cm⁻¹-region (see Figure S4.10). The contribution at 3700-3450 cm⁻¹ is attributed to isolated OH-groups, while the broad contribution at 3450-3000 cm⁻¹ can be identified as the stretching frequencies of H-bonded hydroxyl groups. These might be located on the surface but also deeper in the structure. Indeed exclusive surface hydroxylation wouldn't explain the high fraction of chemisorbed water detected in TGMS (see § 3.4.2). Also the calculated Ir^{III/IV}-trimers showed that hydroxyl groups appear in place of the μ -oxo-bridging species as a result of the reduction of Ir^{IV} to Ir^{III}. Contributions at 3000-2800 cm⁻¹ were attributed by other authors to H-bonded hydroxyls.⁴⁰ This is however unlikely at such low wavenumbers and one should rather consider C-contamination from the atmosphere. Due to their highly hydrous and hydroxylated surface, the Ir-oxohydroxides are probably prone to adsorbing atmospheric contamination. No change in this contribution was however observed during the experiment and the effect of these C-contaminations was thus neglected.

The stepwise CO-adsorption was performed at liquid nitrogen temperature in order to inhibit reactive mechanisms. During the stepwise addition to P_{eq,CO}=10mbar, only minor changes could be

observed in the DRIFTS-spectra in the 2000-2150 cm^{-1} region where the CO-vibration is expected (see Figure S4.11). The absence of a strong signal indicates that no stable Ir-CO complex was formed at low temperature. Weak adsorption is to be expected as iridium is in an $\text{Ir}^{\text{III/IV}}$ -state. CO-adsorption studies have been performed mostly on metallic Ir-samples⁴²⁻⁴⁴ or isolated Ir^{III} -sites^{45,46}. On metallic Ir, it appears that atop-bonding of CO predominates and is characterized by a large frequency upshift of the adsorbed-CO-vibration from approx. 2010 cm^{-1} to 2093 cm^{-1} with increasing coverage due to intermolecular coupling.⁴³ Adsorption of CO on Ir^{3+} is thought not to be stable and was only reported through a reactive process forming Ir^{I} -carbonyl complexes at higher temperatures.⁴⁵ The CO-induced oxidation of Ir^0 to Ir^{I} has also been evoked to explain the formation of $\text{Ir}^{\text{I}}(\text{CO})_2$ -complexes in supported Ir^0 -compounds.⁴⁷ No IR-signals of CO-adsorbates on Ir^{IV} was reported so far to the best of our knowledge. At liquid nitrogen temperature no significant IR-evidence of CO-adsorption on Ir-oxohydroxide is thus to be expected.

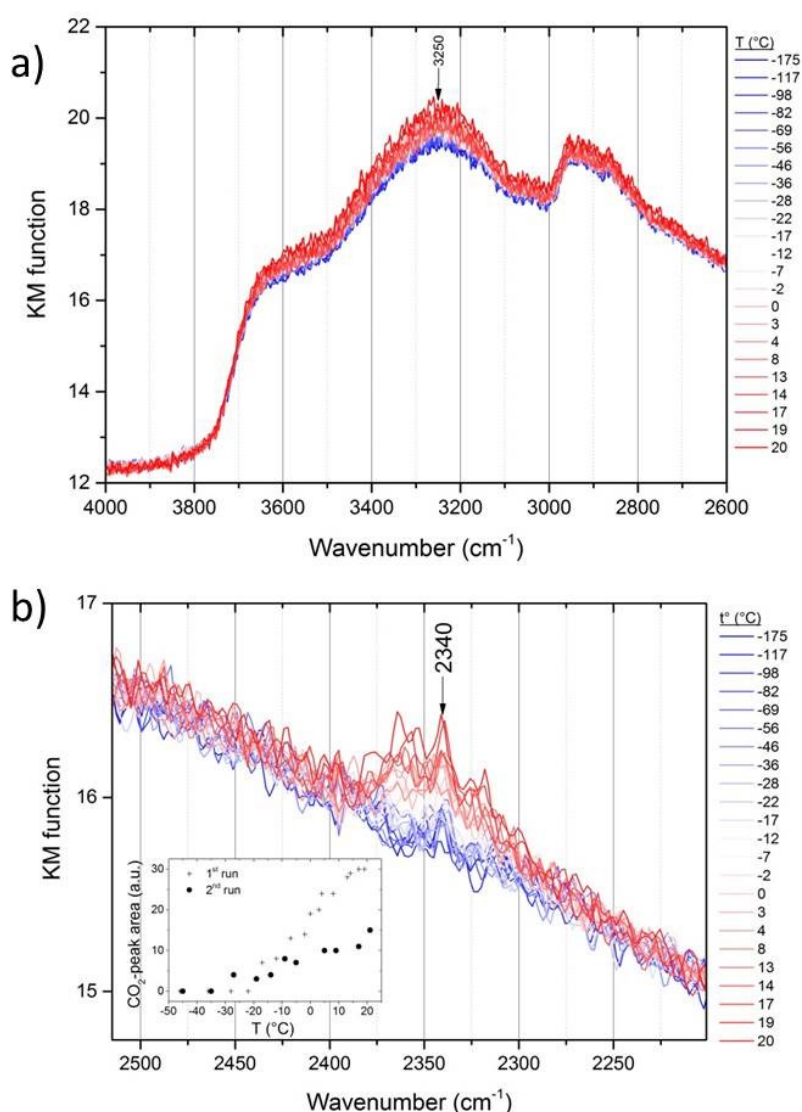


Figure 4.9 DRIFTS spectra of MW_5 under 10 mbar CO during the warm-up procedure from liquid-nitrogen- to room-temperature (a) in the OH-region and (b) in the CO_2 -region. The inset in (b) shows the approx. area under the CO_2 -related peak as a function of temperature during the first experiment and during its repetition with the same sample.

After low-temperature CO-addition, the sample was allowed to warm-up gradually to room temperature. As expected, the pressure measured inside the in-situ cell increased with temperature but levelled off at -50°C and started dropping, (see Figure S4.12). This indicates that CO was being removed from the gas phase. Enlarged areas of the spectra recorded during the warm-up procedure show the appearance of a sharp feature at 2340cm⁻¹ around -30°C (Figure 4.9.b)). Such a signal corresponds to adsorbed CO₂ and explains why the pressure drops as CO is not directly replaced with CO₂ in the gas phase. The asymmetric stretching of gas phase CO₂ only shows up at higher temperatures as a broad feature centered around 2350cm⁻¹. Additional sharper features in the 2380-2320 cm⁻¹ probably correspond to other CO₂-adsorption configurations. The early onset at -30°C indicates low activation barriers for the CO-oxidation mechanism, which is in line with the calculations reported earlier for the reaction of O¹⁻ with CO.³⁸ Concomitantly a general increase in the intensity of the broad OH-feature centered around 3250 cm⁻¹ could be observed (see Figure 4.9.a). We suggest that water present in the bulk is slowly migrating to the surface with increasing temperature and forming more H-bonds.

After degassing overnight, the CO-adsorption at room temperature was repeated. The inset in Figure 4.9.b) shows that the second CO-addition cycle also resulted in CO₂-evolution at the same onset temperature of approx. -30°C, however with much lower intensity, indicating the irreversibility of the reaction.

4.4.8. CO-titrated O-species and link with OER-performance

In order to study the effect of the CO-treatment on the sample structure, MW_5 was placed inside an air-tight cell designed for in-situ Raman studies that could be connected to the CO-reactor setup described earlier. Raman-spectra of MW_5 taken before and after CO-treatment (see Figure S4.14) showed no significant change in the broad features attributed to the oxo-bridged Ir^{III/IV}-oxohydroxide structure. This indicates that the majority of μ -oxo-bridging O-species giving rise to the Raman signals are not involved in the CO-oxidation. It remains that if the CO-titration is indeed limited to the surface, changes might not be visible as the measurements are not surface-sensitive.

However, Figure 4.10 shows that the CO-treatment had a dramatic effect on OER-performance of MW_5. In terms of OER-activity (Figure 4.10.a)), the CO-treatment resulted in a loss of approx. 47% if one considers the indicator $j_{\eta=0,35V}$. Stability during CP at 10 mA.cm⁻² also significantly decreased after the CO-treatment as significantly higher potentials had to be reached in an earlier stage in order to maintain the anodic current. This clear effect of CO-treatment on OER-performance confirms that the O*-species titrated in the CO-experiment play an important role for the OER-performance of the Ir-oxohydroxide.

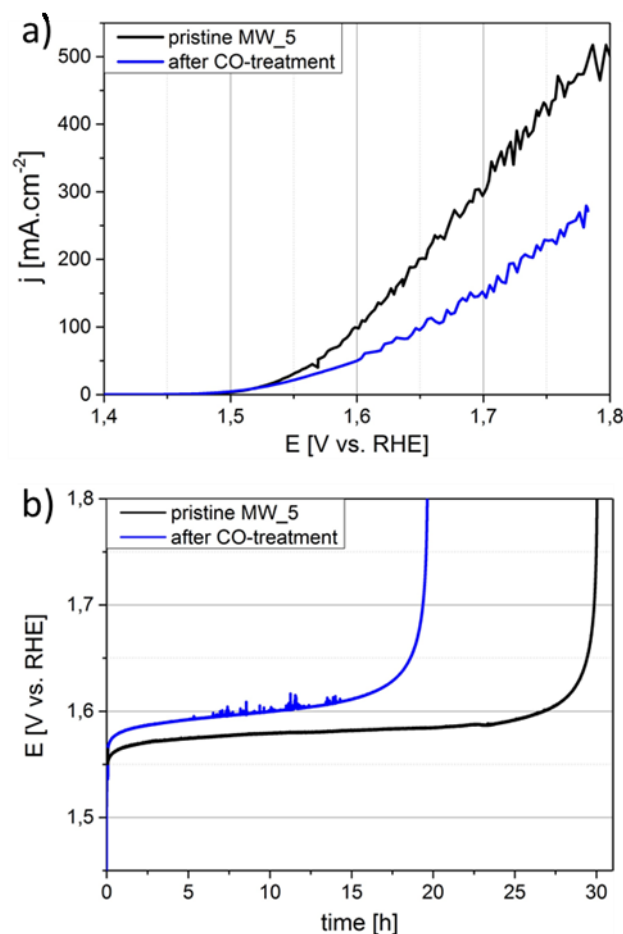


Figure 4.10 CO-treated MW_5 was tested (a) for OER-activity using LSV and (b) for OER-stability using CP and compared to pristine MW_5 for electrode loadings of $20\mu\text{g}_{\text{Ir}}\cdot\text{cm}^{-2}$.

We report elsewhere on a synchrotron-based quasi in-situ study of CO-oxidation on AA-IrO_x.³⁸ The Ir-oxohydroxide reference compound was exposed to CO in a NAP-XPS reactor. As in the RT-experiment discussed in the previous paragraph, CO₂ evolution was detected upon dosing pure CO. No changes in the Ir 4f-XPS signal could be detected. However a diminution of the NEXAFS pre-edge signal of the O¹⁻-species at 529 eV indicates that these ROS are consumed when oxidizing CO to CO₂. We conclude that the O¹⁻-species detected by NEXAFS are identical with the O*-species titrated in the RT-CO-experiment. The changes in OER-performance of MW_5 before and after CO-titration confirm that the O¹⁻-species stabilized in the particular hydrous Ir^{III/IV}-environment of the Ir-oxohydroxide is deeply involved in the structure of the precursor to the catalytically active OER-sites. We attribute the fact that the sample still exhibits OER-reactivity to the electrode preparation process, which involves sonication and thus exposes new sites that hadn't been reached by CO before. Moreover at OER-potentials some of the active sites are probably regenerated, just as in the classical activation procedure for iridium films. The CO-titration however lead to irreversible damage of the active sites, suggesting that not only the O¹⁻-species was consumed. More surface-sensitive methods like surface enhanced Raman spectroscopy (SERS) might give access to additional changes caused by the CO-titration and help in the identification of other crucial structural features of the active site precursors.

4.5. Conclusion

Our results confirm the prominent role of the so far little studied class of Ir^{III/IV}-oxohydroxides in OER-catalysis. Better insight into the compound structure was given by careful TEM-analysis, which confirmed that the amorphous oxohydroxide phase is distinct from crystalline IrO₂. Trends observed in the Raman spectra were linked to decreasing Ir^{III}:Ir^{IV} determined by the increasing base:Ir. For this purpose, the amorphous compounds were modelled as trimeric Ir-structures calculated via DFT. We showed that for the Ir^{IV}-richer compounds, a μ -oxo-bridged Ir^{IV}-trimer explains the observed Raman spectra. Once Ir^{III}-species are incorporated in such a structure, concerted vibrational modes involving the μ -oxo-bridges disappear, which explains the missing contributions in the spectra of the Ir^{III}-richer samples. We used the previously developed DFT-based model^{18,19} to analyze the XPS- and NEXAFS-spectra of several samples and could show that the Ir^{III}-rich samples accommodate a higher amount of stable formally O⁻-species. These species were quantitatively estimated in a reactive CO-titration experiment. Correlating trends in O⁻-concentration and OER-performance lead us to the conclusion that the O⁻-species stabilized in a highly hydrated, Ir^{III}-rich environment act as precursor sites for the OER-catalysis. The CO-titration experiment also showed the involvement of sub-surface O⁻-species. This highlights the OER-relevance of O⁻-mobility inside the catalyst structure. Our findings are in line with the results of Fierro et al. showing that oxygen species from Ir-oxide-catalysts participate in the oxidation of water and suggests that the particularly good OER-performance of our Ir-oxohydroxides might be linked to an OER mechanism involving lattice-O⁻-species instead of only surface-adsorbed intermediates. A similar potential-dependent mechanism involving oxygen from the catalyst has been suggested by Diaz-Morales et al. for OER on Au.⁴⁸ The OER involves the stepwise oxidation of oxygen from O^{II}, to O⁻ and finally O. Theoretical studies have highlighted the scaling relationship between the different reaction steps and emphasized the need to find an optimum for the binding energies of the different reaction intermediates.^{49,50} We suggest that the O⁻-species present in the particular configuration of the amorphous, highly hydrated Ir^{III/IV}-oxohydroxide give access to such an optimum. It remains to clarify how exactly the O⁻ participates in the OER-mechanism and most importantly how the immediate environment influences its reactivity. However, the differences observed between our compounds and the AA-IrOx benchmark, show the importance of O⁻-mobility and suggest that the three-dimensional structure of the Ir-oxohydroxide is an important aspect of OER-catalysis. As a conclusion the identification of the OER-relevant O⁻-species stabilized in Ir^{III/IV}-oxohydroxide is a significant advances in the design of a more targeted approach to finding an optimal OER-catalyst. The described fingerprints will help to identify mechanistic features in future in-situ NAP-XPS/XAS studies. The proposed hydrothermal synthesis of Ir^{III/IV}-oxohydroxides is a powerful tool for the targeted design of outstanding OER-catalysts suitable for commercial applications.

4.6. Acknowledgements

This work was supported by the German Bundesministerium für Wirtschaft und Energie as part of the Ekolyzer project. We thank the HZB for the allocation of beamtime at the Bessy II synchrotron

radiation source. Our special thanks go to Detre Teschner and Andrey Tarasov for their thorough proofreading of the present work and fruitful scientific discussions.

4.7. Supporting information

Electrochemical testing

The tests were conducted in a standard three-compartment glass cell containing approx. 100mL of H_2SO_4 (0.5 mol.L^{-1}). The reference electrode was a saturated calomel electrode (SCE) at +0,241V vs. standard hydrogen electrode (SHE), the counter-electrode was a platinized wire. The samples were deposited on the anode (rotating disk electrode, RDE, Pine Research Instrumentation) using catalyst inks dried for 30min at 60°C . The inks were prepared by suspending 4mg of sample in 6 mL Milli-Q H_2O and 4 mL isopropanol (Sigma Aldrich), followed by sonication for 30min. Prior to use, the RDE was repeatedly cleaned with Milli-Q water and isopropanol, after mirror-polishing with alumina bead slurries (Buehler, $1 \mu\text{m}$ and $0,05 \mu\text{m}$). Measurements were carried out with a VSP-multichannel potentiostat (Biologic Instruments) and were corrected at 85% for ohmic drop using high-frequency impedance determination of the electrolyte resistance (4 measurements, 100kHz, 20mV amplitude, open circuit potential).

Transmission Electron Microscopy

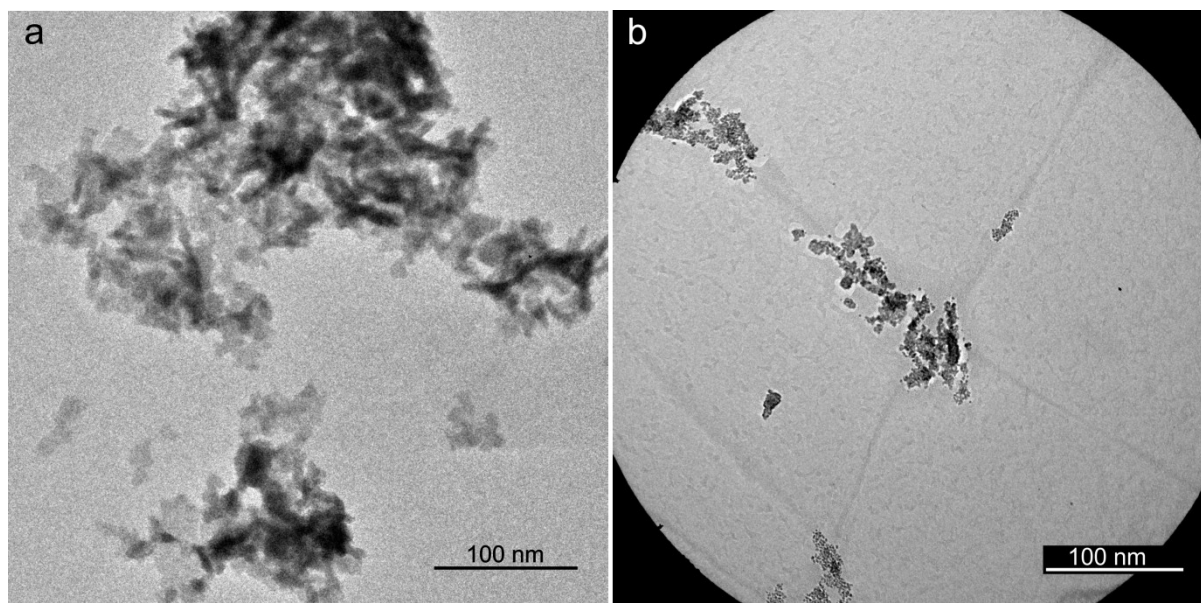


Figure S4.1 (a) Image of sample area obtained after SAED pattern (Figure 4.1.a) and (b) sample area before SAED pattern (Figure 4.1.b).

Raman spectroscopy

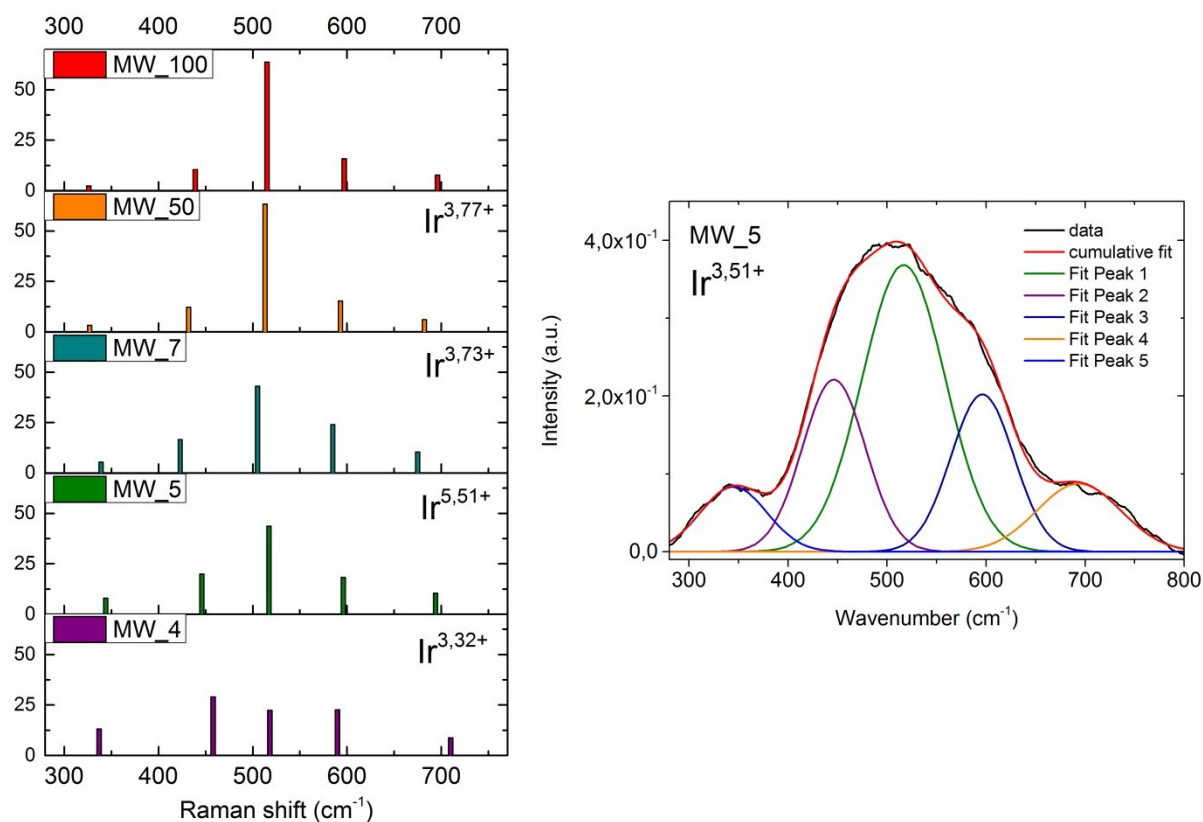


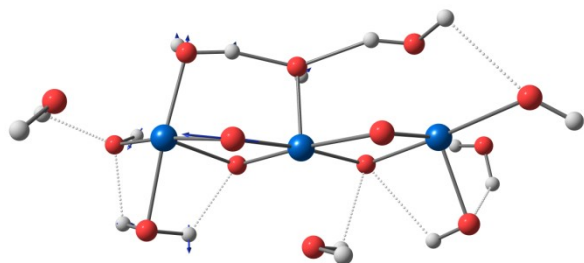
Figure S4.2 shows the relative peak areas and positions of the five Gaussian peaks used to tentatively fit the Raman data recorded for MW_4, MW_5, MW_7, MW_50 and MW_100 (left). The resulting fit for MW_5 is shown on the right as an example.

Table S4.1 List of parameters for peaks I-V after fitting.

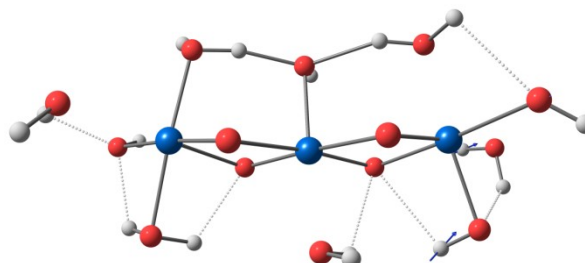
Sample	Peak I		Peak II		Peak III		Peak IV		Peak V	
	Center (cm ⁻¹)	Area (%)	Center (cm ⁻¹)	Area (%)	Center (cm ⁻¹)	Area (%)	Center (cm ⁻¹)	Area (%)	Center (cm ⁻¹)	Area (%)
MW_4	337	13	458	29	518	22	590	23	710	9
MW_5	344	8	446	20	517	44	596	18	694	10
MW_7	339	5	423	17	505	43	585	24	675	10
MW_50	327	3	432	12	513	63	593	15	682	6
MW_100	326	2	439	10	515	64	597	16	696	8

Calculated dominant Raman modes

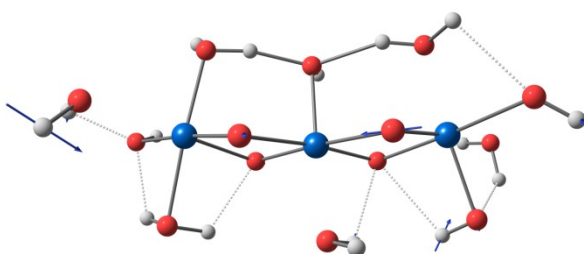
484 cm^{-1}



580 cm^{-1}



602 cm^{-1}



621 cm^{-1}

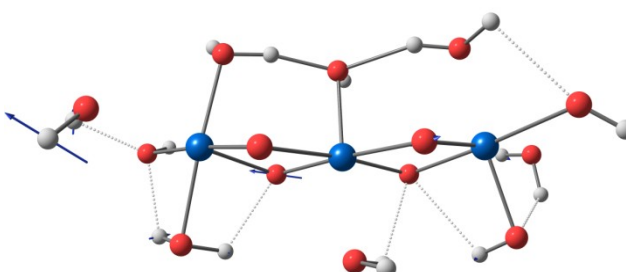
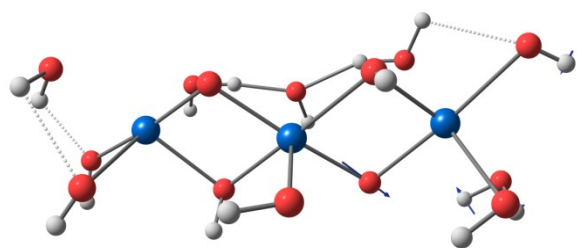


Figure S4.3 Overview of the normal modes that dominate the calculated Raman spectrum of the $\text{Ir}^{\text{IV}}\text{Ir}^{\text{IV}}\text{Ir}^{\text{IV}}$ trimer. The lower frequency is dominated by a μ -oxo vibration, the larger 3 by hydroxo vibrations.

637 cm^{-1}



685 cm^{-1}

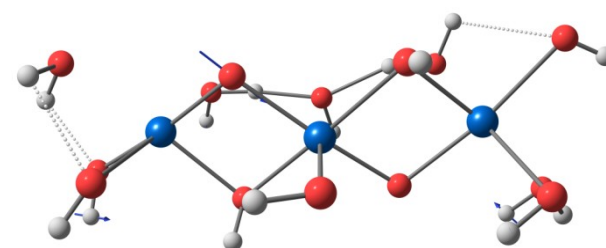


Figure S4.4 Overview of the normal modes that dominate the calculated Raman spectrum of the singly reduced trimer $\text{Ir}^{\text{IV}}\text{Ir}^{\text{III}}\text{Ir}^{\text{IV}}$. The spectrum is dominated by μ -oxo vibrations. These vibrations are more localized than the ones of the oxidized trimer and therefore shifted to higher frequencies as compared to those of the oxidized trimer.

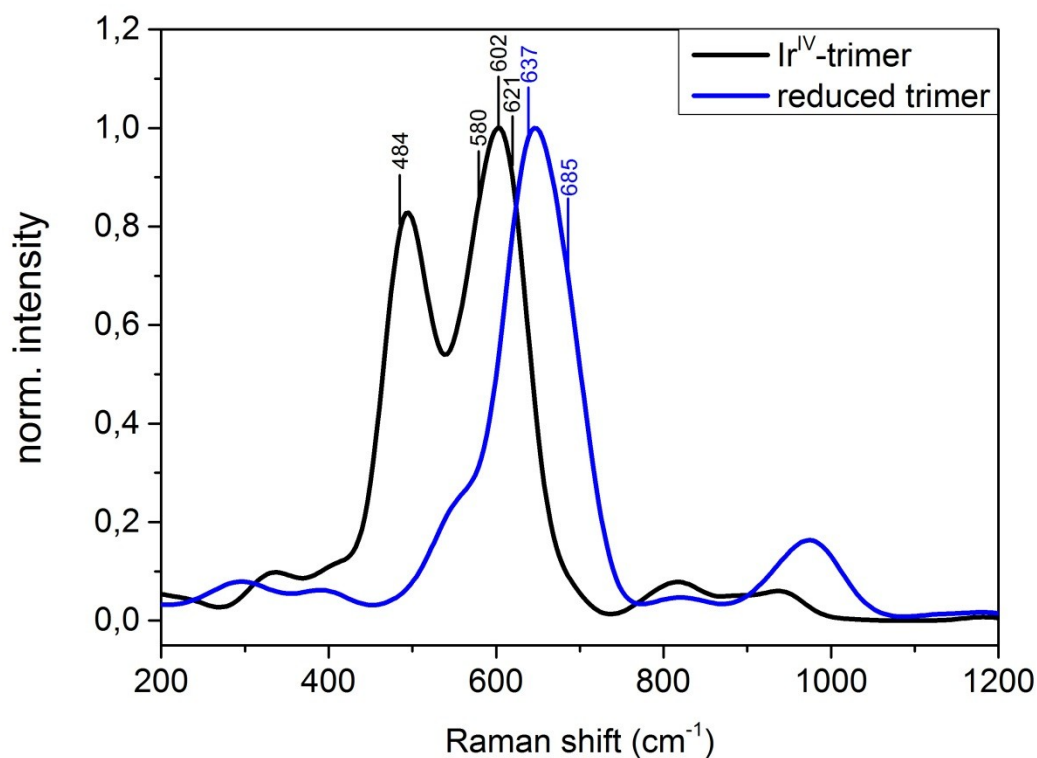


Figure S4.5 Calculated Raman spectra of the IR-trimer in its oxidized and reduced form. The main Raman-active modes shown in Figure S4.3 and Figure S4.4 are indicated.

Cartesian coordinates [\AA] of geometry-optimized clusters

$\text{Ir}^{\text{IV}} \text{Ir}^{\text{IV}} \text{Ir}^{\text{IV}}$ trimer model

O	-0.56662317939086	-0.42446133106470	-1.18044659219642
O	0.53933184468527	-0.32091685050492	1.00858281161036
O	2.30366298946447	-1.20586656560217	-0.69779842648356
O	-1.90599078260942	1.07598119453924	0.91166810754166
H	-1.53097301277179	-3.25489224375562	-0.09012289084337
H	1.92511596734510	-1.58878237440869	0.12575551261695
H	0.37717843934692	2.85311584618865	0.00133458101118
O	-0.77787927880585	-2.89689546543435	0.41371405575550
O	-0.10271796498406	2.18041950238608	-0.49755875677927
Ir	1.07778653529812	0.48152273141922	-0.70634419072276
Ir	-1.32127378436932	-0.83808429047232	0.59907985395111
H	2.63012423392848	1.69933910598993	-2.21599403866367
H	1.95725186419958	0.77363596894144	-3.29793736388329
O	1.77576990687063	1.40962685705603	-2.59574474175234

O	-2.05098852209210	-1.47756452825712	2.37449890043553
H	3.10628003363515	-0.71041313637929	-0.41743820628628
H	-1.68010750492233	1.22072671391972	1.84161607193362
O	2.90942460831755	1.30254759112380	-0.29322932051304
H	3.01488454542175	1.63303307988711	0.60375751674304
O	-3.10383513476772	-1.45566127115077	0.13237576638231
Ir	-3.90938410216041	-1.75075274082773	1.86917582325691
O	-5.74333056890572	-1.93462786806336	1.18503042016313
H	-6.23570125876549	-2.65244138509053	1.59938424858513
H	-0.89970338288247	1.85920949526814	0.07627493280330
O	-4.66600467710594	-2.12644053775424	3.90803398088771
H	-4.02888817976186	-1.74686239818963	4.52869086722102
H	-4.41244509268387	-3.07379634445428	3.78456549040318
O	-3.59967244747833	-3.69695772713004	2.19939728334663
H	-2.69871378717513	-3.75073478612836	2.54795966643378
O	-4.40261804852076	0.34016785140485	1.62806747334439
H	-3.64041585653329	0.74837083160021	1.14531758131545
H	-5.15812735157836	0.26970772556010	1.02313659966838
H	-0.95813193924798	-3.14481352761636	1.34034080971374

Reduced Ir^{IV}Ir^{III}Ir^{IV} trimer model

O	-0.570358	-0.422373	-1.026096
O	0.553681	-0.162797	1.214576
O	2.213967	-1.126480	-1.059332
O	-2.040979	1.005309	0.872191
H	-2.910224	-2.616053	-0.273926
H	1.131855	-0.908140	1.424803
H	0.405780	2.727704	0.405782
O	-0.586269	-2.823721	0.441029
O	-0.087555	2.237194	-0.263131
Ir	1.120110	0.510986	-0.646806
Ir	-1.263207	-0.979007	0.638369
H	2.594117	1.521561	-2.117675
H	2.180908	0.156926	-2.744553
O	1.836814	1.056620	-2.566728

O	-2.077383	-1.308238	2.336025
H	3.092470	-0.976206	-0.688142
H	-1.900655	1.139817	1.818600
O	2.808653	1.688333	-0.347020
H	3.426859	1.323224	0.292213
O	-3.095166	-1.716098	0.031979
Ir	-3.935651	-1.811137	1.886967
O	-5.809904	-2.167954	1.197620
H	-6.406221	-2.326899	1.937300
H	-0.930796	1.850058	0.179269
O	-4.501778	-2.058726	3.939077
H	-3.808682	-1.566933	4.402106
H	-4.116716	-2.987900	3.779730
O	-3.538665	-3.716037	2.407640
H	-2.580466	-3.818070	2.337273
O	-4.474593	0.204210	1.387744
H	-3.643314	0.618261	0.994561
H	-5.120415	0.007383	0.691141
H	0.257066	-2.758378	-0.027444

Photoemission spectroscopy

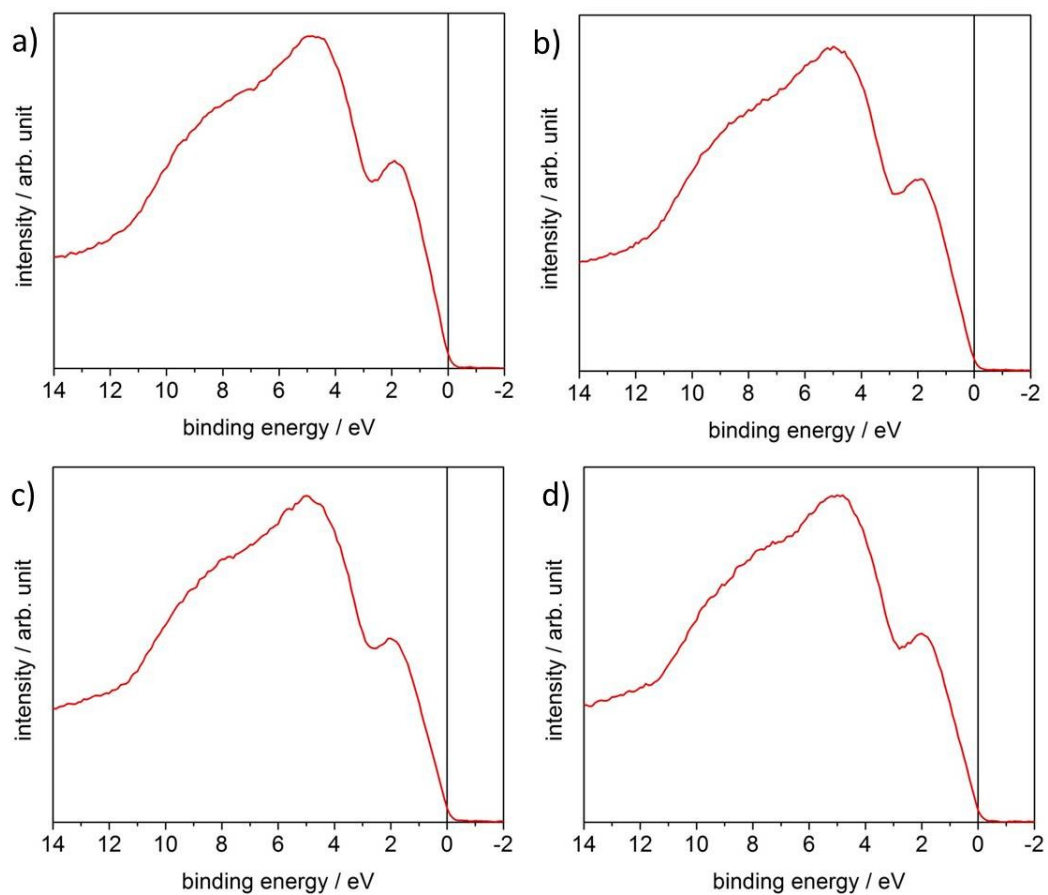


Figure S4.6 XPS-spectra of MW-prepared Ir-oxohydroxides in the valence band-region at excitation energies of 450 eV for (a)MW_5, (b) MW_10, (c) MW_50 and (d) MW_100.

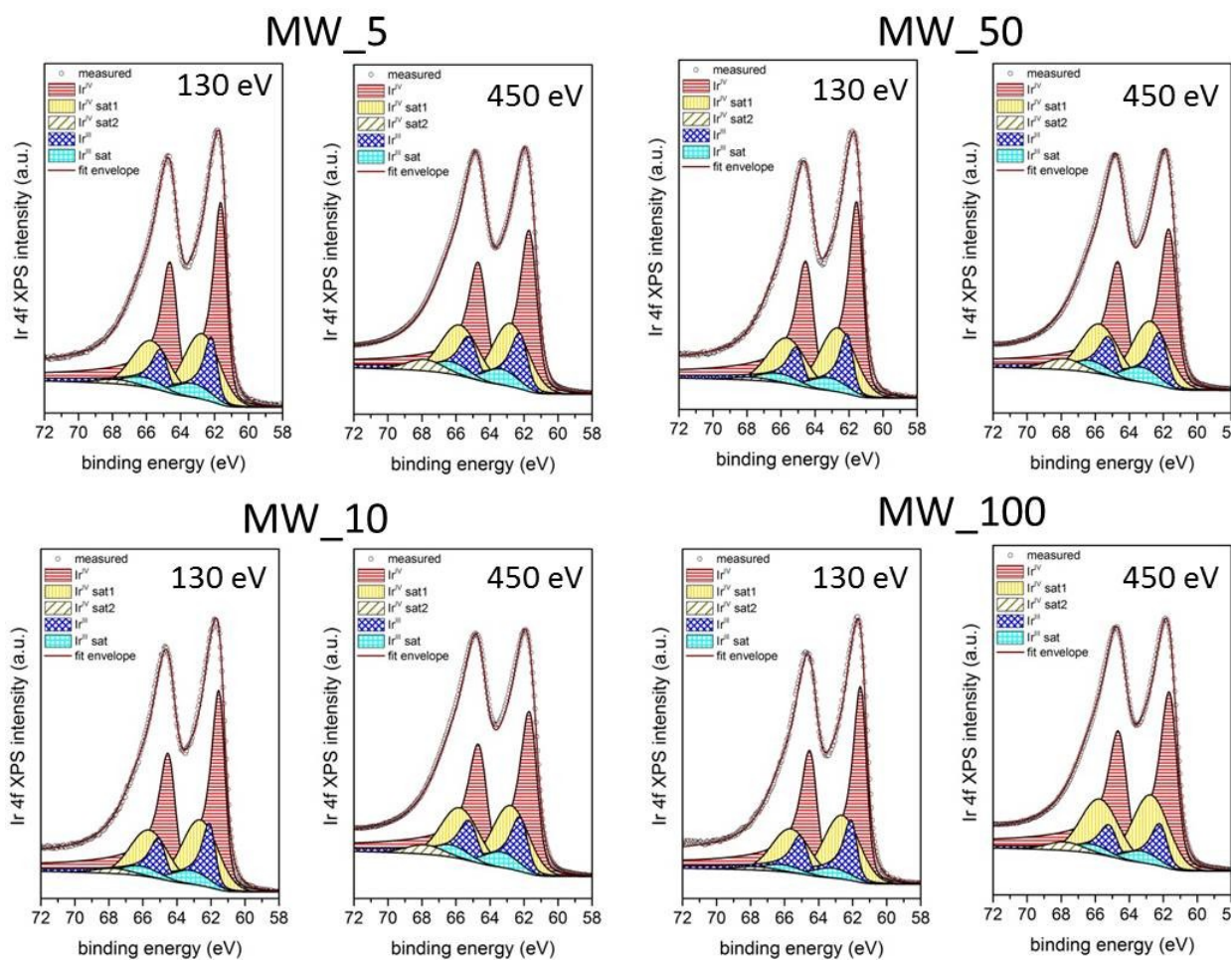


Figure S4.7 XPS-spectra of the MW-prepared Ir-oxohydroxides in the Ir 4f-region at kinetic energies of 130 and 450 eV.

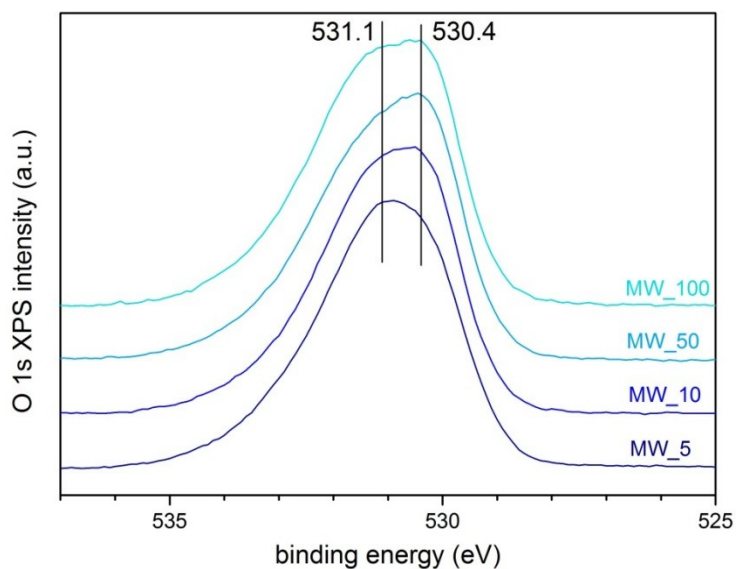


Figure S4.8 XPS-spectra of MW-prepared Ir-oxohydroxides in the O 1s-region at excitation energies of 450 eV

RT- CO-oxidation

The reactor setup was equipped with an on-line gas analyzer (X-Stream, Emerson/Rosemount) to quantify O₂, CO and CO₂. The temperature in the catalyst bed could be directly monitored by an analog connection to the gas analyzer. Every gas line was equipped with a mass-flow controller (E1-flow, Bronkhorst). The CO-gas line was equipped with a carbonyl remover, consisting of a tube filled with inert SiC and heated to 300°C as well as a CO₂-trap consisting of a crushed-KOH-filled cartridge. The carrier gas line was equipped with a water and oxygen filter. The reactor itself was a U-tube with an inner diameter of 5 mm, made of glass-lined steel.

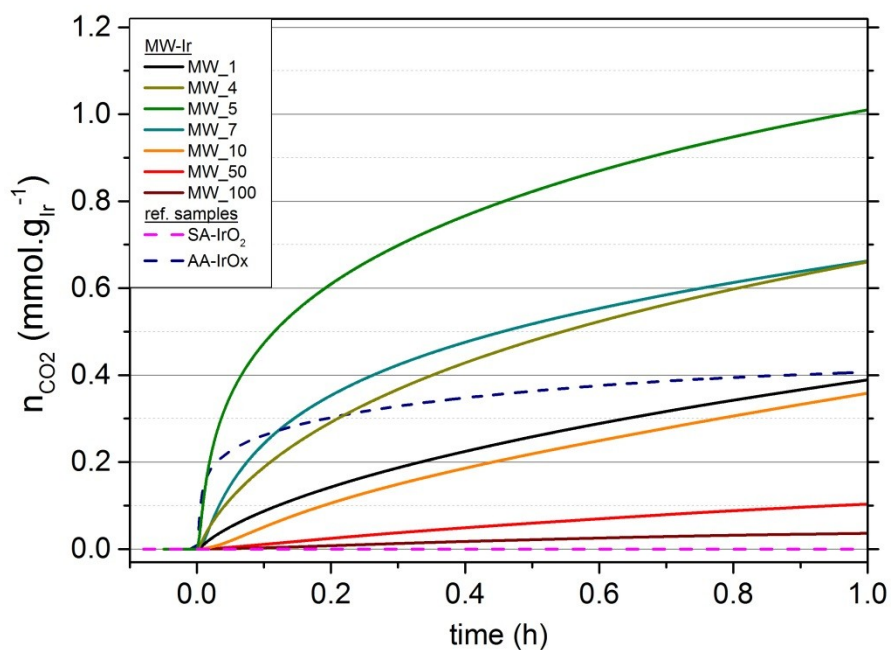


Figure S4.9 CO₂ evolved during the first switch from 100%-He to 1%-CO/He for the MW-Ir-compounds as well as the reference samples

DRIFTS

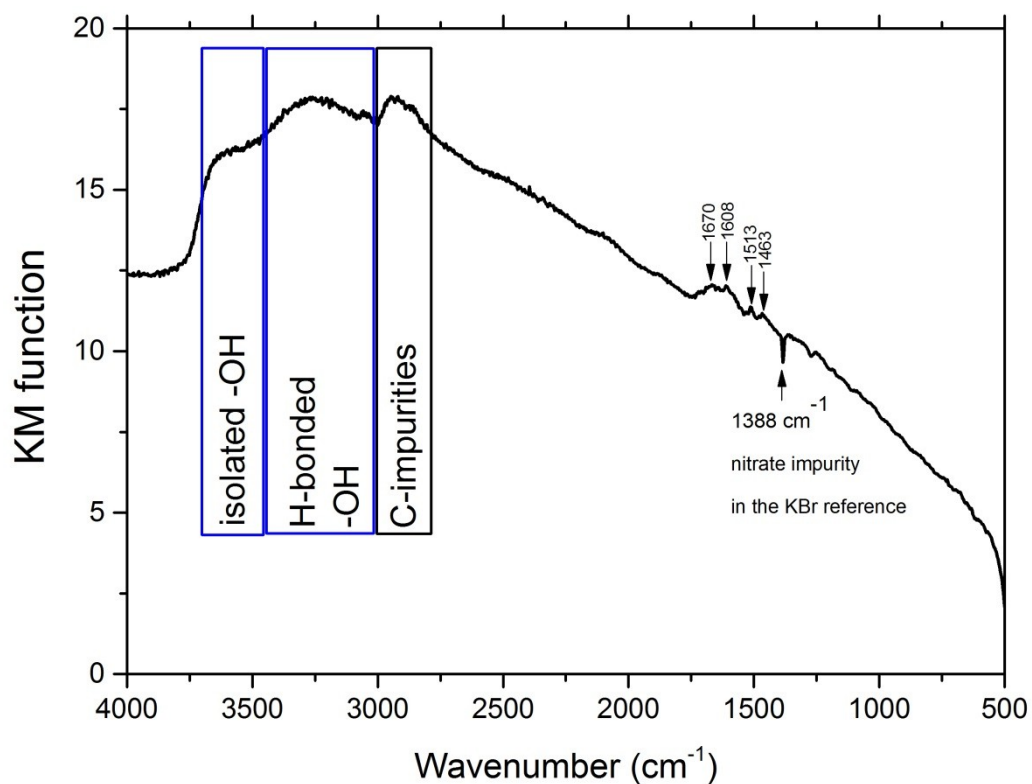


Figure S4.10 DRIFTS spectra recorded for MW_5 at RT after degassing overnight at 40°C in vacuum.

Small contributions between 1670 and 1450 cm⁻¹ are attributed to the vibrations modes of various carbonate species probably formed during the synthesis from atmospheric CO₂ dissolved in the basic precursor solution.⁵¹

Low-temperature CO-adsorption

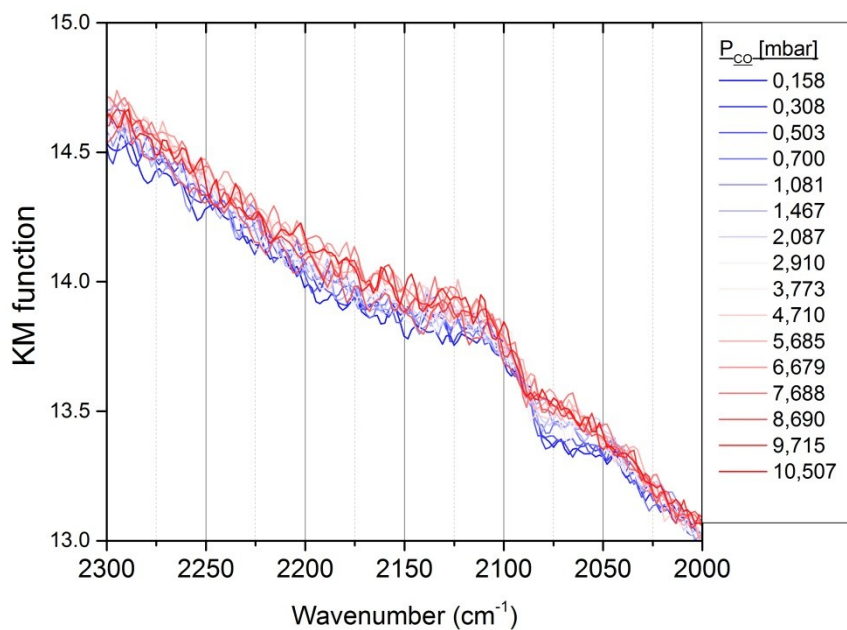


Figure S4.11 shows the small changes in DRIFTS-spectra of MW_5 upon gradual CO-addition at 77K

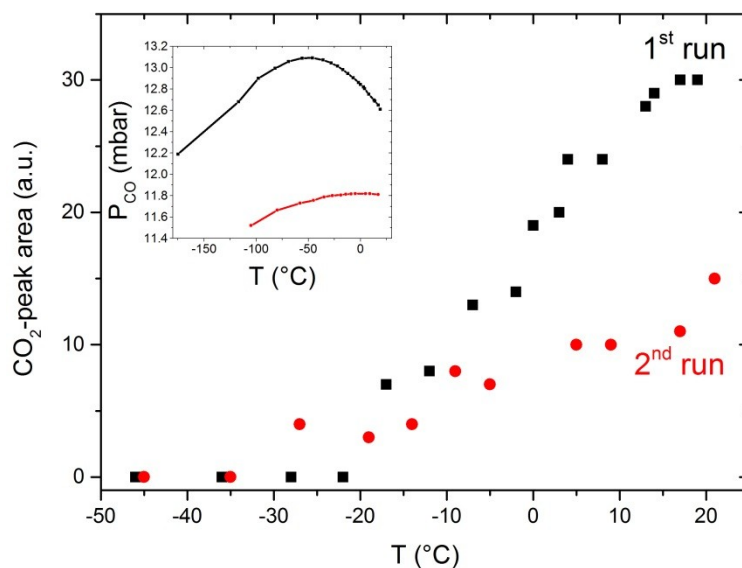


Figure S4.12 Integrated CO₂-signals observed during the warm-up in the first and second cycle as well as the measured pressure in the in-situ cell (inset).

CO-oxidation of MW_5 in the Raman cell

Approx. 40 mg of sample MW_5 were placed in an air-tight cell designed for on-stream Raman-spectroscopic investigation of powdered catalysts. The Raman spectra are recorded through a quartz window.

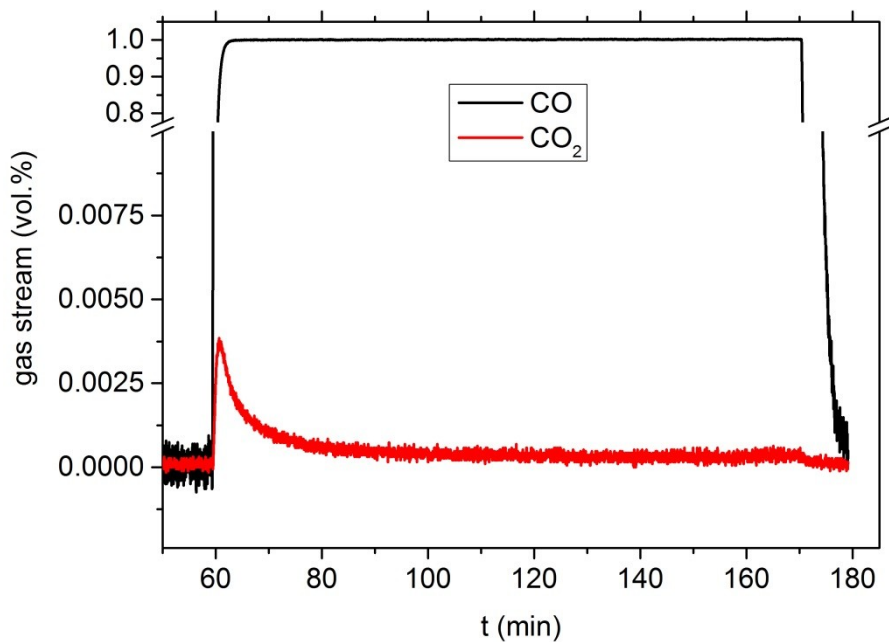


Figure S4.13 Gas stream signals during the CO-treatment of MW_5 in the Raman cell

Raman spectra before/after CO-oxidation

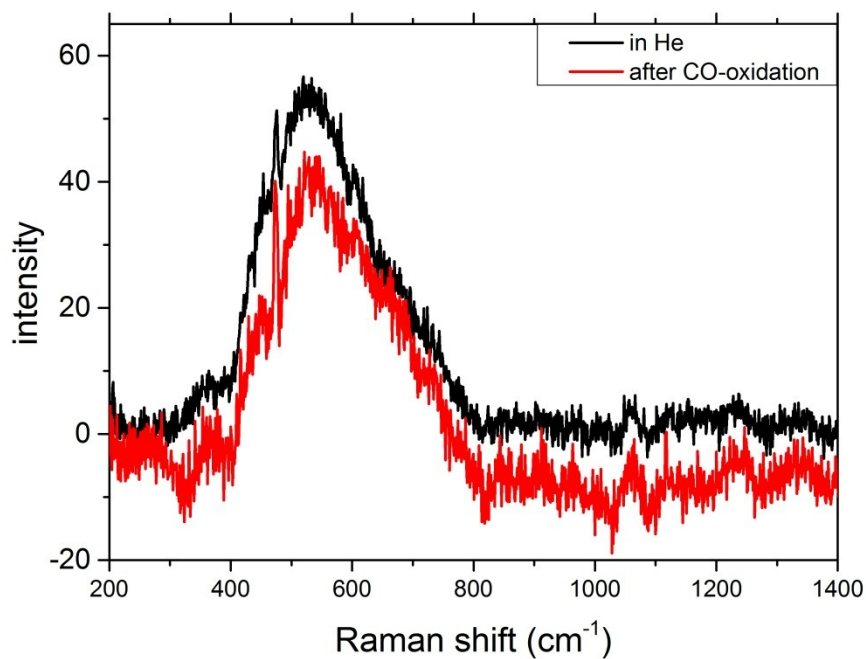


Figure S4.14 shows the background-subtracted Raman spectra of MW_5 recorded before and after CO-treatment at room temperature for 1h in the Raman-cell.

4.8. References

- (1) McCrory, C. C. L.; Jung, S.; Ferrer, I. M.; Chatman, S. M.; Peters, J. C.; Jaramillo, T. F. *Journal of the American Chemical Society* **2015**, *137*, 4347.
- (2) Katsounaros, I.; Cherevko, S.; Zeradjanin, A. R.; Mayrhofer, K. J. J. *Angewandte Chemie International Edition* **2014**, *53*, 102.
- (3) Bernicke, M.; Ortel, E.; Reier, T.; Bergmann, A.; Ferreira de Araujo, J.; Strasser, P.; Kraehnert, R. *ChemSusChem* **2015**, *8*, 1908.
- (4) Bockris, J. O. M.; Otagawa, T. *Journal of the Electrochemical Society* **1984**, *131*, 290.
- (5) Frazer, E. J.; Woods, R. *Journal of Electroanalytical Chemistry and Interfacial Electrochemistry* **1979**, *102*, 127.
- (6) Vuković, M. *Journal of Applied Electrochemistry* **1987**, *17*, 737.
- (7) Reier, T.; Oezaslan, M.; Strasser, P. *ACS Catalysis* **2012**, *2*, 1765.
- (8) Beni, G.; Schiavone, L. M.; Shay, J. L.; Dautremont-Smith, W. C.; Schneider, B. S. *Nature* **1979**, *282*, 281.
- (9) Cherevko, S.; Reier, T.; Zeradjanin, A. R.; Pawolek, Z.; Strasser, P.; Mayrhofer, K. J. J. *Electrochemistry Communications* **2014**, *48*, 81.
- (10) Reier, T.; Teschner, D.; Lunkenbein, T.; Bergmann, A.; Selve, S.; Kraehnert, R.; Schlögl, R.; Strasser, P. *Journal of the Electrochemical Society* **2014**, *161*, F876.
- (11) Hintermair, U.; Sheehan, S. W.; Parent, A. R.; Ess, D. H.; Richens, D. T.; Vaccaro, P. H.; Brudvig, G. W.; Crabtree, R. H. *Journal of the American Chemical Society* **2013**, *135*, 10837.
- (12) Diaz-Morales, O.; Hersbach, T. J. P.; Hettterscheid, D. G. H.; Reek, J. N. H.; Koper, M. T. M. *Journal of the American Chemical Society* **2014**, *136*, 10432.
- (13) Huang, J.; Blakemore, J. D.; Fazi, D.; Kokhan, O.; Schley, N. D.; Crabtree, R. H.; Brudvig, G. W.; Tiede, D. M. *Physical Chemistry Chemical Physics* **2014**, *16*, 1814.
- (14) Zhao, Y.; Vargas-Barbosa, N. M.; Strayer, M. E.; McCool, N. S.; Pandelia, M.-E.; Saunders, T. P.; Swierk, J. R.; Callejas, J. F.; Jensen, L.; Mallouk, T. E. *Journal of the American Chemical Society* **2015**, *137*, 8749.
- (15) Minguzzi, A.; Locatelli, C.; Lugaresi, O.; Achilli, E.; Cappelletti, G.; Scavini, M.; Coduri, M.; Masala, P.; Sacchi, B.; Vertova, A.; Ghigna, P.; Rondinini, S. *ACS Catalysis* **2015**, *5*, 5104.
- (16) Minguzzi, A.; Lugaresi, O.; Achilli, E.; Locatelli, C.; Vertova, A.; Ghigna, P.; Rondinini, S. *Chemical Science* **2014**, *5*, 3591.
- (17) Sanchez Casalongue, H. G.; Ng, M. L.; Kaya, S.; Friebel, D.; Ogasawara, H.; Nilsson, A. *Angewandte Chemie International Edition* **2014**, *53*, 7169.
- (18) Pfeifer, V.; Jones, T. E.; Velasco Vélez, J. J.; Massué, C.; Arrigo, R.; Teschner, D.; Girgsdies, F.; Scherzer, M.; Greiner, M. T.; Allan, J.; Hashagen, M.; Weinberg, G.; Piccinin, S.; Hävecker, M.; Knop-Gericke, A.; Schlögl, R. *Surface and Interface Analysis* **2015**, n/a.
- (19) Pfeifer, V.; Jones, T. E.; Velasco Velez, J. J.; Massue, C.; Greiner, M. T.; Arrigo, R.; Teschner, D.; Girgsdies, F.; Scherzer, M.; Allan, J.; Hashagen, M.; Weinberg, G.; Piccinin, S.; Havecker, M.; Knop-Gericke, A.; Schlogl, R. *Physical Chemistry Chemical Physics* **2016**, *18*, 2292.
- (20) Wang, Y.-Z.; Zhao, Y.-X.; Gao, C.-G.; Liu, D.-S. *Catalysis Letters* **2008**, *125*, 134.
- (21) Knop-Gericke, A.; Kleimenov, E.; Hävecker, M.; Blume, R.; Teschner, D.; Zafeiratos, S.; Schlögl, R.; Bukhtiyarov, V. I.; Kaichev, V. V.; Prosvirin, I. P.; Nizovskii, A. I.; Bluhm, H.; Barinov, A.; Dudin, P.; Kiskinova, M. In *Advances in Catalysis*; Academic Press: 2009; Vol. Volume 52, p 213.
- (22) Neese, F. *WIREs Computational Molecular Science* **2012**, *2*, 73.
- (23) Becke, A. D. *Physical Review A* **1988**, *38*, 3098.
- (24) Pantazis, D. A.; Chen, X.-Y.; Landis, C. R.; Neese, F. *Journal of Chemical Theory and Computation* **2008**, *4*, 908.
- (25) Lenthe, E. v.; Snijders, J. G.; Baerends, E. J. *The Journal of Chemical Physics* **1996**, *105*, 6505.
- (26) Grimme, S.; Ehrlich, S.; Goerigk, L. *Journal of Computational Chemistry* **2011**, *32*, 1456.

- (27) McCrory, C. C. L.; Jung, S.; Peters, J. C.; Jaramillo, T. F. *Journal of the American Chemical Society* **2013**, *135*, 16977.
- (28) Algara-Siller, G.; Kurasch, S.; Sedighi, M.; Lehtinen, O.; Kaiser, U. *Applied Physics Letters* **2013**, *103*, 203107.
- (29) Zan, R.; Ramasse, Q. M.; Jalil, R.; Georgiou, T.; Bangert, U.; Novoselov, K. S. *ACS Nano* **2013**, *7*, 10167.
- (30) Gammer, C.; Mangler, C.; Rentenberger, C.; Karnthaler, H. P. *Scripta Materialia* **2010**, *63*, 312.
- (31) Huang, Y. S.; Lin, S. S.; Huang, C. R.; Lee, M. C.; Dann, T. E.; Chien, F. Z. *Solid State Communications* **1989**, *70*, 517.
- (32) Moulder, J. F.; Chastain, J.; King, R. C. *Handbook of X-ray photoelectron spectroscopy: a reference book of standard spectra for identification and interpretation of XPS data*; Perkin-Elmer Eden Prairie, MN, 1992.
- (33) Fierro, S.; Nagel, T.; Baltruschat, H.; Comninellis, C. *Electrochemistry Communications* **2007**, *9*, 1969.
- (34) Reier, T.; Pawolek, Z.; Cherevko, S.; Bruns, M.; Jones, T.; Teschner, D.; Selve, S.; Bergmann, A.; Nong, H. N.; Schlögl, R.; Mayrhofer, K. J. J.; Strasser, P. *Journal of the American Chemical Society* **2015**, *137*, 13031.
- (35) Kast, P.; Friedrich, M.; Teschner, D.; Girgsdies, F.; Lunkenbein, T.; d'Alnoncourt, R. N.; Behrens, M.; Schloegl, R. *Applied Catalysis A* **2015**, *502*, 8.
- (36) Willinger, M. G.; Zhang, W.; Bondarchuk, O.; Shaikhutdinov, S.; Freund, H.-J.; Schlögl, R. *Angewandte Chemie* **2014**, *126*, 6108.
- (37) Lin, J.; Qiao, B.; Li, L.; Guan, H.; Ruan, C.; Wang, A.; Zhang, W.; Wang, X.; Zhang, T. *Journal of Catalysis* **2014**, *319*, 142.
- (38) Pfeifer, V.; Jones, T. E.; Wrabetz, S.; Massué, C.; Velasco Vélez, J. J.; Arrigo, R.; Scherzer, M.; Piccinin, S.; Hävecker, M.; Knop-Gericke, A.; Schlögl, R. *Angewandte Chemie International Edition* **2016**, *submitted*.
- (39) Brewer, S. H.; Wicaksana, D.; Maria, J.-P.; Kingon, A. I.; Franzen, S. *Chemical Physics* **2005**, *313*, 25.
- (40) Ito, S.; Abe, Y.; Kawamura, M.; Kim, K. H. *Journal of Vacuum Science & Technology B* **2015**, *33*, 041204.
- (41) Lezna, R. O.; Kunimatsu, K.; Ohtsuka, T.; Sato, N. *Journal of the Electrochemical Society* **1987**, *134*, 3090.
- (42) Marinova, T. S.; Chakarov, D. V. *Surface Science* **1989**, *217*, 65.
- (43) Reinalda, D.; Ponc, V. *Surface Science* **1980**, *91*, 113.
- (44) Zou, S.; Gómez, R.; Weaver, M. J. *Langmuir* **1997**, *13*, 6713.
- (45) Gelin, P.; Coudurier, G.; Taarit, Y. B.; Naccache, C. *Journal of Catalysis* **1981**, *70*, 32.
- (46) Mihaylov, M.; Ivanova, E.; Thibault-Starzyk, F.; Daturi, M.; Dimitrov, L.; Hadjiivanov, K. *Journal of Physical Chemistry B* **2006**, *110*, 10383.
- (47) Solymosi, F.; Novak, E.; Molnar, A. *Journal of Physical Chemistry* **1990**, *94*, 7250.
- (48) Diaz-Morales, O.; Calle-Vallejo, F.; Munck, C. d.; Koper, M. T. M. *Chem. Sci.* **2013**, *4*, 2334.
- (49) Man, I. C.; Su, H.-Y.; Calle-Vallejo, F.; Hansen, H. A.; Martínez, J. I.; Inoglu, N. G.; Kitchin, J.; Jaramillo, T. F.; Nørskov, J. K.; Rossmeisl, J. *ChemCatChem* **2011**, *3*, 1159.
- (50) Rossmeisl, J.; Logadottir, A.; Nørskov, J. K. *Chemical Physics* **2005**, *319*, 178.
- (51) Hadjiivanov, K. I.; Vayssilov, G. N. *Advances in Catalysis* **2002**, *47*, 307.

5. Summary and final conclusions

A main bottleneck for PEM-based water electrolysis to become a cost-effective solution for chemical energy storage is the low stability of most available electrocatalysts under acidic OER-conditions. So far, only Ir-based compounds have proven to be able to combine high activity and stability in acidic OER.¹ However, if an Ir-based system is to be implemented into a PEM-electrolyzer intended for wide-spread use, the Ir-utilization has to be optimized in order to minimize material costs.

The primary aim of the present work was to explore new synthesis strategies for the preparation of Ir-based OER-catalysts with emphasis on an optimal utilization of the loaded Ir. For this purpose, our initial target was the morphological optimization of an Ir-based system via the design of small Ir-nanoparticles supported on a conductive and corrosion-resistant current collector. ATO was chosen as support, due to its corrosion resistance in acidic media.² Hydrothermal synthesis strategies involving safe precursors have been proposed in the literature for the preparation of highly nanostructured ATO.^{3,4} We adapted such a synthesis procedure by taking advantage of newly developed MW-supported hydrothermal synthesis reactors. Such setups allow for fast hydrothermal treatment of precursor solutions with precise control over synthetic parameters and give access to highly nanostructured materials.⁵ We achieved the preparation of 5 nm-ATO particles with conductivities comparable to those of commercially available compounds.

Homogenously dispersed 2-4 nm Ir-particles were loaded onto the ATO-support via a second MW-supported hydrothermal step. Excellent OER-performance was observed for the produced Ir/ATO for loadings below $100 \mu\text{g}_{\text{Ir}}\cdot\text{cm}^{-2}$. The catalyst showed superior properties to the best benchmarks reported by Mc Crory et al. in their recent benchmarking effort of OER-catalysts tested under industrially relevant conditions.^{6,7} Combined TGMS, TPR and XPS-analysis showed that the loaded amorphous Ir-particles consisted of an Ir^{III/IV}-oxohydroxide. The presence of mixed oxidation states has been argued by Minguzzi et al. to be essential for the good OER-performance of amorphous, hydrated Ir-compounds.^{8,9} As a result we suspected that the excellent OER-performance observed for our Ir/ATO might be due to a large extent to the chemical nature of the produced Ir-phase.

Our next step was to test the OER-relevance of the Ir^{III/IV}-oxohydroxide phase. For this purpose, we decided to probe for OER-relevant structural features by gradually altering the sample and testing the OER-performance of the resulting products. For this purpose, the Ir/ATO-compound was submitted to thermal treatment at 250-350°C under inert and oxidative atmospheres. Indeed TGMS showed that critical changes such as major dehydroxylation occur within this temperature range. The dramatic depletion of OER-performance observed for the samples calcined at 250°C in Ar was linked to fast dehydroxylation under inert atmosphere. This highlights the importance of the chemisorbed water fingerprint for the OER-performance of Ir^{III/IV}-oxohydroxides. Following thermal treatment at 350°C, vibrational spectroscopy as well as careful TEM-investigation showed that small crystalline IrO₂-domains formed. The result was a strong depletion in initial OER-activity, which resulted in mediocre stability under industrially relevant galvanostatic OER-conditions, in line with the results recently presented by Reier et al.¹⁰

After showing that the excellent OER-performance of the MW-produced Ir/ATO was strongly linked to the high intrinsic activity of the Ir^{III/IV}-oxohydroxide phase, we decided to investigate the pure Ir^{III/IV}-oxohydroxide without the contribution of the ATO-support, in order to gain a deeper

understanding of the OER-relevant features. This led us to the design of a MW-supported hydrothermal synthesis of a series of pure amorphous Ir-oxohydroxides. Systematic variations of synthesis conditions were used to identify critical preparation parameters. UV-Vis analysis of precursor solutions revealed that the initial base:Ir ratio determines the synthesis yield as it controls the efficient hydrolysis and oligomerization of Ir-chloride precursors. For intermediate KOH:Ir around 5:1, a pure amorphous Ir-compound was obtained at maximal yields. At higher KOH:Ir, XRD and SEM-EDX revealed the undesired formation of a metallic Ir-core embedded in a thick oxidic Ir-layer. TPR- and XPS-analysis confirmed a mixed Ir^{III/IV}-oxidation state for the produced compounds and showed a gradual increase towards Ir^{IV} for increasing KOH:Ir. Concomitantly, TGMS showed that the chemisorbed water fraction gradually diminished for increasing KOH:Ir.

The assessment of the OER-performance revealed that the pure Ir^{III/IV}-oxohydroxide prepared from KOH:Ir=5:1 was also the best OER-catalyst. The performance was even better than for the MW-produced Ir/ATO and clearly surpassed the benchmarks reported by McCrory et al.^{6,7} With increasing KOH:Ir, *i.e.* Ir-oxohydroxides closer to the Ir^{IV}-oxidation state and containing less chemisorbed water, the OER-performance clearly diminished. The OER-relevance of the chemisorbed water fingerprint is in line with the adverse effect of dehydroxylation at 250°C in Ar observed for the Ir/ATO. Additionally, the importance of the Ir^{III}-species is consistent with the sharp depletion in OER-performance observed for Ir/ATO calcined at 350°C. Several recent studies have highlighted the involvement of mixed-oxidation Ir-phases formed in-situ under OER-conditions.^{8,9,11-14} These observations suggested that our Ir^{III/IV}-oxohydroxides might constitute a precursor phase accommodating a high number of sites for efficient OER-catalysis stabilized in a highly hydrated Ir^{III/IV} environment.

Recent findings by Fierro et al. have shown that lattice oxygen species from Ir-oxide-catalysts participate in the OER in addition to surface-adsorbed intermediates.¹⁵ This study suggested the OER-relevance of certain lattice-O-species in Ir-oxides. In order to search for such OER-relevant reactive oxygen species accommodated by the Ir^{III/IV}-oxohydroxide matrix, we analyzed the NEXAFS-spectra of the O K-edge using the descriptive model of the electronic structure of Ir-oxides recently developed by Pfeifer et al.^{16,17} We could show that our best Ir^{III}-rich Ir-oxohydroxide catalyst contained high amounts of O 2p hole states, formally O⁻, identified by a pre-edge feature at 529 eV. The detected O⁻-amount diminishes with increasing Ir^{IV}-content of the samples. Comparing the relative O⁻-amount with the trend in OER-performance within the batch of MW-produced Ir-oxohydroxides led us to the conclusion that the O⁻-species were linked to the good OER-performance of the Ir-oxohydroxides. In order to determine the O⁻-amount accessible in the different samples and compare quantitative trends to the evolution in OER-performance, we used a reactive CO-titration procedure. Indeed, recent results by Pfeifer et al.¹⁸ have shown that O⁻ accommodated by an Ir^{III/IV}-oxohydroxide easily oxidizes CO at room temperature. We could establish a loose linear trend indicating a link between good OER-performance of our Ir-oxohydroxides and a high content of O⁻-species. The high amount of titrated O⁻-species and slow reaction kinetics showed that the titration was not limited to the surface and that sub-surface-O⁻ migrated to the surface during the CO-titration experiment. The OER-relevance of the O⁻-species was confirmed by testing our best catalyst before and after CO-titration. We observed a strong depletion in OER-performance after CO-titration, which confirmed that the consumption of O⁻ via CO led to irreversible damage to the catalyst.

The comparison of these trends with the results obtained for an amorphous Ir-oxohydroxide benchmark extensively studied by Pfeifer et al.^{16,17} yielded another important piece of the puzzle. Indeed, the trends in O¹⁻-concentration detected via NEXAFS and CO-titration matched the evolution in OER-performance within our batch of MW-produced Ir^{III/IV}-oxohydroxides. However, the benchmark compound exhibited a strong NEXAFS-feature attributed to O¹⁻, comparable to our best MW-produced catalyst. This observation was in stark contrast to the small amount of CO-titrated O¹⁻-species. We concluded that the O¹⁻-species present in the benchmark compound showed a strongly reduced ability to migrate towards the surface during CO-titration in comparison to our own compounds. Considering that the benchmark exhibited by far the worst OER-performance, this suggests that the mobility of sub-surface O¹⁻-species in Ir^{III/IV}-oxohydroxides plays an important part in the superior OER-performance of these catalysts. It therefore seems that the mechanism suggested by Fierro et al. for the involvement of lattice-O-species should be extended in the case of Ir-oxohydroxides to include the three-dimensional matrix of the compounds as OER-relevant O¹⁻-species probably migrate from the sub-surface to the surface.¹⁵ The ex-situ characterization of our compounds strongly indicates such a scenario. However, in-situ identification of species involved in the OER on Ir-oxohydroxides will be crucial in order to confirm this hypothesis. The current optimization of electrocatalytic cells for synchrotron-based in-situ NAP-XPS/XAS will allow conducting such studies in the near future. The study of the migration of O¹⁻-species towards the catalyst surface might be of prime importance for a better mechanistic understanding of OER on Ir^{III/IV}-oxohydroxides.

I conclude that our innovative MW-supported hydrothermal synthesis strategy constitutes a powerful tool for the preparation of Ir^{III/IV}-oxohydroxides with superior intrinsic OER-performance properties. Key structural features present in the highly hydrated Ir^{III}-rich matrix, such as reactive O¹⁻-species mobile within the amorphous matrix were identified. This constitutes an important step towards the targeted preparation of high-performance Ir-based OER-catalysts allowing for low electrode loadings. These findings thus pave the way towards the cost-effective implementation of PEM-based electrolyzers for large-scale chemical energy storage.

References

- (1) Carmo, M.; Fritz, D. L.; Mergel, J.; Stolten, D. *International Journal of Hydrogen Energy* **2013**, *38*, 4901.
- (2) Cachet, H.; Froment, M.; Zenia, F. *Journal of the Electrochemical Society* **1996**, *143*, 442.
- (3) Nütz, T.; Felde, U. z.; Haase, M. *The Journal of Chemical Physics* **1999**, *110*, 12142.
- (4) Nütz, T.; Haase, M. *Journal of Physical Chemistry B* **2000**, *104*, 8430.
- (5) Conrad, F.; Massue, C.; Kühn, S.; Kunkes, E.; Girgsdies, F.; Kasatkin, I.; Zhang, B.; Friedrich, M.; Luo, Y.; Armbrüster, M.; Patzke, G. R.; Behrens, M. *Nanoscale* **2012**, *4*, 2018.
- (6) McCrory, C. C. L.; Jung, S.; Ferrer, I. M.; Chatman, S. M.; Peters, J. C.; Jaramillo, T. F. *Journal of the American Chemical Society* **2015**, *137*, 4347.
- (7) McCrory, C. C. L.; Jung, S.; Peters, J. C.; Jaramillo, T. F. *Journal of the American Chemical Society* **2013**, *135*, 16977.
- (8) Minguzzi, A.; Locatelli, C.; Lugaresi, O.; Achilli, E.; Cappelletti, G.; Scavini, M.; Coduri, M.; Masala, P.; Sacchi, B.; Vertova, A.; Ghigna, P.; Rondinini, S. *ACS Catalysis* **2015**, *5*, 5104.
- (9) Minguzzi, A.; Lugaresi, O.; Achilli, E.; Locatelli, C.; Vertova, A.; Ghigna, P.; Rondinini, S. *Chemical Science* **2014**, *5*, 3591.
- (10) Reier, T.; Teschner, D.; Lunkenbein, T.; Bergmann, A.; Selve, S.; Kraehnert, R.; Schlögl, R.; Strasser, P. *Journal of the Electrochemical Society* **2014**, *161*, F876.
- (11) Sanchez Casalongue, H. G.; Ng, M. L.; Kaya, S.; Friebel, D.; Ogasawara, H.; Nilsson, A. *Angewandte Chemie International Edition* **2014**, *53*, 7169.
- (12) Huang, J.; Blakemore, J. D.; Fazi, D.; Kokhan, O.; Schley, N. D.; Crabtree, R. H.; Brudvig, G. W.; Tiede, D. M. *Physical Chemistry Chemical Physics* **2014**, *16*, 1814.
- (13) Hintermair, U.; Sheehan, S. W.; Parent, A. R.; Ess, D. H.; Richens, D. T.; Vaccaro, P. H.; Brudvig, G. W.; Crabtree, R. H. *Journal of the American Chemical Society* **2013**, *135*, 10837.
- (14) Diaz-Morales, O.; Hersbach, T. J. P.; Hetterscheid, D. G. H.; Reek, J. N. H.; Koper, M. T. M. *Journal of the American Chemical Society* **2014**, *136*, 10432.
- (15) Fierro, S.; Nagel, T.; Baltruschat, H.; Comninellis, C. *Electrochemistry Communications* **2007**, *9*, 1969.
- (16) Pfeifer, V.; Jones, T. E.; Velasco Vélez, J. J.; Massué, C.; Arrigo, R.; Teschner, D.; Girgsdies, F.; Scherzer, M.; Greiner, M. T.; Allan, J.; Hashagen, M.; Weinberg, G.; Piccinin, S.; Hävecker, M.; Knop-Gericke, A.; Schlögl, R. *Surface and Interface Analysis* **2015**, n/a.
- (17) Pfeifer, V.; Jones, T. E.; Velasco Vélez, J. J.; Massué, C.; Greiner, M. T.; Arrigo, R.; Teschner, D.; Girgsdies, F.; Scherzer, M.; Allan, J.; Hashagen, M.; Weinberg, G.; Piccinin, S.; Hävecker, M.; Knop-Gericke, A.; Schlögl, R. *Phys Chem Chem Phys* **2016**, *18*, 2292.
- (18) Pfeifer, V.; Jones, T. E.; Wrabetz, S.; Massué, C.; Velasco Vélez, J. J.; Arrigo, R.; Scherzer, M.; Piccinin, S.; Hävecker, M.; Knop-Gericke, A.; Schlögl, R. *Angewandte Chemie International Edition* **2016**, submitted.

6. Appendix I: List of samples

Table 6.1 List of relevant samples described in this work with corresponding nomenclature and their associated FHI-database ID

Sample name	Sample nature	Synthesis conditions	FHI-database
MW-ATO	ATO	MW, 270°C, 1h	18966
MW-Ir/ATO	30 mol.% Ir-oxohydroxide on ATO	MW, 250°C, 1h	19527
Ir_250_O₂	MW-Ir/ATO calcined	21%O ₂ /Ar, 250°C, 1h	22132
Ir_350_O₂	MW-Ir/ATO calcined	21%O ₂ /Ar, 350°C, 1h	22133
Ir_250_Ar	MW-Ir/ATO calcined	Ar, 250°C, 1h	22134
Ir_350_Ar	MW-Ir/ATO calcined	Ar, 350°C, 1h	22135
MW_1	Ir-oxohydroxide	MW, KOH:Ir=1:1, 250°C, 1h	21009, 21010
MW_4	Ir-oxohydroxide	MW, KOH:Ir=4:1, 250°C, 1h	21404, 21405
MW_5	Ir-oxohydroxide	MW, KOH:Ir=5:1, 250°C, 1h	21011, 21012
MW_7	Ir-oxohydroxide	MW, KOH:Ir=7:1, 250°C, 1h	21130, 21131
MW_10	Ir-oxohydroxide	MW, KOH:Ir=10:1, 250°C, 1h	21013, 21014
MW_50	Ir-oxohydroxide	MW, KOH:Ir=50:1, 250°C, 1h	21015, 21016
MW_100	Ir-oxohydroxide	MW, KOH:Ir=100:1, 250°C, 1h	21017, 21018
AA-IrO_x	Ir-oxohydroxide	Commercial sample (Alfa Aesar, Premion, 99.99%)	20233
SA-IrO₂	Crystalline IrO ₂	Commercial sample (Sigma Aldrich, 99.9%)	21285

7. Appendix II: UV-Vis study of redox-processes and hydrolysis in K_2IrCl_6 /KOH-solutions

UV-Vis-absorption spectra have been used to study the reduction, hydrolysis and condensation phenomena occurring in the KOH/ K_2IrCl_6 precursor solutions used in the MW-supported hydrothermal synthesis. An important goal in preparing these solutions is to hydrolyze Ir-chloride precursors. Indeed chloro-iridate complexes are stable in solution even at high temperature and pressure and do not yield a solid product after hydrothermal treatment.

7.1. UV-Vis studies of solvated Ir-species in the literature

The first thorough description of the electronic structure of hexachloroiridate-III and -IV has been published by C. Jørgensen in 1958.¹ Jørgensen used ligand field theory and nonrelativistic symmetry considerations in order to describe the electronic structure of octahedral halogen iridate complexes. Hexachloroiridate $IrCl_6^{2-}$ is a $5d^5$ low spin complex, presenting strong absorption bands both in the visible and in the UV-range. These bands are mostly due to ligand-to-metal charge transfer (LMCT) and give a deep red/brown color to the complex in water.¹ Jørgensen's non-relativistic assignment of the absorption wavelengths accurately describes the strong LMCT-bands at 232, 410, 434 and 487nm observed for K_2IrCl_6 0,01M dissolved in water. A more accurate description of the electronic structure, involving relativistic effects such as spin-orbit coupling and the description of π -bonding was performed in 1983 by Goursot et al.² and confirmed in 1984 by Lopey and Case³. By taking into account spin-orbit coupling phenomena, Goursot et al. could assign the weak bands observed between 578 and 590nm and at 306nm to a superposition of LMCT bands and d-d transitions resulting from spin-orbit-coupling. The band between 578 and 590nm is especially weak because the LMCT is Laporte-forbidden as it corresponds to the transition from a ligand π -orbital to a metal d-orbital. The dotted line present in Figure 7.1 is the absorption spectra of a 0,01mol.L⁻¹ K_2IrCl_6 solution and is well in line with the features expected for $IrCl_6^{2-}$.

In presence of base, strong changes in the UV-Vis spectrum of $IrCl_6^{2-}$ occur. These changes are sometimes mistaken for hydrolysis of the hexachloroiridate $IrCl_6^{2-}$ complex.⁴ In reality under basic conditions, $IrCl_6^{2-}$, which is a well-known outer-sphere oxidant, first reduces to $IrCl_6^{3-}$ following reaction (5.1):

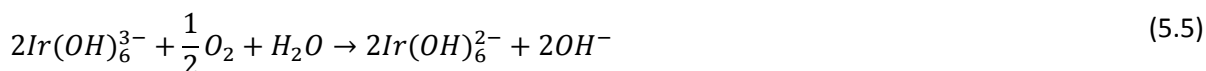


This first rapid step leads to the formation of the $5d^6$ -complex $IrCl_6^{3-}$. The metal- t_{2g} -orbitals are now filled, which explains the disappearance of the strong LMCT-bands. In an early paper, C. Jørgensen described the resulting UV-Vis absorption spectra of $IrCl_6^{3-}$ using crystal field theory.⁵ Two weak bands corresponding to spin-allowed d-d transitions to the singlet state are experimentally observed at 356 and 415nm.

The field of certainties stops at this point, as the hydrolysis pathways and products are a little studied field. Jørgensen already noted that unlike the very stable IrCl_6^{2-} , IrCl_6^{3-} exhibits a strong propensity towards slow hydrolysis. He also noted the uncertainty that remained over the state of aquation of IrCl_6^{3-} over time. Poulsen et al. and Moggi et al. described the aquation rates of IrCl_6^{3-} in acidic media and could observe the aquation of IrCl_6^{3-} to $\text{Ir}(\text{H}_2\text{O})\text{Cl}_5^{2-}$ under heating following reaction (5.2).^{6,7}



In 1976, Beutler and Gamsjäger were the first ones to report the preparation of hexa-aquairidium(III) from IrCl_6^{2-} treated with base following reaction (5.3).⁸ Gamsjäger distinguishes between $\text{Ir}(\text{OH}_2)_6^{3+}$ under acidic/neutral conditions and $\text{Ir}(\text{OH})_6^{3-}$ under basic conditions. In a later paper, the OH^- -exchange kinetics of hexahydroxoiridate-(III) were studied by ^{18}O -labeling exchange experiments.⁹ It was shown that the inner sphere hydroxyl ligands were quite labile and could be easily exchanged at higher $[\text{OH}^-]$. Also at high $[\text{OH}^-]$, monomeric Ir(III)-species are strongly favored, whereas at lower $[\text{OH}^-]$, polymeric Ir-species are suspected. It should also be noted at this point that in all studies, authors emphasize possible re-oxidation of Ir^{3+} to Ir^{4+} by dissolved oxygen following reaction (5.4) and (5.5). After reduction, there is thus a competition between the two slow hydrolysis and re-oxidation reactions described by (5.3), (5.4) and (5.5).



After several hours of hydrolysis in basic conditions, broad bands in the 560-590nm-region are observed. Gamsjäger et al. already mentioned the probable formation of iridium-oligomers. Castillo-Blum et al. were the first to report binuclear, hydroxo- and oxo-bridged aquairidium-complexes produced during hydrolysis.¹⁰ However literature remains very vague on the subject and little characterization is provided. More recently Pankratov et al. proposed a possible mechanism for the formation of binuclear mixed-valence peroxo-bridged iridium complexes.¹¹ They used EPR to prove their findings, investigated however only highly concentrated basic solutions. In this case, as pointed out by Gamsjäger et al. in their ^{18}O -labelling study, oligomeric Ir-species do not form due to the rapid exchange kinetics of hydroxo-ligands in the iridium-complexes. Thus, in the case of lower base:Ir ratios, the chemistry of hydrolysis products might be much more complex with probable formation of iridium-oligomers involving the whole variety of valence states and bonds aforementioned, including the peroxo-bridges evidenced by Pankratov et al.

Table 7.1 Absorption bands of iridium-complexes reported in the literature

Species	Wavelength λ (nm)	Type	Reference
$\text{Ir}^{\text{IV}}\text{Cl}_6^{2-}$	232	LMCT	1,2
	269	d-d transition	2,12
	306	LMCT	2,3,12
		-weak contribution from d-d transition involving spin-orbit coupling	
		LMCT	2,3
	388	d-d transition	2,12
	410	LMCT	1,2
	434	LMCT	1,2
	487	LMCT	1,2
	578-590	-Laporte-forbidden LMCT -d-d transition involving spin-orbit coupling	2,3
$\text{Ir}^{\text{III}}\text{Cl}_6^{3-}$	356	d-d transition to singlet state	5,8,13
	415	d-d transition to singlet state	5,8,13
$\text{Ir}^{\text{III}}(\text{H}_2\text{O})_6^{3+}$	265		8,13
	310-317		5,8,13

7.2. UV-Vis study of precursor solution for the MW-synthesis

For the purpose of understanding processes occurring in the precursor solutions used for the synthesis of pure Ir-oxohydroxides described in chapter 3, solutions containing $0,01\text{mol.L}^{-1}$ K_2IrCl_6 and KOH at various KOH:Ir-ratios were studied using a Lambda 650 UV-vis spectrometer (Perkin Elmer). Figure 7.1 shows the UV-Vis spectra of solutions of K_2IrCl_6 ($0,01\text{mol.L}^{-1}$) mixed with KOH after one hour of ageing at room temperature for varying KOH:Ir ratios. After one hour, all solutions with KOH:Ir above 4:1 exhibited only two weak bands at 346-356 nm and 413-415 nm attributed to the reduction product IrCl_6^{3-} . Only for KOH:Ir=1:1 and 1:10, the LMCT-features of IrCl_6^{2-} are still clearly recognizable, indicating only partial reduction of IrCl_6^{2-} to of IrCl_6^{3-} .

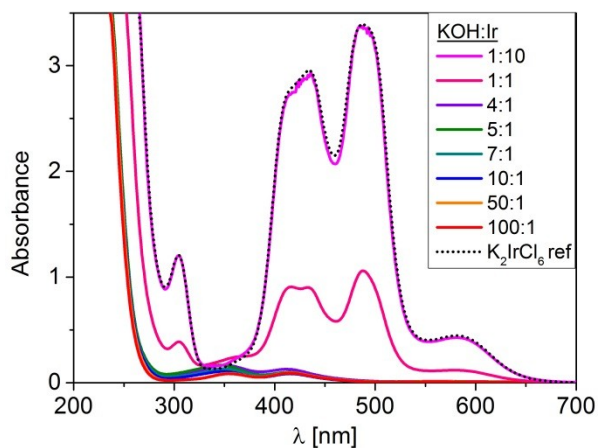


Figure 7.1 UV-Vis absorption spectra of different KOH/ K_2IrCl_6 solutions at RT one hour after mixing (K_2IrCl_6 0,01 mol.L⁻¹, varying KOH:Ir ratio).

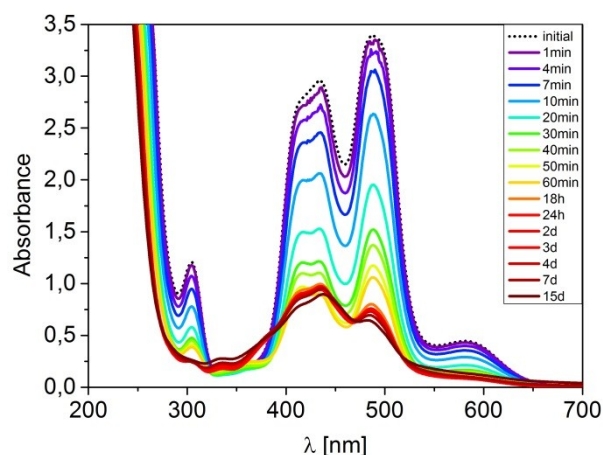


Figure 7.2 UV-Vis absorption spectra of a KOH/ K_2IrCl_6 (KOH:Ir=1:1) solution at RT after mixing over 15 days

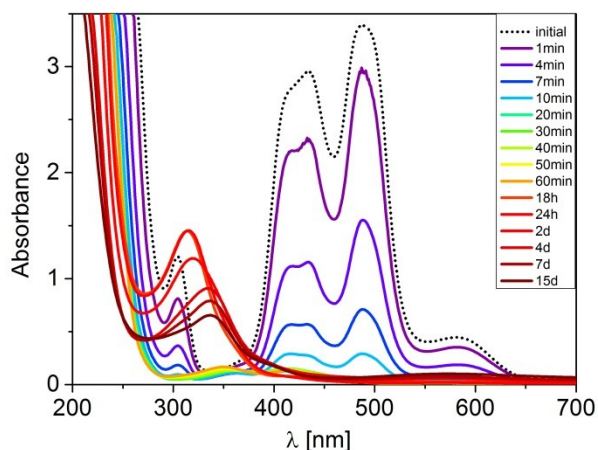


Figure 7.3 UV-Vis absorption spectra of a KOH/ K_2IrCl_6 (KOH:Ir=4:1) solution at RT after mixing over 15 days

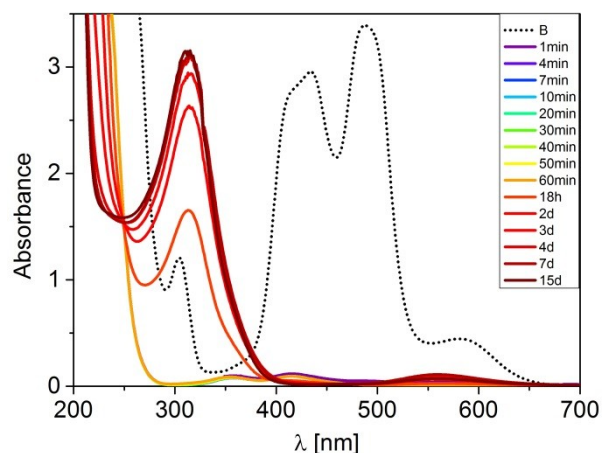


Figure 7.4 UV-Vis absorption spectra of a KOH/ K_2IrCl_6 (KOH:Ir=50:1) solution at RT after mixing over 15 days

UV-Vis spectra could not be recorded during the MW-supported hydrothermal treatment of the precursor solutions. However, the study of the slow evolution of the solutions over time at room temperature also yields information on processes occurring on a more rapid scale during the MW-treatment. Figure 7.2, Figure 7.3 and Figure 7.4 illustrate these phenomena as they show the evolution at room temperature over time of the absorption spectra of K_2IrCl_6 /KOH-solutions with respective ratios of 1:1, 4:1 and 50:1. In the case of the 1:1 ratio, even after 15 days at room temperature, the characteristic $IrCl_6^{2-}$ -LMCT bands are still present in addition to the weak $IrCl_6^{3-}$ bands, indicating unsuccessful hydrolysis. On the other extreme, Figure 7.4 illustrates the evolution of a KOH:Ir=50:1-solution. Reduction to $IrCl_6^{3-}$ was almost instantaneous, with almost complete disappearance of the LMCT-bands after one minute and observed gas bubble evolution. Up to 1h, mostly the $IrCl_6^{3-}$ -bands are visible. Only then slow hydrolysis of $IrCl_6^{3-}$ at room temperature starts and explains the appearance of a strong and stable absorption band at 315 nm attributed to Gamsjäger's hexahydroxoiridiate-(III) complex. Concomitantly, the rise of a weak band at 560 nm is observed (see Figure 7.5). This band could be explained by the presence of the binuclear superoxo-bridged Ir^{IV} -complex proposed by Pankratov et al. that would result from re-oxidation via dissolved

oxygen. The exact nature of the species responsible for such bands remains however to be clarified. It is also to be noted that no precipitates formed. This is in line with the fast hydroxyl ligand exchanges described by Gamsjäger et al. Such processes hinder efficient oligomerization and condensation of a solid product.

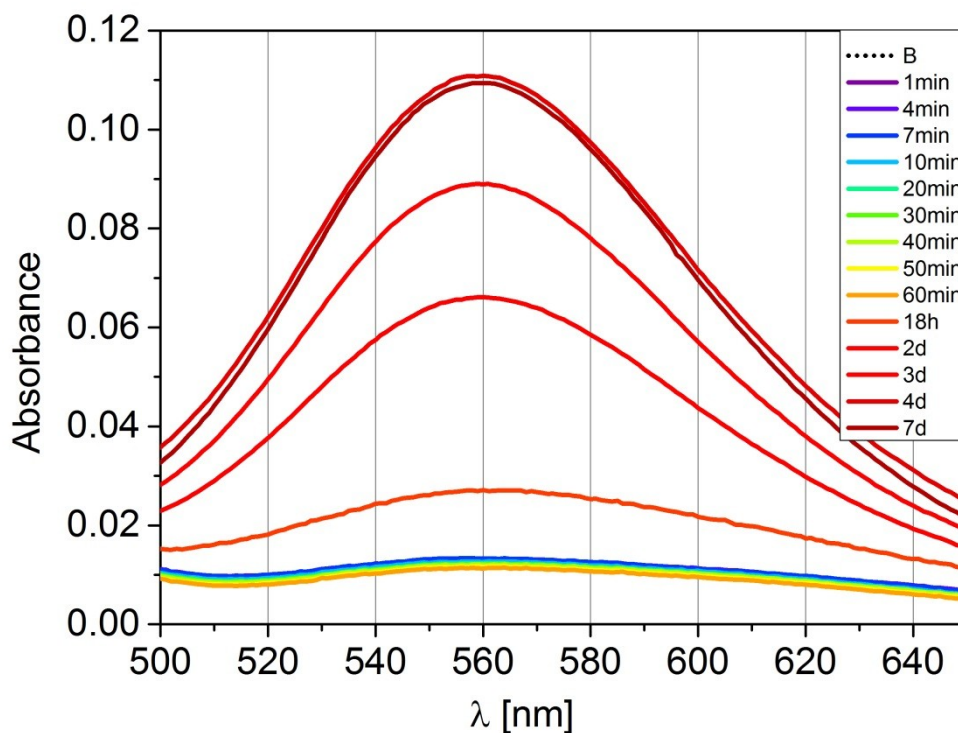


Figure 7.5 Enlargement of the UV-Vis spectra obtained for KOH:Ir=50:1

Figure 7.3 illustrates the case of the KOH:Ir=4:1 solution. In this case the stoichiometry allows for the reduction of IrCl_6^{2-} to IrCl_6^{3-} and for the replacement of the chloride ligands with hydroxyls. At first the spectra behave in a similar fashion as for KOH:Ir=50:1 with total reduction followed by the appearance of a strong absorption band at 315nm attributed to the hexahydroxoiridate-(III). However after reaching a stable maximum between 18 and 24h, after 2 days the band at 315nm diminishes in intensity and shifts towards higher values with a concomitant increase of a very broad band centered around 575nm. Experimentally, after 24h the formation of a precipitate is observed. Taking into account Gamsjäger's observation of oligomeric species formed from hexahydroxoiridate-(III) at lower $[\text{OH}^-]$ it can be suspected that after hydrolysis of IrCl_6^{3-} to hexahydroxoiridate-(III), oligomeric species are formed, that show a strong propensity towards condensation. Thus the KOH:Ir-ratio proves to be critical not only in reducing and hydrolyzing Ir^{IV} -chloride precursors. The remaining $[\text{OH}^-]$ obviously influences the formation and condensation of Ir-oligomers. The fast exchange kinetics of hydroxyl groups in hexahydroxoiridate-(III) at high pH probably hinder oligomer formation and thus explain the preferred monomeric or dimeric species at higher KOH:Ir. A recent report by Zhao et al. also showed that part of the hexahydroxoiridate-(III) formed in such a reaction scheme can be reoxidized by oxygen dissolved from air, leading to the presence of $\text{Ir}^{\text{III/IV}}$ -hydrolysis products in the solution.¹⁴

As a result, it appears that a UV-Vis in-situ study of the during the MW-treatment could yield valuable information on the complex hydrolysis and oligomerization processes leading to the production of Ir^{III/IV}-oxohydroxides. This however presupposes a better understanding of the species in presence, especially those responsible for the broad bands observed after hydrolysis at room temperature in the 560-575 nm region.

7.3. References

- (1) Jørgensen, C. K. *Molecular Physics* **1959**, *2*, 309.
- (2) Goursoot, A.; Chermette, H.; Daul, C. *Inorganic Chemistry* **1984**, *23*, 305.
- (3) Lopez, J. P.; Case, D. A. *The Journal of Chemical Physics* **1984**, *81*, 4554.
- (4) Zhao, Y.; Hernandez-Pagan, E. A.; Vargas-Barbosa, N. M.; Dysart, J. L.; Mallouk, T. E. *Journal of Physical Chemistry Letters* **2011**, *2*, 402.
- (5) Chr. Klixbüll Jørgensen, Å. B. *Acta Chemica Scandinavica* **1956**, *10*, 500.
- (6) Poulsen, I. A.; Garner, C. S. *Journal of the American Chemical Society* **1962**, *84*, 2032.
- (7) Moggi, L.; Varani, G.; Manfrin, M. F.; Balzani, V. *Inorganica Chimica Acta* **1970**, *4*, 335.
- (8) Beutler, P.; Gamsjäger, H. *J. Chem. Soc., Chemical Communications* **1976**, 554.
- (9) Rodgers, K. R.; Gamsjaeger, H.; Murmann, R. K. *Inorganic Chemistry* **1989**, *28*, 379.
- (10) Silvia E. Castillo-Blum, D. T. R. *Journal of the Chemical Society, Chemical Communications* **1986**.
- (11) Pankratov, D. A.; Komozin, P. N.; Kiselev, Y. M. *Russian Journal of Inorganic Chemistry* **2011**, *56*, 1794.
- (12) Glebov, E. M.; Pozdnyakov, I. P.; Melnikov, A. A.; Chekalin, S. V. *Journal of Photochemistry and Photobiology A: Chemistry* **2014**, *292*, 34.
- (13) Ioroi, T.; Kitazawa, N.; Yasuda, K.; Yamamoto, Y.; Takenaka, H. *Journal of the Electrochemical Society* **2000**, *147*, 2018.
- (14) Zhao, Y.; Vargas-Barbosa, N. M.; Strayer, M. E.; McCool, N. S.; Pandelia, M.-E.; Saunders, T. P.; Swierk, J. R.; Callejas, J. F.; Jensen, L.; Mallouk, T. E. *Journal of the American Chemical Society* **2015**, *137*, 8749.

8. Appendix III: ICP-OES-study of Ir-dissolution during OER-catalysis

In order to assess the importance of Ir-dissolution via corrosive processes during OER, selected Ir-compounds were tested in a custom-made electrochemical flow-through cell allowing for time-resolved analysis of dissolved species in the flowing electrolyte via ICP-OES.

8.1. Experimental setup

The cell body and all channels (diameter 2 mm) were mechanically manufactured from Polyether ether ketone (PEEK), and the electrolyte inlet and outlet were connected via Tygon® tubing (2 mm inner diameter). Both channels were connected in a straight line. The flow channels, the working- and counter-electrodes at the bottom of the cell were encircled with a silicone gasket to avoid electrolyte leaks and in order to protect the flow cell channels and working electrode from contaminations. A coil-shaped platinized platinum wire (125 µm diameter, 99.99%, Science Products GmbH), placed along the flow channel following the electrolyte flow, was used as the counter electrode, while the reference electrode (SCE, Gamry, reference potential +241 mV vs. SHE) was inserted in a separate compartment. A 1mm Luggin capillary-like channel allows connectivity between the working and the reference electrode compartment. All potentials are expressed vs the SHE potential scale. The potentiostat used for the electrochemical measurements is a Bio-Logic SP-150, while the embedded EC-Lab software was used to electrochemically monitor the catalysts.

The resulting electrolyte stream is continuously fed into the ICP-OES (Spectroblue EOP, Ametek) by means of a peristaltic pump at a flow rate of 0.33 mL.min⁻¹, through a quartz nebulizer operating at nebulizer gas flow rates of between 0.8 and 0.85 L.min⁻¹ (Ar, purity 99,999%). Transient signals of Ir were recorded continuously with an integration interval of 100 ms and 2 sweeps per reading. Calibration was performed using 7 standard solutions (100, 50, 10, 5, 1, 0.5 ppm Ir and a blank solution prepared from Merck CertiPUR®). The RF power was set to 1400 W with a plasma gas flow rate of 15 L.min⁻¹.

Catalyst inks were prepared by suspending 4 mg of catalysts in 6 mL Millipore-filtered H₂O and 4 mL of isopropanol (Sigma Aldrich). The suspension was subsequently sonicated for 30min. The resulting ink was then drop-casted onto the anode by using a micropipette in order to reach an iridium-loading of 50 µg_{Ir}.cm⁻² and dried for 30 min at 60°C. The electrolyte consisted of a 0.5 mol.L⁻¹ H₂SO₄-solution.

The samples were examined using an electrochemical standard protocol. All electrochemical measurements were corrected at 85% for ohmic drop using high-frequency impedance spectroscopy (4 measurements, 100 kHz, 20 mV amplitude, open circuit potential, E_{oc}). A first LSV to 1,6 V vs. RHE at 5 mV.s⁻¹ was used to assess the initial sample activity. After 1 min at open circuit potential, current densities were ramped up by 10 µA.s⁻¹ to 10 mA.cm⁻² and maintained at this value for two hours in a typical CP-based stability test. The concomitant corrosion-related dissolution of Ir in the solution was studied via ICP-OES-based screening of the flowing electrolyte.

8.2. Results

Recorded CP-curves curves appeared very noisy in comparison to the results obtained using RDE-electrodes, which is due to the more efficient bubble-removal under rotation. Otherwise, the anodic potential-curves were in line with the CP-curves obtained on RDE (see Figure S3.16). Dissolved Ir-traces remained extremely low for all samples throughout the 2h-CP-measurement. Levels of approx. 15 ppb are too close to the detection limit of ICP-OES to distinguish Ir-signals from background noise. However during the initial current ramp to $10 \text{ mA}\cdot\text{cm}^{-2}$, stronger Ir-signals reaching 50 and 40 ppb were recorded for respectively MW_7 (Figure 8.1.c) and MW_50 (Figure 8.1.d). Such signals might be linked to loosely attached Ir-particles removed mechanically by oxygen bubbles during the onset of OER at $10 \text{ mA}\cdot\text{cm}^{-2}$. Broader Ir-dissolution features were observed for the AA-IrO_x benchmark (Figure 8.1.a) and the best OER-catalyst MW_5 (Figure 8.1.b). These more important Ir-dissolution features were observed for up to 15 min in the case of MW_5 (Figure 8.1.b) but remained at levels below 30 ppb. Mechanical removal of loosely attached Ir-particles might again account for such observations.

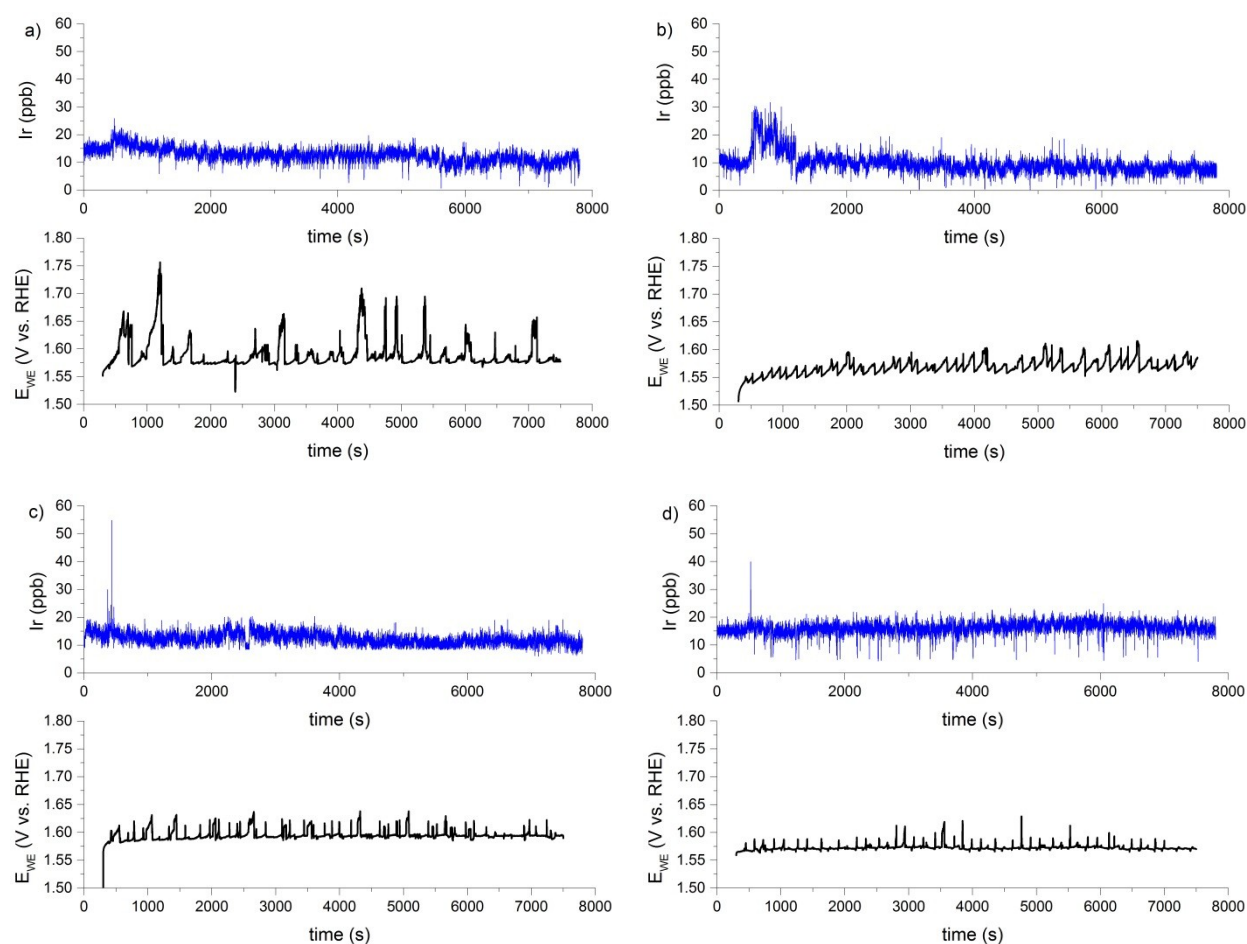


Figure 8.1 Ir-species detected via ICP-OES (blue lines) in the electrolyte flowing through an electrochemical water splitting cell during a CP-measurement conducted at $10 \text{ mA}\cdot\text{cm}^{-2}$ (anode potentials in black vs. SHE) for anodes coated with (a) AA-IrO_x, (b) MW_5, (c) MW_7, (d) MW_50.

Strikingly, despite similar behavior during the CP-test for all four samples, major changes in OER-activity were observed when comparing the initial and final LSV-based activity assessment (Figure 8.2). MW_5 was the only compound that didn't show major changes in OER-activity, remaining the

most active compound (Figure 8.2.b). On the opposite, AA-IrO_x, MW_7 and MW_50 showed all three a significant decrease in OER-activity, reflected by weaker LSV-slopes. This effect is less strong for MW_7. This indicates that all samples but MW_5 were significantly deactivated during CP at 10 mA.cm⁻².

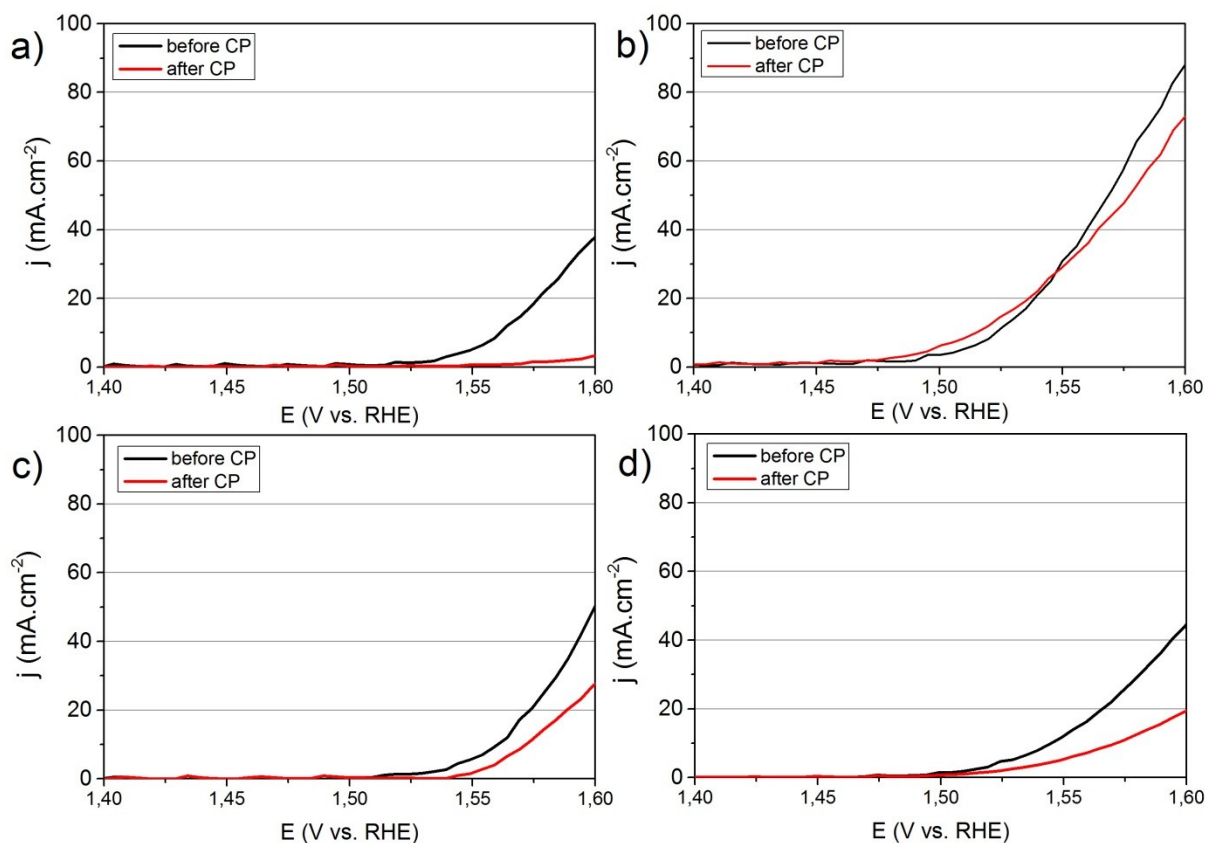


Figure 8.2 LSV-measurements (5 mV.s⁻¹) before (black line) and after the 2h-CP-stability test (red line) for (a) AA-IrO_x, (b) MW_5, (c) MW_7, (d) MW_50.

Since MW_5 was the samples that showed the most significant, albeit small, Ir-dissolution and yet remained the most stable, we conclude that the deactivation of Ir-oxohydroxides under acidic OER-conditions at potentials below 1,6 V vs. RHE cannot be explained solely based on corrosion-related Ir-dissolution. Otherwise, one would have expected strong Ir-dissolution signals, especially for AA-IrO_x, which was the most significantly deactivated. As a result, other phenomena must be responsible for the significant deactivation of AA-IrO_x, MW_7 and MW_50. We suggest that potential-dependent alterations to the particular Ir^{III/IV}-oxohydroxide structure might be responsible for the deactivation. A similar in-situ study relying on XPS and NEXAFS to study structural changes in the Ir^{III/IV}-oxohydroxide might yield important clues on such potential-dependent modifications. Differences observed between MW_5 and other compounds should reveal features responsible for the superior resilience of MW_5.

9. Information about the author

Personal information

Name Cyriac Massué
Date of birth 12/06/1987
Email cyriac.massue@polytechnique.org

Education

Since 2012 *Fritz-Haber Institute of the Max-Planck Society, Berlin (Germany)*
AC Department (Prof. Schloegl)
PhD student as part of the “Ekolyzer” project
The focus of the project is energy storage through hydrogen production. The aim is set on the development of a cost-effective PEM-electrolyzer setup that could be implemented on a large scale into a power grid relying on renewable energy sources.

2010 – 2011 *Eidgenössische Technische Hochschule, Zürich (Switzerland)*
MSc Chemistry

2007 – 2010 *Ecole Polytechnique, Paris (France)*
Ingénieur diplômé de l’Ecole Polytechnique

2005 – 2007 *Lycée Sainte-Geneviève, Versailles (France)*
post-secondary program (*classe préparatoire*) leading to France’s nationwide entrance exams to the *Grandes Ecoles*

2005 *Lycée International des Pontonniers, Strasbourg (France)*
French and German High School Graduation

List of publications

- [1] F. Conrad, C. Massué, S. Kühn, E. Kunkes, F. Girgsdies, I. Kasatkin, B. Zhang, M. Friedrich, Y. Luo, M. Armbrüster, G. R. Patzke, M. Behrens: Microwave-hydrothermal synthesis and characterization of nanostructured copper substituted ZnM_2O_4 ($M = Al, Ga$) spinels as precursors for thermally stable Cu catalysts; *Nanoscale*, **2012**, 4, 2018-2028
- [2] V. Pfeifer, T. E. Jones, J. J. Velasco Vélez, C. Massué, R. Arrigo, D. Teschner, F.

Girgsdies, M. Scherzer, M. T. Greiner, J. Allan, M. Hashagen, G. Weinberg, S. Piccinin, M. Hävecker, A. Knop-Gericke, R. Schlögl: The electronic structure of iridium and its oxides; *Surface and Interface Analysis*, **2015**, n/a-n/a

- [3] V. Pfeifer, T. E. Jones, J. J. Velasco Vélez, C. Massué, M. T. Greiner, R. Arrigo, D. Teschner, F. Girgsdies, M. Scherzer, J. Allan, M. Hashagen, G. Weinberg, S. Piccinin, M. Hävecker, A. Knop-Gericke, R. Schlögl: The electronic structure of iridium oxide electrodes active in water splitting; *Phys Chem Chem Phys*, **2016**, *18*, 2292-2296

Talks at conferences

- 3/2016** 18th ISE Topical Meeting "Oxygen Electrocatalysis in Chemical Energy Conversion and Storage Technologies", Gwangju, Korea; Title: The role of amorphous Ir-oxohydroxides for the Oxygen Evolution Reaction
- 6/2013** 3rd Russian-German Seminar on Catalysis "Bridging the Gap between Model and Real Catalysis. Energy-Related Catalysis", Burduguz, Russia; Title: Mn/Sn-mixed oxides for the Oxygen Evolution Reaction

Poster contributions at conferences as presenting author

- 3/2016** 18th ISE Topical Meeting "Oxygen Electrocatalysis in Chemical Energy Conversion and Storage Technologies", Gwangju, Korea; Title: Characterization of amorphous Ir-oxohydroxides for the Oxygen Evolution Reaction
- 8/2015** 12th European Congress on Catalysis "Catalysis: Balancing the use of fossil and renewable resources", Kazan, Russia; Title: Mn-based water oxidation catalysts supported on tin oxide and TaON.
- 8/2013** EMRS IVth World Materials Summit, "Materials: A key enabling technology for secure energy & sustainable development", Strasbourg, France; Title: Making energy storage affordable. Mn-based Water Oxidation Catalysts for H₂-production.